

# **First-Principles Studies of Transition Metal Doped Systems and Hyperfine Coupling Constants of Muoniated Butyl Radicals**

by

Yakun Chen

B.Sc., Peking University, Beijing, China, 1999

M.Sc., Institute of Chemistry, Chinese Academy of Sciences, Beijing, China, 2003

A THESIS SUBMITTED IN PARTIAL FULFILMENT OF  
THE REQUIREMENTS FOR THE DEGREE OF

DOCTOR OF PHILOSOPHY

in

The Faculty of Graduate Studies

(Chemistry)

The University Of British Columbia

(Vancouver)

March, 2010

© Yakun Chen 2010

# Abstract

The first part of the thesis examines, using density functional theory (DFT) calculations, the effects of introducing transition metals (TMs) into different systems, including small Au clusters; carbon nanotubes (CNTs); pristine and defected boron nitride nanotubes (BNNTs). The results show that the frontier molecular orbitals of the TM modified systems are usually localized around the doping site and the reactivities of these systems are often improved. In the case of small TM clusters, both  $\text{PtAu}_m$  and  $\text{Au}_n$  tend to be planar in their ground state.  $\text{N}_2$  and  $\text{O}_2$  adsorption onto these clusters results in different adsorption configurations due to different orbital interactions. With regard to the TM modified CNTs, the endo-TM-doped CNTs are less stable than the corresponding exo-doped isomers due to the large geometric strain caused by deformation. The exo-doped SWCNTs are better electron donors than their endo-doped counterparts. As for the Pt modified BNNTs, binding energy analysis revealed that a Pt atom can move freely on a pristine BNNT. But the Pt atom is trapped between the B–B bond at the defect site if a Stone-Wales defect exists. In both cases, the hosting BNNTs are wide-gap semiconductors with slightly improved reactivities. In comparison, BNNTs doped with Pt atoms are narrow-gap semiconductors with greatly enhanced reactivities.

Both MP2/EPR-III and B3LYP/EPR-III calculations were used to optimize butyl isomers and calculate hyperfine coupling constants (HFCCs) to explain experimental data. The C–Mu distance was elongated to 1.076 times the corresponding equilibrium C–H bond length to mimic vibrationally average  $\beta$ -muoniated radical geometries so as to calculate the muon HFCCs. Some muon HFCCs and most proton HFCCs were satisfactorily reproduced by the B3LYP calculations due to error cancellations, whereas other cases were better predicted by the MP2 calculations. The torsional potential energy surface (PES) of the sec-butyl radical was also studied. The cis conformation, which was observed in experiments, was unobtainable using some common DFT functionals, but can be identified by calculations using wavefunction theory or some modified hybrid functionals. Changes in basis set only modify the shape of the PES slightly.

# Table of Contents

<b>Abstract</b>	ii
<b>Table of Contents</b>	iii
<b>List of Tables</b>	vi
<b>List of Figures</b>	viii
<b>List of Abbreviations</b>	xiii
<b>Acknowledgements</b>	xv
<b>Dedication</b>	xvii
<b>Statement of Co-Authorship</b>	xviii
<b>Chapter 1 Introduction</b>	1
1.1 Schrödinger equation	1
1.2 Born-Oppenheimer approximation	2
1.3 Wavefunction theory	3
1.3.1 Hartree-Fock theory	4
1.3.2 Correlated wavefunction theory	5
1.4 Density functional theory	9
1.4.1 Theoretical foundation of DFT	9
1.4.2 Kohn-Sham DFT	10
1.4.3 Approximate functionals	11
1.4.4 Chemical concepts associated with DFT	13
1.5 Transition metals in different environments	14
1.5.1 TM clusters—Chapter 2	14
1.5.2 TM doped SWCNTs—Chapter 3	15
1.5.3 Interactions between Pt and BNNTs—Chapter 4	16
1.6 Hyperfine coupling constants of muoniated radicals	17
1.6.1 Muon HFCC calculations—Chapter 5	17

1.6.2 Torsional PES of sec-butyl radical—Chapter 6 . . . . .	19
<b>Bibliography . . . . .</b>	<b>20</b>
<b>Chapter 2 Theoretical Studies of Au<sub>m</sub> and PtAu<sub>n</sub> Clusters and Their N<sub>2</sub> and O<sub>2</sub> Adsorption</b>	
<b>Complexes . . . . .</b>	<b>25</b>
2.1 Introduction . . . . .	25
2.2 Computational details . . . . .	26
2.3 Results and discussions . . . . .	27
2.3.1 Au <sub>m</sub> and PtAu <sub>n</sub> clusters . . . . .	27
2.3.2 Adsorptions of N <sub>2</sub> and O <sub>2</sub> . . . . .	32
2.3.3 N <sub>2</sub> and O <sub>2</sub> adducts . . . . .	35
2.4 Conclusions . . . . .	41
<b>Bibliography . . . . .</b>	<b>42</b>
<b>Chapter 3 Theoretical Studies of Transition Metal-Doped Single-Walled Carbon Nanotubes</b>	
. . . . .	46
3.1 Introduction . . . . .	46
3.2 Computational details . . . . .	48
3.3 Results and discussions . . . . .	50
3.4 Conclusion . . . . .	57
<b>Bibliography . . . . .</b>	<b>58</b>
<b>Chapter 4 Density Functional Study of Interaction of Atomic Pt with Pristine and Stone-</b>	
<b>Wales-Defected Single-Walled Boron Nitride Nanotubes . . . . .</b>	<b>61</b>
4.1 Introduction . . . . .	61
4.2 Computational details . . . . .	63
4.3 Results and discussions . . . . .	64
4.3.1 Pristine and SW-defected (5,5) BNNTs . . . . .	64
4.3.2 Pt absorption on pristine and SW-defected BNNTs . . . . .	66
4.3.3 Pt-doped (5,5) BNNTs . . . . .	69
4.4 Conclusion . . . . .	71
<b>Bibliography . . . . .</b>	<b>72</b>
<b>Chapter 5 First-Principles Studies of the Hyperfine Coupling Constants for Muoniated</b>	
<b>Butyl Radicals . . . . .</b>	<b>5</b>
5.1 Introduction and background . . . . .	75
5.2 Remarks on the calculations . . . . .	78



5.3	Methodology and results . . . . .	79
5.3.1	Geometries and molecular structures . . . . .	79
5.3.2	Overview of HFCC calculations . . . . .	83
5.3.3	Vibrational averaging of muon HFCCs . . . . .	85
5.3.4	Benchmark calculations for HFCCs . . . . .	87
5.4	Results and discussion: comparisons with experiment . . . . .	89
5.4.1	Isobutyl and tert-butyl radicals formed from isobutene . . . . .	89
5.4.2	Sec-butyl radicals formed from 2-butene . . . . .	93
5.4.3	Sec-butyl radicals formed from 1-butene . . . . .	96
5.5	Overall performance of theoretical calculations . . . . .	98
5.6	Conclusions . . . . .	99
<b>Bibliography . . . . .</b>		<b>102</b>
<b>Chapter 6 First-principles Studies of the Torsional Potential Energy Surface of the Sec-Butyl Radical . . . . .</b>		<b>108</b>
6.1	Introduction . . . . .	108
6.2	Computational details . . . . .	110
6.3	Results and discussions . . . . .	110
<b>Bibliography . . . . .</b>		<b>119</b>
<b>Chapter 7 Conclusions and Future Directions . . . . .</b>		<b>121</b>
<b>Bibliography . . . . .</b>		<b>126</b>
<b>Appendices</b>		
<b>Appendix A Supporting Information for Chapter 3 . . . . .</b>		<b>127</b>

# List of Tables

Table 2.1	Natural electron configurations of atoms of the low-lying clusters. The atomic sites are shown in Figure 2.1. . . . .	29
Table 3.1	Relative energies (in eV) for each TM-doped SWCNT of different doping configuration and spin multiplicity. The data of the most stable exo- and endo-doped SWCNTs are shown in the third column. Spin multiplicities are shown in the parentheses. . . . .	50
Table 3.2	Calculated partial charges and spin charges of the most stable endo- and exo-doped SWCNTs. In columns 2 to 4, the first and second numbers of each pair are for the endo- and exo-doped systems, respectively. . . . .	53
Table 4.1	Bond lengths (in Å), binding energies (in kcal/mol), and partial charges on Pt for Pt absorptions on pristine (5,5) BNNTs at different sites. Symmetrically equivalent bonds are only listed once. . . . .	65
Table 4.2	Bond lengths (in Å), binding energies (in kcal/mol), and partial charges on Pt for Pt absorptions on type-1 SW-defected (5,5) BNNTs at different sites. . . . .	67
Table 4.3	Surrounding bond lengths (in Å), partial charges and spin densities of Pt in Pt-doped (5,5) BNNTs. . . . .	71
Table 5.1	Calculated proton and muon HFCCs of butyl and Mu-butyl isomers. Atoms are labeled according to Figure 5.2. In the last column, the ‘H’ in the parenthesis denotes that the HFCCs were calculated at their equilibrium structures for the unsubstituted radicals (H atoms only). The ‘Mu’ in the parenthesis means that the HFCC highlighted in <i>italic</i> was calculated based on the structure, whose C–Mu bond was intentionally stretched to 1.076 times the equilibrium C–H bond length. The HFCC values for 1-butyl (n4) were based on the geometry from MP2/EPR-II calculations. . . . .	84
Table 5.2	Experimental and theoretical HFCCs (in MHz) for protons in unsubstituted ethyl and for muons and protons in muoniated ethyl. The MP2/EPR-III and B3LYP/EPR-III calculations for the Mu-ethyl radical were carried out on a modified geometry whose C–Mu bond was stretched to 1.076 times the equilibrium C– bond length. . . . .	88

Table 6.1 Relative energies and geometric parameters of the stationary structures of the sec-butyl radical. The numbers in each column are calculated at MP2/cc-pVDZ (before the slash) and B3LYP/cc-pVDZ (after the slash) levels, respectively. Bond lengths are in Å. Bond angles and dihedral angles ( $\theta$ ) are in degrees. Energies are in kcal/mol. Relative energies ( $E_{ele}$ ) are measured from the global minimal trans-like confirmation. The vibrationally corrected energies are shown in the last two columns for regular (hydrogen) and muoniated isotopomers, respectively. . . . . 117

# List of Figures

Figure 1.1	A graphene hexagonal sheet and two unit chiral vectors $a_1$ and $a_2$ that are used to define chiral vectors. Dark black dots indicate that rolling up according to these chiral vectors will result in metallic SWCNTs. . . . .	16
Figure 2.1	Optimized structures of low-lying $Au_m$ and bimetallic $PtAu_n$ clusters. The Pt and Au atoms are in dark green and yellow, respectively. For open-shell clusters, natural spin charge on each atomic site is also shown. . . . .	28
Figure 2.2	The frontier orbitals of $Au_m$ and $PtAu_n$ clusters. The orbital energies of the highest occupied molecular orbitals and the lowest unoccupied molecular orbitals are marked by black and red bars, respectively. For open-shell systems, $\alpha$ -spin and $\beta$ -spin orbitals are grouped on the left and the right of each column, respectively. . . . .	31
Figure 2.3	The optimized structures of $N_2$ -cluster adsorption complexes. The relative energy (in kcal/mol) measured from the most stable complex, the adsorption energy (in kcal/mol), the N–N bond length (in Å), and the HOMO-LUMO gap (in eV) are listed below each optimized structure descendingly. For open-shell systems, the first and the second values of the HOMO-LUMO gap are for $\alpha$ spin and $\beta$ spin, respectively. . . . .	33
Figure 2.4	The optimized structures of $O_2$ -cluster adsorption complexes. The relative energy (in kcal/mol) measured from the most stable complex, the adsorption energy (in kcal/mol), the N–N bond length (in Å), and the HOMO-LUMO gap (in eV) are listed below each optimized structure descendingly. For open-shell systems, the first and the second values of the HOMO-LUMO gap are for $\alpha$ spin and $\beta$ spin, respectively. . . . .	34
Figure 2.5	The total density of states (DOS) and local DOS (LDOS) projected onto each element of the $PtAu_2-N_2$ and $PtAu_2-O_2$ adducts. Green vertical lines mark the Fermi levels. . . . .	38
Figure 2.6	Molecular orbitals relevant to the bonding interactions between the diatomic fragment and the $PtAu_2$ fragments in the $PtAu_2N_2$ and $PtAu_2O_2$ adducts. HOMO– $p$ denotes the $p$ th orbital below the HOMO. Orbital energies (in eV) are shown in the parentheses. Partial charges are marked beside atomic sites. . . . .	39

Figure 2.7	Natural spin densities of the atoms in the open-shell $N_2/O_2$ -cluster complexes. The Pt, Au, N, and O atoms are in dark green, yellow, blue, and red, respectively. . . . .	40
Figure 3.1	Schematic drawings of the model (5,5) SWCNT with partial charge distribution, doping site, and doping configurations. The dopant, labelled by ‘X’, is surrounded by three neighboring carbon atoms (C1, C2, and C3). X–C1 is a vertical bond; X–C2 and X–C3 are slant bonds. The partial charge distribution in the exo-Sc-doped (5,5) SWCNT is also shown as a color overlay in (c). The values of partial charges are scaled according to the colored bar at the bottom. Color green indicates a positive charge and color red, a negative charge. The darker the color (red or green), the larger the magnitude of the partial charge on the atom. . . . .	49
Figure 3.2	Geometric parameters of the pristine and TM-doped SWCNTs. The rest parameters are measured on the Y-axis of the left side. The covalent radius of each element is reproduced from Ref. 28. Translational vectors are indicators of the elongation along the longitudinal direction. . . . .	52
Figure 3.3	Frontier crystal orbitals of the pristine, Sc-, and Fe-doped SWCNTs. Orbital energies (in eV) are shown in the parentheses. . . . .	55
Figure 3.4	Density of states (DOS) of the exo-Sc-doped (5,5) SWCNT. The DOS of $\alpha$ -spin and $\beta$ -spin electrons are shown in the upper and lower panels, respectively. Fermi levels are marked by the vertical dotted lines. . . . .	56
Figure 4.1	Optimized geometries, frontier orbitals, and density of states (DOS) of pristine and Stone-Wales-defected (5,5) BNNTs. Blue and pink spheres represent N and B atoms, respectively. Orbital energies are shown in the parentheses. In the DOS plots, black curves indicate the total DOS, while blue and green curves indicate N and B local DOS, respectively. Red vertical lines mark the Fermi levels. . . . .	64
Figure 4.2	Optimized geometries, frontier orbitals, and density of states (DOS) of Pt-adsorbed pristine (5,5) BNNTs. Purple, blue, and pink spheres represent Pt, N, and B atoms, respectively. Orbital energies are shown in the parentheses. In the DOS plots, black curves indicate the total DOS, while purple, blue, and green curves indicate Pt, N and B local DOS, respectively. Red vertical lines mark the Fermi levels. . . . .	66
Figure 4.3	Optimized geometries, frontier orbitals, and density of states (DOS) of Pt-adsorbed type-1 Stone-Wales-defected (5,5) BNNTs. Purple, blue, and pink spheres represent Pt, N, and B atoms, respectively. Orbital energies are shown in the parentheses. In the DOS plots, black curves indicate the total DOS, while Purple, blue, and green curves indicate Pt, N, and B local DOS, respectively. Red vertical lines mark the Fermi levels. . . . .	68

Figure 4.4	Optimized geometries, frontier orbitals, and density of states (DOS) of Pt-doped (5,5) BNNTs. Purple, blue, and pink spheres represent Pt, N, and B atoms, respectively. Orbital energies are shown in the parentheses. In the DOS plots, black curves indicate the total DOS, while purple, blue, and green curves indicate Pt, N, and B local DOS, respectively. Red vertical lines mark the Fermi levels. The curves above the x-axis indicate $\alpha$ -spin DOS and those below, $\beta$ -spin components. . . . .	70
Figure 5.1	Hydrogenation or muonation (Mu) of different butene isomers. Only the carbon skeleton is shown. The dots on the product side indicate locations of the radical center. The identification of possible conformers are given in parentheses and their corresponding geometries are displayed in Figs. 5.2 and 5.3. . . . .	80
Figure 5.2	Optimized structures of ethyl, tert-butyl (or t-butyl), isobutyl, sec-butyl, and n-butyl radicals. H and C atoms are shown by small (light) and large (dark) spheres, respectively. . . . .	81
Figure 5.3	Optimized gauche and cis conformations of 1-butene. H and C atoms are shown by small (light) and large (dark) labeled spheres, respectively. . . . .	82
Figure 5.4	Figure 3 in paper I. Temperature dependences for the muon HFCC, $A'_\mu(T)$ , for the Mu-t-butyl (solid cyan-blue triangles, present experiment study; shaded green squares from Ref. 44; shaded brown squares, from Ref. 65) and Mu-isobutyl (solid black triangles, present study). Error bars in the present study are meant to reflect estimates of systematic error as well. Also shown are EPR data points for the unsubstituted isobutyl radical (solid green circles and green trend lines). The colored trend lines are based on classical calculations for different torsional barriers (see legend) and several theory points are plotted on the Y-axis at 0 K, discussed in paper I. The vertical dashed line denotes the melting point of bulk isobutene, at 133 K. The sharp discontinuity in $A'_\mu(T)$ for the muoniated t-butyl is noteworthy. . . . .	90
Figure 5.5	Figure 4 in paper I. Temperature dependences for the $\beta$ -proton HFCC, $A_p(T)$ , for the muoniated and unsubstituted t-butyl radicals. Upper data points and plots for the $\text{CH}_3$ protons of muoniated t-butyl (present experimental data, solid magenta triangles; data from Ref. 44, shaded purple squares). The two solid green circles are representative of EPR measurements for the methyl protons of the unsubstituted radical, indicated by the temperature-independent (dashed-black) guide line, with that for the $\mu\text{SR}$ data falling just below (dot-dashed green line). The red and magenta trend lines shown are classical calculations for the temperature dependence for very different torsional barriers (see legend), and are discussed in paper I, as are the theory points shown at 131 and 28 MHz on the Y-axis at 0 K. Note the marked increase in methyl proton HFCC at low temperature (red line). It is also noteworthy that there is no discontinuity in these proton HFCCs at the phase transition. . . . .	91

Figure 5.6 Figure 12 in paper I. Temperature dependences for the HFCCs,  $A'_\mu(T)$  and  $A_p(T)$ , for the sec-butyl radicals formed from cis- and trans-2-butene. The black triangles and guide line to the eye are  $A'_\mu(T)$  for the cis isomer, while the cyan-blue triangles and fitted trend line is for the trans isomer. Small differences seen in the muon HFCCs between cis and trans isomers in the solid phase are not seen in the liquid (the cis points have been shifted by 3 K for clarity). Noteworthy are the distinct discontinuities seen in  $A'_\mu(T)$  for both the Mu-sec-butyl isomers at the melting point of their parent 2-butenes (134 K for cis-2-butene, vertical dashed line) and (168 K for trans-2-butene, vertical dotted line). The red triangles and fitted red trend line are the  $\beta$ -proton HFCC for the  $\text{CH}_3$  group of the Mu-sec-butyl radical formed from trans-2-butene,  $A_{p,\text{CH}_3}(T)$ . The dramatic discontinuity seen in  $A_{p,\text{CH}_3}(T)$  is also noteworthy. The short broken-red guide line is the same proton environment in the liquid phase. The lower data points and fitted magenta trend line are the proton HFCC of the CHMu group for both the cis (green triangles) and trans (magenta) isomers, which are indistinguishable by experiment. Note the lack of any discontinuity in these CHMu proton HFCCs at the bulk melting points. A number of calculated HFCCs are shown on the Y-axis at 0 K and these, along with the fitted color trend lines, are discussed in paper I. . . . . 94

Figure 5.7 Figure 8 in Paper I. Temperature dependences for the HFCCs of reduced muon,  $A'_\mu(T)$ , and proton  $A_p(T)$ , of the sec-butyl radical formed from Mu addition to 1-butene. The cyan-blue triangles and fitted blue trend line are for the  $A'_\mu(T)$  data, while the red triangles, and red and orange trend lines are DFT- and MP2-calculated fits for  $A_{p,\text{CH}_2}(T)$  in the solid and liquid phases, respectively. The magenta triangles and fitted magenta trend line are the experimental data and DFT-calculated HFCCs for  $A_{p,\text{CH}_2\text{Mu}}(T)$ , with the mauve triangles and guide line to the data for the  $\gamma$ -protons of the terminal methyl groups,  $A_{p,\gamma-\text{CH}_3}(T)$ . The three uppermost black triangles and the black curve are liquid phase experimental data and the trend line (based on MP2 calculations) for the muoniated n-butyl formed from 1-butene, respectively. EPR data are also shown for the proton HFCCs of the unsubstituted sec-butyl radical. The solid orange circles are for the methylene protons and solid green circles for the terminal methyl group. The fitted torsional barriers from the colored trend lines are shown in the legend. Theoretical results are discussed in paper I. The vertical dashed line at 88 K marks the melting point of bulk 1-butene. It is noteworthy that there is no discontinuity at the phase transition for the temperature-dependent muon HFCCs, whereas there is a gap for the proton HFCCs of the methylene group of muoniated sec-butyl formed from 1-butene. . . . . 97

Figure 6.1	Optimized structures of the stationary points on the torsional potential energy surface of the sec-butyl radical. . . . .	111
Figure 6.2	Torsional energy profiles of the sec-butyl radical predicted: (a) from different theoretical methods with the cc-pVDZ basis set; (b) from DFT methods with the cc-pVDZ basis set, showing no cis-like conformation; (c) from DFT methods with the cc-pVDZ basis set, showing relative flat curves around $\theta = 55^\circ$ ; (d) from DFT methods with the cc-pVDZ basis set, showing the cis-like conformation; (e) from B3LYP methods with different basis sets; (f) from MP2 methods with different basis sets. . . . .	113
Figure A.1	Band structures for pristine and doped (5,5) SWCNTs. For spin-unsaturated systems, the left panel is for $\beta$ spin and the right panel, $\alpha$ spin. . . . .	130



# List of Abbreviations

BNNT	boron nitride nanotube
BO	Born-Oppenheimer
BOA	Born-Oppenheimer approximation
CASSCF	complete active space self consistent field
CC	coupled cluster
CCSD	coupled cluster singles and doubles
CCSD(T)	coupled cluster singles, doubles, and perturbative triples
CI	configuration interaction
CISD	configuration interaction singles and doubles
CNT	carbon nanotube
DFT	density functional theory
DOS	density of states
EPR	electron spin resonance
FMO	frontier molecular orbital
FT	Fourier transform
GGA	generalized gradient approximation
hBN	hexagonal boron nitride
HEG	homogeneous electron gas
HF	Hartree-Fock
HFCC	hyperfine coupling constant
HK	Hohenberg-Kohn
HOCO	highest occupied crystal orbital
HOMO	highest occupied molecular orbital
KS	Kohn-Sham
LDA	local density approximation

LSDA	local spin density approximation
LUCO	lowest unoccupied crystal orbital
LUMO	lowest unoccupied molecular orbital
MCSCF	multi-configurational self-consistent field
MD	molecular dynamics
MO	molecular orbital
MP <sub>n</sub>	<i>n</i> th order Møller-Plesset perturbation theory
MPPT	Møller-Plesset perturbation theory
MRCI	multi-reference configuration interaction
Mu	muon/muonium
NBO	natural bond analysis
NEC	natural electronic configuration
PBC	periodic boundary condition
PE	potential energy
PES	potential energy surface
PIMC	path integral Monte Carlo
RSPT	Rayleigh-Schrödinger perturbation theory
SCF	self-consistent field
SW	Stone-Wales
SWCNT	single-walled carbon nanotube
TM	transition metal
TST	transition state theory
UEG	uniform electron gas
WF	wavefunction/wave function
WFT	wavefunction theory
ZPC	zero-point correction
ZPE	zero-point energy
μSR	muon spin resonance

# Acknowledgements

“Now this is not the end. It is not even the beginning of the end. But it is, perhaps, the end of the beginning”.

These words were quoted from the respectable Sir Winston Churchill by Prof. Donald G. Fleming when he wanted to tell me how far we were from the final version of a collaborative paper. This is also true to describe my current situation: I am single and with very little knowledge about my future even I am looking forward to one of the highest academic degrees. Though my parents care more about marital status than the content of this dissertation, I thank them first and most for their never-ending support.

I wish to thank my supervisor Dr. Yan Alexander Wang for offering me an opportunity to enter the computational chemistry division from a different background. I appreciate that he allowed me to choose my study topics and supported me for over six years. This thesis would have been impossible without his patient work and invaluable advices.

I thank former postdoctoral fellow Dr. Wei Quan Tian who instructed me a lot when I was at the doorway to the computational chemistry mansion and helped me choose the first subject as my starting project. And even after he left this group, I have still received a lot of help and valuable information from him. My warm thanks also go to a former labmate, M.Sc. Lei Vincent Liu, for his generous share of his study on boron nitride nanotubes that I can incorporate into this dissertation. His strong knowledge about the nanotubes helped me in my other nanotube studies. I also feel lucky that I have learned many from a labmate Dr. Yu Adam Zhang, who is extremely knowledgeable in fundamental theoretical chemistry. Former postdoctoral fellow Dr. Baojing Zhou have offered a lot of valuable suggestions and information. My labmate Steven Hepperle helped me know more about the language, the culture, the country and the hospitality of Canadian people besides his technical assistants. And even the junior labmate Mr. Ping Xiang has been supportive so much. I wish them a successful future and a happy life.

Many thanks are due to Prof. Donald G. Fleming for his interesting experimental results that allowed me to have a chance to practice my theoretical calculations on a simple yet interesting system that allows me to have some valuable knowledge other than plain electronic structure calculations of molecules. With his warm help, I also acquired a lot about scientific writing in English that would still benefit me in the future.

Some friends from other research laboratories, Dr. Terry Liu, Dr. Xiaoji Xu, Dr. Zhan Zhang,

and their supervisors have also kindly offered me chances to participate in their projects, to share ideas and to coauthor papers.

Also, I must thank Prof. Mark Thachuck, Prof. Roman Krems and Roman Baranowski who have spent valuable time on maintaining the computational environment so that I can complete those projects.

I thank Dr. Baojing Zhou, Dr. QiChi Hu, Dr. Hui Wang, Dr. Zhan Zhang, Dr. Yongbin Chang, Dr. Yi Cao, Dr. Jianjun Dai and many other friends who played badminton or tennis with me so that I am in good shape to study.

Appreciations also belong to Dr. Qun Zhang, Dr. Ye Wang, Dr. Ying Li, Dr. Zheng Yang, Dr. Qifeng Li, Dr. Da Chen, Dr. Yuquan Zou, Dr. Jian Jiang, and Dr. Shunxing Su at FPI, Dr. Zheng Shi at NRC, MSc. Yunfeng Zhao at ICAS (China) who have been supportive from all aspects. I wish them the best.

# Dedication

To my family and my friends

# Statement of Co-Authorship

- The study in Chapter 2 was proposed by a former post doctoral fellow Dr. Wei Quan Tian (the second author) followed by his many technical helps. Calculations, data-analysis, and manuscript-preparation were conducted by Yakun Chen (the first author). Yan Alexander Wang (the correspondence author) supported and supervised the study, and edited the manuscript.
- The study in Chapter 3 was proposed, conducted, analyzed and written by Yakun Chen (the first author). Assistance and proofreading were adopted from Lei Vincent Liu (the second author). Wei Quan Tian (the third author) offered technical support and discussions throughout the study. Yan Alexander Wang (the correspondence author) supported and supervised the study, and proofread the manuscript.
- The proposal, some calculations, and the preliminary manuscript-proofreading of the study in Chapter 4 was mainly attributed to Lei Vincent Liu (the second author). Complementary calculations, data analysis, and manuscript preparation were carried out by Yakun Chen (the first author). Yan Alexander Wang (the correspondence author) supported and supervised the study, and edited the manuscript.
- The study in Chapter 5 was at request of and in collaboration with Professor Donald G. Fleming (the second author). Calculations, data analysis, and manuscript-preparation were conducted by Yakun Chen (the first author). Professor D. G. Fleming also offered advice and proofread the manuscript. Yan Alexander Wang (the correspondence author) supported and supervised the study, and proofread the manuscript.
- The study in Chapter 6 was proposed, carried out, analyzed and written by Yakun Chen (the first author). Yan Alexander Wang (the correspondence author) supported and supervised the study, and edited the manuscript.

# Chapter 1

## Introduction

### 1.1 Schrödinger equation

Most substances are composed of atoms, which can be further decomposed into nuclei and electrons. To describe the motion of these small particles, it is crucial to solve the following Schrödinger equation:

$$i\hbar \frac{\partial}{\partial t} \Psi = \hat{H} \Psi, \quad (1.1)$$

where  $\hat{H}$  is the Hamiltonian operator, and  $\Psi$  is the wavefunction.<sup>1</sup> The Hamiltonian operator consists of the kinetic energy operator  $\hat{T}$  and potential energy operator  $\hat{V}$ :

$$\hat{H} \equiv \hat{T} + \hat{V}. \quad (1.2)$$

Without any magnetic field, the non-relativistic form of the kinetic energy operator can be expressed as (in atomic units)

$$\hat{T} = \sum_i -\frac{1}{2m_i} \nabla_i^2. \quad (1.3)$$

If the potential operator  $\hat{V}$  is time independent, Eq. 1.1 reduces to the time-independent Schrödinger equation:<sup>2</sup>

$$\hat{H} \Psi(\mathbf{X}) = E \Psi(\mathbf{X}), \quad (1.4)$$

where  $E$  is the total energy of the system, and  $\mathbf{X}$  represents both the spatial and the spin coordinates of the particles. In this thesis, molecular or atomic systems are of interest. Correspondingly, the time-independent coulombic potential operator has the general form

$$\begin{aligned} \hat{V} &= \sum_{i>j} \frac{1}{|\mathbf{r}_i - \mathbf{r}_j|} + - \sum_{\substack{A=1,N \\ i=1,n}} \frac{Z_A}{|\mathbf{r}_i - \mathbf{R}_A|} + \sum_{A>B} \frac{Z_A Z_B}{|\mathbf{R}_A - \mathbf{R}_B|} \\ &= \hat{V}_{ee} + \hat{V}_{Ne} + \hat{V}_{NN}, \end{aligned} \quad (1.5)$$

where  $Z$  is the nuclear charge,  $\mathbf{r}$  and  $\mathbf{R}$  are the electron and nuclear (spatial) coordinates,  $N$  and  $n$  are the numbers of nuclei and electrons, and  $(A, B)$  and  $(i, j)$  are the indices of the nuclei and

electrons, respectively. Without loss of generality, the wavefunction has the following form:

$$\Psi_k = \Psi^{(k)}(\dots \mathbf{R}_A \dots, \dots \mathbf{r}_i \dots), \quad (1.6)$$

where  $k$  denotes the  $k$ th (excited) state. Solving the time-independent Schrödinger equation to find (approximate) eigenfunctions and eigenvalues is the primary goal of quantum chemistry.

## 1.2 Born-Oppenheimer approximation

The molecular Hamiltonian operator of a molecular or an atomic system can be decomposed as

$$\hat{H} = \hat{T}_N + \hat{T}_e + \hat{V}_{Ne} + \hat{V}_{NN} + \hat{V}_{ee}, \quad (1.7)$$

where  $\hat{T}_N$  and  $\hat{T}_e$  are the kinetic energy operators for the nuclei and electrons, respectively. Therefore, the wavefunction for this Hamiltonian operator will have nuclear and electron motions coupled.

Born and Oppenheimer wisely separated the motion of the nuclei from the motion of the electrons in the 1920s.<sup>3</sup> Due to their large mass difference, nuclei move much slower than electrons. Accordingly, the Born-Oppenheimer (BO) approximation was formulated, where electron motion is assumed to adjust instantly with nuclear position change. This ‘time-scale’ separation works satisfactorily for most of common molecular or atomic systems. The detailed mathematic derivation of the BO approximation via the intermediate adiabatic approximation can be found in the literature.<sup>4,5</sup>

Within the framework of the BO approximation, nuclei experience the potential energy created by the presence of electrons. Hence, the total wavefunction  $\Psi_{tot}$  can be expressed as the product of the nuclear wavefunction  $\Psi_N$  and the electron wavefunction  $\Psi_e$ , with the latter depending only parametrically on nuclear positions,

$$\Psi_{tot}(\mathbf{R}, \mathbf{r}) = \Psi_N(\mathbf{R})\Psi_e(\mathbf{r}|\mathbf{R}). \quad (1.8)$$

Therefore, the nuclei can be regarded as moving on the potential hypersurface or potential energy surface (PES) predetermined by the electronic energy  $E_e$ , which is an important quantity pursued in most quantum chemistry calculations by solving the electronic Schrödinger equation:

$$\hat{H}_e \Psi_e(\mathbf{r}|\mathbf{R}) = E_e(\mathbf{R})\Psi_e(\mathbf{r}|\mathbf{R}), \quad (1.9)$$

in which the electronic Hamiltonian is

$$\hat{H}_e = \hat{T}_e + \hat{V}_{Ne} + \hat{V}_{ee} + \hat{V}_{NN}. \quad (1.10)$$



After the motions of the nuclei and the electrons are separated, the classical nuclei approximation is often further adopted. Classical molecular dynamics (MD) studies and some theories usually have adopted this approximation.<sup>5</sup> However, care must be taken if the nuclear mass is small when non-classical behavior, like tunneling, is not negligible and cannot be directly attainable from a calculation assuming classical nuclei.<sup>6</sup>

From now on, the focus will be mainly on the electronic Schrödinger equation and its solution. The properties and reactivities of the molecules of interest can be obtained subsequently from electronic wavefunctions.

### 1.3 Wavefunction theory

According to a basic postulate in quantum mechanics, the eigenfunctions of a Hamiltonian operator form a complete set.<sup>7</sup> Consequently, any wavefunction can be expressed as a linear combination of these eigenfunctions of the complete set. Then, finding (approximate) eigenfunctions becomes the first step towards understanding the electronic structure of various systems.

Generally speaking, every eigenstate  $\Psi$  is an extremum state against any small changes of the wavefunction,<sup>8,9</sup> that is

$$\delta\langle\Psi|\hat{H}|\Psi\rangle = 0. \quad (1.11)$$

Particularly, this stationary principle can be reduced to the variational principle for the ground-state wavefunctions:<sup>7</sup>

$$\langle\tilde{\Psi}|\hat{H}|\tilde{\Psi}\rangle \geq E_0, \quad (1.12)$$

where  $\tilde{\Psi}$  denotes an arbitrary normalized trial wavefunction and  $E_0$  is the ground-state energy. Because most chemical systems are in their ground states and the excitation energy can be hardly overcome at ambient temperature, we will concentrate on the discussion of the ground-state wavefunctions in this thesis.

In addition to the stationary or variational principle, electrons are fermions, and therefore, must obey Fermi-Dirac statistics. Consequently, the wavefunction that describes the state of a many-electron system must also fulfill the Fermi statistical principle. In other words, the wavefunction must be antisymmetric, *i.e.* the wavefunction changes its sign when the coordinates of any two electrons are interchanged:

$$\Psi(\dots, i, \dots, j, \dots) = -\Psi(\dots, j, \dots, i, \dots). \quad (1.13)$$

This property is the Pauli exclusion principle, named after Wolfgang Pauli.<sup>10</sup> This requirement is usually met by expressing wavefunctions using Slater determinants that automatically satisfy the Pauli principle.<sup>11,12</sup>

### 1.3.1 Hartree-Fock theory

A very early attempt to solve Eq. 1.10 is Hartree-Fock (HF) theory,<sup>13</sup> which also forms the foundation of many correlated wavefunction theories (WFTs). The electronic wavefunction in HF theory is a single Slater determinant comprising single electron spin orbitals. The determinant has the necessary antisymmetric property in that interchange of any two columns or rows changes the sign of the determinant. This antisymmetric property guarantees wavefunctions built from Slater determinants satisfy the Pauli exclusion principle automatically.

Based on the variational principle, the total electronic energy is minimized, subject to the constraint that the spin orbitals are orthonormal. As a consequence, the HF equation can be derived as<sup>14</sup>

$$\left[ \hat{h} + \sum_{b=1}^{occ} (\hat{J}_b - \hat{K}_b) \right] \chi_a = \sum_{b=1}^{occ} \varepsilon_{ba} \chi_b, \quad (1.14)$$

where  $a$  and  $b$  are orbital indices,  $\chi$  are spin orbitals,  $\{\varepsilon_{ba}\}$ 's are the Lagrange multipliers to impose the orbital orthonormality,  $\hat{h} = -\frac{1}{2}\nabla^2 + \hat{V}_{ext}$  is a one-electron core operator, and  $\hat{J}_b$  and  $\hat{K}_b$  are the Coulomb and exchange operators, respectively.  $\hat{J}_b$  and  $\hat{K}_b$  are defined through their actions upon a spin orbital:

$$\hat{J}_b(1)\chi_a(1) = \left[ \int \chi_b^*(2) \mathbf{r}_{12}^{-1} \chi_b(2) d\mathbf{x}_2 \right] \chi_a(1), \quad (1.15)$$

$$\hat{K}_b(1)\chi_a(1) = \left[ \int \chi_b^*(2) \mathbf{r}_{12}^{-1} \chi_a(2) d\mathbf{x}_2 \right] \chi_b(1). \quad (1.16)$$

The above HF equation, e.q. 1.14, can be unitarily transformed into an eigenvalue-like canonical form:

$$\left[ \hat{h} + \sum_{b=1}^{occ} (\hat{J}_b - \hat{K}_b) \right] \chi_a \equiv \hat{F} \chi_a = \varepsilon_a \chi_a, \quad (1.17)$$

where  $\varepsilon_a$  is the orbital energy of  $\chi_a$  and  $\hat{F}$  is the Fock operator. Accordingly, the ground-state electronic energy of a many-electron system in HF theory is

$$E = \sum_{a=1}^{occ} \varepsilon_a - \frac{1}{2} \sum_{a=1}^{occ} \sum_{b=1}^{occ} (J_{ab} - K_{ab}), \quad (1.18)$$

where

$$J_{ab} = \int \int \chi_a^*(1) \chi_b^*(2) \mathbf{r}_{12}^{-1} \chi_b(2) \chi_a(1) d\mathbf{x}_1 d\mathbf{x}_2,$$

and

$$K_{ab} = \int \int \chi_a^*(1) \chi_b^*(2) \mathbf{r}_{12}^{-1} \chi_a(2) \chi_b(1) d\mathbf{x}_1 d\mathbf{x}_2.$$

HF theory was not widely utilized until the computer technology was significantly improved and the practical Roothaan equations and Pople-Nesbet equations were derived with wavefunctions

expanded in terms of the basis sets.<sup>15,16</sup> The canonical spin orbitals obtained from a HF calculation are usually delocalized due to the constraint in orthonormality.<sup>14</sup>

As a byproduct of the HF theory, Koopmans' theorem was developed to interpret the physical significance of these canonical HF orbitals: the energy of an occupied orbital is the approximate ionization energy, whereas the energy of a virtual (unoccupied) orbital is the approximate electron affinity, with the assumption that all other orbitals are frozen during the electron detachment and attachment processes.<sup>14,17</sup>

### 1.3.2 Correlated wavefunction theory

Even though the HF theory was a big step towards the first-principle solutions of the Schrödinger equation, researchers realized that exact wavefunctions for many-electron systems are never single Slater determinants. The electron correlation effect, which is usually small in magnitude but important to electronic interactions, is unfortunately not taken into account in any HF calculations. Because the HF energy is an upper limit to the exact electronic energy, the correction energy defined as the difference between the exact electronic energy and the HF energy,  $E_{corr} = E_{exact} - E_{HF}$ , is always negative semi-definite. Theoretical chemists and physicists have developed several correlated WFTs to incorporate this many-body quantum effect. In the following, some correlated WFTs will be introduced, all of which will be employed or examined in Chapter 5 and 6 of this thesis.

#### Configuration Interaction Theory

Configuration Interaction (CI) theory is the simplest correlated WFT in terms of its idea but not its implementation.<sup>14</sup> The central idea is based on the variational principle, not with respect to the orbitals as in the HF theory, but with respect to different configurations (as defined below).

A HF calculation generates a set of spin orbitals: occupied and unoccupied. The occupied orbitals are used to form the ground-state HF wavefunction. The unoccupied orbitals, also called virtual orbitals, are not occupied and therefore not variationally optimized during the HF self-consistent-field procedure. With the electron number invariant, any electron arrangement within the entire set of spin orbitals makes an electron configuration. Specifically, configurations differing from the HF wavefunction by  $n$  spin orbitals are called  $n$ -tuply excited determinants or  $n$ th order configurations. For example, the singly excited determinants can be expressed as  $|\Psi_a^r\rangle$ , which denotes that an electron is relocated from the occupied spin orbital  $\chi_a$  to the virtual spin orbital  $\chi_r$ , and so on, for higher excited configurations.

The full CI wavefunction is constructed by a linear combination of all possible configurations, that is

$$|\Psi_{CI}\rangle = c_{HF}|\Psi_{HF}\rangle + c_S|\Psi_S\rangle + c_D|\Psi_D\rangle + c_T|\Psi_T\rangle + \cdots, \quad (1.19)$$

where  $S$ ,  $D$ , and  $T$  stand for singly, doubly, and triply excited determinants and  $c$ 's represent the

expansion coefficients. The central task in a CI calculation is to find the coefficients variationally.

The Lagrangian multiplier strategy is then used to find those coefficient under the constraint that the CI wave function is normalized. The Lagrangian function  $L$  can be written as:

$$\begin{aligned}
L &= \langle \Psi_{CI} | \hat{H} | \Psi_{CI} \rangle - \lambda (\langle \Psi_{CI} | \Psi_{CI} \rangle - 1) \\
&= \sum_{i=0} \sum_{j=0} a_i a_j \langle \Psi_i | \hat{H} | \Psi_j \rangle - \lambda \left( \sum_{i=0} \sum_{j=0} a_i a_j \langle \Psi_i | \Psi_j \rangle - 1 \right) \\
&= \sum_{i=0} a_i^2 H_{ii} + \sum_{i=0} \sum_{j \neq 0} a_i a_j \langle \Psi_i | \hat{H} | \Psi_j \rangle - \lambda \left( \sum_{i=0} a_i^2 - 1 \right)
\end{aligned} \tag{1.20}$$

where  $\lambda$  is the Lagrangian multiplier,  $\Psi_i$  and  $\Psi_j$  are configuration wavefunctions, and  $a_i$  and  $a_j$  are the expansion coefficients for them. The variational principle requires that all the first order derivatives of the Lagrangian function with respect to the expansion coefficients be zero:

$$\frac{\partial L}{\partial a_i} = \sum_j a_j \langle \Psi_i | \hat{H} | \Psi_j \rangle - \lambda a_i = 0. \tag{1.21}$$

For convenience,  $H_{ij}$  can be used to represent  $\langle \Psi_i | \hat{H} | \Psi_j \rangle$ . Therefore, Eq. 1.21 can be rearranged into a matrix representation:

$$\begin{bmatrix} H_{00} - \lambda & H_{01} & \cdots & H_{0j} & \cdots \\ H_{10} & H_{11} - \lambda & \cdots & H_{1j} & \cdots \\ \vdots & \vdots & \ddots & \cdots & \cdots \\ H_{j0} & H_{j1} & \cdots & H_{jj} & \cdots \\ \vdots & \vdots & \cdots & \vdots & \ddots \end{bmatrix} \begin{bmatrix} a_1 \\ a_2 \\ \vdots \\ a_j \\ \vdots \end{bmatrix} = \begin{bmatrix} 0 \\ 0 \\ \vdots \\ 0 \\ \vdots \end{bmatrix}.$$

The corresponding matrix equation can be expressed as:

$$\mathbf{H}\mathbf{A} = \mathbf{A}\mathbf{E}, \tag{1.22}$$

where  $\mathbf{E}$  is used to denote the Lagrangian multiplier. It is actually the CI energy.

In principle, the CI approach that finds the coefficients by solving linear equations is equivalent to the problem of finding the eigenvalues and eigenfunctions of the full CI Hamiltonian matrix.<sup>7,14</sup> If the eigenvalues of this full CI matrix are ordered ascendingly,  $E_i \leq E_j$  for  $i < j$ , the lowest eigenvalue corresponds to the upper limit of the ground-state energy and the  $n$ th eigenvalue corresponds to the upper limit of the energy of the  $(n - 1)$ th excited state. As demonstrated in the previous section, the HF wavefunction is the best single Slater-determinant wavefunction as the ground-state solution to a many-electron Schrödinger equation. Not surprisingly, in a CI ground-state wavefunction, the coefficient before the HF configuration is much bigger than the coefficients before any

other configurations.

The abovementioned approach of the full CI calculation is computationally demanding. Therefore, truncated CI methods, such as CI doubles (CID) and CI singles and doubles (CISD), are normally implemented in practical quantum chemistry calculations.<sup>14</sup>

## Perturbation Theory

In contrast to CI theory, which uses the exact Hamiltonian and approximates the wavefunctions by adding more and more excited configurations subject to the variational principle, perturbation theory in quantum chemistry starts with an approximate Hamiltonian, the zeroth order Hamiltonian ( $\hat{H}_0$ ), which has its exact eigenfunctions  $\{\Phi_i^{(0)}\}$  and eigenvalues  $\{E_i^{(0)}\}$  available. Here the superscript ‘(0)’ stands for the zeroth order correction, and the subscript  $i$  denotes the  $i$ th excited state. This zeroth order Hamiltonian should be close to the exact Hamiltonian of interest and only differ by a small perturbation  $\hat{H}'$  so that  $\hat{H}_0 + \hat{H}' = \hat{H}_{exact}$ . Following Rayleigh-Schrödinger perturbation theory (RSPT) introduced below, the exact wavefunctions and energies can be expressed as the perturbed wavefunctions and eigenvalues with an number of perturbation terms.<sup>7,14</sup>

According to RSPT, a parameter  $\lambda$  is introduced to gradually turn on the perturbation so that  $\hat{H} = \hat{H}_0 + \lambda\hat{H}'$ .<sup>7</sup> Consequently, the energy eigenvalues and eigenfunctions can be expanded into a Taylor series with respect to  $\lambda$ ,

$$E_i = E_i^{(0)} + \lambda E_i^{(1)} + \lambda^2 E_i^{(2)} + \dots, \quad (1.23)$$

and

$$|\Psi_i\rangle = |\Phi_i^{(0)}\rangle + \lambda |\Phi_i^{(1)}\rangle + \lambda^2 |\Phi_i^{(2)}\rangle + \dots, \quad (1.24)$$

where the superscript denotes the order of the correction. Substituting Eqs. 1.23 and 1.24 into  $\hat{H}|\Psi_i\rangle = (\hat{H}_0 + \lambda\hat{H}')|\Psi_i\rangle = E_i|\Psi_i\rangle$  gives

$$\begin{aligned} (\hat{H}_0 + \lambda\hat{H}')(|\Phi_i^{(0)}\rangle + \lambda|\Phi_i^{(1)}\rangle + \lambda^2|\Phi_i^{(2)}\rangle + \dots) = \\ (E_i^{(0)} + \lambda E_i^{(1)} + \lambda^2 E_i^{(2)} + \dots)(|\Phi_i^{(0)}\rangle + \lambda|\Phi_i^{(1)}\rangle + \lambda^2|\Phi_i^{(2)}\rangle + \dots). \end{aligned} \quad (1.25)$$

Since this equation holds irrespective of the  $\lambda$  value, the terms containing  $\lambda^n$  on the left-hand side must be equal to the terms containing  $\lambda^n$  on the right-hand side. Therefore, one has equations for each  $n$ :

$$\begin{aligned} \hat{H}_0|\Phi_i^{(0)}\rangle &= E_i^{(0)}|\Phi_i^{(0)}\rangle, \\ \hat{H}_0|\Phi_i^{(1)}\rangle + \hat{H}'|\Phi_i^{(0)}\rangle &= E_i^{(0)}|\Phi_i^{(1)}\rangle + E_i^{(1)}|\Phi_i^{(0)}\rangle, \\ &\dots \end{aligned} \quad (1.26)$$

Subsequently, the energy corrections can be obtained by multiplying both sides of the above equations from the left by  $\langle \Phi_i^{(0)} |$  and integrating over the entire space. As a result, the  $n$ th energy correction is found to be  $E_i^{(n)} = \langle \Phi_i^{(0)} | \hat{H}' | \Phi_i^{(n-1)} \rangle$ , which is closely associated with the  $(n - 1)$ th order wavefunction corrections. Actually, it can be proved that the knowledge of up to  $k$ th order wavefunction corrections enables one to obtain the  $(2k + 1)$ th order energy correction.<sup>7</sup> Therefore, the question of finding the  $(2n + 1)$ th order energy correction becomes a matter of finding the wavefunctions corrections up to  $|\Phi_i^{(n)}\rangle$ . Since the equations for the wavefunction corrections are inhomogeneous differential equations, a viable way to solve this problem is to expand the wavefunction corrections in terms of  $\{\Phi_k^{(0)}\}$ , the complete set of eigenfunctions of the known zero-th order Hamiltonian. The  $n$ th order wavefunction correction can then be expressed as

$$|\Phi_i^{(n)}\rangle = \sum_k' c_k^{(n)} |\Phi_k^{(0)}\rangle = \sum_k' |\Phi_k^{(0)}\rangle \langle \Phi_k^{(0)} | \Phi_i^{(n)} \rangle, \quad (1.27)$$

in which, the prime on the summation symbol means the  $i = k$  term should be excluded from the sum as a result of the intermediate normalization condition. By multiplying Eq. 1.27 with  $\langle \Phi_k^{(0)} |$  from the left and integrating over the entire space, the coefficients  $\{c_k^{(n)}\}$  and the wavefunction corrections are obtained as a consequence.

Using the HF Hamiltonian as the known exact solvable Hamiltonian, Møller and Plesset developed Møller-Plesset perturbation theory (MPPT), which closely follows the RSPT procedure.<sup>14,18</sup> The HF Hamiltonian  $\hat{H}_{HF} = \sum_{i=1}^N \hat{F}(i) = \sum_{i=1}^N [\hat{h}(i) + v^{HF}(i)]$  defined earlier in Eq. 1.17 is used as the zeroth order Hamiltonian, where  $\hat{F}(i)$  is the Fock operator for the  $i$ th occupied orbital. Then, the perturbation  $\hat{H}'$  is the difference between the exact Hamiltonian and the HF Hamiltonian:  $\hat{H}' = \sum_{i < j} \mathbf{r}_{ij}^{-1} - \sum_i \hat{v}^{HF}(i)$ . By following RSPT, the popular MPPT theory to  $n$ th order, which is commonly abbreviated to MP $n$  is obtainable.<sup>14</sup>

## Coupled Cluster Theory

Coupled cluster (CC) theory was first implemented in chemistry in 1978.<sup>19–21</sup> The central idea in CC theory, similar to CI theory, is to express the exact wavefunction as a linear combination of Slater determinants including the reference configuration  $\Psi_0$  and the excited configurations. The CC wavefunction is defined as

$$\Phi_{CC} = e^{\hat{T}} \Psi_0, \quad (1.28)$$

where  $e^{\hat{T}} = 1 + \hat{T} + \frac{1}{2!} \hat{T}^2 + \frac{1}{3!} \hat{T}^3 + \dots = \sum_{k=0}^{\infty} \hat{T}^k / k!$  and the cluster operator  $\hat{T} = \hat{T}_1 + \hat{T}_2 + \hat{T}_3 + \dots$ . The  $i$ th order cluster operator  $\hat{T}_i$  operating on the reference configuration (usually the HF determinant) results in a linear combination of  $i$ th order excited configurations  $\hat{T}_i = \sum_{a_1 \dots a_i}^{occ} \sum_{r_1 \dots r_i}^{virt} t_{a_1 \dots a_i}^{r_1 \dots r_i} \Psi_{a_1 \dots a_i}^{r_1 \dots r_i}$ , where  $\{t_{a_1 \dots a_i}^{r_1 \dots r_i}\}$  are the amplitudes and are the key variables to a CC problem. Since the full CI wavefunction is the exact wave function in principle, the CC wavefunction, based on a similar

expansion, is another viable way to express the exact wavefunction.

With the  $\Phi_{CC}$  expression, the Schrödinger equation becomes  $\hat{H}e^{\hat{T}}\Psi_0 = Ee^{\hat{T}}\Psi_0$ . Multiplying both sides of this equation on the left by  $\Psi_0$  and integrating over the whole space, one has the CC electronic energy expression  $E_{CC} = \langle \Psi_0 | \hat{H} e^{\hat{T}} | \Psi_0 \rangle$ . After some mathematical treatment, we have:

$$\begin{aligned} E_{CC} &= \langle \Psi_0 | H | (1 + \hat{T}_1 + \hat{T}_2 + 1/2 \hat{T}_1^2) \Psi_0 \rangle \\ &= E_0 + \sum_{a < b}^{occ} \sum_{r < s}^{virt} (t_{ab}^{rs} + t_{ab}^{rs} + t_{ab}^{rs}) (\langle \phi_a \phi_b | \phi_r \phi_s \rangle - \langle \phi_a \phi_b | \phi_s \phi_r \rangle). \end{aligned} \quad (1.29)$$

Therefore, the total energy is completely determined by the singly and doubly excited configuration amplitudes as well as the two-electron integrals. The amplitudes are obtained by solving the non-linear equations which are obtained by projecting the CC Schrödinger equation onto the excited configurations,<sup>4</sup>

$$\sum_{s=1}^m a_{rs} x_s + \sum_{t=2}^m \sum_{s=1}^{t-1} b_{rst} x_s x_t + c_r = 0, \quad r = 1 \dots m \quad (1.30)$$

where  $x$ 's are unknown amplitudes, and  $a_{rs}$ ,  $b_{rst}$ , and  $c_r$  are constants involving orbital energies and electron-repulsion integrals over basis functions. Solving this set of equations gives us the amplitudes and therefore  $E_{CC}$  and  $\Psi_{CC}$ .

Compared with CI theory, the beauty of CC theory is that the excitations are better organized with more clear-cut physical origins so that CC calculations converge faster. In other words, with the same level excitations, a CC calculation can recover more accurate correlation corrections.<sup>4,14,22</sup>

## 1.4 Density functional theory

### 1.4.1 Theoretical foundation of DFT

Without pursuing wavefunctions, density functional theory (DFT) tries to solve the electronic structure problem using of the electron density. The ground-state electron density is a fundamental variable that determines all other ground-state properties of a many-electron system. This has been formulated in the well-known Hohenberg-Kohn theorems.<sup>8,23</sup> The first theorem states that the non-degenerate ground-state electron density determines one and only one possible external potential up to a constant. The second HK theorem is an analogue to the variational principle in WFT.<sup>8,23</sup> These two theorems build a solid foundation for contemporary DFT.

Subject to the constraint that the density normalizes to the total number of electrons and a given fixed external potential  $v(\mathbf{r})$ , one has a variational formula in terms of the density, that is

$$\frac{\partial E_v}{\partial \rho(\mathbf{r})} = \mu, \quad (1.31)$$

where  $\mu$  is the Lagrangian multiplier to impose the density normalization and has the physical meaning of the chemical potential of the system.<sup>9</sup>

### 1.4.2 Kohn-Sham DFT

Although the HK theorems provided a sound foundation for DFT, practical DFT calculations were still not widely performed until Kohn and Sham devised the Kohn-Sham (KS) scheme.<sup>24</sup> The basic idea of the KS DFT is to use an auxiliary non-interacting system containing single electron orbitals to incorporate most of the total electronic energy, including the major part of the kinetic energy and classical potential energies, and to leave the other non-classical effect in an exchange-correlation term.

The Hamiltonian of this non-interacting system is the sum of the individual Hamiltonians for each non-interacting electron:

$$\hat{H}_{KS} = \sum_{i=1}^N \left[ \frac{1}{2} \nabla_i^2 + \hat{v}_{eff}(i) \right] \quad (1.32)$$

$$= \hat{T}_s + \sum_{i=1}^N \hat{v}_s(i), \quad (1.33)$$

where  $T_s[\rho] = \langle \sum_{i=1}^{occ} \frac{1}{2} \nabla^2 \rangle$  is the total kinetic energy of the auxiliary non-interacting system,  $\hat{v}_{eff}(i)$  is the potential experienced by the non-interacting electrons and keeps the density of the non-interacting system identical to that of the interacting system. The wavefunction of this auxiliary non-interacting system is also a Slater determinant comprising the occupied spin orbitals. The total energy of the noninteracting system is  $E_{non} = \sum_{i=1}^{occ} \epsilon_i$ , where  $\epsilon_i$  is the energy of each non-interacting electron. Therefore, the chemical potential of this noninteracting system is  $\mu_{KS} = \frac{\partial T_s}{\partial \rho} + v_{eff}$ .

Using the kinetic energy expression of the non-interacting system, the total energy of the interacting system can be reorganized as<sup>8</sup>

$$E_{tot} = T_s + E_{ext} + E_J + E_{XC}. \quad (1.34)$$

In this equation,  $E_{ext} = \int \rho(\mathbf{r}) v_{ext}(\mathbf{r}) d\mathbf{r}$  is the energy due to the external potential  $v_{ext}(\mathbf{r})$ , the Coulomb energy,

$$E_J = \frac{1}{2} \iint \frac{\rho(\mathbf{r})\rho(\mathbf{r}')}{|\mathbf{r} - \mathbf{r}'|} d\mathbf{r} d\mathbf{r}' \quad (1.35)$$

corresponds to the classical electrostatic energy between electrons, and  $E_{XC} = E_X + E_C + T_C$  is the exchange correlation energy containing all other non-classical effects. In the latter case,  $T_C = T_{int} - T_s \geq 0$  is the difference between the kinetic energies of the true interacting system and of the auxiliary non-interacting system.  $E_X$  and  $E_C$  are the exchange and correlation energies due to Fermi and Coulomb holes, respectively.<sup>8</sup>



Applying the variational principle to Eq. 1.34 in terms of the orbitals subject to the orthonormality constraint, the (canonical) equations have the form<sup>8</sup>

$$\left[ \frac{1}{2} \nabla^2 + v_{eff} \right] \psi_i = \varepsilon_i \psi_i, \quad (1.36)$$

where  $v_{eff}(\mathbf{r}) = v_{ext}(\mathbf{r}) + \int \frac{\rho(\mathbf{r}')}{|\mathbf{r}-\mathbf{r}'|} d\mathbf{r}' + \frac{\partial E_{xc}}{\partial \rho(\mathbf{r})}$ . The KS equations can be solved just like the case for the non-interacting system.<sup>8,9,24,25</sup> Thus, with the solution of the non-interacting system, the total energy of the interacting system can be expressed as<sup>8</sup>

$$E_{tot} = \sum_{i=1}^{occ} \varepsilon_i - \int v_{eff}(\mathbf{r}) \rho(\mathbf{r}) d\mathbf{r} + \int v_{ext}(\mathbf{r}) \rho(\mathbf{r}) d\mathbf{r} + E_J[\rho] + E_{XC}[\rho]. \quad (1.37)$$

The KS potential  $v_{eff}$  is a local (universal) potential for all orbitals, in contrast to the non-local potential in the HF theory.

### 1.4.3 Approximate functionals

The KS scheme provides an amenable way to calculate the electronic structure within DFT. Nevertheless, the exact form of the exchange correlation-functional is still unknown. Inspired researchers have developed and are developing approximate exchange-correlation functionals for accurate predictions of the electronic energy.

For the exchange functional, an early attempt is the local density approximation (LDA) or local spin density approximation (LSDA).<sup>5,8,24</sup> For the uniform/homogeneous electron gas (UEG/HEG) model, Bloch and Dirac showed that the exact exchange functional is<sup>8</sup>

$$E_X^{LSD} = A_x \sum_{\sigma} \int \rho_{\sigma}(\mathbf{r})^{4/3} d\mathbf{r}, \quad (1.38)$$

where  $A_x = 1.5 \times [3/4\pi]^{1/2}$  and the subscript  $\sigma$  denotes the two spin states. The LDA or LSDA is exact for the UEG, which does not actually exist, though it is a good starting point for modeling more realistic systems. It is not surprising those approximations fail in the study of typical molecular systems where electron density is far from being homogeneous. Thus, the generalized gradient approximation (GGA) functionals were formulated to simulate inhomogeneity:

$$E_X^{GGA} = E_X^{LSD} \sum_{\sigma} \int F[x_{\sigma}] \rho_{\sigma}(\mathbf{r})^{4/3} d\mathbf{r}, \quad (1.39)$$

where  $x = \frac{|\nabla \rho_{\sigma}|}{\rho_{\sigma}^{4/3}}$ . Using the GGA and adjusting  $F[x]$  to the exact exchange, Becke formulated a

popular GGA exchange functional *B88* with  $F[x]$  defined as<sup>26</sup>

$$F[x] = \frac{bx^2}{1 + 6bx \sinh^{-1} x}, \quad (1.40)$$

where  $b$  is a fitting parameter. Still, the *B88* exchange functional violates two important formal properties that an exact exchange should obey.<sup>27</sup> On the bright side, the right asymptotic behavior is recovered by this exchange functional. In an in-depth study, researchers found that further modification of the parameter  $b$  of the *B88* exchange functional would improve the behavior of the low-density and high-density gradient regions away from nuclei without compromising its accuracy in predicting the atomic exchange energy. This promoted the design of the *PW91* exchange functional with a new  $F$  function:

$$F = \frac{bx^2 - (b - 5(36\pi)^{-5/2})x^2 e^{-1.6455x^2} - 10^{-6}x^d}{1 + 6bx \sinh^{-1} x - \frac{10^{-6}x^d}{A_x}}, \quad (1.41)$$

where  $b$  is fitted to be 0.0042,  $d$  is fitted to be 4, and  $A_x = 1.5 \times [3/4\pi]^{1/2}$ .<sup>28</sup> This is still not the end of the story. A study on the selection of the values of  $d$  and  $b$  was carried out by the Truhlar group. *MPW* type exchange functionals with  $b = 0.0046$  and  $3.2 \leq d \leq 4.0$  were developed and better performance was observed by testing with several training sets.<sup>29</sup>

The *PW91* exchange and *PW91* correlation functionals also formed the basis for another exchange-correlation PBE functional that was developed by fulfilling formal properties.<sup>27</sup> Nevertheless, in designing the PBE functional, the developers mainly focused on those formal properties closely related to the electronic energy, instead of attempting to satisfy as many as possible formal constraints. For its promising origin, good performance, and simple form that is usually associated with fast convergence, the PBE exchange-correlation functional is used in this thesis and its performance is also discussed in Chapter 6 in comparison with other functionals.

The construction of correlation functionals is more complicated in that some formal properties of the correlation energy are not as simple as those of the exchange energy. As a good starting point, the early approximate VWN correlation functional was fabricated based on quantum Monte Carlo data on the UEG system.<sup>30</sup> Colle and Salvetti developed the Colle-Salvetti (CS) correlation energy expression,<sup>31</sup> which was used as a basis for other correlation functionals. The idea in CS is based on the analysis of the formula of the density matrix difference between the exact electronic energy and the HF energy. The expression was fit for helium to obtain the explicit form

$$E_c = -0.04918 \int \rho(\mathbf{r}) \frac{1 + 0.173W e^{-0.58/\beta}}{1 + \frac{0.8}{\beta}} d\mathbf{r}, \quad (1.42)$$

where  $W$  and  $\beta$  are functions of  $\mathbf{r}$ . GGA correlation functionals like LYP,<sup>32</sup> *B88*,<sup>33</sup> and *PW91*,<sup>34</sup> which modify LDA correlation functionals based on the study of the non-LDA Coulomb hole for the

weakly inhomogeneous electron gas, were developed in a similar manner. In 1995, Becke devised a *B95* meta-correlation functional which satisfies four criteria:<sup>35</sup>

1. the correlation functional can be reduced to the UEG limit;
2. the correlation energies from same-spin and opposite-spin are distinguished;
3. the correlation energy is self-interaction free;
4. the correlation energy of some atomic systems can be well reproduced.

The *B95* functional satisfies all the above four criteria, while CS and LYP correlation functionals violate the first two and *B88*, *P86* and *PW91* satisfy three out of four criteria. The performances of several correlation functionals are studied in Chapter 6.

Becke also claims credit for the most popular exchange-correlation functional—B3LYP.<sup>36</sup> Becke first developed a hybrid half—and—half functional that combined exact exchange, local exchange, and correlation functionals.<sup>37</sup> Later, he envisioned incorporating the exact exchange together with GGA exchange-correlation functionals using three parameters, in the form:<sup>38</sup>

$$E_{xc} = E_{xc}^{LDA} + a_0(E_x^{exact} - E_x^{LDA}) + a_x E_x^{Bx88} + a_c E_c^{PWc91}. \quad (1.43)$$

The exchange part together with the LYP correlation functional constituted the most popular B3LYP exchange-correlation functional.<sup>36</sup> B3LYP also is widely used in this thesis and its performance is also demonstrated in Chapter 6 for the sec-butyl radical.

#### 1.4.4 Chemical concepts associated with DFT

DFT not only offers a viable way to obtain the ground-state electronic structure of a coulombic system, but also provides many valuable physical and chemical concepts at the same time.<sup>8,9,39</sup> The chemical potential of an electronic system,  $\mu$ , which is closely related to the electronegativity  $\chi$  by the relation,  $\chi = -\mu$ , can be obtained in DFT

$$\mu = \left. \frac{\partial E}{\partial N} \right|_{v(r)}, \quad (1.44)$$

where the subscript indicates the external potential is the same for different number of electrons  $N$ . In accordance with Mulliken's scale, the electronegativity  $\chi$  can be expressed as the negative average of the ionization energy  $E_I$  and the electron affinity  $E_A$ :  $\chi = (E_I + E_A)/2$ . In a practical KS DFT calculation, this value is obtained approximately from the highest occupied molecular orbital (HOMO) and the lowest unoccupied molecular orbital (LUMO) energies ( $\varepsilon_H$  and  $\varepsilon_L$ ):  $\chi \approx -(\varepsilon_L + \varepsilon_H)/2$ .

Another important chemical concept is softness or hardness, which measures the polarizability of a system. In a DFT calculation, the hardness  $\eta = \left. \frac{\partial^2 E}{\partial N^2} \right|_{v(r)}$  can be obtained from the following

approximate expression:

$$\eta \approx \frac{(\varepsilon_L - \varepsilon_H)}{2}. \quad (1.45)$$

Besides these indices, DFT also provides some clues about the position of preferential reaction sites in a molecular system. A chemical reaction, especially the reaction that leads to the formation of covalent bonds, is dictated by electron flow due to the perturbation between reactants. The Fukui equation,<sup>40</sup>

$$f(\mathbf{r}) = \left. \frac{\partial \rho(\mathbf{r})}{\partial N} \right|_{v(\mathbf{r})}, \quad (1.46)$$

gives a direct guideline about the electron flow probability at each point in space. The two frontier molecular orbitals, HOMO and LUMO that dictate the reactivity are actually approximate Fukui functions that guide the electron flow during chemical reactions. The above chemical concepts and their applications are used in the following chapters to predict the properties and reactivities of transition metal based materials.

## 1.5 Transition metals in different environments

We have studied transition metals (TMs) in different systems using DFT. TMs in the *d*-block usually have unfilled *nd* orbitals and (partially) filled  $(n+1)s$  orbitals as their outermost electron shells. The valence *d* orbitals are usually tighter to the TM nucleus compared to the valence *s* orbital and act mostly as polarization functions on the valence *s* orbitals.<sup>41,42</sup> At the same time, the electron repulsive interactions within the *d* shell tend to enlarge the *d* shell radius.<sup>41</sup> These complications in the valence shell give the TMs intriguing properties and reactivities that enable them to be used in various manners. Moreover, the complications also make the properties of TM-containing materials difficult to predict. Unlike main group elements, whose electronic structures can usually be predicted satisfactorily by relatively simple rules (*e.g.* the octet rule), TM elements, even with some *ad hoc* models like the 18-electron rule for coordination complexes, cannot be easily explained or predicted accurately. For such situations, first-principles computations become an important tool for investigating TM containing systems. Due to the large number of (valence) electrons, DFT with balanced accuracy and efficiency, has become the major tool to study TM materials. Also, the basis sets that have the core electrons represented by effective core potentials can be used to reduce the computational cost.

### 1.5.1 TM clusters—Chapter 2

The study of metal clusters, especially TM clusters, is one of the hotspots in material science because of their extraordinary catalytic properties. The catalytic ability of TM clusters greatly depends on the charge, composition and even molecular geometry. A good example is the cluster-catalyzed Degussa process, where C–N coupling is achieved by the consecutive dehydrogenation of methane

and ammonia addition.  $\text{PtAu}^+$ , as well as monoatomic  $\text{Pt}^+$ , is rather preferred over any other small  $\text{Pt}_m\text{Au}_n^{+/-,0}$  clusters to catalyze this chemical process.<sup>43–47</sup> Experimental and theoretical studies showed that the binding energy between the cluster and the carbene intermediate must be within a certain range to maintain the binding without preventing the addition of ammonia.<sup>47</sup> The same principle can be generalized (referred as the Sabatier principle) and its fulfillment is desired in multi-step reactions.<sup>48</sup> At the same time, TM elements in the middle of the periodic table (such as Os, Os oxides and Cr) can also be used as catalysts for the dehydrogenation of methane, but with an emphasis on the lowered reaction barriers by spin inversion.<sup>49–51</sup> Therefore, it can be seen that studies of TM clusters have to span large configurational spaces and spin multiplicity spaces to be conclusive.

In Chapter 2, small clusters containing Au and Pt are studied. Among all the TM elements, Pt and other Pt group elements have been widely used for many catalysis reactions. Gold, though usually used as coinage metal because of its preciousness and inertness, possesses specific catalytic properties in cluster form or when supported on certain substrates.<sup>52</sup> By doping atomic Pt into small Au clusters, new materials or catalysts may be available with tuned properties and reactivities.

The Pt-Pt, Au-Au and Pt-Pt bondings have been shown to be dominated by delocalized  $6s$ - $6s$  interactions that rest in the relativistic  $s$  contraction effect. Therefore, this scalar relativistic effect must be considered. The spin-orbit coupling effects, proven to affect mainly the binding energy, are not critical in determining the relative stability of the clusters.<sup>53</sup> Therefore, the DFT Hamiltonian and the LanL2DZ basis set are sufficient in this TM cluster study with the scalar relativistic effect partially incorporated in the effective core potential.

### 1.5.2 TM doped SWCNTs—Chapter 3

A single-walled carbon nanotube (SWCNT) can be regarded as a single layer of graphene sheet rolled up in the direction of a chiral vector  $(m, n)$  into a cylinder until the  $(0, 0)$  point is superposable with  $(m, n)$  point. This chiral vector  $(m, n)$  can be decomposed into a linear combination of two unit vectors  $a_1$  and  $a_2$  (Figure 1.1). By understanding that a  $(m, n)$  SWCNT comes from a graphene sheet in a particular way, characterized by the integer pair  $(m, n)$ , one can explain the dependence of SWCNT electronic structure on the chiral vector.<sup>54–59</sup> The key point relevant to the SWCNT electronic structure, especially electric conductivity, is that graphene is semi-metallic with valence and conduction bands degenerate at only six corners of the hexagonal first Brillouin zone. Thus, rolling up a single layer of graphite into 1D nanotubes may result in metallic or semiconductive SWCNTs, depending on whether the longitudinal  $k$  vectors of the nanotube can pass the degenerate points in the band structure of the graphene. If the longitudinal  $k$  vector goes through these degenerate corner points, the SWCNT is conductive, which corresponds to the  $(m, n)$  vectors that satisfy  $m - n = 3l$  ( $l$  is an integer). If the longitudinal  $k$  vector does not intersect these points, the resultant SWCNT is semiconductive. This relation between the chiral vector index and the electric conductivity is well

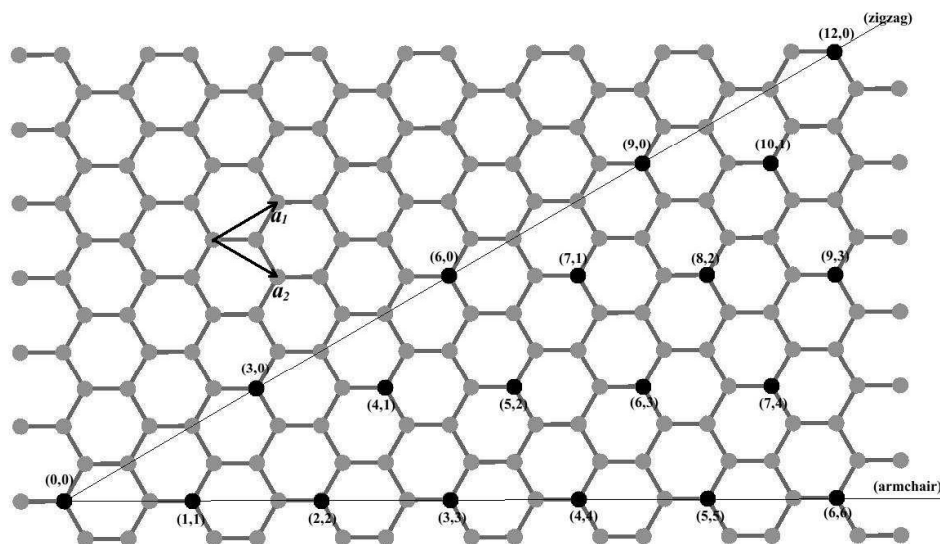


Figure 1.1: A graphene hexagonal sheet and two unit chiral vectors  $a_1$  and  $a_2$  that are used to define chiral vectors. Dark black dots indicate that rolling up according to these chiral vectors will result in metallic SWCNTs.

illustrated in detail in several references.<sup>58,59</sup>

Interactions between CNTs and metals, especially TMs, have been of great interest recently, because studies of these interactions may result in many new materials with intriguing properties and reactivities. For example, SWCNTs loaded with Pd atoms are a good methane detector.<sup>60</sup> Nevertheless, to the best of our knowledge, endo doped SWCNTs have never been studied even though the endo doping may introduce new physics to the CNT-based materials. In Chapter 4, we look into the possibility of doping TMs into SWCNTs interiorly.

### 1.5.3 Interactions between Pt and BNNTs—Chapter 4

An isoelectronic structure of a benzene molecule is the borazine molecule— $B_3N_3H_6$ . Therefore, one could imagine the existence of boron nitrogen analogues of the graphene and carbon nanotubes: hexagon boron nitride (hBN) and single wall boron nitride nanotubes (BNNTs). Different from its homonuclear carbon analogues, however, BNNTs are insulating with only a few exceptions.<sup>61</sup> The physical explanation can be understood by looking at the electronic structure of the layered hBN. The hBNs are mostly insulating because the B and N atoms are so ionic that the valence electrons

are tightly bound to the nuclei. As a result, hBN sheets rolled-up eventually remain insulating due to the flat bands along MK directions near the Fermi level (see Ref. 59). Regardless of whether the longitudinal  $k$  vector passes the K point, the BNNTs are still insulating except some zigzag BNNTs that have extremely small tubular radii. Thus, the study of BNNT can be conducted using a cluster/truncated model with the terminal dangling bonds saturated with H atoms. The interactions of atomic Pt and pristine, Stone-Wales (SW) defected and singly vacant (5,5) BNNTs are studied in Chapter 4.

## 1.6 Hyperfine coupling constants of muoniated radicals

Muon ( $\mu^+$ ) is a fundamental particle that is usually produced from the following nuclear reactions:<sup>62</sup>

$$\pi^+ \rightarrow \mu^+ + \nu_\mu \quad (1.47)$$

$$\mu^+ + e \rightarrow Mu \cdot \quad (1.48)$$

$$\mu^+ \rightarrow e^+ + \nu_e + \bar{\nu}_\mu \quad (1.49)$$

When muons are produced, they are almost always spin polarized. This makes muonium, which consists of a muon and an electron, a good magnetic resonance probe compared with regular magnetic probes whose spin polarization is only achieved at low temperature or in strong magnetic fields. Therefore, muon(ium)s are introduced widely into many chemical systems as a magnetic probe. Recently, some experiments that shine muonium beams on various butene isomers were conducted at TRIUMF, Canada. Corresponding theoretical computations were required to assign observed muon and proton hyperfine coupling constants (HFCCs) and to give deep insight into the physics behind HFCCs and their temperature-dependent (T-dependent) behaviors.

### 1.6.1 Muon HFCC calculations—Chapter 5

The mass of a muon is only one ninth that of a proton. Thus, muonium can be regarded as a light hydrogen isotope along the lines of hydrogen, deuterium and tritium. This seemingly harmless difference actually turns to be a big problem in the calculations of some properties of muoniated radicals.

The HFCC,  $a_N$ , originates from the Fermi contact interaction of electron spin with the nuclear spin.<sup>63</sup> Without using the true quantum mechanical spin Hamiltonian that contains differential operators determined from relativistic quantum mechanics, the HFCC can be calculated using an effective spin Hamiltonian on the effective spin state functions.<sup>64</sup> That is, the value of the HFCC is

proportional to the electron spin density at the nucleus of interest and can be expressed as<sup>65</sup>

$$\begin{aligned} a_N &= \frac{4\pi}{3} \beta_e \beta_N g_e g_N \langle S_Z \rangle^{-1} \rho_N^{\alpha-\beta} \\ &= \frac{4\pi}{3} \beta_e \beta_N g_e g_N \sum_{\mu, \nu} P_{\mu, \nu}^{\alpha-\beta} \langle \phi_\mu(r) | \delta(r - r_n) | \phi_\nu(r) \rangle, \end{aligned} \quad (1.50)$$

where  $\beta_e$  is the Bohr magneton,  $\beta_N$  is the nuclear magneton;  $g_e$  is the free-electron  $g$ -value,  $g_N$  is the nuclear  $g$ -value,  $\langle S_Z \rangle$  is the expectation value of the  $z$ -component of the total electron spin (1/2 for a doublet, 1 for a triplet, *etc.*),  $\rho_N^{\alpha-\beta}$  is the spin density at the nucleus of interest, and  $P_{\mu, \nu}^{\alpha-\beta}$  is the spin density matrix.

For a regular molecule containing heavy nuclei, HFCCs calculated using optimized equilibrium geometry are quite satisfactory. Nevertheless, atoms in any molecule must vibrate around their equilibrium position, even at zero temperature, due to the quantized zero point vibration. Therefore, any property sensitive to the geometry change must be influenced by the zero point vibrations at all times. Both ESR (HFCC) and NMR are subject to this vibrational effect, and the vibrational corrections can be as large as 10 %.<sup>66</sup> In one extreme, the light mass of muon(ium) causes the muonium to be further away from its equilibrium position in a molecule compared with other hydrogen isotopes at the same position in an isotopomer. Thus, the vibrationally averaged muon HFCC can be quite different from the proton HFCC in an isotopomer even though all isotopomers share the same equilibrium structure.<sup>67</sup> This dynamic/vibrational effect can be compensated for in many ways.

An instructive way to calculate vibrationally-averaged molecular properties was developed by Lounila and coworkers',<sup>68</sup> who expressed the property of a molecule,  $P$ , at a certain geometry as a Taylor series in terms of the normal coordinates,  $X_i$ , off the equilibrium geometry,  $X_e$ , that is

$$P(X_i) = P_e + \sum_i P_i X_i + \frac{1}{2} \sum_{i,j} P_{i,j} X_i X_j + \dots \quad (1.51)$$

where  $P_i$  and  $P_{i,j}$  are the first and second order derivatives of  $P(X_i)$  with respect to  $X_i$  and  $X_j$ . Therefore, the vibrationally-average property can be expressed as

$$\langle P \rangle = P_e + \sum_i P_i \langle X_i \rangle + \frac{1}{2} \sum_{i,j} P_{i,j} \langle X_i X_j \rangle + \dots \quad (1.52)$$

At the average molecular geometry, one simply has  $X_i \equiv \langle X_i \rangle$  by definition, and hence, at this geometry, the molecular property is:

$$P_a = P(\langle X_a \rangle) = P_e + \sum_i P_i \langle X_i \rangle + \frac{1}{2} \sum_{i,j} P_{i,j} \langle X_i \rangle \langle X_j \rangle + \dots \quad (1.53)$$



By comparing the above two equations, the averaged property can be written as

$$\langle P \rangle = P_a + \frac{1}{2} \sum_{i,j} P_{i,j} (\langle X_i X_j \rangle - \langle X_i \rangle \langle X_j \rangle) + \dots . \quad (1.54)$$

In this regard, the molecular property calculated at the averaged geometry includes the entire first order vibrational correction and partial harmonic corrections. Therefore, a property calculation using the averaged molecular geometry can include major vibrational corrections. In a muonium-containing molecule, the muonium is the only atom whose average position is largely different from its equilibrium position. Luckily, the averaged geometry parameters for a typical  $\beta$ -muoniated alkyl radical can be found in a path integral Monte Carlo study.<sup>69</sup> The detailed HFCC calculations and discussions can be found in Chapter 5.

### 1.6.2 Torsional PES of sec-butyl radical—Chapter 6

As a byproduct of the muon HFCC study, geometry optimizations of several radicals were found to depend greatly on the computational methods applied. This gave us a good opportunity to investigate the performances of different Hamiltonians and basis sets since the accuracy is a question in two dimensions—Hamiltonian and basis set. The torsional PES of sec-butyl is studied in Chapter 6 using various Hamiltonians and basis sets. Different WFT methods, including HF, MP2, CISD, CCSD, and different exchange-correlation functionals of Kohn-Sham DFT are examined. As for the basis set, Pople basis sets and correlation consistent basis sets are tested.

# Bibliography

- [1] E. Schrödinger. An undulatory theory of the mechanics of atoms and molecules. *Phys. Rev.*, 28:1049–1070, 1926.
- [2] E. Schrödinger. Quantisierung als eigenwertproblem. *Ann. d Physik.*, 79:361–376, 1926.
- [3] M. Born and R. Oppenheimer. Quantum theory of the molecules. *Ann. d Physik.*, 84:457–484, 1927.
- [4] F. Jensen. *Introduction to Computational Chemistry*. John Wiley & Sons, Ltd, 2nd edition, 2006.
- [5] J. Kohanoff. *Electronic Structure Calculations for Solids and Molecules: Theory and Computational Methods*. Cambridge University Press, 1st edition, 2007.
- [6] T. Miyazaki, editor. *Atom Tunneling Phenomena in Physics, Chemistry and Biology*. Springer, 2004.
- [7] I. N. Levine. *Quantum Chemistry*. Prentice Hall, 5th edition, 2000.
- [8] R. G. Parr and W. Yang. *Density-Functional Theory of Atoms and Molecules*. Oxford University Press, 1st edition, 1989.
- [9] P. W. Ayers. *Variational principles for describing chemical reactions*. PhD thesis, the University of North Carolina at Chapel Hill, 2001.
- [10] W. Pauli. Über den einfluß der geschwindigkeitsabhängigkeit der elektronenmasse auf den Zeemaneffekt. *Z. Physik*, 31:373–385, 1925.
- [11] J. C. Slater. The self-consistent field and the structure of atoms. *Phys. Rev.*, 32:332–348, 1928.
- [12] J. C. Slater. Note on Hartree’s method. *Phys. Rev.*, 35:210–211, 1930.
- [13] V. Fock. Näherungsmethode zur losung des quantenmechanischen mehrkörperprobleme. *Z. Phys.*, 61:126–148, 1930.
- [14] A. Szabo and N. S. Ostlund. *Modern Quantum Chemistry*. Dover Publications, Inc., 1996.

- [15] C. C. J. Roothaan. New developments in molecular orbital theory. *Rev. Mod. Phys.*, 23:69–89, 1951.
- [16] J. A. Pople and R. K. Nesbet. Self-consistent orbitals for radicals. *J. Chem. Phys.*, 22:571–572, 1954.
- [17] T. A. Koopmans. Über die zuordnung von wellenfunktionen und eigenwerten zu den einzelnen elektronen eines atoms. *Physica*, 1:104–113, 1933.
- [18] C. Møller and M. S. Plesset. Note on an approximation treatment for many-electron systems. *Phys. Rev.*, 46:618–622, 1934.
- [19] P. R. Taylor, G. B. Bacskay, N. S. Hush, and A. C. Hurley. The coupled-pair approximation in a basis of independent-pair natural orbitals. *Chem. Phys. Lett.*, 41:444–449, 1976.
- [20] R. J. Bartlett and G. D. Purvis. Many-body perturbation theory, coupled-pair many-electron theory, and the importance of quadruple excitations for the correlation problem. *Int. J. Quantum Chem.*, 14:561–581, 1978.
- [21] J. A. Pople, R. Krishnan, H. B. Schlegel, and J. S. Binkley. Electron correlation theories and their application to the study of simple reaction potential surfaces. *Int. J. Quantum Chem.*, 14:545–560, 1978.
- [22] C. J. Cramer. *Essential of Computational Chemistry*. John Wiley & Sons, Ltd., 2nd edition, 2004.
- [23] P. Hohenberg and W. Kohn. Inhomogeneous electron gas. *Phys. Rev.*, 136:B864–867, 1964.
- [24] W. Kohn and L. J. Sham. Self-consistent equations including exchange and correlation effects. *Phys. Rev.*, 140:A1133–A1138, 1965.
- [25] R. O. Jones and O. Gunnarsson. The density functional formalism, its applications and prospects. *Rev. Mod. Phys.*, 61:689–746, 1989.
- [26] A. D. Becke. Density functional exchange-energy approximation with correct asymptotic behavior. *Phys. Rev. A*, 38(6):3098–3100, 1988.
- [27] J. P. Perdew, K. Burke, and M. Ernzerhof. Generalized gradient approximation made simple. *Phys. Rev. Lett.*, 77:3865–3868, 1996.
- [28] J. P. Perdew. Generalized gradient approximations for exchange and correlation: A look backward and forward. *Physica B*, 172:1–6, 1991.
- [29] B. J. Lynch, P. L. Fast, M. Harris, and D. G. Truhlar. Adiabatic connection for kinetics. *J. Phys. Chem. A*, 104:4811–4815, 2000.

- [30] S. H. Vosko, L. Wilk, and M. Nusair. Accurate spin-dependent electron liquid correlation energies for local spin density calculations: a critical analysis. *Can. J. Phys.*, 58:1200–1210, 1980.
- [31] R. Colle and O. Salvetti. Approximate calculation of the correlation energy for the closed shells. *Theoret. Chim. Acta (Berl.)*, 37:329–334, 1975.
- [32] C. Lee, W. Yang, and R. G. Parr. Development of the Colle-Salvetti correlation-energy formula into a functional of the electron density. *Phys. Rev. B*, 37:785–789, 1988.
- [33] A. D. Becke. Correlation energy of an inhomogeneous electron gas: A coordinate-space model. *J. Chem. Phys.*, 88:1053–1062, 1988.
- [34] J. P. Perdew and Y. Wang. Accurate and simple analytic representation of the electron-gas correlation energy. *Phys. Rev. B*, 45:13244–13249, 1992.
- [35] A. D. Becke. Density-functional thermochemistry. IV. A new dynamical correlation functional and implications for exact-exchange mixing. *J. Chem. Phys.*, 104:1040–1046, 1996.
- [36] K. Raghavachari. Perspective on “Density functional thermochemistry. III. The role of exact exchange”. *Theor. Chem. Acc.*, 103:361–363, 2000.
- [37] A. D. Becke. A new mixing of Hartree-Fock and local density-functional theories. *J. Chem. Phys.*, 98:1372–1377, 1993.
- [38] A. D. Becke. Density functional thermochemistry. III. The role of exact exchange. *J. Chem. Phys.*, 98:5648–5672, 1993.
- [39] P. Geerlings, F. De Proft, and W. Langenaeker. Conceptual density functional theory. *Chem. Rev.*, 103:1793–1873, 2003.
- [40] K. Fukui, T. Yonezawa, and H. Shingu. A molecular orbital theory of reactivity in aromatic hydrocarbons. *J. Chem. Phys.*, 20:722–725, 1952.
- [41] G. Frenking and N. Fröhlich. The nature of the bonding in transition-metal compounds. *Chem. Rev.*, 100:717–774, 2000.
- [42] M. D. Morse. Clusters of transition-metal atoms. *Chem. Rev.*, 86:1049–1109, 1986.
- [43] M. Aschi, M. Brönstrup, M. Diefenbach, J. N. Harvey, D. Schröder, and H. Schwarz. A gas-phase model for the  $\text{Pt}^+$ -catalyzed coupling of methane and ammonia. *Angew. Chem., Int. Ed.*, 37:829–832, 1998.

- [44] M. Diefenbach, M. Brönstrup, M. Aschi, D. Schröder, and H. Schwarz. Hcn synthesis from methane and ammonia: mechanisms of  $\text{Pt}^+$ -mediated C-N coupling. *J. Am. Chem. Soc.*, 121:10614–10625, 1999.
- [45] K. Koszinowski, D. Schröder, and H. Schwarz. Probing cooperative effects in bimetallic clusters: Indications of C-N coupling of  $\text{CH}_4$  and  $\text{NH}_3$  mediated by the cluster ion  $\text{PtAu}^+$  in the gas phase. *J. Am. Chem. Soc.*, 125:3676–3677, 2003.
- [46] K. Koszinowski, D. Schröder, and H. Schwarz. Reaction of platinum-carbene clusters  $\text{Pt}_n\text{CH}_2^+$  ( $n=1-5$ ) with  $\text{O}_2$ ,  $\text{CH}_4$ ,  $\text{NH}_3$ , and  $\text{H}_2\text{O}$ : Coupling processes versus carbide formation. *Organometallics*, 22:3809–3819, 2003.
- [47] K. Koszinowski, D. Schröder, and H. Schwarz. C-N coupling of methane and ammonia by bimetallic platinumium-gold cluster cations. *Organometallics*, 23:1132–1139, 2004.
- [48] H. Knözinger and K. Kochloefl. Heterogeneous catalysis and solid catalysts. In *Ullmann's Encyclopedia of Industrial Chemistry*, pages 1–110. Wiley-VCH Verlag, 2005.
- [49] G. Zhang, S. Li, and Y. Jiang. Dehydrogenation of methane by gas-phase Os: a density functional study. *Organometallics*, 22:3820–3830, 2003.
- [50] G. Zhang, S. Li, and Y. Jiang. Density functional study on the mechanisms of the reactions of gas-phase  $\text{OsO}_n^+$  with methane. *Organometallics*, 23:3656–3667, 2004.
- [51] R. Georgiadis and P. B. Armentrout. Transitional and electronic energy dependence of chromium ion reactions with methane. *J. Phys. Chem.*, 92:7067–7074, 1988.
- [52] D. J. Gorin and F. D. Toste. Relativistic effects in homogeneous gold catalysis. *Nature*, 446:395–403, 2007.
- [53] L. Xiao and L. Wang. Structures of platinum clusters planar or spherical. *J. Phys. Chem. A*, 108:8605–8614, 2004.
- [54] M. S. Dresselhaus, G. Dresselhaus, and R. Saito. Carbon fibers based on  $\text{C}_{60}$  and their symmetry. *Phys. Rev. B*, 45:6234–6242, 1992.
- [55] J. W. Mintmire, B. I. Dunlap, and C. T. White. Are fullerene tubules metallic? *Phys. Rev. Lett.*, 68:631–634, 1992.
- [56] M. Dresselhaus, G. Dresselhaus, and P. Avouris. *Introduction to Carbon Materials Research*. Springer-Verlag, Berlin, 2001.
- [57] Ph. Avouris, M. Radosavljevic, and S. J. Wind. Carbon nanotube electronics and optoelectronics. In S. V. Rotkin and S. Subramoney, editors, *Applied Physics of Carbon Nanotubes: Fundamentals of Theory, Optics and Transport Devices*, pages 227–251. Springer, 2005.

- [58] G. Dresslhaus, M. A. Pimenta, R. Saito, J. C. Charlier, S. D. M. Brown, P. Corio, A. Marucci, and M. S. Dresselhaus. On the  $\pi$ - $\pi$  overlap energy in carbon nanotubes. In *Science and Application of Nanotubes*, pages 275–295. Kluwer Academic/Plenum Publishers, New York, 2000.
- [59] F. Ducastelle, X. Blase, J. M. Bonard, J. Ch. Charlier, and P. Petit. Electronic structure. *Lect. Notes Phys.*, 677:199–276, 2006.
- [60] Y. Lu, J. Li, J. Han, H. T. Ng, C. Binder, C. Partridge, and M. Meyyappan. Room temperature methane detection using palladium loaded single-walled carbon nanotube sensors. *Chem. Phys. Lett.*, 391:344–348, 2004.
- [61] H. J. Xiang, J. Yang, J. G. Hou, and Q. Zhu. First-principles study of small-radius single-walled BN nanotubes. *Phys. Rev. B*, 68:035427, 2003.
- [62] C. J. Rhodes. Muonium—the second radioisotope of hydrogen and its contribution to free radical chemistry. *J. Chem. Soc., Perkin Trans.*, 2:1379–1396, 2002.
- [63] W. Kuzelnigg. Origin and meaning of the Fermi contact interaction. *Theoretica Chimica Acta*, 73:173–200, 1988.
- [64] G. H. Lushington. The effective spin hamiltonian concept from a quantum chemical perspective. In M. Kaupp, M. Bühl, and V. G. Malkin, editors, *Calculation of NMR and EPR Parameters*, pages 33–41. WILEY-VCH, 2004.
- [65] W. Weltner. *Magnetic Atoms and Molecules*. Dover, New York, 1989.
- [66] T. A. Ruden and K. Ruud. Ro-vibrational corrections to NMR parameters. In M. Kaupp, M. Bühl, and V. G. Malkin, editors, *Calculation of NMR and EPR Parameters*, pages 153–173. WILEY-VCH, 2004.
- [67] S. L. Thomas and I. Carmichael. Hyperfine interactions in muonium-containing radicals. *Physica B*, 374-375:290–294, 2006.
- [68] J. Lounila, R. Wasser, and P. Diehl. Effects of anharmonic vibrations on molecular properties. *Molecular Physics*, 62(1):19–31, 1987.
- [69] M. C. Böhm, R. Ramirez, and J. Schulte. Finite-temperature properties of the muonium substituted ethyl radical  $\text{CH}_2\text{MuCH}_2$ : nuclear degrees of freedom and hyperfine splitting constants. *Mol. Phys.*, 103:2407–2436, 2005.

## Chapter 2

# Theoretical Studies of $\text{Au}_m$ and $\text{PtAu}_n$ Clusters and Their $\text{N}_2$ and $\text{O}_2$ Adsorption Complexes<sup>1</sup>

### 2.1 Introduction

With their special properties and reactivities, metal clusters have drawn a lot of attention in diverse research fields such as physics, chemistry, and materials sciences.<sup>1–6</sup> In comparison with their bulk counterparts, the unique size of small clusters contributes to their theoretical and practical importance. Because of their tunable electronic structure, bimetallic clusters are superior to homonuclear ones in many aspects. For example, bimetallic Ru-Pt clusters are good catalysts for hydrogenation of  $\text{PhC}_2\text{Ph}$  with enhanced or even unprecedented catalytic activities and selectivities.<sup>7</sup> Also, a series of bimetallic clusters containing many combinations of different transition metal elements have potential luminescence that can be used in photocatalysis at room temperature.<sup>8</sup>

Particularly, Au and Pt, two third-row transition metal elements, have distinct properties and reactivities. Pt is chemically active and is usually used as catalyst for various reactions. Au, is often chemically inert and is often employed as a coinage metal. Putting these two precious metal elements together, especially in small clusters, has resulted in many new advanced materials. For instance, CO adsorption on Pt can be enhanced by coating layers of Pt over a Au substrate.<sup>9</sup> Many experimental results suggest that bimetallic clusters of Au and Pt are better catalysts for many chemical reactions with much improved catalytic abilities than homonuclear Pt or Au clusters, because of the cooperative effect between Pt and Au. The silica-supported bimetallic Pt-Au clusters can activate absorbed CO by significantly lowering the stretching frequency of the  $\text{C}\equiv\text{O}$  bond and hence weakening the  $\text{C}\equiv\text{O}$  bond, whereas pure Pt catalysts do not have such potency.<sup>10</sup> Small Pt-Au bimetallic clusters also are recognized for their excellent performance in catalyzing the coupling reaction of  $\text{CH}_4$  and  $\text{NH}_3$  to produce the precursor for the important Degussa process.<sup>11–13</sup>

Because traditional molecular spectroscopic techniques have intrinsic limits in characterizing these small clusters, theoretical calculations have become a powerful tool to gain deeper insights

---

<sup>1</sup>A version of this chapter will be submitted for publication. Chen, Y. K.; Tian, W. Q. and Wang, Y. A. Theoretical Studies of  $\text{Au}_m$  and  $\text{PtAu}_n$  Clusters and Their  $\text{N}_2$  and  $\text{O}_2$  Adsorption Complexes.

into the electronic structure of such clusters.<sup>14–17</sup> Recently, a series of density functional theory (DFT) calculations demonstrated that small Au clusters favor planar geometries, because the relativistic effect enhances *s-d* hybridization and *d-d* interaction.<sup>18,19</sup> Some other DFT studies have suggested that small Pt clusters favor non-planar geometries with high spin multiplicities.<sup>20–22</sup> It is then interesting to investigate the closely related Pt-Au bimetallic clusters for their geometric structures, catalytic activities and selectivities.<sup>23</sup>

There are quite a few theoretical studies of adsorptions and reactions of small molecules (*e.g.*, CO, O<sub>2</sub>, *etc.*) on metal clusters, especially on Pt-Au bimetallic clusters.<sup>14–17</sup> Experimentally, the Pt-Au clusters were found to be good catalytic candidates to reduce various nitrogen oxide species in the presence of O<sub>2</sub> and small hydrocarbons,<sup>24,25</sup> in a desired, environmentally friendly reaction route towards producing N<sub>2</sub> rather than other competing processes involving N<sub>2</sub>O. O<sub>2</sub> concentration plays an important role in this better reaction path. Additional theoretical studies of the adsorption of N<sub>2</sub> and O<sub>2</sub> on the Pt-Au clusters can provide the necessary guidance in designing high-performance catalysts for the reduction of nitrogen oxide species. Besides this reaction, O<sub>2</sub> adsorption on metal clusters is also crucial for many other processes. For example, the cathode reaction of a fuel cell, typically the oxygen reduction reaction that throttles the fuel cell efficiency and performance, is greatly affected by the binding patterns of O<sub>2</sub>.<sup>26</sup> Without a doubt, N<sub>2</sub> and O<sub>2</sub> adsorption onto these clusters are of practical significance. Their adsorption complexes are investigated in this study.

Because of the large number of *d* electrons of the constituent atoms, calculations of the transition metal clusters have proven to be one of the most difficult tasks in quantum chemistry. DFT, combined with effective core potentials and their related basis sets, is a powerful, efficient tool to study such clusters, based on high-quality exchange-correlation functionals.<sup>27</sup> We thus adopted the Kohn-Sham DFT method in this study.

## 2.2 Computational details

Full geometry optimizations of the metal clusters were carried out using the spin-unrestricted Kohn-Sham DFT method implemented in Gaussian03, with the PBEPBE exchange-correlation functional.<sup>28,29</sup> Harmonic vibrational frequencies were computed to verify the nature of the stationary points on the potential energy surface. The double-zeta basis sets LanL2DZ and additional *f*-type polarization functions ( $\alpha_f = 0.75$ ) for both Au and Pt atoms were employed with the core electrons represented by the corresponding effective pseudopotentials.<sup>30</sup> An integration grid containing 99 radial shells and 590 angular points per shell was adopted to avoid spurious imaginary frequencies.<sup>31</sup> Electronic energies corrected for zero-point vibrational energy were used to establish the relative stability of metal cluster isomers. Properties were analyzed using the hybrid functional B3LYP with the PBEPBE optimized geometries.<sup>32,33</sup> The standard Pople’s 6-31G(d) basis set was used for nitrogen and oxygen. Partial charges and spin densities were calculated based on the natural bond



orbital analysis.<sup>34</sup>

To systematically sample the stationary points on the ground-state potential energy surface of the  $\text{Au}_m$  clusters, many topologically important structures were created as initial guesses. For the  $\text{PtAu}_n$  clusters, the same sets of initial geometries were used with each nonequivalent Au position replaced by a Pt atom. Though many isomers were found for larger clusters, only the isomers lying within 10 kcal/mol of the ground-state structure were reported.

To study the adsorption complexes, we considered all clusters lying within 10 kcal/mol of the most stable isomer.  $\text{N}_2$  and  $\text{O}_2$  were placed at those topologically significant sites for subsequent geometry optimizations of the adsorption complexes.

## 2.3 Results and discussions

### 2.3.1 $\text{Au}_m$ and $\text{PtAu}_n$ clusters

The structures of the most stable  $\text{Au}_m$  and  $\text{PtAu}_n$  clusters and isomers (lying within 10 kcal/mol of the ground state) and the natural spin densities of the open-shell clusters are shown in Figure 2.1. The corresponding natural electronic configurations (NECs) are listed in Table 2.1.

The predicted bond length and the frequency of the stretching mode of the ground-state  $\text{Au}_2$  are 2.535 Å and 171.3  $\text{cm}^{-1}$ , respectively, in good agreement with the experimentally observed values (2.473 Å and 190.9  $\text{cm}^{-1}$ ).<sup>35,36</sup> NEC analysis shows a slight electron promotion from 5*d* to 6*s* in both Au atoms and indicates the participation of the 5*d* orbital in the bond formation of  $\text{Au}_2$ .

As for the  $\text{PtAu}$ , the ground state has a  $^2\Sigma^+$  electronic configuration. The bond length and fundamental vibrational frequency are 2.488 Å and 179.3  $\text{cm}^{-1}$ , respectively, very close to the results obtained in some earlier high-level calculations using complete active space multiconfiguration self-consistent-field method (2.601 Å and 168  $\text{cm}^{-1}$ ) and multireference singles and doubles configuration interaction (MRCISD) method (2.544 Å and 194  $\text{cm}^{-1}$ ).<sup>37</sup> The charge distribution of  $\text{PtAu}$  reflects the very small electronegativity difference between atomic Pt and atomic Au. In the  $\text{PtAu}$  cluster, only a small amount of negative charge is transferred from the Pt atom to the Au atom. The net spin charge is primarily localized on the Pt atom (see Figure 2.1). NEC analysis indicates that the spin charge comes from the unfilled 5*d* orbital of the Pt atom, whose  $\alpha$ -spin and  $\beta$ -spin valence NECs are  $6s^{0.54}d^{4.95}$  and  $6s^{0.43}d^{4.07}$ , respectively.

Two low-lying  $\text{Au}_3$  structures were identified (Figure 2.1): an angular (bent) isomer with apex angle of 144.7°, and an isocenes triangular structure lying 1.73 kcal/mol above, with apex angle of 67.9°. In the angular  $\text{Au}_3$ , the Au(I)–Au(II)/Au(III) distance is 2.603 Å. In the triangular  $\text{Au}_3$  isomer, the Au(I)–Au(II) and Au(II)–Au(III) distances are 2.630 and 2.936 Å, respectively. This indicates that the Au(I)–Au(II)/Au(III) interaction in the angular isomer is stronger than that in the triangular one. Most of the spin density is evenly located on the two equivalent Au atoms in both  $\text{Au}_3$  isomers. According to the NEC analysis, the middle Au atom in the angular  $\text{Au}_3$  undergoes

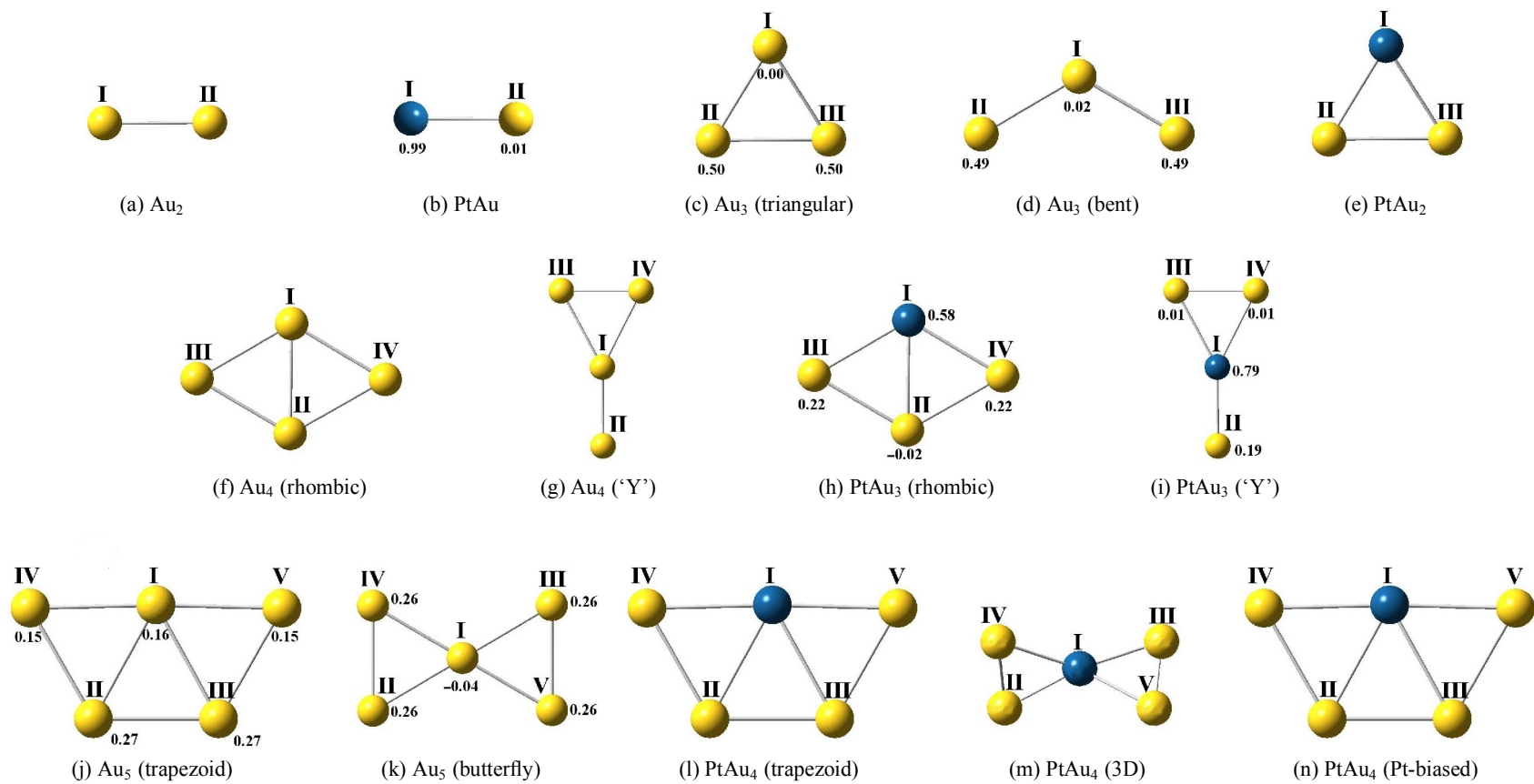


Figure 2.1: Optimized structures of low-lying  $Au_m$  and bimetallic  $PtAu_n$  clusters. The Pt and Au atoms are in dark green and yellow, respectively. For open-shell clusters, natural spin charge on each atomic site is also shown.

Cluster	Atom	Sites	Natural Electron Configuration
Au <sub>2</sub>	Au	I, II	[core]6s <sup>1.04</sup> 5d <sup>9.95</sup> 6p <sup>0.01</sup>
PtAu	Pt	I	[core]6s <sup>0.96</sup> 5d <sup>9.02</sup> 6p <sup>0.01</sup>
	Au	II	[core]6s <sup>1.10</sup> 5d <sup>9.90</sup> 6p <sup>0.01</sup>
Au <sub>3</sub> (obtuse)	Au	I	[core]6s <sup>1.17</sup> 5d <sup>9.88</sup> 6p <sup>0.03</sup>
	Au	II, III	[core]6s <sup>1.00</sup> 5d <sup>9.95</sup>
Au <sub>3</sub> (acute)	Au	I	[core]6s <sup>0.85</sup> 5d <sup>9.95</sup> 6p <sup>0.03</sup>
	Au	II, III	[core]6s <sup>1.14</sup> 5d <sup>9.93</sup> 6p <sup>0.02</sup>
PtAu <sub>2</sub>	Pt	I	[core]6s <sup>0.66</sup> 5d <sup>9.49</sup> 6p <sup>0.02</sup>
	Au	II, III	[core]6s <sup>0.96</sup> 5d <sup>9.93</sup> 6p <sup>0.02</sup>
Au <sub>4</sub> (rhombic)	Au	I, II	[core]6s <sup>0.73</sup> 5d <sup>9.95</sup> 6p <sup>0.04</sup>
	Au	III, IV	[core]6s <sup>1.35</sup> 5d <sup>9.91</sup> 6p <sup>0.01</sup>
Au <sub>4</sub> ('Y')	Au	I	[core]6s <sup>1.15</sup> 5d <sup>9.87</sup> 6p <sup>0.04</sup>
	Au	II	[core]6s <sup>1.23</sup> 5d <sup>9.93</sup>
	Au	III, IV	[core]6s <sup>0.92</sup> 5d <sup>9.95</sup> 6p <sup>0.02</sup>
PtAu <sub>3</sub> (rhombic)	Pt	I	[core]6s <sup>0.65</sup> 5d <sup>9.29</sup> 6p <sup>0.04</sup>
	Au	II	[core]6s <sup>0.77</sup> 5d <sup>9.95</sup> 6p <sup>0.04</sup>
	Au	III, IV	[core]6s <sup>1.22</sup> 5d <sup>9.90</sup> 6p <sup>0.01</sup>
PtAu <sub>3</sub> ('Y')	Pt	I	[core]6s <sup>1.01</sup> 5d <sup>9.06</sup> 6p <sup>0.05</sup>
	Au	II	[core]6s <sup>1.25</sup> 5d <sup>9.85</sup>
	Au	III, IV	[core]6s <sup>0.94</sup> 5d <sup>9.93</sup> 6p <sup>0.02</sup>
Au <sub>5</sub> (trapezoid)	Au	I	[core]6s <sup>0.93</sup> 5d <sup>9.89</sup> 6p <sup>0.05</sup>
	Au	II, III	[core]6s <sup>1.01</sup> 5d <sup>9.93</sup> 6p <sup>0.03</sup>
	Au	IV, V	[core]6s <sup>1.15</sup> 5d <sup>9.92</sup> 6p <sup>0.01</sup>
Au <sub>5</sub> (butterfly)	Au	I	[core]6s <sup>0.98</sup> 5d <sup>9.87</sup> 6p <sup>0.07</sup>
	Au	II-V	[core]6s <sup>1.07</sup> 5d <sup>9.93</sup> 6p <sup>0.02</sup>
PtAu <sub>4</sub> (trapezoid)	Pt	I	[core]6s <sup>0.67</sup> 5d <sup>9.40</sup> 6p <sup>0.05</sup> 6d <sup>0.01</sup>
	Au	II, III	[core]6s <sup>0.92</sup> 5d <sup>9.94</sup> 6p <sup>0.03</sup>
	Au	IV, V	[core]6s <sup>1.11</sup> 5d <sup>9.92</sup> 6p <sup>0.01</sup>
PtAu <sub>4</sub> (3D)	Pt	I	[core]6s <sup>0.91</sup> 5d <sup>9.40</sup> 6p <sup>0.05</sup> 6d <sup>0.01</sup>
	Au	II, III	[core]6s <sup>0.93</sup> 5d <sup>9.94</sup> 6p <sup>0.02</sup>
	Au	IV, V	[core]6s <sup>0.98</sup> 5d <sup>9.93</sup> 6p <sup>0.02</sup>
PtAu <sub>4</sub> (Pt-biased)	Au	I	[core]6s <sup>0.84</sup> 5d <sup>9.92</sup> 6p <sup>0.05</sup>
	Pt	II	[core]6s <sup>0.77</sup> 5d <sup>9.44</sup> 6p <sup>0.03</sup>
	Au	III	[core]6s <sup>0.82</sup> 5d <sup>9.94</sup> 6p <sup>0.03</sup>
	Au	IV	[core]6s <sup>0.77</sup> 5d <sup>9.44</sup> 6p <sup>0.03</sup>
	Au	V	[core]6s <sup>1.25</sup> 5d <sup>9.92</sup> 6p <sup>0.01</sup>

Table 2.1: Natural electron configurations of atoms of the low-lying clusters. The atomic sites are shown in Figure 2.1.

electron promotion from 5d to 6s and electrons migrate from the two terminal Au atoms to the central one. In contrast, in the triangular Au<sub>3</sub>, the apex Au atom donates its electrons to the basal

Au atoms. The most stable PtAu<sub>2</sub> is also an isosceles triangular cluster with the apex angle of 67.7° and the Pt–Au bond length of 2.579 Å. Electrons flow from the 5*d* and 6*s* orbitals of two basal Au atoms to the 5*d* orbital of the apex Pt atom.

As to the clusters larger than the trimer, the low-lying Au<sub>*m*</sub> and PtAu<sub>*n*</sub> clusters are constituted of colaterally packed triangular building blocks to form (near) 2-dimensional structures. In the low-lying PtAu<sub>*n*</sub> clusters, the Pt atom tends to maximize its coordination number to stabilize the cluster by forming a maximal number of bonds with the surrounding atoms.

In the case of the Au<sub>4</sub> clusters, the ground state is a singlet planar rhombic structure, which is essentially degenerate with a singlet Y-shaped structure found in an earlier study.<sup>38</sup> The PtAu<sub>3</sub> has a <sup>2</sup>A'' ground state with a puckered rhombic configuration and a folding angle of 27.2°. An essentially degenerate <sup>2</sup>A' Y-shaped isomer lies 0.97 kcal/mol above the ground-state of PtAu<sub>3</sub> with the Pt atom at the center. In the rhombic Au<sub>4</sub> and PtAu<sub>3</sub> clusters, the atoms at positions I and II donate their electrons to the 6*s* orbital of the Au atoms at sites III and IV. In the Y-shaped Au<sub>4</sub> and PtAu<sub>3</sub> clusters, the Au atoms at positions III and IV donate their electrons to the apex atom. Spin densities in the two PtAu<sub>3</sub> clusters are mainly located on the Pt atom.

The most stable isomer of Au<sub>5</sub> is a <sup>2</sup>A' planar trapezoid-like structure, as reported earlier.<sup>38</sup> A <sup>2</sup>B<sub>2u</sub> butterfly-like configuration lies 8.15 kcal/mol above the most stable trapezoid isomer. In both these two low-lying Au<sub>5</sub> clusters, all the Au atoms undergo electron promotion from 5*d* to 6*s* to form Au–Au bonds and Au at site I contributes electrons to the other four Au atoms. The most stable isomer of PtAu<sub>4</sub> is also a planar trapezoid-like structure with the Pt atom lying at the middle of the long parallel side to maximize its coordination number. A 3-dimensional isomer with a twisted butterfly-like geometry lies 2.39 kcal/mol above the trapezoidal PtAu<sub>4</sub>. Another PtAu<sub>4</sub> (Pt-biased) isomer is 8.62 kcal/mol higher than the trapezoidal structure. The substitution of Au by a Pt atom at site II in the trapezoidal Au<sub>5</sub> cluster distorts the cluster to a nonplanar structure. In all these three PtAu<sub>4</sub> isomers, electron transfer from 6*s* to 5*d* occurs to the Pt atom and the Pt atom withdraws electrons from the other Au atoms, yielding a negative partial charge.

To gauge the reactivity of these clusters, their Kohn-Sham frontier orbitals and the orbital energies of these clusters are shown in Figure 2.2. The highest occupied molecular orbital (HOMO) of Au<sub>2</sub> is a  $\sigma$  orbital and the lowest unoccupied molecular orbital (LUMO) is a  $\sigma^*$  orbital. The large HOMO-LUMO gap and the low HOMO energy (–7.2 eV) make the Au<sub>2</sub> cluster inert to electrophilic attack. In PtAu, the HOMO is mainly the 5*d* orbital of the Pt atom and has a much better donating ability with an increased orbital energy (–6.8 eV). The LUMO is again a  $\sigma^*$  orbital with a similar orbital energy to the LUMO of Au<sub>2</sub>. For most larger clusters, the HOMOs of the PtAu<sub>*n*</sub> clusters are mainly composed of the 5*d* orbitals of the Pt atom and have orbital energies close to –6.0 eV. The HOMOs of the Au<sub>*m*</sub> clusters are delocalized over the entire cluster and have orbital energy lower than –6.0 eV. The LUMOs of the PtAu<sub>*n*</sub> and Au<sub>*m*</sub> clusters are typically  $\sigma^*$  orbitals and have similar orbital energies of about –4.0 eV. Therefore, the attacking electrophiles will readily locate the reactive Pt center of the bimetallic clusters because the Pt atom of the bimetallic clusters

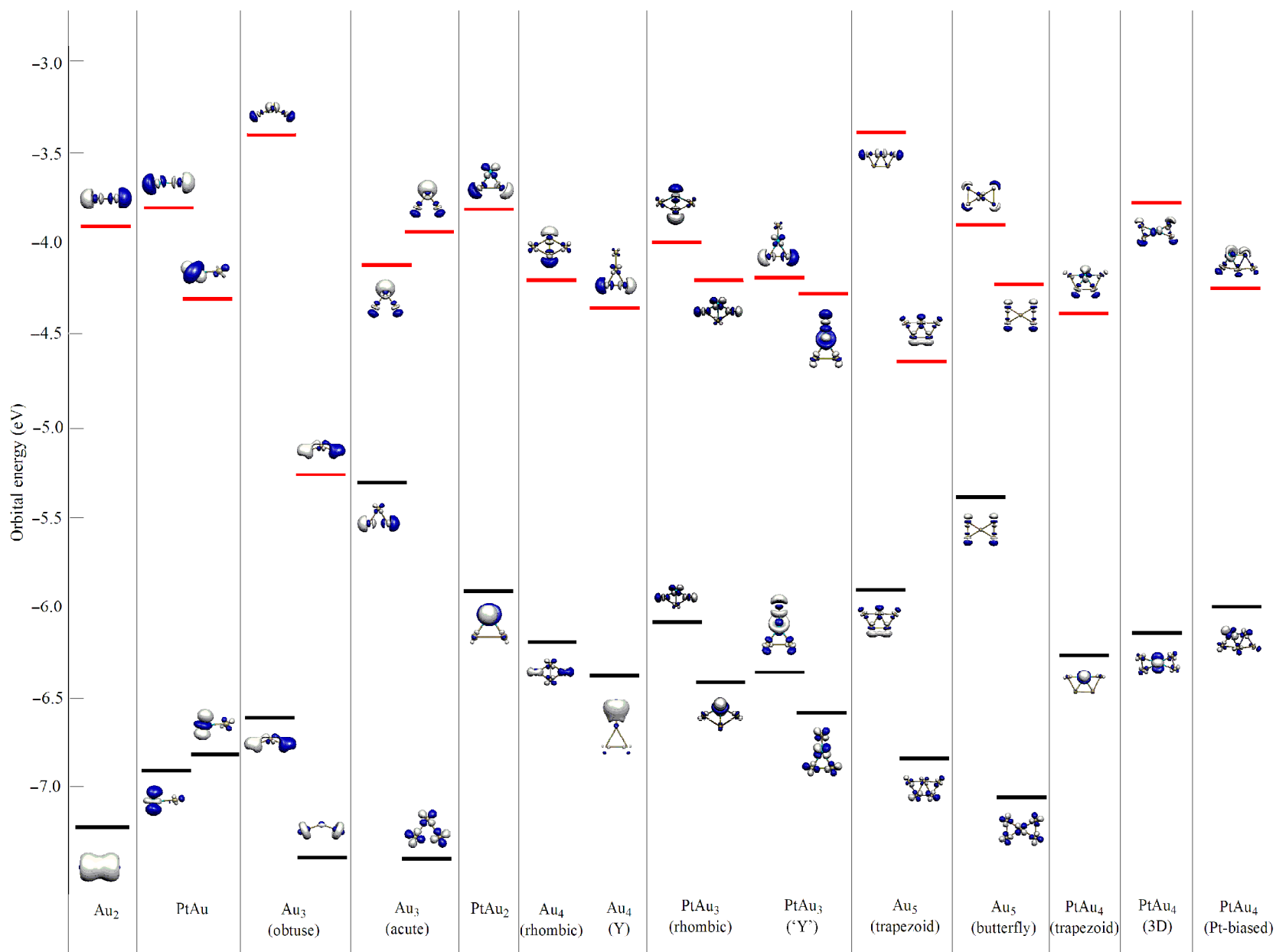


Figure 2.2: The frontier orbitals of  $\text{Au}_m$  and  $\text{PtAu}_n$  clusters. The orbital energies of the highest occupied molecular orbitals and the lowest unoccupied molecular orbitals are marked by black and red bars, respectively. For open-shell systems,  $\alpha$ -spin and  $\beta$ -spin orbitals are grouped on the left and the right of each column, respectively.

accumulates more negative charge than the Au atom of the corresponding pure  $\text{Au}_m$  clusters of the same size at the same position.

### 2.3.2 Adsorptions of $\text{N}_2$ and $\text{O}_2$

With the optimized low-lying clusters in hand, the complexes formed by adsorbing  $\text{N}_2$  and  $\text{O}_2$  onto these low-lying clusters were studied. Thirty three  $\text{N}_2$ -cluster and forty eight  $\text{O}_2$ -cluster complexes were obtained from geometry optimization. The Hessians of these optimized structures were calculated to verify the nature of these complexes. Figures 2.3 and 2.4 show the structures of energetic minima. The adsorption energies are shown in the two Figures. Negative adsorption energies denote exothermic adsorption. Within the same chemical composition, the energy of the most stable isomer was taken to be the reference point in calculating the relative energies of all possible complexes. The N–N and O–O bond lengths are listed to illustrate the interaction strengths between the diatomic molecules and the metal clusters. The HOMO-LUMO gaps are also displayed to illuminate electronic properties.

In all adsorption complexes, to stabilize the complexes through enhanced electrostatic interaction, the metal clusters donate electrons to the  $\text{O}_2/\text{N}_2$  diatomic molecular fragments based on the charge analysis (see below). Almost always, the binding energies of  $\text{O}_2/\text{N}_2$ -bimetallic cluster complexes are larger than that of the complexes formed between  $\text{N}_2/\text{O}_2$  and the corresponding pure Au clusters of the same size. Binding  $\text{N}_2/\text{O}_2$  to the Pt atom of the bimetallic clusters typically has an adsorption energy of about 30 kcal/mol, larger than that to the pure Au clusters (20 kcal/mol). For the binary  $\text{PtAu}_m$  clusters, the high adsorption energy correlates specifically to the binding of  $\text{O}_2$  or  $\text{N}_2$  to the Pt atom rather than to the Au atoms, because the HOMO is mainly localized on the Pt atom in the bimetallic clusters. The adsorption complexes formed by pure Au clusters are similar to the complexes formed by the small diatomic molecules and the bimetallic clusters on the Au site. Therefore, the complexes involving pure Au clusters are not discussed specifically.

Geometrically, both  $\text{O}_2$  and  $\text{N}_2$  prefer to bind to the clusters to the side within the plane of the cluster. Even though the major lobe of the HOMOs of these clusters are atop the clusters, the side-on binding enables the clusters to donate electrons to form both  $\sigma$  and  $\pi$  bonds. In contrast, if the diatomic molecule binds to the cluster top, only a  $\sigma$  bond will be formed instead.

$\text{N}_2$ -adsorption complexes also distinguish themselves from the  $\text{O}_2$ -adsorption complexes in many aspects that will be discussed below based on the representative  $\text{O}_2/\text{N}_2$ - $\text{PtAu}_2$  complexes. Since the precursor  $\text{PtAu}_2$  cluster donates electrons to either  $\text{N}_2$  or  $\text{O}_2$  fragments upon the formation of complexes, the HOMO of the  $\text{PtAu}_2$  cluster must play an important role. The HOMO of  $\text{PtAu}_2$  mainly locates on the Pt atom and is composed of the  $5d$  orbital of the Pt atom (23%  $5d_{z^2}$ , 68%  $5d_{x^2-y^2}$ , and 4%  $6s$ ) with some minor contributions from the two basal Au atoms (*ca.* 5% from their  $5d$  orbitals). This particular composition of the HOMO makes the adsorbate diatomic molecules preferentially attach to the Pt atom.

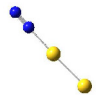
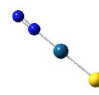
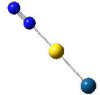
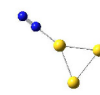
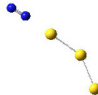
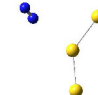
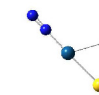
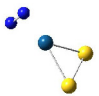
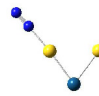
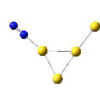
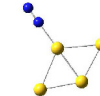
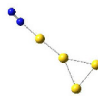
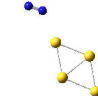

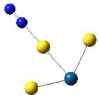
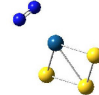
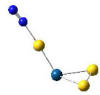
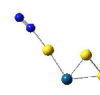

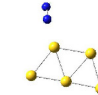
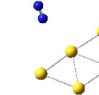
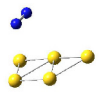
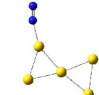
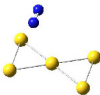
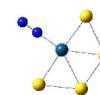
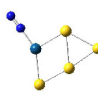
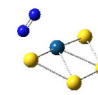
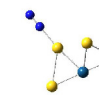

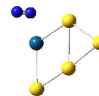
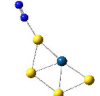
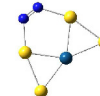
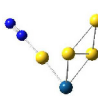
						
$\text{Au}_2\text{N}_2^A$	$\text{PtAuN}_2^A$	$\text{PtAuN}_2^B$	$\text{Au}_3\text{N}_2^A$	$\text{Au}_3\text{N}_2^B$	$\text{Au}_3\text{N}_2^C$	$\text{PtAu}_2\text{N}_2^A$
0.00	0.00	15.43	0.00	4.18	11.91	0.00
-12.29	28.91	13.48	11.91	7.73	0.00	33.24
1.123	1.134	1.125	1.126	1.123	1.117	1.136
2.55	1.12, 2.77	2.26, 3.24	1.41, 3.02	1.44, 2.99	1.36, 2.71	2.48
						
$\text{PtAu}_2\text{N}_2^B$	$\text{PtAu}_2\text{N}_2^C$	$\text{Au}_4\text{N}_2^A$	$\text{Au}_4\text{N}_2^B$	$\text{Au}_4\text{N}_2^C$	$\text{Au}_4\text{N}_2^D$	$\text{PtAu}_3\text{N}_2^A$
14.22	17.97	0.00	1.28	7.27	11.66	0.00
19.02	15.27	12.52	11.24	5.25	0.85	30.03
1.167	1.127	1.123	1.124	1.122	1.120	1.135
2.64	2.29	2.88	2.97	2.15	1.88	1.55, 2.45
						
$\text{PtAu}_3\text{N}_2^B$	$\text{PtAu}_3\text{N}_2^C$	$\text{PtAu}_3\text{N}_2^D$	$\text{PtAu}_3\text{N}_2^E$	$\text{Au}_5\text{N}_2^A$	$\text{Au}_5\text{N}_2^B$	$\text{Au}_5\text{N}_2^C$
15.67	17.43	23.13	24.31	0.00	0.58	3.32
14.36	12.60	6.87	5.72	3.77	3.19	0.45
1.125	1.157	1.124	1.125	1.123	1.124	1.118
1.88, 2.62	1.58, 2.42	2.34, 2.08	1.52, 1.96	1.25, 2.31	1.25, 2.39	1.25, 2.36
						
$\text{Au}_5\text{N}_2^D$	$\text{Au}_5\text{N}_2^E$	$\text{Au}_5\text{N}_2^F$	$\text{PtAu}_4\text{N}_2^A$	$\text{PtAu}_4\text{N}_2^B$	$\text{PtAu}_4\text{N}_2^C$	$\text{PtAu}_4\text{N}_2^D$
3.54	5.26	11.75	0.00	2.71	20.56	21.04
0.23	6.66	0.17	32.65	38.56	12.09	11.61
1.117	1.125	1.117	1.133	1.137	1.151	1.125
1.25, 2.36	1.17, 2.31	1.14, 2.14	2.97	2.72	2.78	2.23
						
$\text{PtAu}_4\text{N}_2^E$	$\text{PtAu}_3\text{N}_2^F$	$\text{PtAu}_4\text{N}_2^G$	$\text{PtAu}_4\text{N}_2^H$	$\text{PtAu}_4\text{N}_2^I$		
21.30	22.59	26.16	27.68	28.55		
11.35	18.68	6.49	4.97	4.10		
1.126	1.163	1.124	1.155	1.125		
2.39	2.53	2.01	2.37	2.01		

Figure 2.3: The optimized structures of  $\text{N}_2$ -cluster adsorption complexes. The relative energy (in kcal/mol) measured from the most stable complex, the adsorption energy (in kcal/mol), the N–N bond length (in Å), and the HOMO-LUMO gap (in eV) are listed below each optimized structure descendingly. For open-shell systems, the first and the second values of the HOMO-LUMO gap are for  $\alpha$  spin and  $\beta$  spin, respectively.

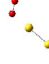


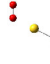
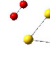
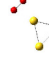
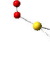
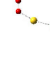



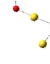
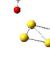
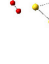
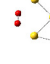
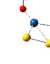
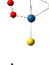
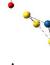

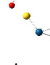

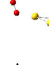



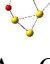
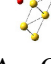

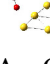
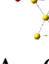
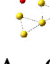
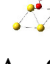
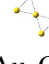
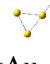
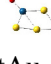
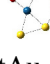
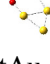
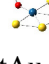

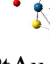

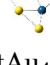





							
Au <sub>2</sub> O <sub>2</sub> <sup>A</sup>	PtAuO <sub>2</sub> <sup>A</sup>	PtAuO <sub>2</sub> <sup>B</sup>	PtAuO <sub>2</sub> <sup>C</sup>	Au <sub>3</sub> O <sub>2</sub> <sup>A</sup>	Au <sub>3</sub> O <sub>2</sub> <sup>B</sup>	Au <sub>3</sub> O <sub>2</sub> <sup>C</sup>	Au <sub>3</sub> O <sub>2</sub> <sup>D</sup>
0.00	0.00	5.34	26.89	0.00	1.40	2.29	4.75
1.15	35.73	30.39	8.84	17.38	15.98	15.09	10.90
1.257	1.302	1.267	1.257	1.297	1.311	1.281	1.273
1.01	2.91, 2.90	2.61, 2.62	1.55, 2.19	2.31, 2.69	1.71, 2.33	0.73, 1.20	1.58, 2.32
							
PtAu <sub>2</sub> O <sub>2</sub> <sup>A</sup>	PtAu <sub>2</sub> O <sub>2</sub> <sup>B</sup>	PtAu <sub>2</sub> O <sub>2</sub> <sup>C</sup>	PtAu <sub>2</sub> O <sub>2</sub> <sup>D</sup>	Au <sub>4</sub> O <sub>2</sub> <sup>A</sup>	Au <sub>4</sub> O <sub>2</sub> <sup>B</sup>	Au <sub>3</sub> O <sub>2</sub> <sup>C</sup>	PtAu <sub>3</sub> O <sub>2</sub> <sup>A</sup>
0.00	6.05	19.13	19.14	0.00	0.29	2.13	0.00
25.02	18.97	5.89	5.88	2.62	2.33	0.49	29.74
1.343	1.323	1.269	1.267	1.263	1.260	1.297	1.275
1.66	1.06	1.20	1.36	1.36	0.81	1.80	1.82, 1.95
							
PtAu <sub>3</sub> O <sub>2</sub> <sup>B</sup>	PtAu <sub>3</sub> O <sub>2</sub> <sup>C</sup>	PtAu <sub>3</sub> O <sub>2</sub> <sup>D</sup>	PtAu <sub>3</sub> O <sub>2</sub> <sup>E</sup>	PtAu <sub>3</sub> O <sub>2</sub> <sup>F</sup>	PtAu <sub>3</sub> O <sub>2</sub> <sup>G</sup>	PtAu <sub>3</sub> O <sub>2</sub> <sup>H</sup>	PtAu <sub>3</sub> O <sub>2</sub> <sup>I</sup>
4.94	18.80	20.13	20.32	20.54	21.03	22.54	24.95
25.77	10.94	9.61	10.17	9.95	9.68	8.17	5.79
1.314	1.266	1.265	1.268	1.261	1.260	1.278	1.301
2.29, 2.39	1.61, 1.73	1.25, 1.78	1.71, 1.87	1.69, 1.78	0.82, 1.11	1.50, 1.62	1.58, 1.91
							
Au <sub>5</sub> O <sub>2</sub> <sup>A</sup>	Au <sub>5</sub> O <sub>2</sub> <sup>B</sup>	Au <sub>5</sub> O <sub>2</sub> <sup>C</sup>	Au <sub>5</sub> O <sub>2</sub> <sup>D</sup>	Au <sub>5</sub> O <sub>2</sub> <sup>E</sup>	Au <sub>5</sub> O <sub>2</sub> <sup>F</sup>	Au <sub>5</sub> O <sub>2</sub> <sup>G</sup>	Au <sub>5</sub> O <sub>2</sub> <sup>H</sup>
0.00	8.98	11.02	13.14	15.51	16.69	17.06	19.76
21.67	12.69	10.65	8.53	6.16	13.13	4.61	1.91
1.340	1.347	1.268	1.268	1.258	1.280	1.309	1.232
2.88, 3.02	2.10, 2.56	1.52, 2.22	1.44, 1.93	1.47, 1.73	1.20, 1.94	1.99, 1.73	1.36, 1.37
							
Au <sub>5</sub> O <sub>2</sub> <sup>I</sup>	PtAu <sub>4</sub> O <sub>2</sub> <sup>A</sup>	PtAu <sub>4</sub> O <sub>2</sub> <sup>B</sup>	PtAu <sub>4</sub> O <sub>2</sub> <sup>C</sup>	PtAu <sub>4</sub> O <sub>2</sub> <sup>D</sup>	PtAu <sub>4</sub> O <sub>2</sub> <sup>E</sup>	PtAu <sub>4</sub> O <sub>2</sub> <sup>F</sup>	PtAu <sub>4</sub> O <sub>2</sub> <sup>G</sup>
26.95	0.00	4.05	4.81	5.65	5.82	6.38	11.55
2.87	34.51	30.46	21.08	28.86	20.07	28.13	14.34
1.250	1.361	1.275	1.343	1.362	1.273	1.337	1.561
0.98, 1.76	2.01	1.71	1.82	1.82	2.04	0.93	1.96
							
PtAu <sub>4</sub> O <sub>2</sub> <sup>H</sup>	PtAu <sub>4</sub> O <sub>2</sub> <sup>I</sup>	PtAu <sub>4</sub> O <sub>2</sub> <sup>J</sup>	PtAu <sub>4</sub> O <sub>2</sub> <sup>K</sup>	PtAu <sub>4</sub> O <sub>2</sub> <sup>L</sup>	PtAu <sub>4</sub> O <sub>2</sub> <sup>M</sup>	PtAu <sub>4</sub> O <sub>2</sub> <sup>N</sup>	
12.83	16.29	21.11	22.93	25.09	27.78	31.03	
13.06	9.60	4.78	2.96	3.19	6.73	3.48	
1.383	1.332	1.269	1.274	1.315	1.278	1.269	
1.99	1.63	1.33	1.20	1.85	1.03	0.79	

Figure 2.4: The optimized structures of O<sub>2</sub>-cluster adsorption complexes. The relative energy (in kcal/mol) measured from the most stable complex, the adsorption energy (in kcal/mol), the N–N bond length (in Å), and the HOMO-LUMO gap (in eV) are listed below each optimized structure descendingly. For open-shell systems, the first and the second values of the HOMO-LUMO gap are for  $\alpha$  spin and  $\beta$  spin, respectively.



To have an overall view of the electronic structures of  $\text{N}_2/\text{O}_2$ -PtAu<sub>2</sub> adsorption complexes, the total density of states (DOS) and the local DOS (LDOS) for selected complexes (PtAu<sub>2</sub>N<sub>2</sub><sup>A,B,C</sup> and PtAu<sub>2</sub>O<sub>2</sub><sup>A,B,C</sup>) and the precursor PtAu<sub>2</sub> are shown in Figures 2.5. The DOS in the valence region (−20 eV below the Fermi level) of these complexes can be divided into three domains according to the source of their origins. In domain I (from −7.0 eV to the Fermi level), the LDOS of the Pt atom dominates the total DOS. In domain II (from −11.0 to −7.0 eV), the total DOS is mainly composed of the LDOS of the Au atoms. In domain III (below −11.0 eV), the LDOS of the diatomic adsorbates have the most contribution. In PtAu<sub>2</sub>N<sub>2</sub><sup>A,B</sup>, adsorption of N<sub>2</sub> on the Pt atom of the clusters shifts the electronic states of the pure bimetallic cluster PtAu<sub>2</sub> in domain I to a lower energy level but keeps domain II almost intact. In the case of O<sub>2</sub> adsorption, the total DOS in both domains I and II moves to lower energy levels regardless of the O<sub>2</sub> adsorption site on the cluster. It is clear that the adsorption of N<sub>2</sub> onto the clusters locally perturbs the electronic structure of the cluster fragment around the adsorption site, whereas O<sub>2</sub> adsorption modulates the LDOS of the cluster to such a large extent that the LDOS of those atoms not directly bound to the O atoms are also influenced. For the complexes with the side-on adsorption pattern (PtAu<sub>2</sub>N<sub>2</sub><sup>B</sup> and PtAu<sub>2</sub>O<sub>2</sub><sup>A,B</sup>), their DOS are characterized by many peaks between −15.0 and −11.0 eV, which arise from the versatile bonding interactions between the adsorbates and the clusters. The  $\pi$  orbitals in the plane of the diatomic adsorbate molecule and the Pt atom of the bimetallic cluster can have  $\sigma$ -type interactions, while the  $\pi$  orbitals perpendicular to this plane can engage in  $\pi$ -type interactions. In contrast, the end-on binding complexes have a few sparsely distributed states in the same energy range, indicating relatively simple bonding interactions between the cluster and the adsorbate. The detailed bonding interactions are further discussed for N<sub>2</sub>- and O<sub>2</sub>-adsorption complexes in the following section.

### 2.3.3 N<sub>2</sub> and O<sub>2</sub> adducts

In most cases, N<sub>2</sub> tends to bind to the clusters in an end-on fashion, except for the bimetallic PtAu<sub>2</sub>N<sub>2</sub><sup>B</sup>, PtAu<sub>3</sub>N<sub>2</sub><sup>C</sup>, and PtAu<sub>4</sub>N<sub>2</sub><sup>C</sup> complexes. To understand the interaction between N<sub>2</sub> and the bimetallic clusters, molecular orbitals relevant to the bonding interactions in the above three N<sub>2</sub>-PtAu<sub>2</sub> complexes are shown in Figure 2.6. Both  $\sigma$  and  $\pi$  orbitals contribute to the bonding interactions in the PtAu<sub>2</sub>N<sub>2</sub><sup>A</sup> complex and a similar set of bonding orbitals can also be found in the PtAu<sub>2</sub>N<sub>2</sub><sup>C</sup> complex. The  $\sigma$  bonds (*e.g.*, HOMO−16 and HOMO−19) that hold the adsorbate and the cluster come from the overlap between the  $\sigma$  type orbital of N<sub>2</sub> and the Pt 6s5d orbitals. The two  $\pi$ -type bonds (*e.g.*, HOMO−17 and HOMO−18) result from the overlap between the two perpendicular  $\pi$  orbitals of N<sub>2</sub> with the 6s5d-type orbitals of Pt. A remarkable feature in PtAu<sub>2</sub>N<sub>2</sub><sup>A,C</sup> is that the binding strength varies greatly according to different binding sites. For example, the HOMO of the ground-state of PtAu<sub>2</sub> is localized on the Pt atom and leads to a stronger N<sub>2</sub>–Pt interaction than any other interaction between N<sub>2</sub> and a Au atom. The situation of N<sub>2</sub> binding to pure Au clusters is

very similar to the case of N<sub>2</sub> binding to the Au atoms in the bimetallic clusters, and hence will not be discussed further.

The PtAu<sub>2</sub>N<sub>2</sub><sup>B</sup> complex has a different set of bonding orbitals from those of the above two complexes, PtAu<sub>2</sub>N<sub>2</sub><sup>A,C</sup>. The HOMO–19, a  $\sigma$ -type bonding orbital, is composed of the 5*d* orbital of Pt and the  $\sigma^*$  orbital of N<sub>2</sub>. The two perpendicular  $\pi$  orbitals of N<sub>2</sub> play different roles here. In the HOMO–18 of PtAu<sub>2</sub>N<sub>2</sub><sup>B</sup>, one  $\pi$  orbital of N<sub>2</sub> overlaps with a *d*-type orbital of Pt to form a  $\sigma$  bond. The other  $\pi$  orbital of N<sub>2</sub> overlaps with another *d*-type orbital of Pt to form a  $\pi$  bond, the HOMO–17. The higher-lying HOMO–4 is comprised of a  $\pi^*$  orbital of N<sub>2</sub> and a *d* orbital of Pt.

Partial charges are labeled on the corresponding atoms in Figure 2.6. Overall, the 2*p* orbitals of N<sub>2</sub> withdraw about 0.2 electrons from the metal clusters in the N<sub>2</sub>-cluster complexes. Electrons migrate towards the N<sub>2</sub> fragment primarily from the direct bonding atoms in the clusters: Pt at site I in both PtAu<sub>2</sub>N<sub>2</sub><sup>A,B</sup> and Au at site III in PtAu<sub>2</sub>N<sub>2</sub><sup>C</sup>. Also, about 0.1~0.2 electrons are promoted from 5*d* to 6*s* on the Pt atom upon the adsorption of N<sub>2</sub>.

Spin densities of open-shell structures were also examined by analyzing the PtAu<sub>3</sub>N<sub>2</sub> complexes (Figure 2.7). It was found that the majority of spin densities stays on the Pt atom in the cluster upon the N<sub>2</sub> adsorption. This indicates that any reaction with radicals will still occur towards the Pt atom of the cluster fragment.

In the N<sub>2</sub>-cluster complexes, the HOMO still mainly localizes on the Pt site but to a less extent compared with the HOMO of the PtAu<sub>2</sub> cluster. This signifies that the HOMO energy of the N<sub>2</sub>-cluster complexes resembles that of the PtAu<sub>2</sub> cluster and the Pt site is vulnerable to electrophilic attack. On the other hand, binding one N<sub>2</sub> molecule to the cluster changes the angular distribution and the extent of the localization of the HOMO on the Pt atom compared with the HOMO of PtAu<sub>2</sub>. The HOMO of PtAu<sub>2</sub>N<sub>2</sub><sup>A</sup> consists of 8% 6*s*, 5% 5*d*<sub>z<sup>2</sup></sub>, 30% 5*d*<sub>x<sup>2</sup>-y<sup>2</sup></sub>, and 8% of 5*d*<sub>xy</sub> of the Pt atom, 26% 5*d* and 18% 6*s* of the Au atoms, and 5% *p<sub>y</sub>* contribution from the N atom at site V (Figure 2.6). The HOMO of PtAu<sub>2</sub>N<sub>2</sub><sup>B</sup> is composed of 46% 5*d*<sub>xy</sub>, 2% 5*d*<sub>x<sup>2</sup>-y<sup>2</sup></sub>, and 2% 5*d*<sub>z<sup>2</sup></sub> of the Pt atom, 11% 6*s* and 38% 5*d* contributions from the two Au atoms, and about 1% *p<sub>y</sub>* component from the N atom at site V (Figure 2.6). The cluster fragments in these two complexes, in which N<sub>2</sub> binds directly to the Pt atom, extend their HOMOs to the two Au atoms. In PtAu<sub>2</sub>N<sub>2</sub><sup>C</sup>, the HOMO stays strongly localized on the Pt atom and has 6% 6*s* and 88% 5*d*<sub>z<sup>2</sup></sub> from the Pt atom and 6% 5*d* orbitals from the two Au atoms. Compared with the PtAu<sub>2</sub> cluster, the localization of the HOMO on the Pt atom remains for the PtAu<sub>2</sub>N<sub>2</sub><sup>C</sup> complex but to a less extent than in the two most stable complexes (PtAu<sub>2</sub>N<sub>2</sub><sup>A,B</sup>). The orientation of the HOMO is markedly different, because of the change in the angular composition of the HOMO upon the adsorption of N<sub>2</sub> onto the cluster.

In contrast to the preferred end-on adsorption pattern in forming the N<sub>2</sub>-cluster complexes, O<sub>2</sub> tends to assume a side-on approach to the clusters. Bonding orbitals of the three different O<sub>2</sub>-PtAu<sub>2</sub> complexes, PtAu<sub>2</sub>O<sub>2</sub><sup>A,B,C</sup>, are drawn in Figure 2.6. In the PtAu<sub>2</sub>O<sub>2</sub><sup>A</sup> complex, the  $\pi$  or  $\pi^*$  orbital of O<sub>2</sub> and the *d*-type orbitals of the Pt atom contribute mostly to the bonding interaction between O<sub>2</sub> and the metal cluster in the complexes. Particularly, the two  $\pi$  bonding orbitals of O<sub>2</sub> overlap with the 5*d*

orbitals of Pt to form a  $\sigma$  bond (HOMO–19) and a  $\pi$  bond (HOMO–17). In addition, the  $\pi^*$  orbital of O<sub>2</sub> participates in the formation of three  $\sigma$  bonds (HOMO–15, HOMO–8, and HOMO–6) and a  $\pi$  bond (HOMO–4). It is very difficult to analyze bonding interactions in PtAu<sub>2</sub>O<sub>2</sub><sup>B</sup> through well-defined O<sub>2</sub> and metal cluster molecular orbitals. Nevertheless, the relevant orbitals are composed of the  $\pi$  and  $\pi^*$  orbitals of O<sub>2</sub> and the 5*d* orbitals from the Pt atom and the involved Au atom. Bonding patterns between O<sub>2</sub> and the Au atom in the bimetallic clusters resemble those between O<sub>2</sub> and the pure Au clusters. Thus, the O<sub>2</sub>-Au<sub>*m*</sub> complexes are not discussed further.

Partial charge analysis indicates that O<sub>2</sub> withdraws more electrons (0.2~0.6 electrons) from the metal clusters than N<sub>2</sub> does in the N<sub>2</sub>-cluster complexes. In PtAu<sub>2</sub>O<sub>2</sub><sup>A</sup>, about 0.5 electrons from the 5*d* orbitals of Pt transfer to the 2*p* orbitals of the two O atoms. In PtAu<sub>2</sub>O<sub>2</sub><sup>B</sup>, both the Pt atom and the Au atom at site II donate electrons, but in different ways: from 6*s* and 5*d* of the Pt atom to the 2*p* orbital of O at site III and from the 6*s* orbital of Au at site II to the O atom at site V. In PtAu<sub>2</sub>O<sub>2</sub><sup>C</sup>, the Au atom at site III depletes electrons from its 5*d* orbitals to the 2*p* orbitals of the O atom at site IV.

The distribution of spin densities in the spin-unsaturated O<sub>2</sub>-cluster complexes is different from that in the N<sub>2</sub>-cluster complexes (Figure 2.7). In PtAu<sub>3</sub>O<sub>2</sub><sup>A,C</sup>, spin densities are on the O atom away from the metal cluster fragment. In PtAu<sub>3</sub>O<sub>2</sub><sup>D</sup>, the total spin density is mainly on the two O atoms. This spin density distribution in the O<sub>2</sub>-adsorption complex prompts any further reactions with radicals towards the two O atoms.

The compositions of the HOMOs of the O<sub>2</sub>-cluster complexes depend strongly on the O<sub>2</sub>-cluster binding pattern. In the clusters where O<sub>2</sub> binds to the Pt atom (PtAu<sub>2</sub>O<sub>2</sub><sup>A,B</sup>), the HOMO is primarily composed of the *p* orbitals on the O atoms and the 5*d* orbitals on the Pt atom. This leads to a large variation in the HOMO energy compared with that of the PtAu<sub>2</sub> cluster. The O atoms are thus susceptible to electrophilic attack in these two complexes (PtAu<sub>2</sub>O<sub>2</sub><sup>A,B</sup>). The HOMO of PtAu<sub>2</sub>O<sub>2</sub><sup>A</sup> is more delocalized to the entire complex and consists of 1% 5*d*<sub>xz</sub>, 10% 5*d*<sub>yz</sub>, 11% 5*d*<sub>x<sup>2</sup>-y<sup>2</sup></sub>, and 7% 5*d*<sub>xy</sub> on the Pt atom, 36% *p*<sub>x</sub>, 9% *p*<sub>y</sub>, and 4% *p*<sub>z</sub> from the two O atoms, and 15% 6*s* and 7% 5*d* from the two Au atoms. In PtAu<sub>2</sub>O<sub>2</sub><sup>B</sup>, the HOMO is mainly located on the O atoms (79% *p*<sub>z</sub> on two O atoms and 21% 5*d*<sub>xz</sub> of the Pt atom) and makes the two O atoms the nucleophilic sites. In PtAu<sub>2</sub>O<sub>2</sub><sup>C</sup>, where O<sub>2</sub> binds to the Au atoms, the HOMO remains strongly localized on the Pt atom as in the PtAu<sub>2</sub> cluster and comes from 81% 5*d*<sub>z<sup>2</sup></sub>, 9% 6*s*, and 3% 5*d*<sub>xz</sub> of the Pt atom, and 2% *p*<sub>x</sub> of the two O atoms, and 3% 5*d*<sub>z<sup>2</sup></sub> of the Au atoms. Further electrophilic attack will prefer the Pt site in PtAu<sub>2</sub>O<sub>2</sub><sup>C</sup>.

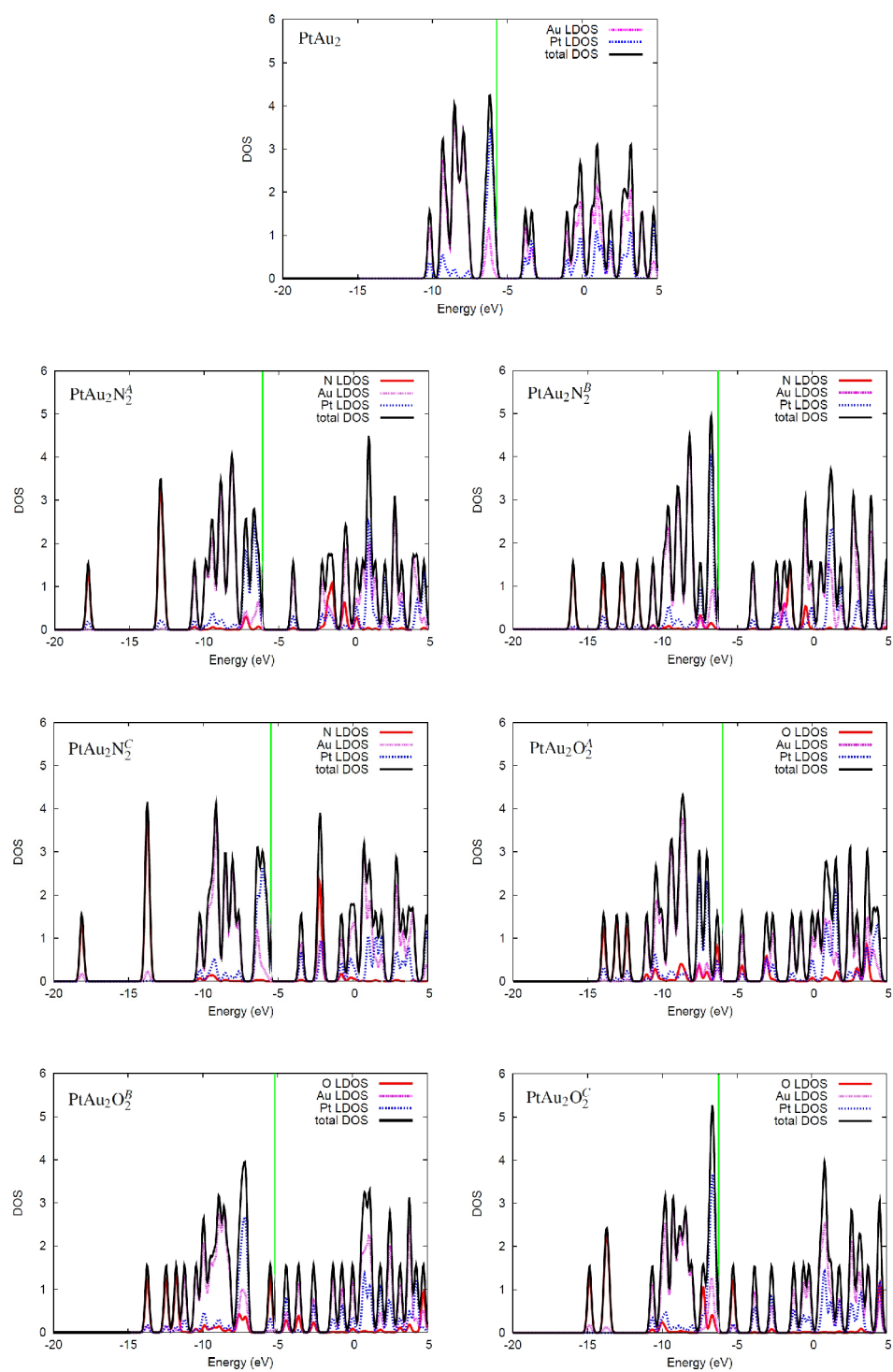


Figure 2.5: The total density of states (DOS) and local DOS (LDOS) projected onto each element of the PtAu<sub>2</sub>-N<sub>2</sub> and PtAu<sub>2</sub>-O<sub>2</sub> adducts. Green vertical lines mark the Fermi levels.

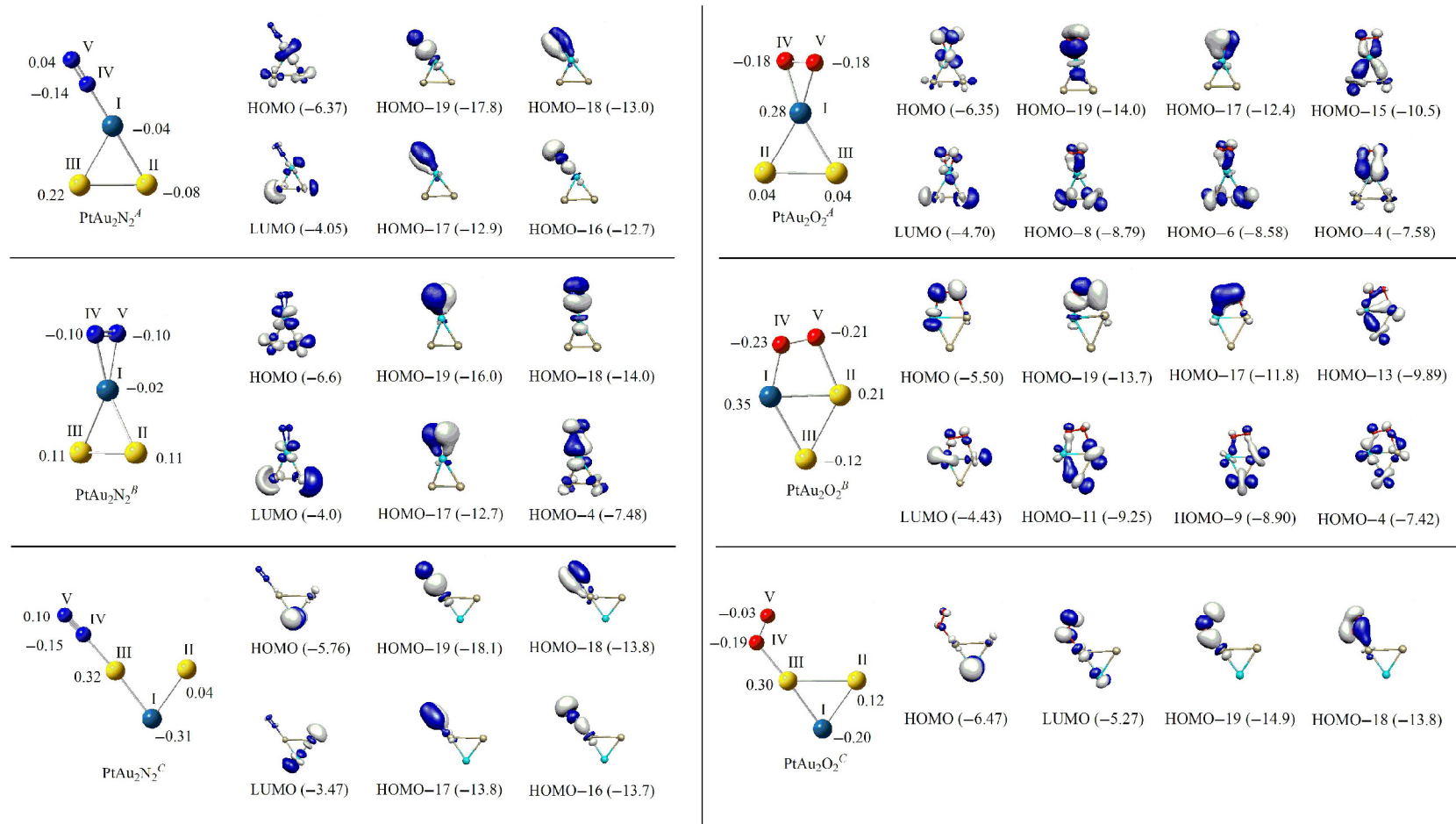


Figure 2.6: Molecular orbitals relevant to the bonding interactions between the diatomic fragment and the PtAu<sub>2</sub> fragments in the PtAu<sub>2</sub>N<sub>2</sub> and PtAu<sub>2</sub>O<sub>2</sub> adducts. HOMO-*p* denotes the *p*th orbital below the HOMO. Orbital energies (in eV) are shown in the parentheses. Partial charges are marked beside atomic sites.

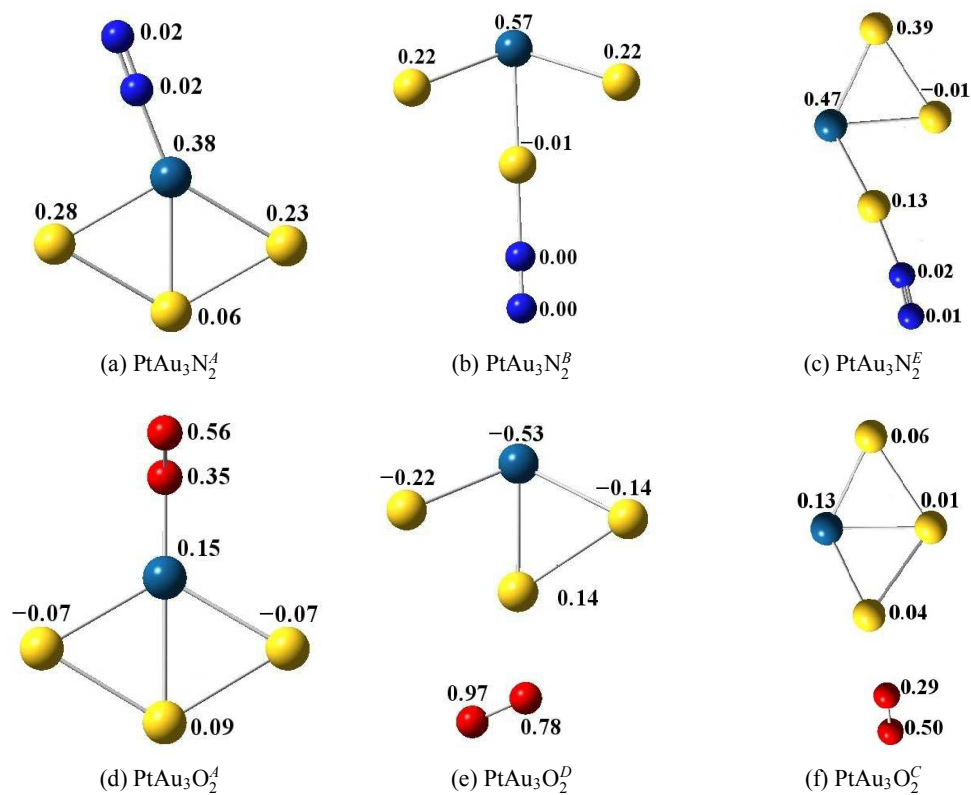


Figure 2.7: Natural spin densities of the atoms in the open-shell  $\text{N}_2/\text{O}_2$ -cluster complexes. The Pt, Au, N, and O atoms are in dark green, yellow, blue, and red, respectively.

## 2.4 Conclusions

We have studied the electronic structures of both pure  $\text{Au}_m$  and bimetallic  $\text{PtAu}_n$  clusters. Clusters larger than a dimer tend to form (near) 2-dimensional structures with basic triangular units. Substitution of one Au atom by Pt in small clusters leads to localized HOMOs and enhanced regioselective electron donating abilities. In open-shell bimetallic clusters, the spin charge density is localized on the Pt atom, which behaves as the active center in reactions with radicals.

We have also studied the  $\text{N}_2$ - and  $\text{O}_2$ -cluster adsorption complexes and found that adsorption onto the Pt site of the bimetallic clusters leads to higher binding energies than adsorption to the pure Au clusters and to the Au atoms of the same bimetallic clusters. In  $\text{N}_2$ -cluster adsorption complexes, clusters donate their electrons to the  $\sigma^*$  orbitals of  $\text{N}_2$ , resulting in an end-on adducting configuration. In  $\text{O}_2$ -cluster adsorption complexes, more complicated cluster- $\text{O}_2$   $\pi$  orbital interactions favor a side-on approach. The HOMOs of the  $\text{N}_2$ -bimetallic cluster adsorption complexes remain localized on the Pt site, but with varied directionality, while the adsorption of  $\text{O}_2$  onto the Pt site delocalizes the HOMO onto the O atoms. For open-shell species, the spin density stays on the cluster fragment in the  $\text{N}_2$ -cluster adsorption complexes, whereas in the  $\text{O}_2$ -cluster adsorption complexes, the spin density gathers around the O atoms instead.

# Bibliography

- [1] S. Link, Z. L. Wang, and M. A. El-Sayed. Alloy formation of gold-silver nanoparticles and the dependence of the plasmon absorption on their composition. *J. Phys. Chem. B*, 103:3529–3533, 1999.
- [2] H. Zhang, D. E. Zelmon, L. Deng, H. K. Liu, and B. K. Teo. Optical limiting behavior of nanosized polyicosahedral gold-silver clusters based on third-order nonlinear optical effects. *J. Am. Chem. Soc.*, 123:11300–11301, 2001.
- [3] M. Gaudry, J. Lermé, E. Cottancin, M. Pellarin, J. L. Vialle, M. Broyer, B. Prével, M. Treilleux, and P. Mélinon. Optical properties of  $(\text{Au}_x\text{Ag}_{1-x})_n$  clusters embedded in alumina: Evolution with size and stoichiometry. *Phys. Rev. B*, 64:085407, 2001.
- [4] M. Stener, K. Albert, and H. Rösch. Relativistic density functional study on the bimetallic cluster  $[\text{Pt}_3\text{Fe}_3(\text{CO})_{15}]_n$  ( $n = 0, 1, 2$ ). *Inorg. Chim. Acta*, 286:30–36, 1999.
- [5] S. T. Bromley and C. R. Catlow. Magnetism and energetics of the 4d bimetallic cluster  $\text{Pd}_6\text{Ru}_6$ . *Int. J. Quantum Chem.*, 91:270–276, 2003.
- [6] H. Tada, F. Suzuki, S. Ito, T. Akita, K. Tanaka, T. Kawahara, and H. Kobayashi. Au-core/Pt-shell bimetallic cluster-loaded  $\text{TiO}_2$ . 1. Adsorption of organosulfur compound. *J. Phys. Chem. B*, 106:8714–8720, 2002.
- [7] R. D. Adams and T. S. Barnard. Does a metal to metal “ligand effect influence the catalytic activity of bimetallic cluster complexes: Synthesis and catalytic activity of  $\text{Pt}_3\text{Ru}_6(\text{CO})$  complex. *Organometallics*, 17:2885–2890, 1998.
- [8] J. Vicente, M. T. Chicote, and S. Hvertas. Heterodi- $[\text{M}\text{Ag}, \text{MAu}]$  ( $\text{M} = \text{Pd}, \text{Pt}$ ), tri- $[\text{PdAg}_2, \text{PtAg}_2, \text{PtAu}_2, \text{Pt}_2\text{M}]$  ( $\text{M} = \text{Ni}, \text{Pt}, \text{Cd}, \text{Hg}$ ), and tetranuclear ( $\text{Pt}_2\text{Ag}_2, \text{Pt}_2\text{Au}_2$ ) 1,1-ethylenedithiolato complexes. *Inorg. Chem.*, 40:6193–6200, 2001.
- [9] M. Ø. Pederson, S. Helveg, A. Ruban, I. Stensgaard, E. Lægsgaard, J. K. Nørskov, and F. Besenbacher. How a gold substrate can increase the reactivity of a Pt overlayer. *Surface Science*, 426:395–409, 1999.
- [10] B. D. Chandler and L. H. Pignolet. DRIFTS studies of carbon monoxide coverage on highly dispersed bimetallic Pt-Cu and Pt-Au catalysts. *Catalysis Today*, 65:39–50, 2001.



- [11] K. Koszinowski, D. Schröder, and H. Schwarz. Probing cooperative effects in bimetallic clusters: Indications of C-N coupling of CH<sub>4</sub> and NH<sub>3</sub> mediated by the cluster ion PtAu<sup>+</sup> in the gas phase. *J. Am. Chem. Soc.*, 125:3676–3677, 2003.
- [12] K. Koszinowski, D. Schröder, and H. Schwarz. Coupling of methane and ammonia by dinuclear bimetallic platinum-coinage-metal cations PtM<sup>+</sup>. *Angew. Chem. Int. Ed.*, 43:121–124, 2004.
- [13] K. Koszinowski, D. Schröder, and H. Schwarz. Additivity effects in the reactivities of bimetallic cluster ions Pt<sub>m</sub>Au<sub>n</sub><sup>+</sup>. *Chemphyschem*, 4:1233–1237, 2003.
- [14] W. Q. Tian, M. Ge, F. Gu, and Y. Aoki. Bimetallic clusters Pt<sub>6</sub>Au: Geometric and electronic structures within density functional theory. *J. Phys. Chem. A*, 109:9860–9866, 2005.
- [15] W. Q. Tian, M. Ge, F. Gu, T. Yamada, and Y. Aoki. Binary clusters AuPt and Au<sub>6</sub>Pt: Structure and reactivity within density functional theory. *J. Phys. Chem. A*, 110:6285–6293, 2006.
- [16] C. Song, Q. Ge, and L. Wang. DFT studies of Pt/Au bimetallic clusters and their interactions with the CO molecule. *J. Phys. Chem. B*, 109:22341–22350, 2005.
- [17] G. Mills, M. S. Gordon, and H. Metiu. Oxygen adsorption on Au clusters and a rough Au(111) surface: The role of surface flatness, electron confinement, excess electrons, and band gap. *J. Chem. Phys.*, 118:4198–4205, 2003.
- [18] R. M. Olson, S. Varganov, M. S. Gordon, H. Metiu, S. Chretien, P. Piecuch, K. Kowalski, S. A. Kucharski, and M. Musial. Where does the planar-to-nonplanar turnover occur in small gold clusters. *J. Am. Chem. Soc.*, 127:1049–1052, 2005.
- [19] H. Häkkinen, M. Moseler, and U. Landman. Bonding in Cu, Ag, and Au clusters: Relativistic effects, trends, and surprises. *Phys. Rev. Lett.*, 89:033401, 2002.
- [20] W. Q. Tian, M. Ge, B. R. Sahu, D. Wang, T. Yamada, and S. Mashiko. Geometrical and electronic structure of the Pt<sub>7</sub> cluster: A density functional study. *J. Phys. Chem. A*, 108:3806–3812, 2004.
- [21] D. Dai and K. Balasubramanian. Electronic structures of Pd<sub>4</sub> and Pt<sub>4</sub>. *J. Chem. Phys.*, 103:648–655, 1995.
- [22] A. Fortunelli. Density functional calculations on small platinum clusters: Pt<sub>n</sub> (n=1–4). *J. Mol. Struct.: Theochem*, 493:233–240, 1999.
- [23] A. Berces, D. A. Hackett, L. Lian, S. A. Mitchell, and D. M. Rayner. Reactivity of niobium clusters with nitrogen and deuterium. *J. Chem. Phys.*, 108:5476–5490, 1998.

- [24] C. Mihut, C. Descorme, D. Duprez, and M. D. Amiridis. Kinetic and spectroscopic characterization of cluster-derived supported Pt-Au catalysts. *J. Catal.*, 212:125–135, 2002.
- [25] M. D. Amiridis, C. Mihut, M. Jaciejewski, and A. Baiker. The selective catalytic reduction of NO by hydrocarbons over Pt- and Ir-based catalysts. *Topics in Catalysis*, 28:141–150, 2004.
- [26] Z. Shi. *Application of first principle methods in the study of fuel cell air-cathode electrocatalysis*, pages 279–329. Springer, 2008.
- [27] M. B. Knickelbein. Reactions of transition metal clusters with small molecules. *Annu. Rev. Phys. Chem.*, 50:79–115, 1999.
- [28] J. P. Perdew, K. Burke, and M. Ernzerhof. Generalized gradient approximation made simple. *Phys. Rev. Lett.*, 77(18):3865–3868, Oct 1996.
- [29] M. J. Frisch, G. W. Trucks, H. B. Schlegel, G. E. Scuseria, M. A. Robb, J. R. Cheeseman, Montgomery, Jr., J. A., T. Vreven, K. N. Kudin, J. C. Burant, J. M. Millam, S. S. Iyengar, J. Tomasi, V. Barone, B. Mennucci, M. Cossi, G. Scalmani, N. Rega, G. A. Petersson, H. Nakatsuji, M. Hada, M. Ehara, K. Toyota, R. Fukuda, J. Hasegawa, M. Ishida, T. Nakajima, Y. Honda, O. Kitao, H. Nakai, M. Klene, X. Li, J. E. Knox, H. P. Hratchian, J. B. Cross, V. Bakken, C. Adamo, J. Jaramillo, R. Gomperts, R. E. Stratmann, O. Yazyev, A. J. Austin, R. Cammi, C. Pomelli, J. W. Ochterski, P. Y. Ayala, K. Morokuma, G. A. Voth, P. Salvador, J. J. Dannenberg, V. G. Zakrzewski, S. Dapprich, A. D. Daniels, M. C. Strain, O. Farkas, D. K. Malick, A. D. Rabuck, K. Raghavachari, J. B. Foresman, J. V. Ortiz, Q. Cui, A. G. Baboul, S. Clifford, J. Cioslowski, B. B. Stefanov, G. Liu, A. Liashenko, P. Piskorz, I. Komaromi, R. L. Martin, D. J. Fox, T. Keith, M. A. Al-Laham, C. Y. Peng, A. Nanayakkara, M. Challacombe, P. M. W. Gill, B. Johnson, W. Chen, M. W. Wong, C. Gonzalez, and J. A. Pople. *Gaussian 03*. Gaussian, Inc., Wallingford, CT, 2004.
- [30] P. J. Hay and W. R. Wadt. Ab initio effective core potentials for molecular calculations: potentials for K to Au including the outermost core orbitals. *J. Chem. Phys.*, 82:299, 1999.
- [31] J. M. L. Martin, Jr. C. W. Bauschlicher, and A. Ricca. On the integration accuracy in molecular density functional theory calculations using Gaussian basis sets. *Comput. Phys. Comm.*, 133:189–201, 2001.
- [32] A. D. Becke. Density functional thermochemistry. III. The role of exact exchange. *J. Chem. Phys.*, 98:5648–5672, 1993.
- [33] C. Lee, W. Yang, and R. G. Parr. Development of the Colle-Salvetti correlation-energy formula into a functional of the electron density. *Phys. Rev. B*, 37:785–789, 1988.

- [34] A. E. Reed, L. A. Curtiss, and F. Weinhold. Intermolecular interactions from a natural bond orbital, donor-acceptor viewpoint. *Chem. Rev.*, 88:899–926, 1988.
- [35] M. D. Morse. Clusters of transition-metal atoms. *Chem. Rev.*, 86:1049–1109, 1986.
- [36] A. M. James, P. Kowdczyk, B. Simard, J. C. Pinegar, and M. D. Morse. The  $A'_{1u}$ - $X^0_{+g}$  system of gold dimer. *J. Mol. Spectrosc.*, 168:248–257, 1994.
- [37] D. Dai and K. Balasubramanian.  $Pt_3Au$  and  $PtAu$  clusters: Electronic states and potential energy surfaces. *J. Chem. Phys.*, 100:4401–4407, 1994.
- [38] V. BonačićKoutecký, J. Burda, R. Mitrić, M. Ge, G. Zampella, and P. Fantucci. Density functional study of structural and electronic properties of bimetallic silver gold clusters: Comparison with pure gold and silver clusters. *J. Chem. Phys.*, 117:3120–3131, 2002.

## Chapter 3

# Theoretical Studies of Transition Metal-Doped Single-Walled Carbon Nanotubes <sup>2</sup>

### 3.1 Introduction

Chemistry and physics of carbon allotropes, especially fullerene and carbon nanotubes (CNTs), have been one of the most active fields in the past two decades. Since the discovery of fullerene<sup>1</sup> and the first fabrication of multi-walled<sup>2</sup> and single-walled carbon nanotubes (SWCNTs),<sup>3</sup> substances containing carbon networks have been intensively and extensively studied with the goal of finding new materials. CNTs have such large longitudinal modulus and low densities that they may be used as structural materials. Because the electronic structure of CNTs depends delicately on the nanotube parameters, such as tube diameter and chirality, selective use of individual CNTs or jointed CNTs (with different tube parameters) provides many opportunities for developing novel electronic devices.<sup>4</sup>

Functionalizations of fullerene and CNTs further expand the domain of application of these carbon-based materials. Many approaches have been designed and developed to functionalize CNTs, including doping light elements into defect sites<sup>5</sup> and ozonization at vacancy sites.<sup>6</sup> Among various functionalized CNTs, some are identified as potential new advanced materials. For instance, SWCNTs functionalized with specific polymers were found to be good candidates for ammonia detection.<sup>7</sup> Photoemission spectroscopic experiments and theoretical studies showed that atomic In transport was influenced by the concentration of defects and offered a novel way to control the transport of atoms.<sup>8</sup>

Ever since the first CNT was formed, the fabrication of CNTs has been closely associated with numerous transition metal (TM) catalysts. Iron and its oxides are intimately involved in the growth mechanism of CNTs, in which the change of oxidation number of Fe plays an important role.<sup>9</sup> CNTs doped with different metal atoms, like Fe,<sup>10</sup> Sm,<sup>11</sup> and Pt,<sup>12,13</sup> were investigated for their potential catalytic and material utilities. Atomic chains of Cr and V adsorbed on CNTs are possible

---

<sup>2</sup>A version of this chapter has been submitted for publication. Chen, Y. K.; Liu, L. V.; Tian, W. Q. and Wang, Y. A. Theoretical Studies of Transition Metal-Doped Single-Walled Carbon Nanotubes.

spintronic materials.<sup>14</sup> Some theoretical studies also indicated SWCNTs coated with atomic Ti can become hydrogen storage materials.<sup>15</sup> Pt- and Ru-double-walled CNT adducts are efficient catalysts for direct methanol fuel cells.<sup>16</sup> Without a doubt, studies of interactions between TM atoms and CNTs not only provide effective ways to fabricate carbon-ring networks, but also offer opportunities for discovering new materials or catalysts.

In the case of functionalized CNTs, the content and the position of the modification are crucial factors in determining the properties and reactivities of the resulting nanosystems. The wall of a fullerene or a single SWCNT divides the space into the interior and the exterior of the tubular system. Modifiers inside and outside nanotubes feel concave and convex surfaces, respectively, which possess very different chemistry and physics. This structural effect has been recently analyzed through the understanding of the bent conjugated  $\pi$  bonds in fullerenes and CNTs,<sup>17</sup> where the different curvatures of the two sides of a tubular wall lead to position-dependent properties and reactivities. For example, an early theoretical study showed that the interior surface of a fullerene is inert to atomic hydrogen and atomic fluorine whereas the exterior surface is highly reactive.<sup>18</sup> The novelty of the chemistry inside CNTs is particularly exemplified by the Menshutkin  $S_N2$  reaction, which was found to be much more favored within SWCNTs over the same reaction in the gaseous phase.<sup>19</sup> Experimental studies of the adsorption of various chemicals inside and outside SWCNTs have been critically reviewed and attention has been drawn to the interaction between oxidizers and the inner wall of SWCNTs.<sup>20</sup> The effect of confinement inside a SWCNT was also demonstrated in a chemical reaction between atomic hydrogen and heptene.<sup>21</sup> Aside from these few revealing studies of the chemical and physical properties of the inner wall of CNTs, the interior space has rarely been considered compared with abundant results on the outer wall. It is necessary to further investigate the positional effect on the asymmetric curved tubular surface.

Thus far, the possibility of functionalizing curved carbon networks from the concave side has been studied mostly using theoretical tools. Studies of the functionalization of SWCNTs by carbene ( $CH_2$ ), imine ( $NH$ ), and atomic oxygen from both sides of the tubular wall showed that the lack of  $\sigma$ -bond formation from the concave inner side of the SWCNT forces light-element compounds to react preferentially with the outside of nanotubes.<sup>22</sup> On the other hand, there have been some occurrences when heteroatoms stay on the inside concave surface. Using nuclear reaction techniques with the aid of theoretical calculations, the endohedral and substitutional Sb- and Te-doped fullerenes were made possible.<sup>23</sup> Based on density functional theoretical studies, the endo-Co-absorbed (8,8) SWCNT was found to be more stable than the exo absorbed one.<sup>24</sup> We thus hope to find out whether some other heteroatoms, especially TM atoms, can be endo-doped into CNTs. Different misalignments of carbon  $\pi$  orbitals from the interior or the exterior of SWCNTs may allow chemical species to stay preferentially inside the nanotubes. TM atoms, with their versatile bonding abilities and large radii, may have a better chance to reside steadily inside CNTs.

In this work, we report the results of our investigation into the possibility for a first-row TM atom to stay inside a (5,5) SWCNT after replacing a carbon atom of the tubular wall with the TM

atom (Figure 3.1).

## 3.2 Computational details

All calculations were performed using the Gaussian03 package.<sup>25</sup> The spin-unrestricted Kohn-Sham density functional method was adopted with the PBE/PBE exchange-correlation functionals developed by Perdew, Burke, and Ernzerhoff.<sup>26</sup> The electronic wavefunctions were expanded in the LanL2DZ atomic basis functions with the core shell electrons represented by the LanL2 pseudo potentials.<sup>27</sup> One-dimensional periodic boundary conditions were employed to model the (5,5) SWCNTs with 100 carbon atoms in the primitive cell (Figure 3.1c), with 40 k-points in the supercell. A carbon atom in the middle of the tube (labeled as ‘X’ in Figure 3.1c) is replaced by a TM atom to model doped SWCNTs. Having realized the wall of the nanotube separates the space into the interior and the exterior, we placed the TM atom both inside and outside the tube hypersurface to investigate the positional effect. Since TM elements usually feature close-lying spin multiplicities, a large set of probable spin multiplicities for each doped SWCNT was fully considered for completeness. Geometry optimization was conducted without any symmetry constraint.

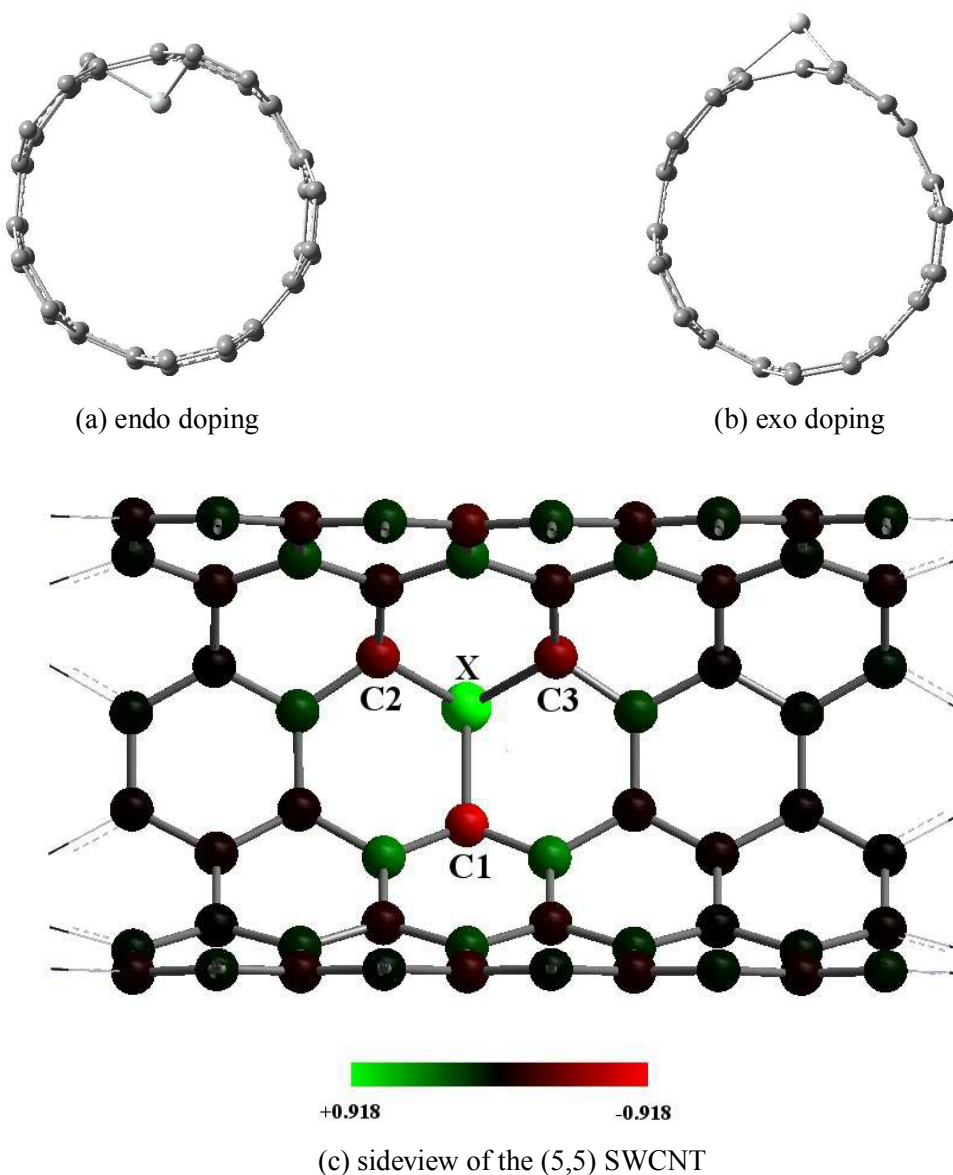


Figure 3.1: Schematic drawings of the model (5,5) SWCNT with partial charge distribution, doping site, and doping configurations. The dopant, labelled by 'X', is surrounded by three neighboring carbon atoms (C1, C2, and C3). X-C1 is a vertical bond; X-C2 and X-C3 are slant bonds. The partial charge distribution in the exo-Sc-doped (5,5) SWCNT is also shown as a color overlay in (c). The values of partial charges are scaled according to the colored bar at the bottom. Color green indicates a positive charge and color red, a negative charge. The darker the color (red or green), the larger the magnitude of the partial charge on the atom.

### 3.3 Results and discussions

In this study, the (5,5) SWCNT was chosen to be the prototype nanosystem for some specific reasons. If the selected nanotube has a very large diameter, the nanotube sidewall will be extremely flat, resembling a single graphene sheet. The physics for the dopant being positioned inside or outside will be essentially the same; it is then meaningless to study. If the diameter is very small, the dopant atom inside the tube will come too close to those carbon atoms on the other end of the diameter opposite to the doping site. As a compromise, we have chosen the (5,5) SWCNT, which has a moderate tube diameter.

Dopant	Configuration	Relative energies (spin multiplicities)		
Sc	exo	0.000 (2)	0.916 (4)	2.547 (6)
	endo	2.361 (2)	2.815 (4)	4.096 (6)
Ti	exo	0.000 (1)	0.475 (3)	1.644 (5)
	endo	2.002 (1)	2.499 (3)	3.844 (5)
V	exo	0.000 (2)	0.382 (4)	1.494 (6)
	endo	2.138 (2)	2.791 (4)	3.997 (6)
Cr	exo	0.000 (3)	0.398 (5)	0.860 (1)
	endo	2.359 (3)	2.811 (5)	2.987 (1)
Mn	exo	0.000 (4)	0.030 (4)	0.603 (6)
	endo	2.069 (4)	2.230 (2)	2.770 (6)
Fe	exo	0.000 (1)	0.193 (3)	0.849 (5)
	endo	2.194 (1)	2.330 (3)	2.995 (5)
Co	exo	0.000 (2)	0.704 (4)	1.907 (6)
	endo	2.072 (2)	2.819 (4)	3.863 (6)
Ni	exo	0.000 (1)	0.052 (3)	0.884 (5)
	endo	1.886 (3)	2.038 (1)	2.732 (5)
Cu	exo	0.000 (2)		
	endo	2.562 (2)		
Zn	exo	0.000 (1)		
	endo	2.860 (1)		
Pd	exo	0.000 (1)	0.228 (3)	
	endo	2.783 (1)	2.908 (3)	
Pt	exo	0.000 (1)	0.289 (3)	
	endo	3.157 (1)	3.482 (3)	

Table 3.1: Relative energies (in eV) for each TM-doped SWCNT of different doping configuration and spin multiplicity. The data of the most stable exo- and endo-doped SWCNTs are shown in the third column. Spin multiplicities are shown in the parentheses.

The relative stabilities of the TM-doped SWCNTs are compared in Table 3.1. For each TM element studied, the most stable structure is *always* the exo-doped. The lowest-lying endo-doped SWCNTs are less stable than the corresponding exo counterparts by about 2.1 eV. This energy dif-



ference between the most stable endo- and exo-doped SWCNTs is relatively constant, irrespective of the type of the dopant TM. This implies that the stability variation mainly comes from the fluctuation in geometric strain from the exo to the endo doping configurations. This dominant effect of geometric strain is further supported by the observation that the energy difference between the endo- and exo-doped SWCNTs in any other same-spin state is very close to 1.9 eV, beside some extreme exceptions like the quartet Sc-doped SWCNTs. One may also find that some TM-doped SWCNTs are readily excited to another close-lying spin state: It costs no more than 0.1 eV to jump from the ground spin state to the nearest excited spin state for exo-Mn-, exo-Ni-, and endo-Fe-doped SWCNTs.

From the cross-section views shown in Figure 3.1, one can gather some common features shared by all TM-doped SWCNTs. The cross sections of the doped SWCNTs are oval close to the doping site, deviating away from the uniform round cross section of a pristine SWCNT. The endo-doped SWCNTs mostly have sticking-in C2 and C3 carbon atoms, whereas the exo-doped SWCNTs have the three closest surrounding carbon atoms (C1, C2, and C3) sticking out of the tube hypersurface. Compared with the undeformed SWCNTs, the inward bonds in the endo-doped SWCNTs create an even larger curvature, bending the six-membered carbon rings around the doping site away from the energetically favored, nearly planar aromatic structure. On the other hand, the extruding carbon atoms of the exo-doped SWCNTs alleviate much of the off-plane strain in the six-membered carbon rings containing the C1, C2, and C3 carbon atoms. To verify this understanding, additional calculations were performed on the exo- and endo-Ti-doped SWCNTs. If we neglect the secondary change in the electronic structure after removing the Ti atom from the doped system, the energy difference between endo and exo dopings is about 0.9 eV, almost half of the energy difference between the endo- and exo-doped SWCNTs. The other remaining half of the energy difference is primarily attributed to the lack of strong TM-carbon  $\sigma$  bonds in the endo-doped SWCNTs compared with the exo-doped SWCNTs.<sup>22</sup> In the endo-doped SWCNTs, the chemical bond between the TM atoms and its three nearest carbon atoms are almost perpendicular to the other bonds of these carbon atoms. Normally, the carbon atoms of a SWCNT are  $sp^2$  hybridized, in favor of coplanar  $\sigma$  bonds for the same carbon atom. In an endo-doped SWCNT, the TM atom bound to the carbon atoms from a perpendicular direction must experience some geometrical strain that also contributes to the instability of the doped nanotubes. Therefore, it is understandable that the exo-doped SWCNTs are energetically more stable than the endo-doped counterparts.

The endo-doped SWCNTs with first-row TM atoms are always less stable than their exo counterparts by a large value, and their energy difference becomes even greater when the TM changes from Ni to Pt. For second- and third-row TM atoms, the endo-doped SWCNTs are expected to be much more unstable than their exo counterparts, because the energetic closeness of the valence  $s$  and  $d$  orbitals of the second- and third-row TM atoms may exert more strain in the endo-doped SWCNTs. Unlike the case of TM adsorption, where the major bonding interaction between the TM atom and the CNT involves the  $p_\pi$  orbital of the carbon atoms, and the adjustment of tubular struc-

ture can stabilize the TM absorbed inside certain SWCNTs, like Co in the (8,8) SWCNT,<sup>24</sup> doping TM atoms into a single-vacancy defect site of a SWCNT internally, regardless of the geometric features of the SWCNT, will always be energetically unfavorable compared with external doping, because of the large strain penalty from endo doping.

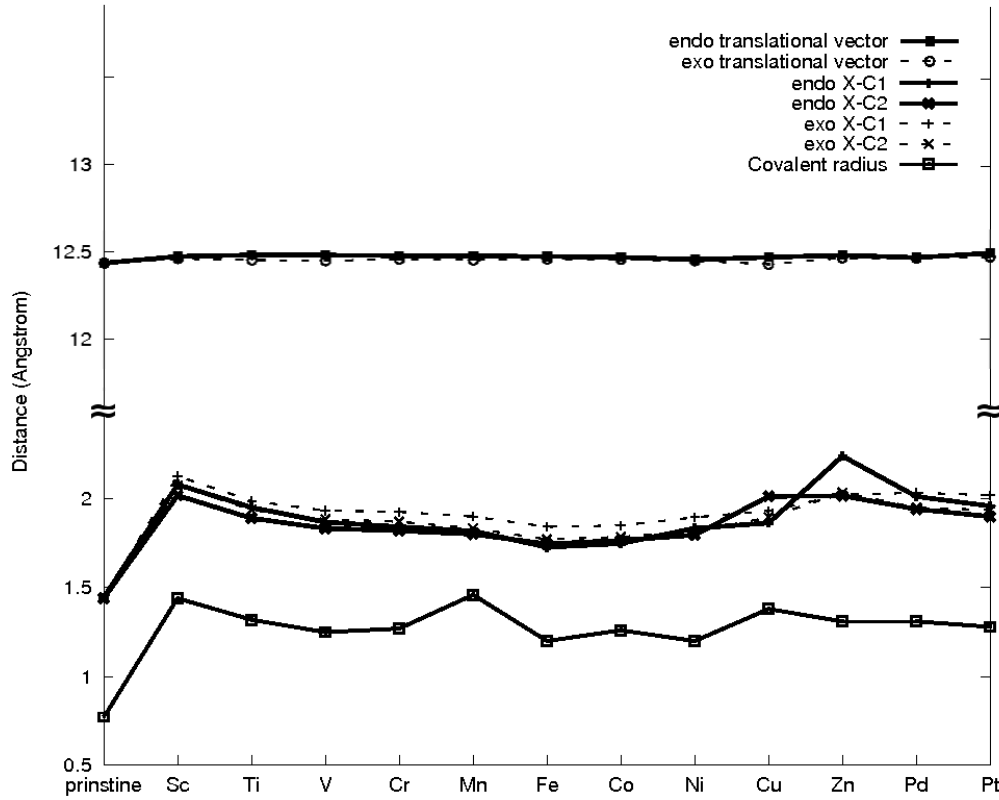


Figure 3.2: Geometric parameters of the pristine and TM-doped SWCNTs. The rest parameters are measured on the Y-axis of the left side. The covalent radius of each element is reproduced from Ref. 28. Translational vectors are indicators of the elongation along the longitudinal direction.

From the optimized geometric parameters shown in Figure 3.2, we can gain more appreciation of structural features of the most stable exo- and endo-doped SWCNTs. Even without any symmetry constraint during geometry optimization, most of the optimized structures, except for the endo-V-doped SWCNT, have essentially  $C_s$  symmetry with the mirror plane passing through the TM atom and perpendicular to the longitudinal direction. In the endo-V-doped SWCNT, the V atom is close to one of the slantwise-bonded carbon atoms, in favor of a lower energy from symmetry breaking. The bond lengths of TM atoms to the three closest carbon atoms in the doped SWCNTs are displayed in Figure 3.1. Whether the nanotube is endo- or exo-doped, the vertical X-C1 bond is longer than the slant X-C2 and X-C3 bonds, except in the endo-Co-, endo-Fe-, and endo-Cu-doped SWCNTs. The longer X-C2 (-C3) bond length indicates that the slant TM-carbon bond is weaker than the

vertical TM-carbon bond. The TM-carbon bond lengths in the exo-doped SWCNTs are always larger than the corresponding bond lengths in the endo doped systems. In comparison with the corresponding slant and vertical C–C bonds in the pristine (5,5) SWCNT, the TM-carbon bond is much longer: over 1.7 Å (vs. 1.4 Å). However, the extended bonds around the doping site do not evoke significant tubular elongation, because the heteroatom is positioned far away from the tubular surface, which minimizes the elongation along the longitudinal direction.

Following the periodic table from left to right in the first row of TM, the atomic size gets smaller except for Cr and Cu whose ground-state electronic configurations change from the preceding  $4s^23d^n$  to  $4s^13d^{n+1}$ . However, TM-carbon bond lengths do not follow this trend in the doped SWCNTs. The TM-carbon bond length decreases from Sc to Fe and increases from Co to the last element Zn in this row. Particularly, Cu- and Zn-doped SWCNTs exhibit very long TM-carbon bonds. For Ni-, Pd-, and Pt-doped SWCNTs, the Pd–C bond is longer than the Pt–C bond and both bonds are still longer than the Ni–C bond, because of lanthanide contraction. The V-, Cr-, and Mn-doped SWCNTs have similar TM-carbon bond lengths because these TM-doped SWCNTs have a gradual increment in the spin multiplicity and therefore have the same number of valence electrons to form chemical bonds.

Dopant	Multiplicities	Mulliken spin densities	Partial charges
Sc	2, 2	–0.009, 0.038	0.703, 0.918
Ti	1, 1		0.512, 0.748
V	2, 2	0.838, 1.241	0.420, 0.626
Cr	3, 3	2.496, 2.638	0.416, 0.553
Mn	4, 4	2.648, 2.715	0.365, 0.547
Fe	1, 1		0.063, 0.216
Co	2, 2	0.194, 0.267	0.022, 0.299
Ni	3, 1	0.396,	–0.057, 0.430
Cu	2, 2	0.089, 0.055	–0.006, 0.553
Zn	1, 1		0.626, 0.825
Pd	1, 1		–0.190, 0.334
Pt	1, 1		0.362, 0.892

Table 3.2: Calculated partial charges and spin charges of the most stable endo- and exo-doped SWCNTs. In columns 2 to 4, the first and second numbers of each pair are for the endo- and exo-doped systems, respectively.

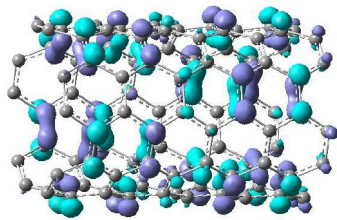
The spin multiplicities, Mulliken spin densities, and partial atomic charges on the metal atoms are collected in Table 3.2. It is well known that elements become less metallic from the left to the right in the same row of the Periodic Table. So, along the same direction, the calculated partial charge on the TM atom decreases and the TM-carbon bond gradually evolves from being highly ionic to somewhat covalent. Also in the same direction, the TM atom of an endo-doped SWCNT carries less (positive) charge than does the same TM atom of the exo-doped systems. Most partial

charges are located within the first four layers of carbon atoms around the TM atom. This is well illustrated in the exo-Sc-doped SWCNT (Figure 3.1c), which has the largest partial charge on the TM dopant atom in this study. For the open shell species, SWCNTs doped with Sc and Co are spin polarized by the TM atoms, whereas SWCNTs doped with V, Cr, and Mn are characterized by localized spin density on the TM atoms.

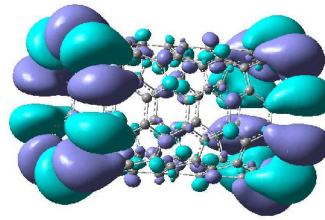
The frontier molecular orbitals are important in interpreting chemical reactivity. We thus exhibit the highest occupied crystal orbitals (HOCOs) and lowest unoccupied crystal orbitals (LUCOs) in Figure 3.3. Most of the doped SWCNTs are narrow-gap semiconductive or (semi)metallic with their Fermi levels around  $-4.0$  eV. Most of the frontier orbitals of the TM-doped SWCNTs are localized near the doping site, either directly on the dopant TM atom or on the closest surrounding carbon atoms. The HOCO energies of the endo-doped SWCNTs are usually lower than those of the exo counterparts by several tenths of an eV, indicating a slightly reduced electron donating ability. When the TM changes from Sc to Zn (except for Mn, Co, and Zn), the HOCO energy, along with the electron donating ability, decreases from  $-4.2$  to  $-4.5$  eV. When the dopant TM atoms are from the same Pt group, the doped SWCNTs show comparable trends in the electronic properties.

The exo-Sc-doped SWCNT, unlike most other TM-doped SWCNTs, opens an  $\alpha$ -spin gap while being  $\beta$ -spin conductive (see Figure 3.4). This trait in the electronic structure makes the exo-Sc-doped SWCNT potentially a spin polarizer that can transport electricity with a single spin state.<sup>14</sup> In both exo- and endo-Sc-doped SWCNTs,  $\alpha$ -spin HOCOs are quite different from  $\alpha$ -spin LUCOs, but  $\beta$ -spin HOCOs are very similar to  $\beta$ -spin LUCOs in both spatial distributions and orbital energy (nearly degenerate). The same understanding can be applied to explain the small band gaps of the endo-V-doped SWCNT (in  $\alpha$  spin) and in the Fe- and Ni-doped SWCNTs. The HOCO and the LUCO of the Sc-doped SWCNTs mainly consist of the neighboring carbon  $p_\pi$  orbitals surrounding the Sc atom. In both endo- and exo-Ti-doped SWCNTs, the HOCOs are mostly composed of carbon  $p$  orbitals, while the LUCOs are made of  $p$  orbitals of the carbon atoms and the  $3d$  orbitals of the Ti atom. If the TM is V, more  $3d$  orbitals of V are involved in forming the frontier orbitals. The endo-Cr-doped SWCNT has a HOCO largely made from the Cr atom, the major electron donation center in the system. The Mn-doped SWCNTs, though with higher spin multiplicities instead, have their frontier orbitals concentrated on the carbon atoms where lie the reactive sites. Regardless of the doping configurations, the Fe-doped SWCNTs feature large Fe contribution to both the HOCO and the LUCO. In the Co- and Ni-doped SWCNTs, the frontier orbitals are mainly built from surrounding carbon  $p$  orbitals. The exo-Ni-, exo-Pd-, and exo-Pt-doped SWCNTs have very similar band structures to the pristine SWCNTs near the Fermi level (see Fig. 8.1 in the Supporting Information). On the other hand, the endo-Ni-, endo-Pd-, and endo-Pt-doped SWCNTs have more localized HOCOs with lower orbital energies.

(a) Pristine SWCNT

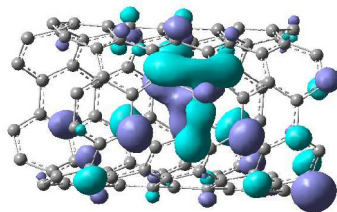


HOCO (−4.48)

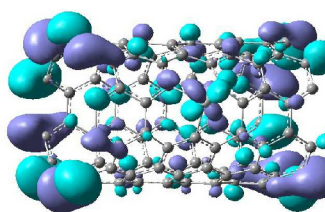


LUCO (−4.46)

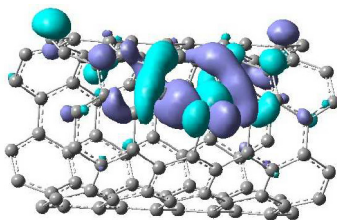
(b) Exo Sc-doped SWCNT



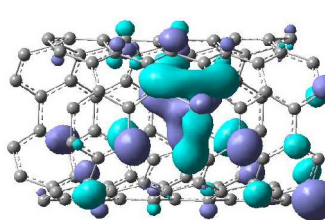
$\alpha$ -HOCO (−4.12)



$\alpha$ -LUCO (−3.97)

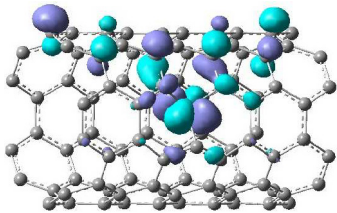


$\beta$ -HOCO (−4.26)

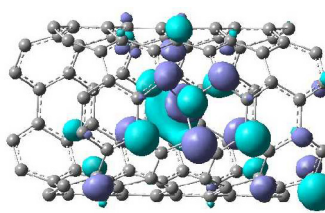


$\beta$ -LUCO (−4.49)

(c) Endo Fe-doped SWCNT

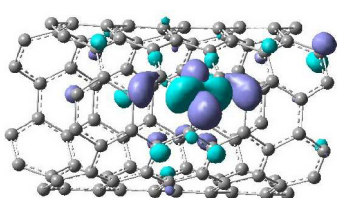


HOCO (−4.66)

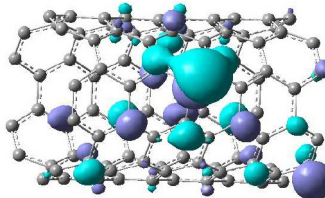


LUCO (−4.38)

(d) Exo Fe-doped SWCNT



HOCO (−4.47)



LUCO (−4.23)

Figure 3.3: Frontier crystal orbitals of the pristine, Sc-, and Fe-doped SWCNTs. Orbital energies (in eV) are shown in the parentheses.

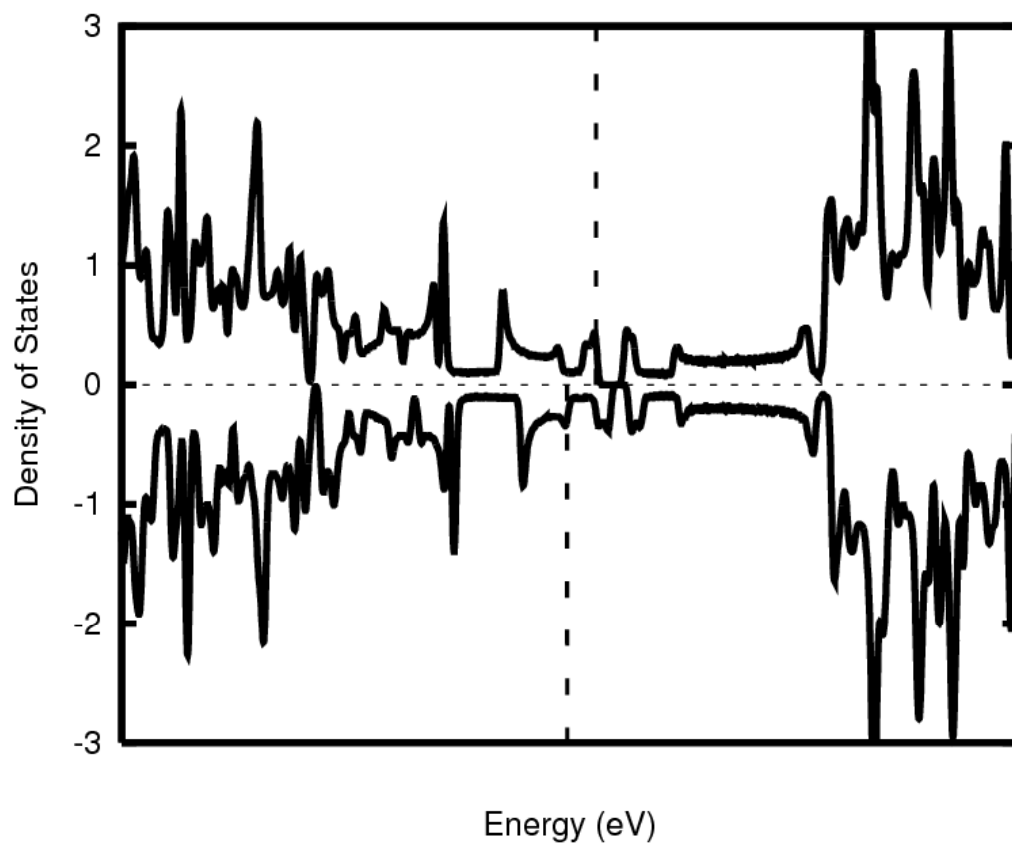


Figure 3.4: Density of states (DOS) of the exo-Sc-doped (5,5) SWCNT. The DOS of  $\alpha$ -spin and  $\beta$ -spin electrons are shown in the upper and lower panels, respectively. Fermi levels are marked by the vertical dotted lines.

### 3.4 Conclusion

We have studied the exo- and endo-TM-doped (5,5) SWCNTs in an effort to find the stable TM-doped SWCNTs and to investigate their properties. The introduction of TM atoms does not significantly elongate the nanotube along the longitudinal direction. The endo-TM-doped SWCNTs are found to be less stable than their exo counterparts by about 2 eV due to the unfavorable TM-carbon bonding interaction and the deformation of the host nanotube upon endo doping. The net charge distribution in a TM-doped SWCNT is localized within the first four layers of the carbon atoms surrounding the dopant TM atom. The spin density of open shell SWCNTs, on the other hand, can be quite delocalized in such systems as the Sc-, Co-, and Cu-doped SWCNTs. The electron donating ability of the exo-TM-doped SWCNTs are superior to their corresponding endo systems. As the TM changes from the left to the right in the first *d*-block of the Periodic Table, the HOCO energy decreases and the doped SWCNT becomes less reactive towards electrophiles. When the SWCNT is doped with TM atoms from the Pt group, though with similar electronic structures, the endo-doped SWCNTs are much less stable than the exo ones. We further speculate that the SWCNTs endo-doped with second- and third-row TM atoms are much more unstable than their exo counterparts, simply because of the collapsing space among the valence *s* and *d* orbitals in the second- and third-row TM elements.

# Bibliography

- [1] H. W. Kroto, J. R. Heath, S. C. O'Brien, R. F. Curl, and R. E. Smalley.  $C_{60}$ : Buckminsterfullerene. *Nature*, 318:162–163, 1985.
- [2] S. Iijima. Helical microtubeules of graphitic carbon. *Nature*, 354:56–59, 1991.
- [3] S. Iijima and T. Ichihashi. Single-shell carbon nanotubes of 1-nm diameter. *Nature*, 363:603–605, 1993.
- [4] P. Avouris. Molecular electronics with carbon nanotubes. *Acc. Chem. Res.*, 35:1026–1034, 2002.
- [5] L. V. Liu, W. Q. Tian, and Y. A. Wang. Chemical reaction of nitric oxides with the 5-1DB defect of the single-walled carbon nanotubes. *J. Phys. Chem. B*, 110:1999–2005, 2006.
- [6] L. V. Liu, W. Q. Tian, and Y. A. Wang. Ozonization at the vacancy defect site of the single-walled carbon nanotube. *J. Phys. Chem. B*, 110:13037–13044, 2006.
- [7] E. Bekyarova, I. Kalinina, M. E. Itkis, L. Beer, N. Cabrera, and R. C. Haddon. Mechanism of ammonia detection by chemically functionalized SWCNTs: in situ electrical and optical study of gas analyte detection. *J. Am. Chem. Soc.*, 129:10700–10706, 2007.
- [8] A. Barinov, H. Üstünel, S. Fabris, L. Gregoratti, L. Aballe, P. Dudin, S. Baroni, and M. Kiskinova. Defect-controlled transport properties of metallic atoms along carbon nanotube surfaces. *Phys. Rev. Lett.*, 99:046803, 2007.
- [9] R. E. Smalley, Y. Li, V. C. Moore, B. Katherine Price, R. Colorado Jr., H. K. Schmidt, R. H. Hauge, A. R. Barron, and J. M. Tour. Single wall carbon nanotube amplification: en route to a type-specific growth mechanism. *J. Am. Chem. Soc.*, 128:15824–15829, 2006.
- [10] I. M. L. Billas, C. Massobrio, M. Boero, M. Parrinello, W. Branz, F. Tast, N. Malinowski, M. Heinebrodt, and T. P. Martin. First principles calculations of iron-doped heterofullerenes. *Comput. Mater. Chem.*, 17:191–195, 2000.
- [11] G. Lu, K. Deng, H. Wu, J. Yang, and X. Wang. Geometric and electronic structure of metal-substitutional fullerene  $C_{59}Sm$  and metal-exohedral fullerenes  $C_{60}Sm$ . *J. Chem. Phys.*, 124:054305–054309, 2006.



- [12] W. Q. Tian, L. V. Liu, and Y. A. Wang. Electronic properties and reactivity of Pt-doped carbon nanotubes. *Phys. Chem. Chem. Phys.*, 8:3528–3539, 2006.
- [13] C. S. Yeung, L. V. Liu, and Y. A. Wang. Adsorption of small gas molecules onto Pt-doped single-walled carbon nanotubes. *J. Phys. Chem. C*, 112:7401–7411, 2008.
- [14] C. K. Yang, J. Zhao, and J. P. Lu. Complete spin polarization for a carbon nanotube with an adsorbed atomic transition-metal chain. *Nano Lett.*, 4(4):561–563, 2004.
- [15] T. Yildirim and S. Ciraci. Titanium-decorated carbon nanotubes as a potential high-capacity hydrogen storage medium. *Phys. Rev. Lett.*, 94:175501, 2005.
- [16] W. Li, X. Wang Z. Chen, M. Waje, and Y. Yan. Pt-Ru supported on double-walled carbon nanotubes as high-performance anode catalysts for direct methanol fuel cells. *J. Phys. Chem. B*, 110:15353–15358, 2006.
- [17] X. Lu and Z. Chen. Curved  $\pi$ -conjugation, aromaticity, and the related chemistry of small fullerenes( $C_{60}$ ) and SWCNTs. *Chem. Rev.*, 105:3643–3696, 2005.
- [18] H. Mauser, A. Hirsch, N. J. R. van Eikema Hommes, and T. Clark. Chemistry of convex versus concave carbon: the reactive exterior and the inert interior of  $C_{60}$ . *J. Mol. Model.*, 3:415–422, 1997.
- [19] M. D. Halls and H. B. Schlegel. Chemistry inside carbon nanotubes: the Menshutkin  $S_N2$  reaction. *J. Phys. Chem. B*, 106:1921–1925, 2002.
- [20] P. Kondratyuk and J. T. Yates, Jr. Molecular views of physical adsorption inside and outside of single-wall carbon nanotubes. *Acc. Chem. Res.*, 40:995–1004, 2007.
- [21] P. Kondratyuk and J. T. Yates, Jr. Effects of molecular confinement inside single walled carbon nanotubes on chemical reactivity – atomic H and 1-heptene. *J. Am. Chem. Soc.*, 129:8736–8739, 2007.
- [22] G. Zheng, Z. Wang, S. Irle, and K. Morokuma. Origin of the linear relationship between  $CH_2/NH/O$ -SWNT reaction energies and sidewall curvature: Armchair nanotubes. *J. Am. Chem. Soc.*, 128:15117–15126, 2006.
- [23] T. Ohtsuki, K. Ohno, K. Shiga, Y. Kawazoe, Y. Maruyama, K. Shikano, and K. Masumoto. Formation of Sb- and Te-doped fullerenes by using nuclear recoil and molecular-dynamics simulations. *Phys. Rev. B*, 64:125402–125406, 2001.
- [24] Y. Yagi, T. M. Briere, M. H. F. Sluiter, V. Kumar, A. A. Farajian, and Y. Kawazoe. Stable geometries and magnetic properties of single-walled carbon nanotubes doped with 3d transition metals: a first-principles study. *Phys. Rev. B*, 69:075414, 2004.

- [25] M. J. Frisch, G. W. Trucks, H. B. Schlegel, G. E. Scuseria, M. A. Robb, J. R. Cheeseman, Montgomery, Jr., J. A., T. Vreven, K. N. Kudin, J. C. Burant, J. M. Millam, S. S. Iyengar, J. Tomasi, V. Barone, B. Mennucci, M. Cossi, G. Scalmani, N. Rega, G. A. Petersson, H. Nakatsuji, M. Hada, M. Ehara, K. Toyota, R. Fukuda, J. Hasegawa, M. Ishida, T. Nakajima, Y. Honda, O. Kitao, H. Nakai, M. Klene, X. Li, J. E. Knox, H. P. Hratchian, J. B. Cross, V. Bakken, C. Adamo, J. Jaramillo, R. Gomperts, R. E. Stratmann, O. Yazyev, A. J. Austin, R. Cammi, C. Pomelli, J. W. Ochterski, P. Y. Ayala, K. Morokuma, G. A. Voth, P. Salvador, J. J. Dannenberg, V. G. Zakrzewski, S. Dapprich, A. D. Daniels, M. C. Strain, O. Farkas, D. K. Malick, A. D. Rabuck, K. Raghavachari, J. B. Foresman, J. V. Ortiz, Q. Cui, A. G. Baboul, S. Clifford, J. Cioslowski, B. B. Stefanov, G. Liu, A. Liashenko, P. Piskorz, I. Komaromi, R. L. Martin, D. J. Fox, T. Keith, M. A. Al-Laham, C. Y. Peng, A. Nanayakkara, M. Challacombe, P. M. W. Gill, B. Johnson, W. Chen, M. W. Wong, C. Gonzalez, and J. A. Pople. *Gaussian 03*. Gaussian, Inc., Wallingford, CT, 2004.
- [26] J. P. Perdew, K. Burke, and M. Ernzerhof. Generalized gradient approximation made simple. *Phys. Rev. Lett.*, 77:3865–3868, 1996.
- [27] P. J. Hay and W. R. Wadt. Ab initio effective core potentials for molecular calculations: potentials for K to Au including the outermost core orbitals. *J. Chem. Phys.*, 82:299, 1999.
- [28] W. W. Porterfield. *Inorganic Chemistry: A Unified Approach*. Academic, New York, 2nd ed. edition, 1993.

## Chapter 4

# Density Functional Study of Interaction of Atomic Pt with Pristine and Stone-Wales-Defected Single-Walled Boron Nitride Nanotubes<sup>3</sup>

### 4.1 Introduction

Molecular borazine ( $B_3N_3H_6$ ), isoelectronic to benzene, has a similar electronic structure to benzene especially in terms of its aromaticity. At the same time, due to their constitutional difference, borazine and benzene also possess some distinct properties. For instance, borazine is usually more reactive than benzene. When these molecular aromatic rings are extended to form layered hexagonal boron nitride (hBN) and carbon graphite networks, their very different properties, in contrast to their molecular counterparts, can be put into diverse uses accordingly. Because of their extraordinary mechanical hardness and chemical inertness, hBN is mostly used as supporting material for catalytic reactions. Noble metal catalysts supported by hBN are very efficient for deep oxidation of organic compounds with the virtue of low light-off temperature and short initiation time.<sup>1</sup> Carbon graphite, on the other hand, is widely used as a lubricant and in electronic devices because of its excellent electric conductivity.

When the two-dimensional graphene and hBN sheets are rolled into nanotubes, further changes take place because of the decreased dimensionality. In zigzag single-walled boron nitride nanotubes (BNNTs), the dipole moment is nonzero due to the alternate layers of B and N atoms, in sharp contrast to the non-polar cases of hBN and armchair BNNTs.<sup>2</sup> Unlike homonuclear carbon systems, boron nitride materials consist of two different elements with distinct electronegativities: N and B atoms are electron donors and acceptors, respectively. Local compositional inhomogeneity distinguishes BNNTs from carbon nanotubes (CNTs) and makes BNNTs more versatile upon any structural transformation and functionalization. However, BNNTs have been much less frequently

---

<sup>3</sup>A version of this chapter has been submitted for publication. Chen, Y. K.; Liu, L. V. and Wang, Y. A. Density Functional Study of Interaction of Atomic Pt with Pristine and Stone-Wales-Defected Single-Walled Boron Nitride Nanotubes.

investigated in comparison with the rich literature on CNTs.

One of the most attractive features is that BNNTs with large diameters have band gaps almost invariant to the tube diameter and chirality. Even with little purification, BNNTs can be readily used in nanoelectronics.<sup>3</sup> As metal catalysts supporting materials, BNNTs have the merit of good thermal conductivity compared to traditional metal oxide supports.<sup>4</sup> The incombustibility at high temperatures and inertness to various chemicals make BNNTs particularly good substrates for catalysis. Strong binding energies between BNNTs and many transition metals also suggest BNNTs would be good candidates as the stationary phase in catalytic processes.<sup>5</sup>

Pristine BNNTs were first synthesized by an arc discharge process followed by a variety of preparation methods, including laser ablation, chemical vapor deposition, and chemical substitution,<sup>6,7</sup> in which transition metals or their oxides play significant roles. Intuitively, there must be some constructive interactions between transition metals or their oxides and BNNTs (or the BNNT precursors) during the growth period of the nanotube. Understanding such interactions will definitely be helpful in improving the fabrication of BNNTs and may also lead to new metal-BNNT complex based materials. Thus it is interesting to study the interaction between some widely available transition metals (e.g., Pt) and BNNTs.

Up to now, most studies have concentrated on zigzag BNNTs, which are energetically more stable than armchair BNNTs of similar diameter. However, because of their structural importance, armchair BNNTs have been frequently identified to play significant roles in many experiments.<sup>8</sup> A high-resolution field emission transmission electron microscopic study showed that BNNTs can interchange between zigzag and armchair conformations upon the presence of structural kinks.<sup>9</sup> Besides the stability issues, the electronic structure of BNNTs around the Fermi level is almost invariant to the geometric parameters (tube diameter and chirality) due to the localized ionic B–N bonds. Thus, studies on armchair BNNTs can be easily transferable to stable zigzag BNNTs.

Defects were also observed in boron nitride based materials mostly due to mechanical fractures. It was suggested that monovacancies exist in hBN under certain conditions.<sup>10</sup> BNNT was shown to be more susceptible to a monovacancy than hBN.<sup>11</sup> These defects influence the properties of BNNTs in many aspects, including growth behavior and reactivity. Recently, studies on formation and properties of these defects, especially the Stone-Wales (SW) defects, have aroused the interests of many researchers. This pentagon-heptagon-heptagon-pentagon (5775) SW defect is energetically more stable than the tetragon-octagon defect (*a.k.a.* 4884 defect) and can easily occur to BNNTs with small diameters.<sup>12,13</sup> A spectroscopic study using a scanning tunneling microscope revealed that the SW defect is localized in terms of its vibrational modes and frontier orbitals.<sup>14</sup> In addition to their structural significance, these SW defects have also been used as active sites for various processes, where the adsorption strengths and reaction products were found to depend strongly on the nature of orbital interactions.

The SW defect was proposed to enhance the field emission of BNNTs.<sup>15</sup> To find new molecular storage materials, the adsorption of some diatomic and polyatomic molecules on the SW defects

were studied and compared with the adsorption on pristine BNNTs.<sup>16</sup> From theoretical studies of molecular hydrogen adsorption on BNNTs, it was found that finetuning the pores (defects) can manipulate the hydrogen adsorption strength of BNNTs.<sup>17</sup> Just recently, much improved reactivity has been suggested based on studies of Ni adsorption on (8,0) BNNT.<sup>18</sup> Not surprisingly, Pt-doped CNTs have already intrigued research interests after being proven to be good catalysts and potential gas sensors.<sup>19,20</sup> The carbon-doped BNNT was also found to be a better O<sub>2</sub> bearer than pristine BNNT.<sup>21</sup> Because BNNT can be both *p*- and *n*-type doped, studies of Pt-doped BNNTs may reveal new materials with novel properties, not available to *n*-doping CNTs.

In this paper, we will further the understanding of how the catalytic activity of Pt, a widely used catalyst in the same group of Ni, varies on pristine and defected BNNTs. Pt absorption on pristine and SW-defected (5,5) BNNTs was studied using spin-unrestricted DFT method. Adsorption strengths and electronic structures were investigated to illustrate the property change of Pt caused by the SW defect in the substrate BNNTs. In comparison, products and properties of doping of atomic Pt into B or N single-vacancies of BNNTs were also studied.

## 4.2 Computational details

All calculations in the current study were carried out using the Gaussian 03 package.<sup>22</sup> The spin-unrestricted Kohn-Sham (KS) equations were solved for the electronic structure. A hybrid functional, B3LYP, was used to approximate the exchange-correlation interactions.<sup>23,24</sup> Wavefunctions were expanded in terms of the LanL2DZ atomic centered basis set of double zeta quality with the core electrons represented by the LanL2 effective core potentials.<sup>25</sup>

A truncated (5,5) BNNT with 45 B and 45 N atoms was used to model the (5,5) BNNTs (Fig. 4.1a). Both ends of the truncated BNNT segment were capped with H atoms to saturate dangling bonds. The chemical formula for both pristine and SW-defected BNNT models is B<sub>45</sub>N<sub>45</sub>H<sub>20</sub>. To study Pt adsorption, a Pt atom was placed at various locations on the pristine BNNT or on top of the SW defect site. Atomic Pt doping into the B and N single-vacancies of (5,5) BNNTs was also studied with their empirical formulas of PtB<sub>44</sub>N<sub>45</sub>H<sub>20</sub> and PtB<sub>45</sub>N<sub>44</sub>H<sub>20</sub>, respectively.

Binding energies were calculated by subtracting the electronic energies of the adduct from the sum of individual fractions. A positive binding energy indicates an exothermic adsorption.

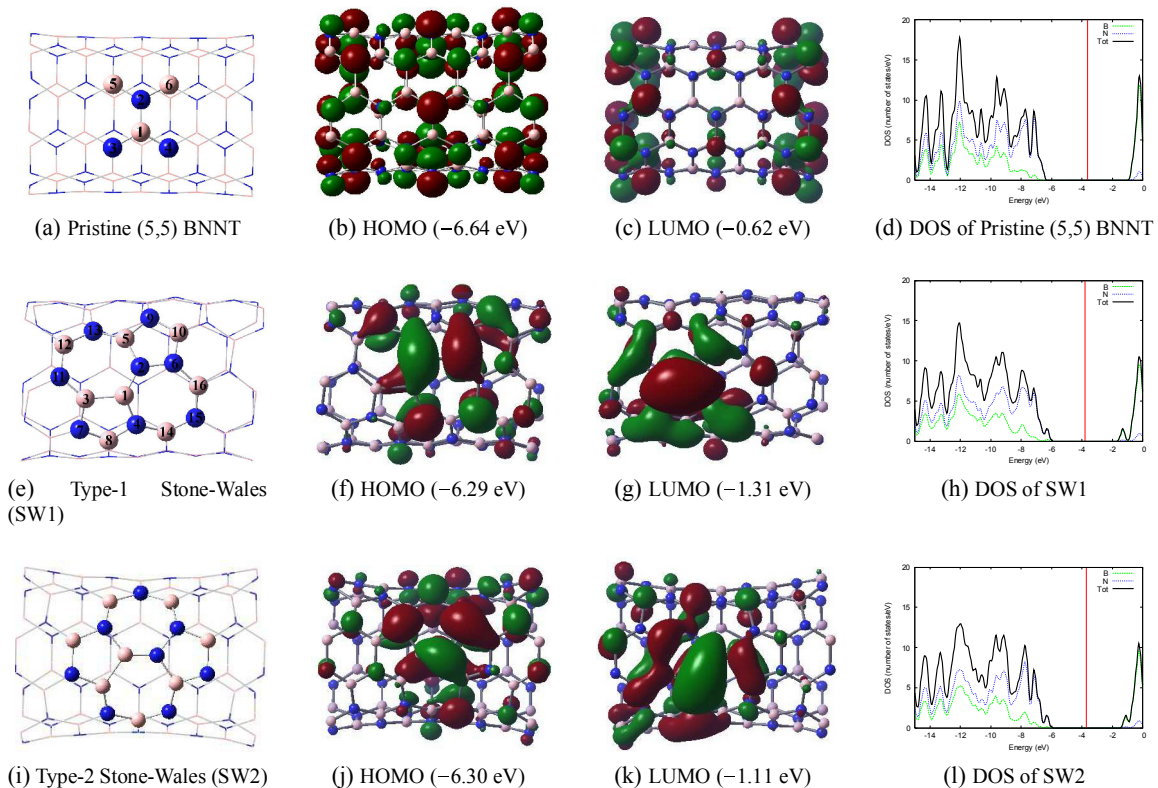


Figure 4.1: Optimized geometries, frontier orbitals, and density of states (DOS) of pristine and Stone-Wales-defected (5,5) BNNTs. Blue and pink spheres represent N and B atoms, respectively. Orbital energies are shown in the parentheses. In the DOS plots, black curves indicate the total DOS, while blue and green curves indicate N and B local DOS, respectively. Red vertical lines mark the Fermi levels.

## 4.3 Results and discussions

### 4.3.1 Pristine and SW-defected (5,5) BNNTs

The optimized pristine and SW-defected (5,5) BNNTs are shown in Fig. 4.1. There are two nonequivalent B–N bonds in a pristine (5,5) BNNT: vertical B–N bonds perpendicular to the longitudinal direction of the tube (*e.g.*, the bond between the B1 and N2 atoms in Fig. 4.1a) and slant B–N bonds (*e.g.*, the bond between the B1 and N3 atoms in Fig. 4.1a). Bond lengths obtained in this study are 1.453 Å for the vertical bonds and 1.455 Å for the slant bonds, as shown in Table 4.1. These bond lengths are in fair agreement with those predicted from an early theoretical study at the PBE1PBE/6-31G(d) level.<sup>16</sup> A 90°-rotation of these two bonds results in two different SW defects: the type-1 SW defect (SW1) with a slant bond rotation (Fig. 4.1b) and the type-2 SW defect (SW2) with a vertical bond rotation (Fig. 4.1c). The formation of pentagons and heptagons

violates the  $[4n + 2]$  aromatic rule and makes these defects less stable electronically compared with the perfect hexagonal structure with six  $\pi$  electrons. Moreover, the formation of the homonuclear N–N and B–B bonds “frustrates” the atoms of the SW defect due to the unfavorable electronic interactions in direct donor-donor and acceptor-acceptor contacts.<sup>8</sup> The electronic energies of SW1 and SW2 were calculated to be 115.9 and 123.8 kcal/mol higher (less stable) than that of pristine BNNT, respectively. An early study<sup>12</sup> showed that the formation energy difference between slant and vertical SW defects decreases as the diameter of the BNNT becomes larger. Together with this early study, our result firmly indicates that the formation energy difference between SW1 and SW2 defects primarily lies in the different rolling-up strain of these two defects.

	Pristine BNNT	PtBNNTa	PtBNNTb
Binding Energy		21.96	20.88
Charge on Pt		−0.009	−0.031
B1–N2 distance	1.453	1.494	1.564
B1–N3 distance	1.455	1.444	1.469
N2–B5 distance	1.455	1.503	1.489
Pt–N2 distance		2.051	2.067
Pt–B1 distance		3.085	2.295

Table 4.1: Bond lengths (in Å), binding energies (in kcal/mol), and partial charges on Pt for Pt absorptions on pristine (5,5) BNNTs at different sites. Symmetrically equivalent bonds are only listed once.

To investigate the electronic structure of pristine and SW-defected (5,5) BNNTs, the density of states (DOS) of each pristine and SW-defected (5,5) BNNTs are shown in Fig. 4.1. The gap between the highest occupied molecular orbital (HOMO) and the lowest unoccupied molecular orbital (LUMO) of the pristine BNNT was calculated to be 6.02 eV, in good agreement with the experimentally measured value:  $5.8 \pm 0.2$  eV.<sup>26</sup> This brings us confidence in the results of our calculations.

The HOMO of the pristine BNNT is composed of delocalized  $p_\pi$  orbitals of the N atoms, and the LUMO consists of the unoccupied  $p_{\pi^*}$  orbitals of the B atoms. The energy difference between these two orbitals makes the pristine BNNT an insulator with a wide band gap. The HOMO-LUMO gaps of the SW-defected BNNTs are narrowed slightly because of the appearance of two island-like electronic states from the defect site. The HOMOs of the SW-defected BNNTs are primarily localized  $p_{\pi^*}$  orbitals of the frustrated N atoms and the LUMOs are mainly localized  $p_\pi$  orbitals of the frustrated B atoms. This computational result is consistent with the observations made in a scanning tunneling study.<sup>14</sup> The orbital-energy-raised HOMO, the orbital-energy-lowered LUMO, and the locality of these two frontier orbitals slightly improve the reactivity of the SW-defected BNNTs compared with the pristine BNNT.

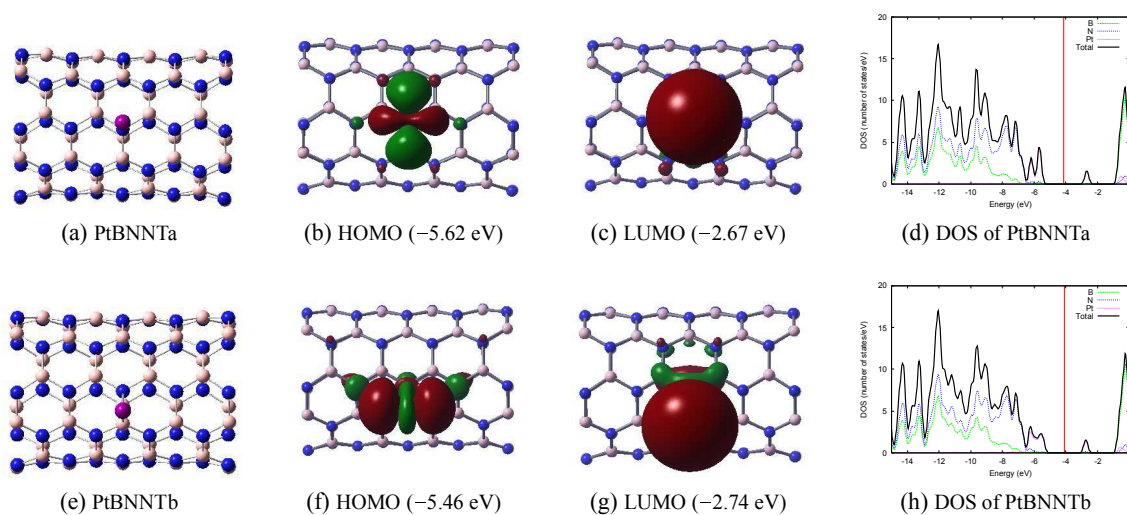


Figure 4.2: Optimized geometries, frontier orbitals, and density of states (DOS) of Pt-adsorbed pristine (5,5) BNNTs. Purple, blue, and pink spheres represent Pt, N, and B atoms, respectively. Orbital energies are shown in the parentheses. In the DOS plots, black curves indicate the total DOS, while purple, blue, and green curves indicate Pt, N and B local DOS, respectively. Red vertical lines mark the Fermi levels.

### 4.3.2 Pt absorption on pristine and SW-defected BNNTs

Pt adsorption on pristine BNNT results in two different local minima, PtBNNTa and PtBNNTb, whose optimized geometries and frontier orbitals are shown in Fig. 4.2. The Pt atom can either locate on top of a N atom (PtBNNTa) or bridge two adjacent B and N atoms (PtBNNTb). The geometric parameters can be found in Table 4.1. For the convenience of discussion, the N and B absorption sites are designate as N2 and B1 in Fig. 4.1.

The Mulliken charge analysis indicates only a small charge transfer between the Pt atom and the pristine BNNT. The binding energies for PtBNNTa and PtBNNTb are about 21.4 kcal/mol, much weaker than that obtained in an early study of Pt adsorption on the sidewall of a zigzag (8,0) BNNT,<sup>5</sup> in which the Pt atom only bridged the two adjacent N–B pair. The weak dependence of the binding energy on the binding site signifies that a Pt atom may migrate on the surface of a pristine BNNT with very low energy barrier. The bond lengths between N2 and its surrounding B atoms are increased upon Pt adsorption in PtBNNTa and PtBNNTb, which indicates weakened N2–B bonds. The DOS drawn in Fig. 4.2 indicates that the interaction between the Pt atom and the pristine BNNT is weak, manifested by only slightly perturbed B and N electronic states below  $-6.5$  eV (compared with the pristine BNNT). Introducing the adsorbate Pt atom narrows the HOMO-LUMO gap to about 2.5 eV by filling Pt electronic states into the gap of the pristine BNNT and makes the Pt-adsorbed BNNT wide-gap semiconductive. The HOMO of PtBNNTa is mainly



composed of Pt 5*d* orbitals, while the LUMO consists of Pt 6*s* and 6*p* orbitals. The decreased band gap enhances the reactivity of the Pt-adsorbed BNNT particularly at the absorbed Pt site and makes the Pt-adsorbed BNNTs more conductive. As the binding energy shrinks from PtBNNTa to PtBNNTb, the HOMO-LUMO gap gets smaller and the adsorption adducts become more reactive.

	SW1	PtSW1a	PtSW1b	PtSW1c	PtSW1d	PtSW1e
Binding Energy		55.41	30.27	28.36	28.11	23.15
Charge on Pt		-0.004	-0.011	0.013	0.014	0.013
B1–N2 distance	1.416	1.452	1.503	1.451	1.436	1.421
B1–B3 distance	1.694	2.363	1.687	1.702	1.691	1.694
B1–N4 distance	1.463	1.465	1.483	1.448	1.601	1.456
N2–B5 distance	1.480	1.473	1.544	1.666	1.463	1.468
N2–N6 distance	1.469	1.466	1.476	1.460	1.470	1.496
Pt atop X–Y bond		B1–B3	B1–N2	N2–B5	B1–N4	N6–B16
Pt–X distance		1.986	2.255	2.033	2.214	2.040
Pt–Y distance		1.992	2.049	2.210	2.070	2.257

Table 4.2: Bond lengths (in Å), binding energies (in kcal/mol), and partial charges on Pt for Pt absorptions on type-1 SW-defected (5,5) BNNTs at different sites.

Without loss of generality, the adsorption of atomic Pt on SW-defected BNNTs was studied on the SW1-defected BNNTs, simply because the SW1 and SW2 structures are essentially the same. Since the frontier orbitals are localized around the defect sites, we focus on the interaction between the Pt atom and the SW-defected region (atoms 1–6 in Fig. 4.1b). The placement of Pt on top of the B1–B3 bond results in the PtSW1a structure (Fig. 4.3a), in which the Pt atom is inserted between two B atoms. In this structure, the strain due to the B–B bond frustration is released and the formation energy goes as high as 58 kcal/mol. Meanwhile, the detachment of these two B atoms alleviates the ring strain by making the bond angles of B3–N7–B8, N7–B8–N4, and B8–N4–B1 very close to the energetically favorable 120°. At the same time, B1 and B3 are found to stick out of the tube hypersurface markedly compared with the SW-defected BNNTs whose atoms at the defect site are fairly within the tube surface. Beside that the B1–B3 distance is elongated by the insertion of Pt and the B1–N2 length is also drastically increased (see Table 4.2).

Differing from Pt absorbed on the pristine BNNTs, the LDOS of Pt of PtSW1a spreads widely from -10.0 to -5.6 eV along with the LDOS of B atoms (Fig. 4.3d), which indicates a strong bonding interaction between Pt and the two nearby B atoms. The HOMO of this structure is composed of Pt *sd* hybridized orbitals and N *p<sub>π</sub>* orbitals that constitute the HOMO of SW1. The HOMO contribution at the N site primarily exposes electron density towards the interior of the BNNT and provides an opportunity for electrophiles inside the tube to react with this site. The LUMO of PtSW1a is composed of Pt 6*s* orbital and B *p<sub>π</sub>* orbitals. This LUMO has an energy of -2.38 eV, higher than that of the LUMO of any other Pt-absorbed pristine or SW defected BNNTs. There-

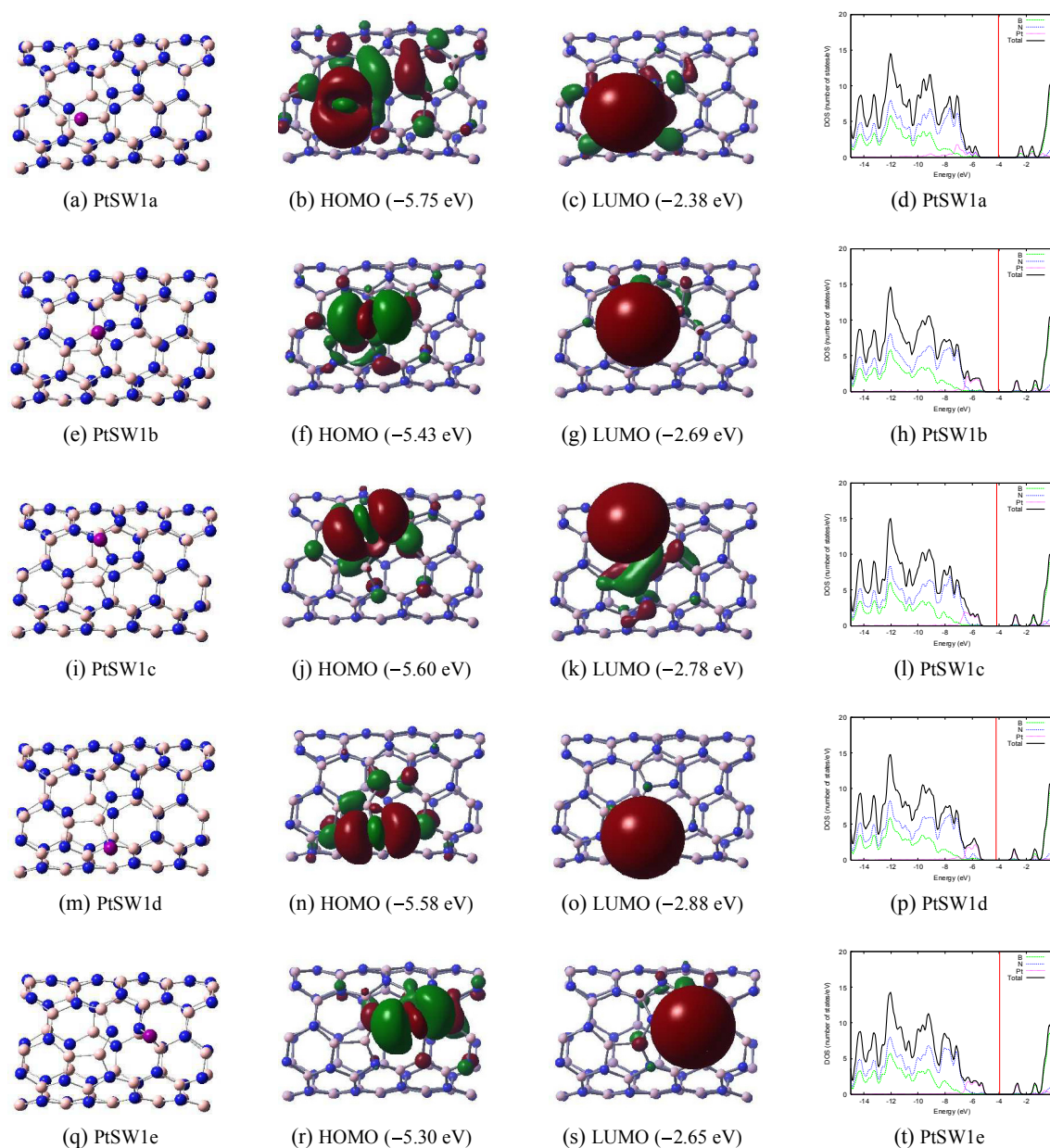


Figure 4.3: Optimized geometries, frontier orbitals, and density of states (DOS) of Pt-adsorbed type-1 Stone-Wales-defected (5,5) BNNTs. Purple, blue, and pink spheres represent Pt, N, and B atoms, respectively. Orbital energies are shown in the parentheses. In the DOS plots, black curves indicate the total DOS, while Purple, blue, and green curves indicate Pt, N, and B local DOS, respectively. Red vertical lines mark the Fermi levels.

fore, PtSW1a is least reactive to both electrophiles and nucleophiles and is the most stable structure among the adducts of Pt and SW1-defected BNNTs. Comprising Pt  $5d6p$  orbitals and unoccupied

B  $p$  orbitals, the first orbital above the LUMO of these Pt-absorbed SW-defected BNNTs also appears as an island-like state at around  $-1.5$  eV, the presence of which distinguishes the adsorption of Pt on the SW defects from the adsorption of Pt on pristine BNNTs.

The binding interaction of the adducts from Pt adsorption on top of the B–N bonds at the defect site are only slightly stronger than that of Pt adsorption on pristine BNNTs. The Pt atom can bridge atop the B1–N2 bond (PtSW1b) with a noticeable N2–B5 bond elongation (Fig. 4.3e). The Pt–B1 bond length here is much shorter than that in PtSW1a because Pt favors adsorption towards electron withdrawing groups. The HOMO of PtSW1b is primarily composed of Pt  $5d$  orbitals and is energetically higher than that of PtSW1a, while the LUMO energy is lower due to large contribution from the Pt  $6s$  orbital. Compared with PtSW1a, PtSW1b is more reactive and less stable. The Pt atom can also bridge atop N2–B5 (PtSW1c) and B1–N4 (PtSW1d) bonds with similar binding strengths and electronic structures (Figures 4.3i and m). Attempts to putting Pt atop the N2–N6 bond did not result in a stationary structure. Depending on the initial trial geometry, the Pt atom either moves towards the N2–B1 bond to form PtSW1b, or towards the N2–B5 bond to form PtSW1c, or towards the N6–B16 bond to form PtSW1e (Fig. 4.3q) because the two close-lying electron donating centers (the two frustrated N atoms) cannot form two bonds with the incoming Pt atom simultaneously. The calculated binding energy of PtSW1e is 23.15 kcal/mol, only marginally higher than that of PtBNNTb. Also, PtSW1e exhibits similar electronic structure to that of PtBNNTb (see Figures 4.1h and 4.2t). Thus, PtSW1e can be regarded as a slightly perturbed PtBNNTb, and the perturbation is the SW defect in the vicinity

Based on all the computational results of Pt absorptions on pristine and SW-defective BNNTs, we can conjecture that atomic Pt on a BNNT with some SW defects will eventually relax into the PtSW1a structure due to its maximal stability. The resulting adduct has reduced reactivity towards either electrophiles or nucleophiles. This conclusion implies that finetuning of the reactivity of the absorbed Pt atom can be achieved through introducing defect sites. Using BNNTs with or without the SW defects can adjust the catalytic ability of the supported Pt atoms to optimize reaction conditions for some reactivity sensitive reactions to satisfy the Sabatier principle.<sup>27</sup>

### 4.3.3 Pt-doped (5,5) BNNTs

The Pt-doped (5,5) BNNTs were also studied with their optimized structures shown in Fig. 4.4. The Pt atom can replace either a N atom (N substitution) or a B atom (B substitution). The N substitution leads to a significantly negative partial charge accumulation on the Pt atom because the electrons flow from the surrounding B atoms to the Pt atom at the center (Table 4.3). The Pt–B bond lengths are comparable to those in PtSW1a. The spin density is primarily located on the Pt atom and its three surrounding B atoms. The Pt LDOS contributes greatly to the total DOS in the region from  $-12.0$  to  $-3.0$  eV, which indicates strong interactions between the Pt atom and the N-vacant BNNT (Fig. 4.4d). The  $\alpha$ -spin HOMO comprises Pt  $5d6s$  and  $6p$  orbitals, which move

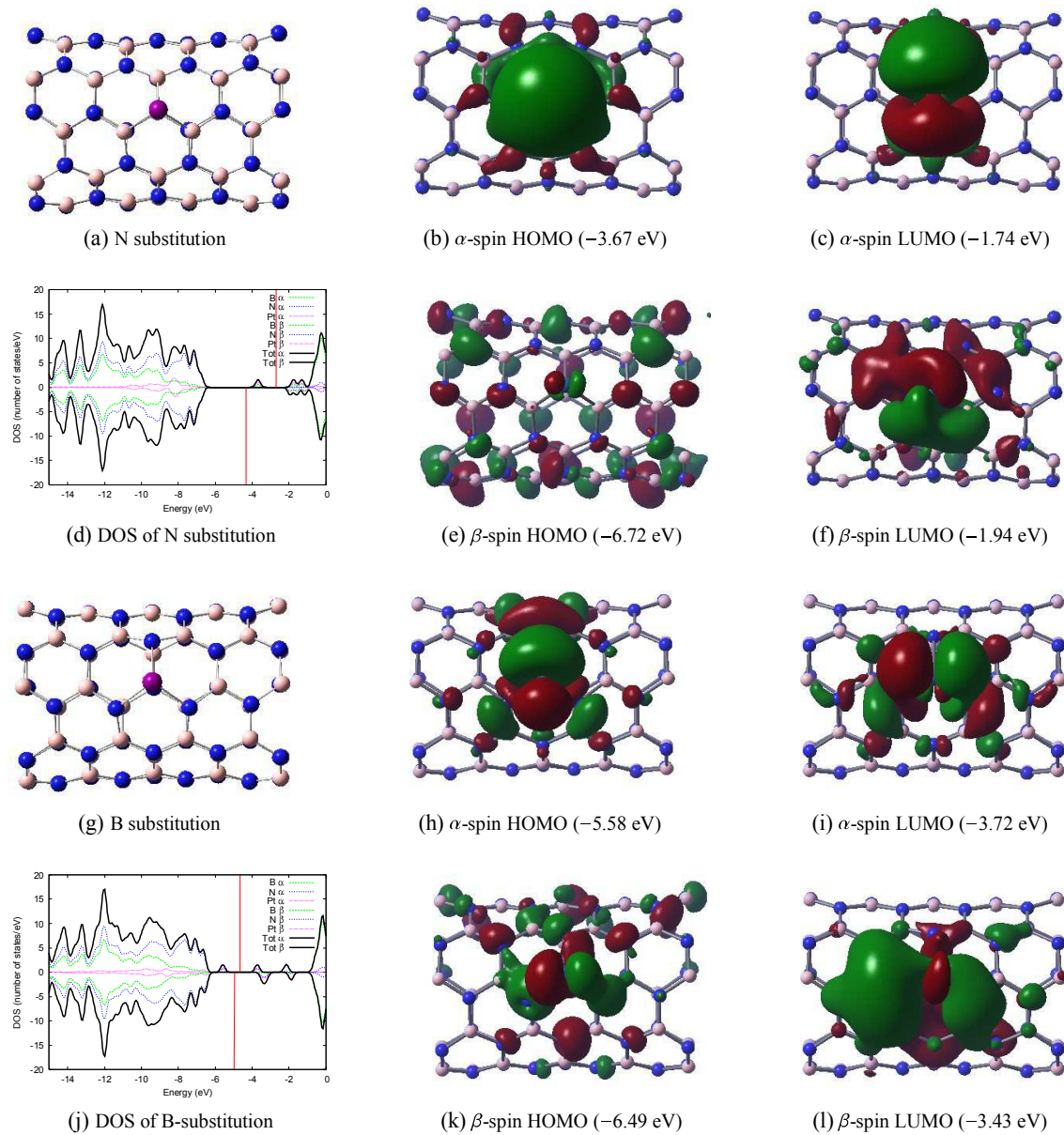


Figure 4.4: Optimized geometries, frontier orbitals, and density of states (DOS) of Pt-doped (5,5) BNNTs. Purple, blue, and pink spheres represent Pt, N, and B atoms, respectively. Orbital energies are shown in the parentheses. In the DOS plots, black curves indicate the total DOS, while purple, blue, and green curves indicate Pt, N, and B local DOS, respectively. Red vertical lines mark the Fermi levels. The curves above the x-axis indicate  $\alpha$ -spin DOS and those below,  $\beta$ -spin components.

the  $\alpha$ -spin HOMO energy upwards to  $-3.67$  eV and make the Pt-doped BNNT a good electron donor. Ascribed to the constituent  $\alpha$ -spin LDOS of the B atoms around the vacancy site and from

the Pt 6s and 6p orbitals, the  $\alpha$ -spin LUMO is also shifted upwards to  $-1.74$  eV and becomes less reactive towards nucleophiles. The  $\beta$ -spin HOMO is composed of the N  $p_{\pi^*}$  orbitals, similar to that of a pristine (5,5) BNNT. The  $\beta$ -spin LUMO is similar to the  $\alpha$ -spin LUMO, but with more contributions from remote B atoms. The band gap is only about 1.9 eV, turning Pt-doped BNNT semiconducting.

	B substitution	N substitution
Charge on Pt	0.363	-0.368
Spin density on Pt	0.540	0.550
Perpendicular bond length	2.080	2.124
Slant bond length	1.969	2.001

Table 4.3: Surrounding bond lengths (in Å), partial charges and spin densities of Pt in Pt-doped (5,5) BNNTs.

Replacing a B atom with a Pt atom also makes the Pt-doped BNNT semiconducting by lowering the energy of the  $\alpha$ -spin LUMO. The  $\alpha$ -spin HOMO is now composed of Pt 5d orbitals. The  $\alpha$ -spin LUMO is made of Pt 5d orbitals and N  $p_{\pi}$  orbitals, which lowers its energy to  $-5.6$  eV. On the other hand, the N contribution to the  $\alpha$ -spin LUMO makes this Pt-doped BNNT a good electron acceptor. The  $\beta$ -spin HOMO is mainly from p orbitals of the N atoms around the vacancy site and Pt 5d orbitals. The  $\beta$ -spin LUMO energy is lowered by the participation of Pt 5d orbitals. Opposite to the Pt doping into the N-vacancy case, the Pt atom that substitutes for a B atom in a BNNT donates 0.36 electrons towards its bonding N atoms and the charge flow is also accompanied by the spin density spreading over the Pt and its three surrounding N atoms. Both orbitals and electrostatic character favor nucleophilic attack: electron-rich molecules such as N<sub>2</sub> or CO shall absorb strongly on the dopant Pt atom.

## 4.4 Conclusion

Spin-unrestricted hybrid DFT calculations were carried out to investigate the interactions between atomic Pt and the pristine, SW-defective, and vacancy defective (5,5) BNNTs. By comparing the binding strengths, we conclude that Pt can move freely on the surface of a pristine BNNT or be trapped between the B–B bond at the defect site of a SW-defected BNNT with decreased reactivity. Electronic structures were studied by analysing the DOS and frontier orbitals of these systems. The Pt atom can modify the electronic structures of the pristine and SW-defective BNNTs by introducing Pt states into the nanotube band gaps and can thus make these nanotubes more reactive.

# Bibliography

- [1] C. A. Lin, J. C. S. Wu, J. W. Pan, and C. T. Yeh. Characterization of boron-nitride-supported Pt catalysts for the deep oxidation of benzene. *J. Catalysis*, 210:39–45, 2002.
- [2] Ş. Erkoç. Structural and electronic properties of single-wall BN nanotubes. *J. Mol. Struct. (THEOCHEM)*, 542:89–93, 2003.
- [3] A. N. Enyashin, V. V. Ivanovskaya, Y. N. Makurin, and A. L. Ivanovskii. Electronic structure of new graphyne-like boron nitride nanotubes. *Doklady Phys. Chem.*, 395:64–68, 2004.
- [4] G. Postole, M. Caldararu, N. I. Ionescu, B. Bonnetot, A. Auroux, and C. Guimon. Boron nitride: a high potential support for combustion catalysts. *Thermochimica Acta*, 434:150–157, 2005.
- [5] X. Wu and X. C. Zeng. Adsorption of transition-metal atoms on boron nitride nanotube: A density functional study. *J. Chem. Phys.*, 125:044711, 2006.
- [6] N. G. Chopra, R. J. Luyken, K. Cherrey, V. H. Crespi, M. L. Cohen, S. G. Louie, and A. Zettl. Boron nitride nanotubes. *Science*, 269:966–967, 1995.
- [7] M. Terrones, J. M. Romo-Herrera, E. Cruz-Silva, F. López-Urías, E. Muñoz-Sandoval, J. J. Velázquez-Salazar, H. Terrones, Y. Bando, and D. Golberg. Pure and doped boron nitride nanotubes. *Materials Today*, 10:30–39, 2007.
- [8] X. Blase, A. De Vita, J. Ch. Charlier, and R. Car. Frustration effects and microscopic growth mechanisms for BN nanotubes. *Phys. Rev. Lett.*, 80:1666–1669, 1998.
- [9] D. Golberg, Y. Bando, L. Bourgeois, K. Kurashima, and T. Sato. Insight into the structure of BN nanotubes. *Applied Phys. Lett.*, 77(13):1979–1981, 2000.
- [10] W. Orellana and H. Chacham. Stability of native defects in hexagonal and cubic boron nitride. *Phys. Rev. B*, 63:125205, 2001.
- [11] A. Zobelli, C. P. Ewels, A. Gloter, O. Stephan, S. Csillag, and C. Colliex. Defective structure of BN nanotubes: From single vacancies to dislocation lines. *Nano. Lett.*, 6(9):1955–1960, 2006.

- [12] W. H. Moon and H. J. Hwang. Theoretical study of defects of BN nanotubes: A molecular-mechanics study. *Physica E*, 28:419–422, 2005.
- [13] Y. Li, Z. Zhou, D. Golberg, Y. Bando, P. von Ragué Schleyer, and Z. Chen. Stone-Wales defects in single-walled boron nitride nanotubes: Formation energies, electronic structures, and reactivity. *J. Phys. Chem. C*, 112:1365–1370, 2008.
- [14] Y. Miyamoto, A. Rubio, S. Berber, M. Yoon, and D. Tománek. Spectroscopic characterization of Stone-Wales defects in nanotubes. *Phys. Rev. B*, 69:121413, 2004.
- [15] P. Dorozhkin, D. Golbert, Y. Bando, and Z. C. Dong. Field emission from individual B-C-N nanotube rope. *Appl. Phys. Lett.*, 81:1083–1085, 2002.
- [16] W. An, X. Wu, J. L. Yang, and X. C. Zeng. Adsorption and surface reactivity on single-walled boron nitride nanotubes containing Stone-Wales defects. *J. Phys. Chem. C*, 111:14105–14112, 2007.
- [17] S. H. Jhi. A theoretical study of activated nanostructured materials for hydrogen storage. *Catalysis Today*, 120:383–388, 2007.
- [18] J. X. Zhao and Y. H. Ding. Theoretical study of Ni adsorption on SWBNNTs with intrinsic defects. *J. Phys. Chem. C*, 112:5778–5783, 2008.
- [19] W. Q. Tian, L. V. Liu, and Y. A. Wang. Electronic properties and reactivity of Pt-doped carbon nanotubes. *Phys. Chem. Chem. Phys.*, 8:3528–3539, 2006.
- [20] C. S. Yeung, L. V. Liu, and Y. A. Wang. Adsorption of small gas molecules onto Pt-doped single-walled carbon nanotubes. *J. Phys. Chem. C*, 112:7401–7411, 2008.
- [21] J. Zhang, K. P. Loh, J. Zheng, M. B. Sullivan, and P. Wu. Adsorption of molecular oxygen on the walls of pristine and carbon-doped (5,5) boron nitride nanotubes: spin-polarized density functional study. *Phys. Rev. B*, 75:245301, 2007.
- [22] M. J. Frisch, G. W. Trucks, H. B. Schlegel, G. E. Scuseria, M. A. Robb, J. R. Cheeseman, Montgomery, Jr., J. A., T. Vreven, K. N. Kudin, J. C. Burant, J. M. Millam, S. S. Iyengar, J. Tomasi, V. Barone, B. Mennucci, M. Cossi, G. Scalmani, N. Rega, G. A. Petersson, H. Nakatsuji, M. Hada, M. Ehara, K. Toyota, R. Fukuda, J. Hasegawa, M. Ishida, T. Nakajima, Y. Honda, O. Kitao, H. Nakai, M. Klene, X. Li, J. E. Knox, H. P. Hratchian, J. B. Cross, V. Bakken, C. Adamo, J. Jaramillo, R. Gomperts, R. E. Stratmann, O. Yazyev, A. J. Austin, R. Cammi, C. Pomelli, J. W. Ochterski, P. Y. Ayala, K. Morokuma, G. A. Voth, P. Salvador, J. J. Dannenberg, V. G. Zakrzewski, S. Dapprich, A. D. Daniels, M. C. Strain, O. Farkas, D. K. Malick, A. D. Rabuck, K. Raghavachari, J. B. Foresman, J. V. Ortiz, Q. Cui, A. G. Baboul, S. Clifford, J. Cioslowski, B. B. Stefanov, G. Liu, A. Liashenko, P. Piskorz, I. Komaromi, R. L.

Martin, D. J. Fox, T. Keith, M. A. Al-Laham, C. Y. Peng, A. Nanayakkara, M. Challacombe, P. M. W. Gill, B. Johnson, W. Chen, M. W. Wong, C. Gonzalez, and J. A. Pople. *Gaussian 03*. Gaussian, Inc., Wallingford, CT, 2004.

- [23] A. D. Becke. Density functional thermochemistry. III. The role of exact exchange. *J. Chem. Phys.*, 98:5648–5672, 1993.
- [24] C. Lee, W. Yang, and R. G. Parr. Development of the Colle-Salvetti correlation-energy formula into a functional of the electron density. *Phys. Rev. B*, 37:785–789, 1988.
- [25] P. J. Hay and W. R. Wadt. Ab initio effective core potentials for molecular calculations: potentials for K to Au including the outermost core orbitals. *J. Chem. Phys.*, 82:299, 1999.
- [26] R. Arenal, O. Stéphan, M. Kociak, A. Loiseau D. Taverna, and C. Colliex. Electron energy loss spectroscopy measurement of the optical gaps on individual boron nitride single-walled and multiwalled nanotubes. *Phys. Rev. Lett.*, 95:127601, 2005.
- [27] H. Knözinger and K. Kochloefl. Heterogeneous catalysis and solid catalysts. In *Ullmann's Encyclopedia of Industrial Chemistry*, pages 1–110. Wiley-VCH Verlag, 2005.



## Chapter 5

# First-Principles Studies of the Hyperfine Coupling Constants for Muoniated Butyl Radicals<sup>4</sup>

### 5.1 Introduction and background

Free radicals are meta stable yet reactive chemical species with unpaired electrons and have long been of interest. Electron paramagnetic resonance (EPR) spectroscopy has been developed over decades as a powerful tool to study and characterize these spin-polarized systems. The study of H-atom isotopic effects by EPR used to be mostly limited to deuterium substitution. With the development of nuclear techniques, the positive muon ( $\mu^+$ ), a radioactive and spin-polarized elementary particle, and particularly the muonium atom ( $\text{Mu}=\mu^+e^-$ ), a remarkably light H-atom isotope ( $m_{\text{Mu}}=0.113$  amu), have been implanted into many systems to investigate the properties of these systems. The muon spin resonance ( $\mu\text{SR}$ ) technique,<sup>1,2</sup> an EPR analogue for characterizing Mu-containing species, has been widely employed to study isotopic effects in a number of chemical systems, including both Mu formation and reaction rates,<sup>3–5</sup> and of particular interest here, muoniated free radicals since their discovery in 1978.<sup>6</sup>

The central measurement in free radical studies, either by EPR or  $\mu\text{SR}$ , is the isotropic hyperfine coupling constant (HFCC) that arises from the interaction between unpaired electrons and nuclear spins. The knowledge of HFCCs provides valuable electronic structural information about the free radical under study. In the past decade alone, the HFCCs of various muoniated radicals have been obtained and characterized, with the aid of theory, in a wide variety of host media and molecular environments.<sup>7–14</sup> The present paper is concentrated on the calculation of HFCCs to explain the experimental data discussed in the companion experimental paper,<sup>15</sup> hereafter referred to as ‘paper I’.

The HFCC is proportional to the electron spin density at the nucleus of interest. At first glance, it might seem that any theoretical method that can be used to calculate the electron density should be amenable to the calculation of HFCCs. However, these tools can fail dramatically in calculating

---

<sup>4</sup>A version of this chapter will be submitted for publication. Chen, Y. K.; Fleming, D. G. and Wang, Y. A. First-Principles Studies of the Hyperfine Coupling Constants for Muoniated Butyl Radicals.

HFCCs, because most theoretical tools are designed to give a good description of valence-shell electron interactions so that most other molecular properties can be satisfactorily predicted.

An early attempt to predict HFCCs by *ab initio* methods can be found in Meyer's 1969 Hartree Fock (HF) calculations.<sup>16</sup> Due to its lack of electron correlation, the HF method was found unsuitable to yield quantitative results for HFCC. Even though several post-HF methods developed subsequently, such as configuration interaction (CI),<sup>17</sup> the multiconfiguration self-consistent-field (MC-SCF) method<sup>18</sup> and coupled cluster (CC) theory,<sup>19,20</sup> were able to include correlation effect, these post-HF methods are usually too demanding on computational resources for routine use for HFCC calculations for even medium size molecules. Normally, second-order Møller-Plesset perturbation theory (MP2) can recover more than 80% of dynamic correlation effects. Generally, MP2 can reproduce experimental HFCCs at an acceptable computational cost.<sup>21,22</sup>

An alternative way to obtain HFCCs is to use density functional theory (DFT), which has become popular in the past decade for its speed and accuracy. This is particularly true for proton HFCC calculations after an early regression analysis had shown DFT to be a promising tool.<sup>23</sup> Nevertheless, the use of approximate exchange-correlation functionals limits the broad utility of the DFT method in the calculation of HFCCs, because good agreement between DFT calculations and experimental results might stem from error cancellations.<sup>24</sup> Several examples of this "artifact" can be found in the calculations of HFCCs for some metal complexes, regardless of the form of the density functionals employed.<sup>25</sup> This could also be the case found for specific muoniated butyl radicals, as discussed more below.

Besides the form of the Hamiltonian adopted in theoretical investigations, the quality of the basis set in a HFCC calculation also plays an important role. To obtain accurate electron (and spin) density around the nucleus, a basis set with uncontracted core shell basis functions is always a prerequisite.<sup>26,27</sup> It is for this reason that EPR-II and EPR-III basis sets, which consist of uncontracted core shell basis functions, have been developed specifically for calculations relevant to EPR studies.<sup>28</sup>

Moreover, it is essential to have good geometric parameters to calculate HFCCs because the electron density at each nucleus is very sensitive to structural changes in molecules.<sup>26,27</sup> Although theoretical studies have also shown that HFCCs of small rigid molecules are often not very sensitive to different computational methods and basis sets employed,<sup>23</sup> that is not the case in the present study. The muoniated adducts formed from muonium addition to butene isomers are complicated geometrically due to the flexible aliphatic chains of the resultant radical isomers, especially those formed from 1-butene. In such cases, theoretical methods must be carefully selected to meet the preliminary geometric requirement. Early studies showed that MP2 was unsatisfactory in calculating hydrogenated alkene radicals because of large spin contamination.<sup>29-32</sup> On the other hand, DFT methods have also been proven inadequate for some conformational calculations due to their inability to account for weak, non-covalent interactions.<sup>33-37</sup> Since both DFT and MP2 methods have their merits and shortcomings in determining the stationary conformations of open-shell species

from different perspectives, both of them were employed and compared side by side in this study with the EPR-III basis set.

Beyond electronic structure and molecular geometry concerns, quantitative HFCC calculations of radicals also demand the inclusion of dynamic and thermal corrections. Even at 0 K, atoms in a molecule vibrate around their equilibrium positions. Therefore, the HFCC of each atom is constantly changing in contrast to the value from a fixed equilibrium structure. This vibrational effect is particularly important in the present study, due to the very light mass of the Mu, only one-ninth that of the H atom. A scheme to compensate for the vibrational effect is introduced in the following sections.

When the temperature increases, higher vibrational states become populated, causing even larger-amplitude vibrations compared with zero-point vibrations, and further thermal corrections need to be considered in calculating temperature-dependent HFCCs to obtain quantitative agreement with experiment. In this study, it is the torsional barrier about the  $C_\alpha-C_\beta$  bond that mainly determines the temperature dependence of the  $\beta$  muon/proton HFCCs. Higher temperatures facilitate the population of higher vibrational states and increase the deviation of the  $\beta$  muonium from the “eclipsed” configuration at 0 K that corresponds to the maximum overlap between the C–Mu bond and the  $p_z$  orbital at the radical center. Therefore, the HFCC of the eclipsed muon or proton decreases when the temperature increases. Concurrently, the corresponding proton HFCC at the “staggered” position increases. Qualitatively speaking, a high rotational barrier translates into a late onset of HFCC change with increasing temperature and a shallow slope in the temperature-dependent region in the muon/proton HFCC plots. Other motions like bond stretching and molecular bending can also affect the temperature dependences of HFCCs, but they are generally associated with larger excitation energies that can only become accessible at much higher temperatures.

The torsional barriers of the  $C_\alpha-C_\beta$  bond rotations were calculated in this study at the MP2/EPR-III level, with the barrier height determined by the difference in the electronic energies between the top of the barrier and the bottom of the potential energy well of internal rotation. The definition of the torsional barrier here differs from the more phenomenological one in paper I, where a simple trigonometric form of the potential energy function was assumed to simulate the torsional potential energy surface. The barrier height calculated in this study is of electronic nature only, whereas the barrier determined in paper I further implicitly includes zero-point vibrational corrections and environmental effects. These additional effects are important, because their contributions to the overall torsional barrier are comparable to the electronic contribution even for the proton HFCCs of the unsubstituted ethyl radical,<sup>38,39</sup> and particularly so in the case of muoniated radicals due to the light muon mass.<sup>40,41</sup> Nevertheless, it is still of interest to compare the electronic barriers determined here with those determined phenomenologically in paper I, where zero-point vibrational corrections were implicitly included.

The actual HFCCs of a free radical can also be greatly affected by the surrounding molecules in condensed phases. However, environmental effects on HFCCs have not been systematically studied

to date; no generic conclusion can be drawn. Noteworthy here is a study by Barone and coworkers of the HFCCs of tyrosyl radicals, where the solvent effect was divided into direct (polarization) and indirect (geometric alteration) contributions.<sup>42</sup> The direct effect, stemming from the spin density redistribution in response to solvent polarization, was found to be dominant in these calculations and caused all the HFCCs in aqueous solution to be smaller than those in vacuum. A  $\mu$ SR study of solvent effects on the HFCCs of the Mu-cyclohexadienyl radical also showed appreciable effects on the muon and proton HFCCs, arising from dipolar interactions.<sup>43</sup> In both cases, polar solvents and polar radicals were involved, in contrast to the largely non-polar environments of the present study. In this study, the lack of solid state parameters for butene isomers, such as crystal structures, is another obstacle. Moreover, the environmental and vibrational effects can be coupled together and can then impact synergistically on the HFCCs, seen in measured temperature dependences in paper I. Similar remarks were made by Percival and coworkers in their study of temperature-dependent muon HFCC for the muoniated tert-butyl in liquid and solid phases.<sup>44</sup> Though very good fits to these data were obtained based on solving the torsional Schrödinger equation, the HFCCs were only semi-empirically determined from the McConnell equation and vibrations other than the  $C_\alpha-C_\beta$  torsion were completely ignored.<sup>45</sup>

Since the first-principles HFCC computation combining both vibrational and environmental effects is still in its infancy, we will focus on the calculations of *in-vacuo* HFCCs at 0 K. The vibrational and environmental effects will be discussed only at a qualitative level.

## 5.2 Remarks on the calculations

Even though it is realized that non-Born-Oppenheimer effects may play a significant role in calculating the properties of muonium containing radicals, all the calculations in this study are within the framework of the Born-Oppenheimer (BO) approximation. Explicit non-BO calculations are still prohibitive at present for the butyl radicals of interest here. Perhaps, the most explicit demonstration of corrections to the BO approximation in Mu systems is found in a study of barrier heights in the isotopomers of the  $H_3$  reaction system.<sup>46</sup> Not surprisingly, the largest correction was for the  $Mu + H_2$  reaction rate, but even so the correction to the barrier height was only 3.8%. We expect a much smaller correction to the C–Mu bond in the case of much heavier muoniated radicals studied here.

For its popularity and earlier success in calculating both molecular geometries and HFCCs,<sup>23</sup> spin-unrestricted B3LYP,<sup>47,48</sup> a hybrid DFT method with the EPR-III basis set<sup>28</sup> implemented in Gaussian 03,<sup>49</sup> has been used to obtain the equilibrium structures and the HFCCs of the butyl radical isomers. As previously commented, the EPR-III basis set affords accurate descriptions of the core shell spin density and was specifically developed for EPR spectroscopy calculations.<sup>28</sup> Despite the good reputation that B3LYP enjoys for efficiency and accuracy in HFCC calculations, it has been recognized that B3LYP, along with most other popular DFT Hamiltonians, is incapable of predicting

weak, non-covalent interactions in molecules and may even lead to wrong conformations.<sup>33–36</sup> Thus, geometry optimization and the corresponding HFCCs have also been calculated at the spin-unrestricted MP2 level of theory with the EPR-III basis set.

Besides the pure electronic structure effect, the importance of incorporating vibrational corrections in HFCC calculations is well known and discussed in a recent review article.<sup>27</sup> Vibrational corrections are particularly important for C–Mu bonds in muoniated radicals.<sup>50–52</sup> Even though the HFCCs of several small radicals have been calculated in Barone’s group with the inclusion of vibrational corrections by a fully automated second-order perturbative approach implemented locally in Gaussian03,<sup>53</sup> this implementation is unavailable to general Gaussian users. In the current study of muoniated butyl radicals, without a direct analytical first-principles evaluation of the dynamic effect of vibrational averaging, the C–Mu distance has been intentionally stretched to 1.076 times the corresponding equilibrium C–H bond length and a HFCC calculation has then been carried out on this modified geometry to account for the vibrational, especially the anharmonic, contribution. The justification for this approach is given in the following section. For convenience, all muon HFCC values reported here are in “reduced” units,  $A'_\mu = A_\mu/3.184$ , which corrects for the gyromagnetic ratio between muon and proton, thereby allowing their direct comparison and to the results in paper I.

## 5.3 Methodology and results

### 5.3.1 Geometries and molecular structures

The first step in a calculation of the HFCCs of the butyl radicals of interest is to determine their equilibrium geometries. As noted earlier, all calculations were carried out within the BO framework using the Gaussian 03 package. This means that all nuclei in the molecules are depicted to move on a potential energy surface (PES). As a consequence, the electronic Hamiltonian is independent of the nuclear mass and all isotopomers have the same equilibrium geometries and electronic structures. Therefore, the optimized conformations of muoniated butyl radicals can be discussed in terms of the corresponding hydrogen isotopomers without loss of generality. The reaction scheme of muonium addition to butene isomers and the corresponding optimized radical adducts are shown in Figs. 5.1–5.3. The geometric optimization results are discussed individually in the following paragraphs. Conventional or common names of these species are used (as in paper I) unless IUPAC names are sometimes cited.

The isobutene precursor has only one geometric isomer with four coplanar carbon atoms. Hydrogen addition to the carbon double bond of isobutene results in two isomers: a tert-butyl (t-butyl) and an isobutyl radical (Fig. 5.1). B3LYP calculations identified only one stereo isomer for each of these two radical products (t and i1 in Fig. 5.2). However, two conformational isomers were found for isobutyl at the MP2 level. In addition to i1 (Fig. 5.2b), a conformational isomer i2 (Fig. 5.2c)

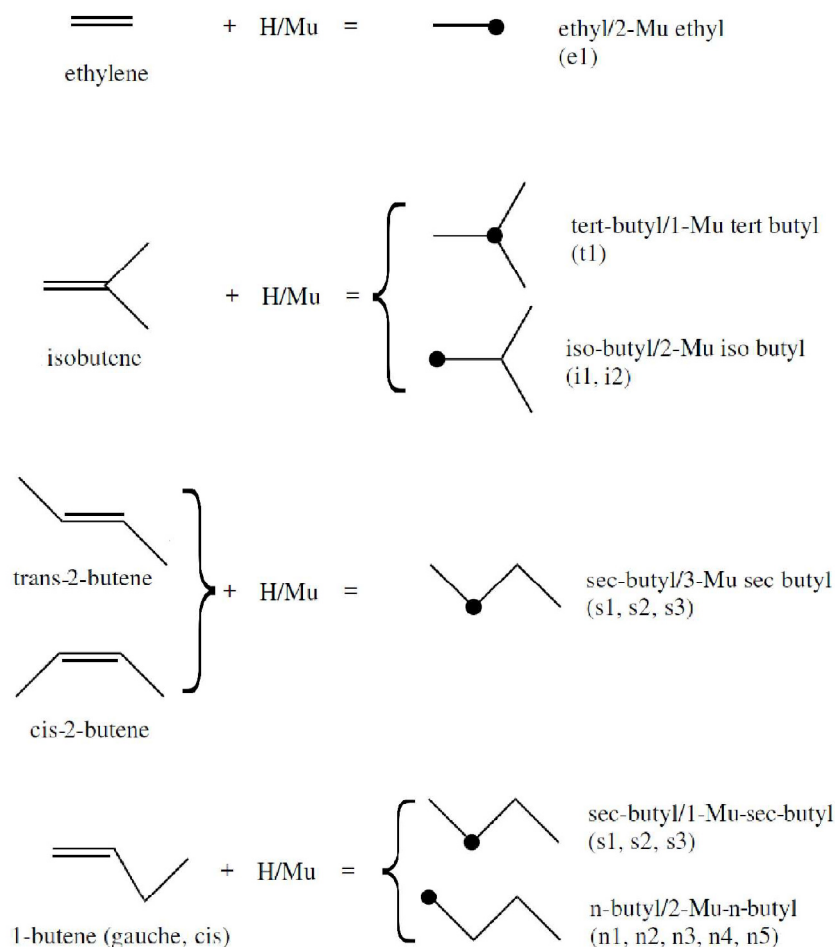
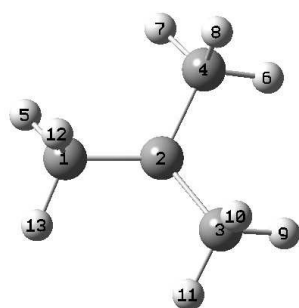


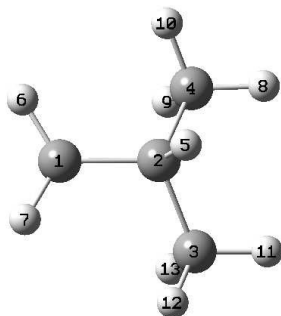
Figure 5.1: Hydrogenation or muonation (Mu) of different butene isomers. Only the carbon skeleton is shown. The dots on the product side indicate locations of the radical center. The identification of possible conformers are given in parentheses and their corresponding geometries are displayed in Figs. 5.2 and 5.3.

was also found with its singly occupied  $p_z$  orbital on the radical center aligning with one of the  $\beta$  methyl groups, instead of a hydrogen atom as in the i1 structure. However, this i2 structure does not correspond to the direct product of Mu/H addition to isobutene. It is thus not discussed further below.

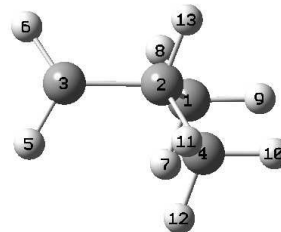
For the 2-butene precursors, textbook knowledge tells us that there are both cis (less stable) and trans (more stable) isomers, and both isomers were confirmed by MP2 and B3LYP calculations



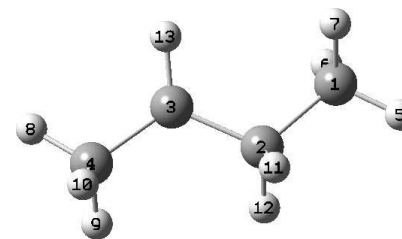
(a) t-butyl (t)



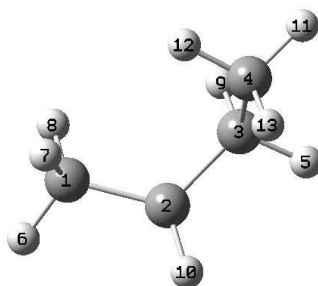
(b) iso-butyl (i1)



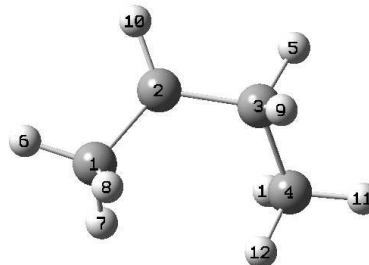
(c) iso-butyl (i2)



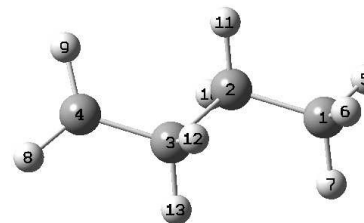
(d) sec-butyl (s1)



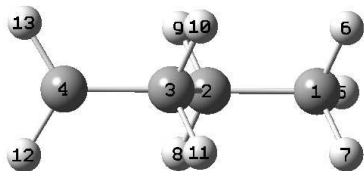
(e) sec-butyl (s2)



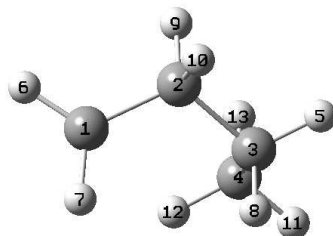
(f) sec-butyl (s3)



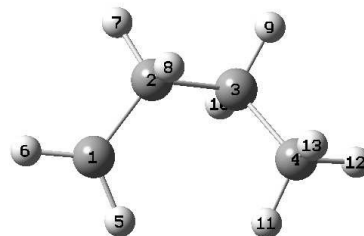
(g) n-butyl (n1)



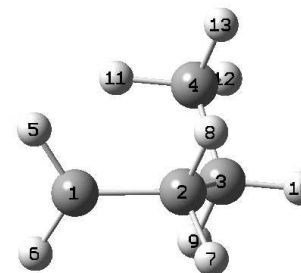
(h) n-butyl (n2)



(i) n-butyl (n3)



(j) n-butyl (n4)



(k) n-butyl (n5)

Figure 5.2: Optimized structures of ethyl, tert-butyl (or t-butyl), isobutyl, sec-butyl, and n-butyl radicals. H and C atoms are shown by small (light) and large (dark) spheres, respectively.

carried out here. Supported by the large and distinct muon HFCC values reported in paper I, one would expect the sec-butyl radicals formed by hydrogen/Mu addition to trans- or cis-2-butene to be s1 (Fig. 5.2d) and s3 (Fig. 5.2f). B3LYP calculations identified only two structures: a trans conformation (Fig. 5.2d) corresponding to the product of hydrogen addition to trans-2-butene, and a gauche conformation (Fig. 5.2e), which is not directly associated with either of the 2-butene precursors. On the other hand, MP2 calculations, in addition to the two rotomers obtained from the B3LYP calculations, also found a cis structure (s3 as in Fig. 5.2f) corresponding to the radical formed from hydrogen addition to cis-2-butene. Since the s2 (gauche) structure has a dihedral angle of the carbon backbone of about  $90^\circ$  and has no eclipsed  $\beta$  hydrogens, it was not observed at 0 K in the experiment (according to the muon HFCC values discussed in paper I). Though there may be some contribution from this s2 conformer at high temperatures, this structure will not be further discussed.

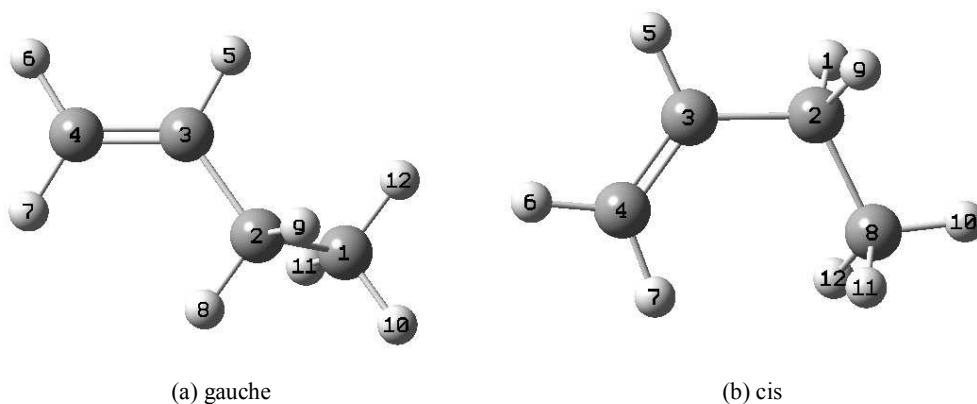


Figure 5.3: Optimized gauche and cis conformations of 1-butene. H and C atoms are shown by small (light) and large (dark) labeled spheres, respectively.

The most problematic cases in this study are the 1-butene isomers and their muonium adducts. To the best of our knowledge, the relative stability of the gauche and cis conformations of 1-butene (Fig. 5.3) is still ambiguous, despite the fact that their existence is well acknowledged theoretically and experimentally. Based on far infrared spectra (FIR) of 1-butene, Bell and coworkers suggested the cis-1-butene isomer to be 0.2 kcal/mol more stable than the gauche one.<sup>54</sup> In the same study, up to 4th-order Møller-Plesset perturbation theory was applied to calculate the electronic energies of the two isomers, but the computational results contradicted the order of relative stability derived



from the FIR data. On the other hand, the experimental results were supported by an earlier study of microwave spectra.<sup>55</sup> We have also carried out CCSD/cc-pVDZ calculations in addition to MP2 and B3LYP calculations on both 1-butene isomers. The gauche conformation was predicted to be the global minimum by all three theoretical methods applied. Though some experimentalists have believed that the cis conformation of 1-butene is more stable than the gauche form at low temperatures, it is worth noting that the gauche form has always been determined to be relatively more abundant than the cis form in all three commonly accessible phases (gas, liquid, and solid).<sup>56</sup> This is also the case in a recent electron momentum spectroscopy investigation of 1-butene in the gas phase, where the gauche (or “skew”) conformer was favored over the cis (or “syn”) form by a mole ratio of 2:1.<sup>57</sup> These experimental results, combined with our theoretical predictions, lend confidence that the 1-butene precursor in the experiments reported in paper I should be mainly in the gauche form. Therefore, our theoretical effort is focused on the corresponding muonium or hydrogen adducts from this gauche form.

Hydrogen/muonium addition to the terminal unsaturated carbon atom of 1-butene results in the same equilibrium structures (sec-butyl radicals) as the adducts from hydrogen/muonium addition to 2-butene. Based on stereochemistry and our calculations, the s1 and s2 conformations are the radicals resulting from hydrogen addition to the gauche 1-butene on the terminal double-bond carbon atom from the less and the more hindered side, respectively. The s3 structure (Fig. 5.2f) is associated with the hydrogen/muonium addition to the terminal double bond carbon atom of the cis-1-butene. The hydrogen/muonium can also add to the non-terminal double bond carbon atoms in 1-butene, forming the n-butyl or 1-butyl radicals (n1 to n5 in Fig. 5.2g-k). B3LYP calculations located three local minima (n1, n2, and n3), whereas MP2 calculations located all five of them (n1–n5). The n3 and n1 butyl conformations can be designated as the radicals produced from hydrogen addition to the non-terminal carbon atom of the double bond of gauche-1-butene from the less and more hindered directions, respectively. The n4 butyl radical stems from hydrogen addition to cis-1-butene. The other two isomers, n2 and n5, are not directly associated with any reaction products formed by hydrogen addition to 1-butene isomers at low temperatures, so these two structures are not discussed further in this study. Again, they might contribute at higher temperatures.

### 5.3.2 Overview of HFCC calculations

Based on the optimized geometries discussed above, the HFCCs calculated at the B3LYP/EPR-III and MP2/EPR-III levels of theory are listed in Table 5.1. The HFCC on any nucleus of a free radical is proportional to the electron spin density at the nucleus of interest and can be decomposed into two contributions: the direct (delocalization) contribution from the singly occupied molecular orbital (SOMO) and the indirect spin polarization contribution due to the correlation effect.<sup>27,58</sup> The direct contribution to the HFCCs of the hydrogen atoms is reflected by the Mulliken spin density. In this study, the Mulliken spin density on the eclipsed  $\beta$  hydrogen was found to be much larger than that

Radical	Atom 5	Atom 6	Atom 7	Atom 8	Atom 9	Atom 10	Atom 11	Atom 12	Atom 13	Theoretical Method
tert-butyl	22.90	22.78	22.87	117.35	22.77	117.37	22.90	117.32	22.75	MP2/EPR-III (H)
	30.63	29.70	30.59	133.06	29.76	133.26	30.61	133.13	29.63	B3LYP/EPR-III (H)
	21.47	22.03	22.89	115.94	22.01	115.97	22.91	<i>131.14</i>	21.32	MP2/EPR-III (Mu)
iso-butyl	28.48	27.98	29.72	130.51	28.04	130.70	29.75	<i>153.72</i>	27.51	B3LYP/EPR-III (Mu)
	117.91	-64.53	-64.53	0.40	-2.50	-1.30	0.40	-1.30	-2.50	MP2/EPR-III (H)
	140.05	-61.26	-61.26	0.44	-1.92	-1.50	0.44	-1.50	-1.92	B3LYP/EPR-III (H)
sec-butyl (s1)	<i>129.89</i>	-63.87	-63.87	0.39	-1.22	-2.70	0.39	-1.22	-2.70	MP2/EPR-III (Mu)
	<i>159.81</i>	-57.77	-57.77	0.53	-2.17	-1.36	0.53	-1.36	-2.17	B3LYP/EPR-III (Mu)
	-1.88	-2.21	-1.49	12.29	46.42	125.69	113.85	47.16	-60.03	MP2/EPR-III (H)
sec-butyl (s2)	-2.10	-1.76	-1.57	12.85	66.24	137.36	126.70	66.65	-61.44	B3LYP/EPR-III (H)
	-1.83	-2.49	-1.44	11.76	46.48	124.14	<i>127.36</i>	45.44	-59.02	MP2/EPR-III (Mu + 2-butene)
	-1.89	-2.06	-1.44	11.47	65.31	134.62	<i>145.17</i>	64.10	-57.74	B3LYP/EPR-III (Mu + 2-butene)
sec-butyl (s3)	-1.88	-2.19	-1.46	11.34	44.71	<i>139.55</i>	113.44	47.20	-58.98	MP2/EPR-III (Mu + 1-butene)
	-1.88	-1.55	-1.36	11.39	63.51	<i>157.28</i>	124.17	65.75	-57.69	B3LYP/EPR-III (Mu + 1-butene)
	14.40	22.92	131.61	34.08	34.22	-60.93	11.63	-3.84	-3.40	MP2/EPR-III (H)
1-butyl (n1)	34.38	20.51	148.24	55.90	28.12	-60.86	12.11	-4.14	-3.42	B3LYP/EPR-III (H)
	14.11	21.70	<i>145.95</i>	32.64	34.36	-59.94	11.07	-3.84	-3.41	MP2/EPR-III (Mu + 1-butene)
	32.52	18.13	<i>168.32</i>	52.78	26.92	-54.12	11.91	-3.72	-3.03	B3LYP/EPR-III (Mu + 1-butene)
1-butyl (n3)	8.15	-0.53	77.52	109.71	110.81	-62.64	0.10	-2.01	-2.52	MP2/EPR-III (H)
	7.33	-0.65	77.15	108.13	<i>123.98</i>	-61.69	0.17	-1.95	-2.81	MP2/EPR-III (Mu + cis 2-butene)
	7.79	-0.88	75.30	<i>121.75</i>	110.27	-61.66	0.21	-1.99	-2.52	MP2/EPR-III (Mu + 1-butene)
1-butyl (n4)	-0.65	0.44	0.48	-66.07	-65.52	-2.54	-1.54	130.21	36.84	MP2/EPR-III (H)
	-0.18	0.82	0.85	-62.03	-62.13	-2.14	-1.73	150.28	54.32	B3LYP/EPR-III (H)
	-0.79	0.59	0.44	-65.41	-64.82	-2.80	-1.49	<i>143.46</i>	35.52	MP2/EPR-III (Mu + 1-butene)
1-butyl (n4)	-0.30	1.05	0.76	-55.92	-55.97	-2.22	-1.44	<i>169.84</i>	51.67	B3LYP/EPR-III (Mu + 1-butene)
	-2.57	-66.26	-64.96	-1.55	35.32	134.81	-1.56	2.07	0.08	MP2/EPR-III (H)
	-2.62	-62.30	-61.34	-1.86	41.61	157.73	-0.82	2.42	0.50	B3LYP/EPR-III (H)
1-butyl (n4)	-2.53	-65.58	-64.23	-1.44	34.05	<i>148.62</i>	-1.58	2.19	0.01	MP2/EPR-III (Mu + 1-butene)
	-2.44	-58.72	-57.70	-1.63	39.70	<i>179.42</i>	-0.89	2.62	0.44	B3LYP/EPR-III (Mu + 1-butene)
	-63.75	-65.04	36.01	122.38	1.00	-2.16	0.94	0.43	-0.20	MP2/EPR-III (H)
	-63.02	-64.36	34.70	<i>134.94</i>	1.05	-2.40	0.91	0.28	-0.23	MP2/EPR-III (Mu + 1-butene)

Table 5.1: Calculated proton and muon HFCCs of butyl and Mu-butyl isomers. Atoms are labeled according to Figure 5.2. In the last column, the ‘H’ in the parenthesis denotes that the HFCCs were calculated at their equilibrium structures for the unsubstituted radicals (H atoms only). The ‘Mu’ in the parenthesis means that the HFCC highlighted in *italic* was calculated based on the structure, whose C–Mu bond was intentionally stretched to 1.076 times the equilibrium C–H bond length. The HFCC values for 1-butyl (n4) were based on the geometry from MP2/EPR-II calculations.

on the staggered hydrogen(s) because the eclipsed  $\beta$  hydrogen atom can share some spin density with the aligned half filled  $p_z$  orbital via hyperconjugation. Therefore, the large muon HFCCs seen near 0 K experimentally for the muoniated butyl radicals in paper I can be assigned to the eclipsed conformations. This is also true for some proton HFCCs in paper I. Another fact in support of assigning eclipsed structures to these radicals is that the incoming Mu/H attacks preferentially to the C=C double bond from the  $p_\pi$  orbital direction and this naturally leads to eclipsed radical products.<sup>59</sup> Some conformations such as i2 and the two 1-butyl (n2 and n5) isomers that do not have eclipsed  $\beta$  hydrogen atoms are not directly formed from H/Mu addition to their alkene precursors at low temperatures, so these structures are only mentioned here without any further discussion.

The proton HFCCs can be satisfactorily obtained at the B3LYP level of theory, but are underestimated by MP2 calculations. The calculated muon HFCCs using equilibrium geometries (entries marked with ‘H’ in Table 5.1) fall some 10–40 MHz (*ca.* 5–20%) below the experimental data, which can be seen in paper I and Fig. 5.1-5.4 shown below, for both MP2 and B3LYP calculations. This difference stems from vibrational effects. As already commented, molecules are not at rest even at 0 K and zero-point motion then affects the (averaged) HFCCs observed. This dynamical effect is especially important in the case of Mu-substituted molecules.<sup>50–52</sup> The light muon mass, about one-ninth that of a proton, makes the average C–Mu bond considerably longer than the C–H bond at the same position in an isotopomer. This effect cannot be accounted for by the clamped nuclei model that is inherent to the BO approximation. Overlooking this vibrational effect can dramatically underestimate the muon HFCCs as noted above. Of course, there is a similar vibrational effect on the C–H bond length, but the proton HFCCs are not affected much.<sup>60</sup> We therefore calculated the proton HFCCs based on equilibrium geometries.

### 5.3.3 Vibrational averaging of muon HFCCs

As a convention, a vibration is usually decomposed into anharmonic and harmonic components, both of which will affect the averaged properties of molecules. The harmonic correction to HFCCs is believed to be dominant over the anharmonic one for most regular molecules.<sup>27</sup> However, this is not true for muoniated radicals, in which anharmonicity, especially in the C–Mu stretching mode, becomes important. Theoretical calculations of HFCCs for small molecular radicals, such as HCO and HOO radicals, showed that anharmonic contributions grew large when a heavy H atom was replaced by a lighter isotope:<sup>50</sup> the anharmonic correction was found to reach up to 45% in the MuCO case. Calculations of the muoniated ethyl radical have also shown appreciable anharmonic corrections to the muon HFCC.<sup>51,60</sup>

To estimate the vibrational corrections to the HFCCs or other molecular properties theoretically, several approaches have been developed. As previously noted, some first-principles attempts to solve the vibrational Schrödinger equation were made by Barone and coworkers by applying perturbation theory within their locally modified code.<sup>53</sup> Instead of the direct analytical analysis, a

path-integral Monte Carlo (PIMC) study was recently carried out to calculate averaged HFCCs of the muoniated ethyl radical,<sup>60</sup> and the results of these calculations are compared with our results in Table 5.2 below. These theoretical results are also very important for us to benchmark the performance of a third approach to estimate vibrationally corrected HFCCs, namely, by changing certain geometric properties, such as bond lengths, from the optimized equilibrium geometry. This third alternative is based on a mathematical treatment that proves the anharmonic and partial harmonic corrections to molecular properties can be obtained at the vibrationally averaged geometry.<sup>61</sup>

Based on this idea, we specifically sought the vibrationally averaged structure of a muoniated radical to calculate anharmonically corrected HFCCs for the Mu-butyl (and Mu-ethyl) radicals. In previous studies of this nature, the C–Mu bond in the muoniated ethyl radical was estimated to be 1.054 times the equilibrium C–H bond length<sup>51</sup> and similarly so for the Mu-methyl radical.<sup>9</sup> In the latter calculation on the Mu-methyl radical, fair agreement with the experimental results cited therein was achieved.<sup>9</sup> The  $\beta$ -H atoms of interest here are formally quite different from the  $\alpha$ -H atoms of the methyl radical. Namely, the  $\beta$ -H atoms are relatively more weakly bound to the  $\beta$ -C atom due to their  $sp^3$  hybridization, in contrast to the  $sp^2$  hybridization at the carbon radical center. This also affects the muonium isotopomer. In the recent PIMC results for the Mu-ethyl radical, an elongation factor for the  $\beta$  C–Mu bond of 1.076 was acquired, which underwent insignificant changes upon large-scale temperature variation in the same PIMC study.<sup>60</sup> Hence, we have adopted this scale factor (1.076) here.

The rationale for this scale factor can be appreciated by noting that the C–Mu stretching mode has an extremely large wavenumber, over  $7000\text{ cm}^{-1}$ , distinguishing it from any other vibrational modes of the radical. Evidently, this wavenumber is associated with a high-energy vibration that is well separated from other vibrational modes. Past experience<sup>60</sup> also suggests that the effect of Mu substitution should be well represented by elongating the C–H bond from its equilibrium value by this factor (1.076) over a wide range of temperatures. It should be noted that the averaged bond distance is not identical to the bond length at the vibrationally averaged geometry, but differs by a small amount related to the harmonic vibrational constant.<sup>61,62</sup> In this sense, deliberately stretching the C–Mu bond by the aforementioned factor of 1.076 can be regarded as an approximation to the true effective geometry of the muoniated radical. In fact, the use of this scheme showed marked improvement in muon HFCC predictions and resulted in a much better overall agreement with the experimental data in paper I, with discrepancies between theory and experiment, particularly near 0 K, of less than 10%. Still, as a final caveat, since the HFCC value is not an odd function about any expansion point in most cases, the harmonic HFCC corrections can never be exactly cancelled to zero, so any static model geometry that includes bond stretching cannot be used to obtain quantitative HFCC values.<sup>20,27</sup> Typical deviation due to harmonic vibrations are reported to be about 10% of the overall HFCC,<sup>27</sup> similar deviations as found here between theory and experiment.

### 5.3.4 Benchmark calculations for HFCCs

A study of the hydrogen and muon HFCCs of the unsubstituted and muoniated ethyl radicals was first carried out to benchmark the performance of the MP2/EPR-III and B3LYP/EPR-III methods applied in the current study and to test the elongation scheme proposed above. It is clear that, at the electronic structural level, MP2 calculations outperform B3LYP calculations because of the better agreement between the HFCCs calculated at the MP2 level and at higher levels of theory, such as MP4, CISD, and CCSD (see 5.2).

To compare with experimental and other theoretical results, we have listed our results for eclipsed and staggered conformers of the muoniated ethyl radical in Table 5.2. The calculated  $\beta$ -proton HFCCs for the unsubstituted ethyl radical are shown as the averaged values for a ‘freely-rotating’  $\text{CH}_3$  group, which can be directly compared with the experimental EPR data (temperature-independence down to 4 K, see Ref. 14).

As shown by the comparisons in Table 5.2,  $\beta$ -muon HFCC calculated at the MP2/EPR-III level of theory using the stretched geometry (scale factor 1.076) are far more accurate than any other calculations, whereas the proton HFCCs in both the ethyl and muoniated ethyl radicals are better predicted by B3LYP/EPR-III. However, this seemingly good agreement with experiment for B3LYP calculations of the proton HFCCs may be largely fortuitous. This can be inferred specifically in comparison with the HFCCs for the unsubstituted ethyl radical determined by Chipman’s high-level *ab initio* calculations.<sup>64</sup> Chipman found that the inclusion of out-of-plane bending at the  $\alpha$  carbon causes an increment (to less negative) of the  $\alpha$ -proton HFCC and a reduced (to less positive) value for the  $\beta$ -proton HFCC. This suggests that the good agreement from B3LYP calculations for the  $\alpha$ -proton HFCC in the muoniated (and also in the unsubstituted) ethyl radical was likely due to error cancellations leading to an overestimation of the HFCC by using a static geometry. In contrast, the MP2/EPR-III calculated  $\alpha$ -proton HFCC, after the same corrections, can be expected to be closer to the experimental data, suggesting it is inherently the better approach. In principle, if the vibrational corrections are considered, the HFCCs predicted by MP2 should also be a better starting point than B3LYP.

Nevertheless in this study, as previously noted, the results of both B3LYP and MP2 calculations are presented to provide a more complete picture of the comparison between theory and experiment for the HFCCs of the butyl radicals of interest. In fact, in some cases, MP2 results agree better with experiment for the proton HFCCs than B3LYP calculations. However, as suggested in paper I, the excellent agreement often seen from B3LYP calculations for the muon HFCCs in the solid phase (at temperatures near 0 K) indicates that these calculations fortuitously “mimic” the effect of guest-host interactions in the solid phase, which were not included in the *in vacuo* calculations presented here. This point will be further addressed in the following discussion.

Isotompomer	$\beta$ H (eclipsed)	$\beta$ H (staggered)	$\beta$ H (averaged)	$\alpha$ H	Theoretical Method
ethyl	141.42	31.82	68.35	-67.22	MP2/EPR-III
	162.67	40.24	81.05	-62.86	B3LYP/EPR-III
	136.97	31.61	66.73	-67.29	MP4/EPR-III
	139.77	33.81	69.13	-71.14	CCSD/EPR-III
			69.3	-65.7	QCISD(T)/TZ2P <sup>17</sup>
			68.7	-62.6	Vibrationally corrected QCISD(T)/TZ2P <sup>17</sup>
			64.95	-67.95	CCSD(T)/TZ2P <sup>17</sup>
			65.17	-72.29	CCSD(T)/Chipman basis set <sup>19</sup>
			76	-63	Experiment <sup>66</sup>
Mu-ethyl	156.11	30.60		-66.48	MP2/EPR-III (elongated C–Mu bond)
	184.69	37.89		-58.25	B3LYP/EPR-III (elongated C–Mu bond)
	195.0	42.6		-46.8	B3LYP/EPR-III//tight-binding equilibrium structure <sup>60</sup>
	222.2	64.2		-59.12	B3LYP/EPR-III//tight-binding PIMC at 25 K <sup>60</sup>
	151	36		-63	Experiment <sup>63</sup>

Table 5.2: Experimental and theoretical HFCCs (in MHz) for protons in unsubstituted ethyl and for muons and protons in muoniated ethyl. The MP2/EPR-III and B3LYP/EPR-III calculations for the Mu-ethyl radical were carried out on a modified geometry whose C–Mu bond was stretched to 1.076 times the equilibrium C– bond length.

## 5.4 Results and discussion: comparisons with experiment

The central outcome of the present work is the calculated muon and proton HFCCs for the butyl radicals. Entries shown in Table 5.1 are all given at 0 K and have been compared with the extrapolated data from  $\mu$ SR measurements for the muoniated butyl radicals and with early EPR measurements for the unsubstituted radicals in paper I. In addition, the temperature-dependences of both the (reduced) muon HFCCs,  $A'_\mu(T)$ , and proton HFCCs,  $A_p(T)$ , were calculated from a classical model in paper I, in which these HFCCs were Boltzmann-weighted and fit to the experimental data. In paper I, on the torsional PES, we assumed three local minima whose hydrogen orientations correspond to eclipsed ( $0^\circ$ ) and staggered ( $\pm 120^\circ$ ) positions. The internal rotation barriers were then determined by fitting to the experimental data. These results are not discussed further in any detail here, but rather, additional points relevant to the comparisons between theory and experiment at 0 K are made on a case-by-case basis.

### 5.4.1 Isobutyl and tert-butyl radicals formed from isobutene

Two muoniated radicals can be formed from muonium addition to isobutene, the Mu-t-butyl (muoniated tert-butyl) and Mu-i-butyl (muoniated isobutyl) radicals, whose  $A'_\mu(T)$  data were compared with theory in Fig. 5.4. After the chemical reaction, a muonium can be attached to the non-terminal carbon atom of an isobutene molecule, resulting in an isobutyl radical, shown by structure i1 in Fig. 5.2b. Our calculations at the MP2/EPR-III level indicate that i1 is 4.90 kcal/mol less stable than the t-butyl radical (Fig. 5.2a). Therefore, isobutyl is less favorable thermodynamically than t-butyl, consistent with its much weaker experimental signal and fewer data points (compared with t-butyl in paper I). The muon HFCC of this Mu-i-butyl (i1) radical was calculated to be 129.9 and 159.8 MHz from MP2 and B3YLP calculations, respectively. The MP2 result agrees much better with the extrapolated experimental data in the solid phase. The MP2 calculation also yielded 117.9 MHz for the  $\beta$  proton HFCC of the unsubstituted isobutyl radical, also in good agreement with the extrapolated experimental data from EPR measurements (plotted in Fig. 5.4). In both cases, the classical fitted temperature dependences was also in acceptably good agreement with experiment, in spite of the scatter nature of the  $\mu$ SR data. It is noteworthy that MP2 calculations here have a better agreement than B3LYP for both the muon and proton HFCCs of the isobutyl radical.

In the case of the Mu-t-butyl radical, over a wider temperature range, in both the solid and liquid phases, both the  $\mu$ SR (Fig. 5.4) and EPR (Fig. 5.5) data are more complete than those for isobutyl. At first glance, the agreement with experiment for  $A'_\mu(T)$  from B3LYP calculation is excellent, from 0 K up to the melting point (light blue trend line in Fig. 5.4). Similar to that reported in Ref. 44 from a solution to the torsional Hamiltonian, we obtained a torsional barrier about the  $C_\alpha$ – $\text{CH}_2\text{Mu}$  bond of  $V_2 = 2.9$  kJ/mol (paper I). Nevertheless, consistent with much earlier UHF calculations,<sup>66,67</sup> the electronic torsional barrier found from the MP2 calculation in this study is 5.8 kJ/mol, much higher than that found for the Mu-ethyl radical (0.7 kJ/mol), due to the presence of two other methyl

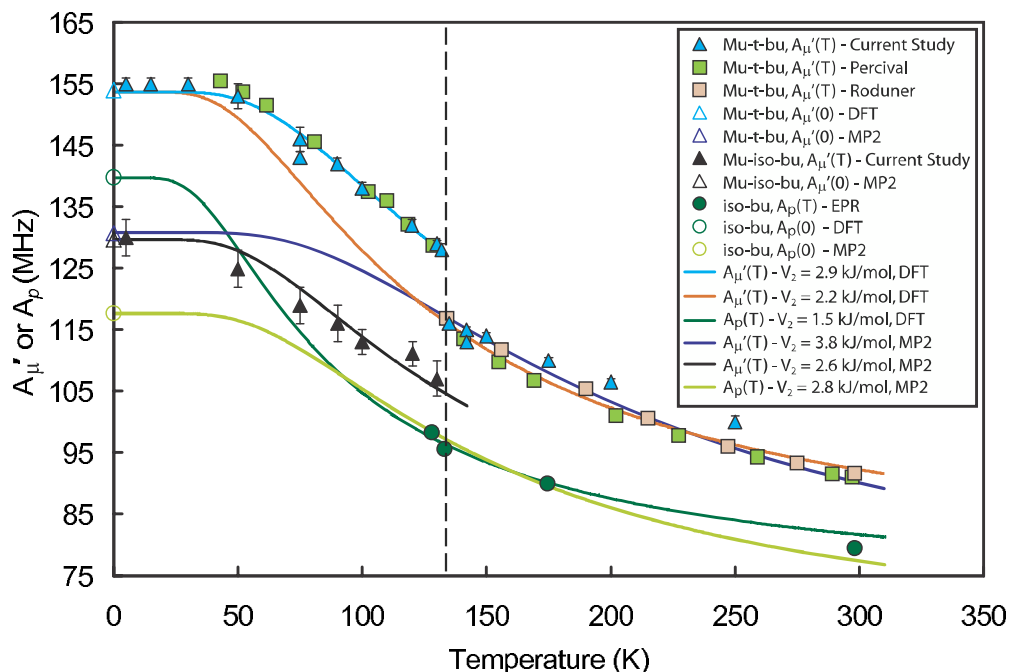


Figure 5.4: Figure 3 in paper I. Temperature dependences for the muon HFCC,  $A'_\mu(T)$ , for the Mu-t-butyl (solid cyan-blue triangles, present experiment study; shaded green squares from Ref. 44; shaded brown squares, from Ref. 65) and Mu-isobutyl (solid black triangles, present study). Error bars in the present study are meant to reflect estimates of systematic error as well. Also shown are EPR data points for the unsubstituted isobutyl radical (solid green circles and green trend lines). The colored trend lines are based on classical calculations for different torsional barriers (see legend) and several theory points are plotted on the Y-axis at 0 K, discussed in paper I. The vertical dashed line denotes the melting point of bulk isobutene, at 133 K. The sharp discontinuity in  $A'_\mu(T)$  for the muoniated t-butyl is noteworthy.

groups on the  $\alpha$ -C atom in the t-butyl radical. Thus, the muon HFCC for Mu-t-butyl is expected to start to decrease at a higher temperature with a shallower slope compared to the Mu-ethyl radical (see Ref. 14), just as is observed.

However, benchmark comparisons of the ethyl radical (Table 5.2) suggest that the above seemingly excellent agreement in comparing experiment with B3YLP results for Mu-t-butyl is likely fortuitous. Such *in vacuo* calculations cannot account for the environmental effects or host-guest interactions that are expected to be important. Experimental evidence for such effects is clearly indicated by the discontinuity or the “gap” in  $A'_\mu(T)$  for the Mu-t-butyl radical, where the muon HFCC drops sharply in the liquid phase precisely at the solid-liquid phase transition point for the isobutene matrix (vertical dashed line in Fig. 5.4), and similarly so (discussed below) for the sec-



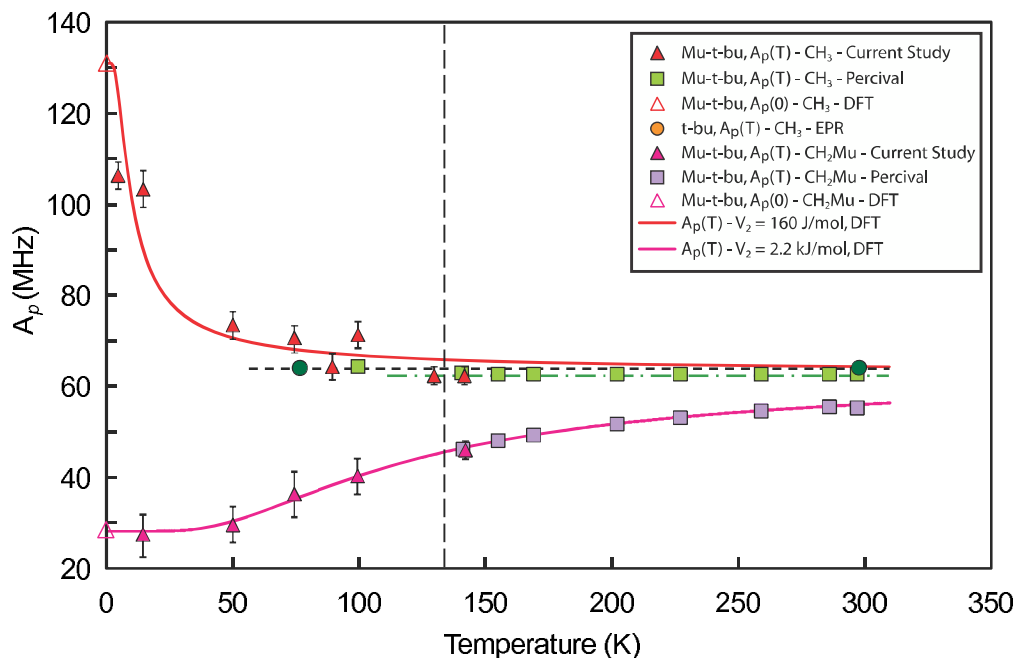


Figure 5.5: Figure 4 in paper I. Temperature dependences for the  $\beta$ -proton HFCC,  $A_p(T)$ , for the muoniated and unsubstituted t-butyl radicals. Upper data points and plots for the  $\text{CH}_3$  protons of muoniated t-butyl (present experimental data, solid magenta triangles; data from Ref. 44, shaded purple squares). The two solid green circles are representative of EPR measurements for the methyl protons of the unsubstituted radical, indicated by the temperature-independent (dashed-black) guide line, with that for the  $\mu$ SR data falling just below (dot-dashed green line). The red and magenta trend lines shown are classical calculations for the temperature dependence for very different torsional barriers (see legend), and are discussed in paper I, as are the theory points shown at 131 and 28 MHz on the Y-axis at 0 K. Note the marked increase in methyl proton HFCC at low temperature (red line). It is also noteworthy that there is no discontinuity in these proton HFCCs at the phase transition.

butyl radicals formed from 2-butene (Fig. 5.6) at the distinct melting points of cis- and trans-2-butene, respectively. Interestingly, a similar effect is not seen for the sec-butyl radical formed from 1-butene, where the temperature-dependent  $A'_\mu(T)$  is continuous at the melting point (Fig. 5.7), a common feature seen for the muoniated ethyl radical.<sup>14</sup>

The origin of this gap remains unclear, due partly to the seemingly conflicting experimental results in the temperature-dependent  $A'_\mu(T)$  data from 2-butene and 1-butene mentioned above, and also partly due to the fact that a similar discontinuity is not seen in the corresponding proton HFCCs,  $A_p(T)$ , for either Mu-t-butyl (Fig. 5.5, cognizant of both the scarcity of and scatter in the data near the melting point) or Mu-sec-butyl (Fig. 5.6). This might suggest that its origin is rooted

in differences in the torsional barriers for the same radical in different phases, as already proposed by other researchers.<sup>44</sup>

The differences in the muon HFCCs seen in the solid and liquid phases for Mu-t-butyl (and Mu-sec-butyl, discussed below) were explored by fitting to different internal rotation barriers (paper I). Such rotational barriers were determined from fitting the experimental data to a classical model and using the HFCCs reported herein. If the same muon HFCCs at 0 K in the solid and liquid phases are assumed, which is equivalent to the assumption that there is no pure environmental effect (spin-polarization and geometric alteration) affecting  $A'_\mu(T)$  and the discontinuity in the temperature-dependent HFCC is solely due to the differences in torsional barriers in different phases, one can indeed get an equally good fit to the liquid phase data (brown trend line in Fig. 5.4) as for the solid (blue trend line in Fig. 5.4). For the solid phase, we adopted a higher rotational barrier, simply because internal rotation is more hindered in the solid phase.<sup>44</sup>

Another possibility is that environmental effects do affect the electron spin density at the muon, and hence the muon HFCC is different in the two phases due to the polarized spin density or the altered molecular geometry. It becomes interesting to appreciate what would happen if we were able to “switch off” the environmental effect due to lattice interactions. We would then expect the  $A'_\mu(T)$  curve for Mu-t-butyl in the solid to be shifted well below where it is actually seen by experiment (dark blue line in Fig. 5.4), below the calculated trend from the B3LYP calculations, because these B3LYP calculations are expected to overestimate the muon HFCC near 0 K, in accordance with the benchmark comparisons of Mu-ethyl discussed earlier (Table 5.2). Thus, in Fig. 5.4, the MP2/EPR-III calculated muon HFCC of 131.1 MHz at 0 K does indeed fall well below both the experimental and the B3LYP calculated data. This reinforces the claim that the MP2/EPR-III method may be fundamentally more accurate than B3LYP for the calculation of the muon HFCCs. B3LYP calculations happen to mimic the effect of lattice interactions and fortuitously enhance the muon HFCCs below the bulk melting point.

More realistically, the two aforementioned effects that cause the discontinuity should influence the temperature-dependent HFCCs at the same time. Nevertheless, the internal rotation barrier difference in the two condensed phases is more likely to be the dominant factor, which is supported by the distinct slopes, and therefore distinct torsional barriers in the liquid and solid phases.

The proton HFCCs of the t-butyl radical (Fig. 5.5), measured both by  $\mu$ SR and EPR, were also investigated here. In the case of Mu-t-butyl, there are two sets of nonequivalent protons, the two protons of the Mu-substituted methyl group ( $\text{CH}_2\text{Mu}$ ) and the other six from the pair of unsubstituted terminal  $\text{CH}_3$  groups. The proton HFCC for the  $\text{CH}_2\text{Mu}$  group calculated at the B3LYP level of theory is in excellent agreement with the temperature-dependent  $A_p(T)$  from two perspectives: the classically calculated thermal average (magenta trend line in Fig. 5.5) and the extrapolated value at 0 K (atoms 5 and 13 in Table 5.1). This is in accordance with what we have also found for the ethyl radical. The torsional barrier determined in paper I from a fit based on the calculated HFCCs is considerably lower (1.9 kJ/mol) than that found for  $A'_\mu(T)$ , in support of the above suggestion

that the origin of the gap seen in the temperature-dependent muon HFCC may be related to different vibrational behaviors in the solid and liquid phases. As noted earlier, the trend with temperature is opposite to that for  $A'_\mu(T)$ . For the unsubstituted methyl groups, the indistinguishable  $\mu$ SR and EPR data are temperature independent up to 300 K. The B3LYP-calculated HFCC values for these freely-rotating methyl groups are also in excellent agreement with the experimental data. This fact lends further testimony to the claim advanced herein, arising from benchmark comparisons with experiment for the ethyl radical (Table 5.2), that the B3LYP method is superior to MP2 in the calculation of  $\beta$  proton HFCCs.

#### 5.4.2 Sec-butyl radicals formed from 2-butene

In contrast to the t-butyl case above and sec-butyl from 1-butene discussed below, where Mu addition places the muon in a terminal  $\text{CH}_2\text{Mu}$  group, Mu addition to cis- or trans-2-butene places it at the central methylene position in the sec-butyl radical,  $\text{CH}_3\text{--CHMu--}\dot{\text{C}}\text{H--CH}_3$ . In this case, there is only one muoniated structure possible for each 2-butene isomer, in contrast to the different products from Mu addition to both isobutene and 1-butene. The two muoniated sec-butyl radicals show a clear distinction in  $A'_\mu(T)$  for the sec-butyIs formed from trans- and cis-2-butene in the solid phase, respectively. This suggests the preservation of the parent geometries of cis- and trans-2-butene so that the radicals formed from different precursors exhibit different muon HFCCs. The muon HFCC (from the  $\text{CHMu}$  group) demonstrates a rather remarkable sensitivity to various environments, with marked discontinuities (“gaps”) in  $A'_\mu(T)$  at the melting points of cis- (134 K) and trans-2-butene (168 K) (vertical dashed lines in Fig. 5.6). Above *ca.* 150 K, the muon HFCC of the sec-butyl formed from cis- and trans-2-butene precursors merge into a single curve, demonstrating that the barriers separating local minima on the PES are mostly overcome and different conformations are easily interconvertible.

B3LYP calculations provide almost quantitative agreement with the data for the trans-2-butyl radical in the solid phase, again mimicking the effect of the lattice interactions that are believed to enhance the muon HFCC. The B3LYP-calculated value at 0 K is 145.2 MHz (Table 5.1, plotted on the Y-axis in Fig. 5.6), only a few MHz above the extrapolated experimental result of *ca.* 140 MHz. Also, a fit to the classical model for  $A'_\mu(T)$  discussed in paper I gives a reasonably good account of the data (blue trend line in Fig. 5.6), for a torsional barrier of 3.0 kJ/ mol, essentially the same good agreement as for the t-butyl radical. The fit temperature-dependent muon HFCC for the sec-butyl radical formed from cis-2-butene lies just above those for the trans one in Fig. 5.6 with a somewhat steeper fall-off, suggesting a lower internal rotation barrier about the  $\text{C}_\alpha\text{--C}_\beta$  bond. This is consistent with the theoretical predictions that the cis conformation is associated with a lower backbone torsional barrier than the trans one.

In like manner to the results for Mu-t-butyl previously discussed, the muon HFCC calculated at the MP2 level of theory (126.2 MHz) agrees well with the  $A'_\mu(T)$  fit from the liquid phase (the

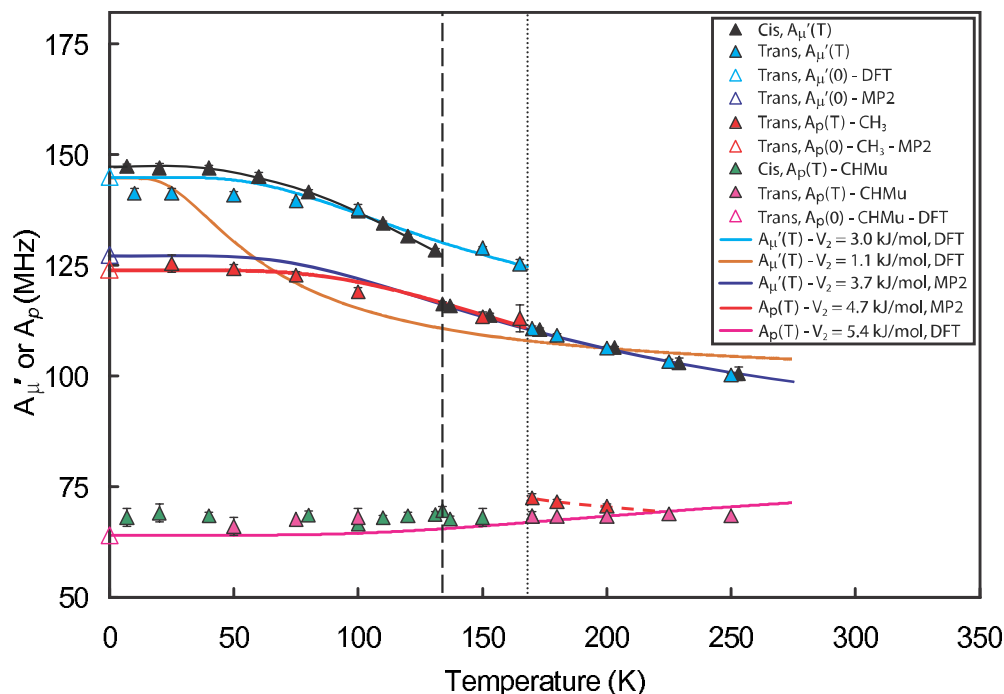


Figure 5.6: Figure 12 in paper I. Temperature dependences for the HFCCs,  $A_{\mu}'(T)$  and  $A_p(T)$ , for the sec-butyl radicals formed from cis- and trans-2-butene. The black triangles and guide line to the eye are  $A_{\mu}'(T)$  for the cis isomer, while the cyan-blue triangles and fitted trend line is for the trans isomer. Small differences seen in the muon HFCCs between cis and trans isomers in the solid phase are not seen in the liquid (the cis points have been shifted by 3 K for clarity). Noteworthy are the distinct discontinuities seen in  $A_{\mu}'(T)$  for both the Mu-sec-butyl isomers at the melting point of their parent 2-butenes (134 K for cis-2-butene, vertical dashed line) and (168 K for trans-2-butene, vertical dotted line). The red triangles and fitted red trend line are the  $\beta$ -proton HFCC for the  $\text{CH}_3$  group of the Mu-sec-butyl radical formed from trans-2-butene,  $A_{p,\text{CH}_3}(T)$ . The dramatic discontinuity seen in  $A_{p,\text{CH}_3}(T)$  is also noteworthy. The short broken-red guide line is the same proton environment in the liquid phase. The lower data points and fitted magenta trend line are the proton HFCC of the CHMu group for both the cis (green triangles) and trans (magenta) isomers, which are indistinguishable by experiment. Note the lack of any discontinuity in these CHMu proton HFCCs at the bulk melting points. A number of calculated HFCCs are shown on the Y-axis at 0 K and these, along with the fitted color trend lines, are discussed in paper I.

dark blue trend line in Fig. 5.6), well below the actual experimental data in solid phase. This is consistent with the theme advanced herein that MP2 calculations of the muon HFCCs are inherently more accurate in the absence of lattice interactions.

With regard to the remarkable gaps seen in  $A_{\mu}'(T)$  for the t-butyl and sec-butyl radicals, it is worth noting that these radicals are formed from planar precursor alkenes: iso- and 2-butenes (trans

and cis). Therefore, those molecules are expected to exhibit quite different packing patterns in the solid phase from those in the liquid phase. On the contrary, 1-butene, on average, is dominated by the non-planar gauche form with a flexible carbon skeleton. Ethylene, though planar, has reduced polarizability compared to butene isomers. Those two species should exhibit relatively less variation in different condensed phases. Thus, it is fair to speculate that the muoniated adducts formed from 1-butene and ethylene precursors are much less influenced by the phase transition at melting point. And their radical product indeed do not exhibit a gap at the melting temperature.

A remarkable feature of Fig. 5.6 is the observation of a large proton HFCC near 0 K, giving an experimental intercept of *ca.* 125 MHz for the muoniated sec-butyl formed from trans-2-butene, in almost exact agreement with the calculated proton HFCC of 124.1 MHz for an eclipsed proton of the terminal methyl group (open red triangle on the Y-axis of Fig. 5.6, atom 10 and third entry for sec-butyl (s1) in Table 5.1). What is significant here is three-fold. First, this large proton HFCC is for the  $\beta$ -atom of the terminal CH<sub>3</sub> group, which would otherwise be expected to exhibit a characteristic value around 70 MHz, of a nearly free rotor, as observed in Mu-t-butyl (Fig. 5.5), in muoniated sec-butyl formed from 1-butene (Fig. 5.7), and in the unsubstituted ethyl radical.<sup>14</sup> Perhaps, the internal rotation of this terminal methyl group about the C $_{\alpha}$ –CH<sub>3</sub> bond is coupled to the torsional mode of the carbon skeleton. Therefore, the barrier of the internal rotation about the MuHC–CH<sub>3</sub> bond is increased due to this coupling. The physical reason for this coupling might be that the muonium of the CHMuCH<sub>3</sub> group is present in the middle of the backbone chain, causing hindered rotation of the terminal methyl group about the C–C bond<sup>40</sup> and raising the overall internal rotation barrier about the C $_{\alpha}$ –CH<sub>3</sub> bond. Second, the temperature-dependent HFCC of this proton,  $A_p(T)$ , also exhibits an even more dramatic discontinuity at the bulk melting point of the trans isomer (168 K) than does  $A'_\mu(T)$ . This, to the best of our knowledge, has not heretofore been reported for any alkyl radical by either  $\mu$ SR or EPR. This discontinuity suggests that host-guest interaction are also impacting the proton HFCC here, causing a significant increase of  $A_p(T)$  in the solid phase. Moreover, this may suggest that the internal rotation about the MuHC–CH<sub>3</sub> bond is indeed coupled with the torsion about the C $_{\alpha}$ –CHMu bond, so that both the muon HFCC and the HFCC of the terminal methyl group have similar behaviors at the melting point of the trans-2-butene precursor. Third, the excellent agreement between theory and experiment seen at 0 K (as noted above) is not from B3LYP calculations, but rather from MP2 calculations. The red trend line in Fig. 5.6 based on the MP2-calculated HFCCs is in excellent agreement with the experimental data in the solid phase, though not so far removed, the B3LYP result of 134.6 MHz at 0 K is about 10 MHz higher. It is puzzling though, and likely connected with the high torsional barrier. The best agreement between theory and experiment for  $A_p(T)$  for these terminal methyl protons is from MP2 calculations, whereas, for all other proton HFCCs in this paper the best agreement is found with B3LYP calculations instead.

The good agreement between B3LYP calculations and experiment for the proton HFCCs of the muoniated butyl isomers of interest is still demonstrated by the proton HFCC for the CHMu unit

of the sec-butyl here. This is clearly shown by the data and solid-line fit in the bottom curve of Fig. 5.6. The temperature-dependent  $A_p(T)$  in paper I is also from the same classical calculation that has characterized other fits, with a 0 K value of 64.1 MHz (atom 12, fourth entry for sec-butyl (s1) in Table 5.1), in excellent agreement with the trend in the experimental data (magenta line in Fig. 5.6). As expected, the trend is again opposite to that for  $A'_\mu(T)$ . Importantly, the MP2-calculated result is 45.4 MHz here, too low. The internal rotation barrier was found to be 5.4 kJ/mol in paper I, essentially the same as that for the rotation of the terminal methyl group of the muoniated sec-butyl formed from trans-2-butene, lending support to the claim of coupling to the torsional modes of the carbon skeleton in the muoniated sec-butyl radical formed from trans-2-butene.

### 5.4.3 Sec-butyl radicals formed from 1-butene

Similar to Mu addition to isobutene that forms both t-butyl and isobutyl with relatively weak signals, two distinct isomers are possibly formed from Mu/H addition to 1-butene, the sec-butyl radical and the primary n-butyl (or 1-butyl) radical from Mu addition to the central carbon,  $\text{CH}_3\text{--CH}_2\text{--CHMu--}\dot{\text{C}}\text{H}_2$  (n1–n5 in Fig. 5.2).

Among the muoniated sec-butyl isomers possibly formed from 1-butene, the trans-like sec-butyl (s1 in Fig. 5.2) is suggested to be the primary candidate for the following reasons. First, Mu is favored to add to the gauche form of 1-butene (gauche conformation in Fig. 5.3) from the least bulky direction, directly yielding the s1 sec-butyl radical. Second, this adduct is also the most stable isomer among all eight potential radical products from 1-butene (s1, s2, s3, and n1–n5 in Fig. 5.2). Finally, the data in Fig. 5.4 exhibit a large muon HFCC around 144 MHz near 0 K due to the eclipsed C–Mu bond (dark blue solid triangles and blue trend line in Fig. 5.7) and a large proton HFCC close to 125 MHz near 0 K (red triangles and guide line in Fig. 5.7) that can only arise from an eclipsed C–H bond. This convincingly eliminates the s2 sec-butyl radical that has no C–H bond on the methylene group.

The muon HFCC for the muoniated sec-butyl radical directly from 1-butene are well accounted for by the MP2 calculated HFCC here, both at 0 K where the theory value of 139.6 MHz (atom 10, fifth entry for sec-butyl (s1) in Table 5.1) falls only a few MHz below experiment and in the fit to  $A'_\mu(T)$  from the classical model calculations (the blue trend line in Fig. 5.4). Unlike muoniated t-butyl or muoniated sec-butyl formed from 2-butene, there is no gap in  $A'_\mu(T)$  at the melting point (88 K) of 1-butene. Also, the B3LYP calculated muon HFCC of 157.2 MHz at 0 K (Table 5.1) is well above the experimental result of 144 MHz, a situation similar to that of the muoniated ethyl radical (Table 5.2). Such observations and particularly the continuous temperature dependence in the muon HFCC between the solid and liquid phases support the view expressed herein that MP2 calculation intrinsically may give a better account of the muon HFCC in the absence of solid-state interactions.

The good agreement between the experiment data and MP2 calculations is also found for the

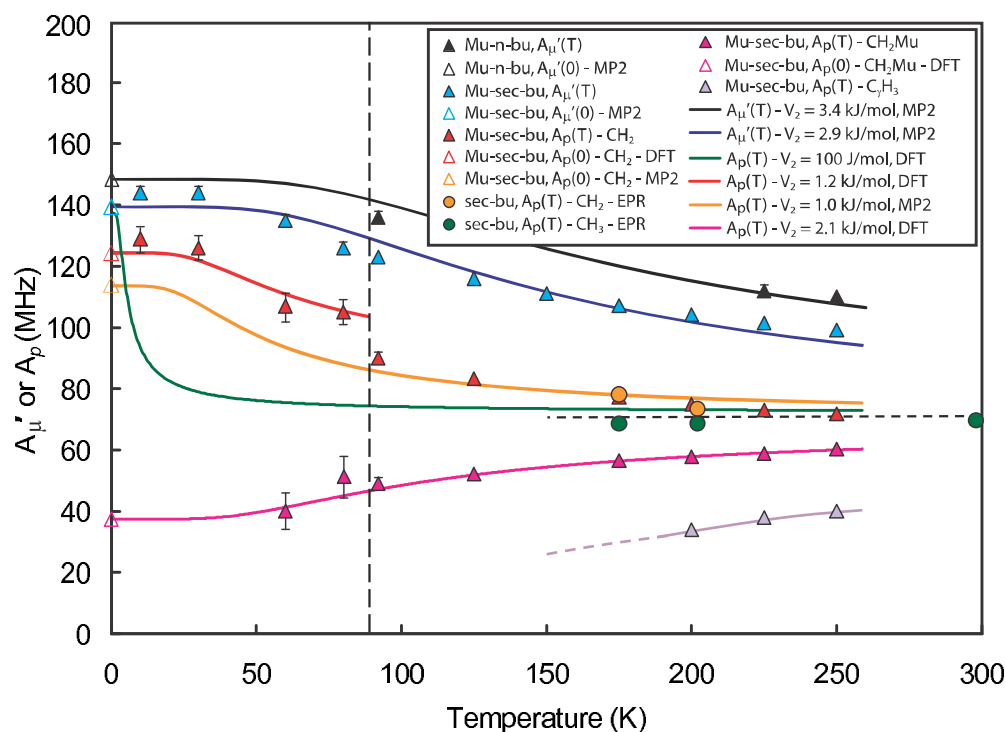


Figure 5.7: Figure 8 in Paper I. Temperature dependences for the HFCCs of reduced muon,  $A'_\mu(T)$ , and proton  $A_p(T)$ , of the sec-butyl radical formed from Mu addition to 1-butene. The cyan-blue triangles and fitted blue trend line are for the  $A'_\mu(T)$  data, while the red triangles, and red and orange trend lines are DFT- and MP2-calculated fits for  $A_{p,CH_2}(T)$  in the solid and liquid phases, respectively. The magenta triangles and fitted magenta trend line are the experimental data and DFT-calculated HFCCs for  $A_{p,CH_2Mu}(T)$ , with the mauve triangles and guide line to the data for the  $\gamma$ -protons of the terminal methyl groups,  $A_{p,\gamma-CH_3}(T)$ . The three uppermost black triangles and the black curve are liquid phase experimental data and the trend line (based on MP2 calculations) for the muoniated n-butyl formed from 1-butene, respectively. EPR data are also shown for the proton HFCCs of the unsubstituted sec-butyl radical. The solid orange circles are for the methylene protons and solid green circles for the terminal methyl group. The fitted torsional barriers from the colored trend lines are shown in the legend. Theoretical results are discussed in paper I. The vertical dashed line at 88 K marks the melting point of bulk 1-butene. It is noteworthy that there is no discontinuity at the phase transition for the temperature-dependent muon HFCCs, whereas there is a gap for the proton HFCCs of the methylene group of muoniated sec-butyl formed from 1-butene.

muon HFCC of the less-produced n-butyl radical (n3 in Fig. 5.2), as shown by the uppermost data points and the fit trend line for  $A'_\mu(T)$  in Fig. 5.7 (black triangles and the black trend line). The n3 structure was chosen for some reasons. First, its precursor is the more stable gauche 1-butene. Second, the n3 radical is designated to be the product of Mu/H addition to a gauche 1-butene from less hindered directions, making n3 the most favorable product among all n-butylys. Furthermore, it

is the only viable candidate giving a trend in  $A'_\mu(T)$  close to (but above) that for the sec-butyl radical (blue triangles and the blue trend line in Fig. 5.7). The theoretical value of 148.6 MHz at 0 K in Table 5.1, shown by the open black triangle in Fig. 5.4, is above the MP2-calculated muon HFCC of 139.6 MHz (open blue triangle in Fig. 5.7) for the more stable Mu-sec-butyl. Because the line widths were too broad from the experiment, there is no data for the muoniated n-butyl radical in the solid phase. However, the calculated trend consists well with the few data points measured in the liquid phase. In comparison, the corresponding B3LYP-calculated value of 179.4 MHz at 0 K (Table 5.1) is way above the experimental intercept.

Similar to the results for the sec-butyl formed from 2-butene, there is also a large proton HFCC for the sec-butyl from 1-butene at 0 K because of the eclipsed proton of the  $\text{CH}_2$  group, with the B3LYP calculated value of 124.2 MHz (atom 11, sixth entry for sec-butyl (s1) in Table 5.1), shown by the open red triangle in Fig. 5.7. The temperature dependence of the experimental data,  $A_p(T)$ , represented by the red line in Fig. 5.7, is drawn simply as a guide to the eye. The classical model employed to fit most of the data in that study breaks down for these methylene proton HFCCs, perhaps due to complicated and fast interconversions between the energetically close-lying isomers.

Two additional proton HFCCs were observed in the data from 1-butene: one due to the protons of the terminal  $\text{CH}_2\text{Mu}$  group (fitted magenta trend line in Fig. 5.7) and the other, much weaker, believed due to the  $\gamma$ -protons of the terminal  $\text{CH}_3$  group (the purple guide line in Fig. 5.7). The DFT calculated averaged proton HFCC of 37.4 MHz at 0 K (atoms 8 and 9 in Table 5.1) agrees excellently with the extrapolated trend for  $\text{CH}_2\text{Mu}$  so as to the fitted trend line for  $A_p(T)$  itself from these B3LYP-calculated proton HFCCs. The opposite temperature dependence to that of  $A'_\mu(T)$  is also noted. The torsional barrier found in paper I is 2.1 kJ/mol, similar to that for  $A'_\mu(T)$  of 3.0 kJ/mol. Again, the HFCCs calculated at the MP2 level of theory fall well below the experimental data. As could be expected, the high temperature (free rotation) limit of these DFT-calculated methylene proton HFCC is 68 MHz, almost identical to the value of 70 MHz measured by EPR (see Fig. 5.7). The purple guide line of Fig. 5.7 has a slope consistent with either DFT or MP2 calculations for the average  $\gamma$ -proton HFCC of *ca* -2 MHz at 0 K.

## 5.5 Overall performance of theoretical calculations

The general level of success found here with the B3LYP/EPR-III method employed in our calculations of the proton HFCCs may have its roots in the parameterization of the basis set that evolved during the development of the EPR-II and EPR-III basis sets using the spin-unrestricted Kohn-Sham equations.<sup>28</sup> The parameterization of these basis sets promotes the performance of the calculations of some molecular magnetic property, yet conceals and mixes some other important underlying physics, such as correlation effects, dynamic/vibrational effects, and environment/host-guest interaction effects. Especially for hydrogen (or muonium), the optimal core shell basis set contraction scheme for an isolated H atom HFCC can be quite different from those of hydrogen atoms



in molecules. That is, the special treatment in designing the EPR-II/EPR-III basis set by fitting to molecular computations may benefit the comparison between the calculated and experimental HFCCs, especially for those hydrogens in regular molecules with heavy nuclei. Nevertheless, this benefit may diminish or even become an obstacle when the unambiguous *in vacuo* HFCCs at 0 K are pursued.

On the other hand, all the calculations in this paper have been within the limits of the BO approximation. Such a model is usually adequate for property calculations, including HFCCs of ordinary chemical species whose nuclear masses are overwhelmingly large compared to the electron mass. However, this approximation is certainly less valid for muoniated species where the muon mass is only 206 times the electron mass.<sup>1,2,60</sup> The basic assumption of a single nuclear configuration may begin to break down. Since quantum tunneling is known to be prominent in Mu reactivity, such as in addition reactions to alkene double bonds,<sup>3</sup> there could also be muonium tunneling effects altering muon positions in the muoniated butyl radicals studied here, particularly in the solid phase. This impacts as well on the classical model for the torsional barrier adopted in paper I. In any muon containing species, there has to be some concern that the motion of the muon is not as separable from the electron motion as is the case of normal molecules with H atoms. As previously remarked, diagonal correction calculations beyond the BO approximation have been carried out for the isotopomers of the H<sub>3</sub> reaction system, with a few percent variation in the barrier heights for the Mu + H<sub>2</sub> reaction in particular.<sup>46</sup>

## 5.6 Conclusions

The HFCCs of muoniated butyl isomers formed from muonium addition to the parent alkenes (reported in paper I) have been investigated through first principles calculations. Based on comparisons with experiment, the muon adducts are believed to be (Mu-)eclipsed radicals. The equilibrium geometries of the butene precursors and Mu-radical products were established by using both B3LYP/EPR-III and MP2/EPR-III calculations, with MP2 found to be more reliable in predicting stable conformers. All calculations were carried out *in vacuo* assuming the BO approximation. To partially account for vibrational anharmonic contributions to the HFCCs in these muoniated butyl radicals, a C–Mu bond elongation scheme with a scaling factor of 1.076 was introduced to distort the equilibrium geometry, followed by the muon HFCC calculations using this modified albeit static structure.

Comparisons of the HFCCs between theory and experiment are complicated by phase transitions between solid and liquid. In the case of the muoniated t-butyl and sec-butyl radicals, formed from planar isobutene and 2-butene isomers, respectively, the temperature dependence of the muon HFCC,  $A'_\mu(T)$ , exhibits a marked discontinuity at the melting point of the surrounding alkene precursor. These discontinuities signify a large contribution to the muon HFCCs from lattice interactions in the solid phase. In these cases, the muon HFCCs appear to be best predicted by B3LYP/EPR-III

calculations. Model calculations in paper I have also established that these B3LYP calculations can account well for the  $A'_\mu(T)$  data in the liquid phase with the proviso that the muon HFCC at 0 K is intrinsically phase independent. On the other hand, MP2/EPR-III calculations yield good agreement between theory and experiment for the muon HFCC in the liquid phase, but predict the HFCC at 0 K some 20–30 MHz below the B3LYP results. In the case of sec-butyl formed from 1-butene (a non-planar precursor on average), there is no gap in  $A'_\mu(T)$  at the melting point and much better agreement in both solid and liquid phases is found from MP2 calculations, in accordance with similar comparative “benchmark” calculations of the muoniated ethyl radical.

We are persuaded that MP2/EPR-III calculations give the best “intrinsic” agreement with the muon HFCCs in the absence of appreciable guest-host interactions. The seemingly good agreement found with experiment for B3LYP/EPR-III calculations is viewed as largely fortuitous. These DFT calculations effectively mimic the effect of lattice interactions in the solid phase due to error cancellation.

The discontinuity in the muon HFCCs at the melting points is only observed for the planar parent alkenes (isobutene and 2-butenes). This observation suggests that more ordered environments in turn facilitate enlarged muon HFCCs in the solid phase. This is in contrast to the less ordered environment of 1-butene where the sec-butyl formed exhibits no such discontinuity in  $A'_\mu(T)$ . Unfortunately, establishing this appreciation from first-principles calculations would involve including the effect of radical-host interactions on the muon HFCCs, which is beyond the level of the calculations reported here.

In contrast to the muon HFCCs, the  $\beta$ -proton HFCCs are, by and large, much more accurately predicted by B3LYP/EPR-III calculations in both phases. In sec-butyl radicals from 1-butene and 2-butene, large proton HFCCs near 0 K are observed, which appear due to the eclipsed C–H bonds from the methylene protons in the 1-butene case but from the protons of the terminal methyl group in the trans-2-butene case. Classical fits to the temperature dependence discussed in paper I reveal large torsional barriers, as would be expected, in both such cases. This result for the terminal CH<sub>3</sub> group of trans-2-butyl, however, is surprising, if not remarkable. In all other examples of the proton HFCCs from (unsubstituted) terminal CH<sub>3</sub> groups, it is essentially the “free-rotor” limit that is observed both in  $\mu$ SR and EPR studies. Moreover, this particular terminal methyl group also exhibits a marked discontinuity in its temperature dependence,  $A_p(T)$ , at the melting point, even more dramatically so than for  $A'_\mu(T)$ , also suggesting that lattice-interaction influences the proton HFCCs. Here, it is MP2 calculations that give a much better account of the  $A_p(T)$  data (including at 0 K): a singular exception to the statement above that the best agreement with the experimental proton HFCC is invariably found in B3LYP calculations. Coupling of the internal rotation about the C $_{\alpha}$ –CH<sub>3</sub> bond with the carbon backbone torsion in the sec-butyl radical may enhance the barrier to the C $_{\alpha}$ –CH<sub>3</sub> internal rotation and possibly explain the better agreement found with MP2 calculations.

There is an important caveat in that the BO approximation assumed throughout our calculations

carried out *in vacuo*. It is within this framework that the conclusions stated above of intrinsically better agreement found from MP2/EPR-III calculations for the muon HFCCs but B3LYP/EPR-III calculations for the proton HFCCs have to be judged. Part of this caveat is most likely rooted in the role played by Mu tunneling in the measurements reported for the muoniated radicals in paper I. Such tunneling effects were not accounted for in the present calculations. Nevertheless, the level of agreement that has been discussed in the present paper is not noticeably better for  $A_p(T)$  than for  $A'_\mu(T)$ , suggesting that the smaller mass ratio between the muon and the electron is likely of little consequence.

# Bibliography

- [1] E. Roduner. Polarized positive muons probing free radicals: a variant of magnetic resonance. *Chem. Soc. Rev.*, 22:337–346, 1993.
- [2] E. Roduner. Muon spin resonance-a variant of magnetic resonance. *Appl. Mag. Res.*, 13:1–14, 1997.
- [3] D. M. Garner, D. G. Fleming, D. J. Arseneau, M. Senba, I. D. Reid, and J. Mikula. Muonium addition reactions in the gas phase: quantum tunnelling in  $\text{Mu}+\text{C}_2\text{H}_4$  and  $\text{Mu}+\text{C}_2\text{D}_4$ . *J. Chem. Phys.*, 93:1732–1740, 1990.
- [4] K. Ghandi, M. D. Bridges, D. J. Arseneau, and D. G. Fleming. Muonium formation as a probe of radiation chemistry in sub- and supercritical carbon dioxide. *J. Phys. Chem. A*, 108:11613–11625, 2004.
- [5] J. J. Pan, D. J. Arseneau, M. Senba, D. M. Garner, and D. G. Fleming. Termolecular kinetics for the  $\text{Mu}+\text{CO}+\text{M}$  recombination reaction: A unique test of quantum rate theory. *J. Chem. Phys.*, 125:014307–014319, 2006.
- [6] E. Roduner, P. W. Percival, D. G. Fleming, J. Hochmann, and H. Fischer. Muonium-substituted transient radicals observed by muon spin rotation. *Chem. Phys. Lett.*, 57:37–40, 1978.
- [7] V. S. Oganessian, A. N. Cammidge, G. A. Hopkins, F. M. Cotterill, I. D. Reid, and U. A. Jayasooriya. Muon spin rotation studies of enediynes. *J. Phys. Chem. A*, 108:1860–1866, 2004.
- [8] F. L. Pratt, S. J. Blundell, Th. Jestädt, B. W. Lovett, R. M. Macrae, and W. Hayes. Muon radical states in some electron donor and acceptor molecules. *Magn. Reson. Chem.*, 38:S27–S32, 2000.
- [9] I. McKenzie, B. Addison-Jones, J. C. Brodovitch, K. Ghandi, S. Kecman, and P. W. Percival. Detection of the muoniated methyl radical. *J. Phys. Chem. A*, 106:7083–7085, 2002.
- [10] R. M. Macrae and I. Carmichael. Comparative theoretical study of Mu addition to the C=O and C=S bonds. *Physica B*, 326:81–84, 2003.

- [11] P. W. Percival, J. C. Brodovitch, K. Ghandi, B. M. McCollum, and I. McKenzie. Organic free radicals in superheated water studied by muon spin spectroscopy. *J. Am. Chem. Soc.*, 127:13714–13719, 2005.
- [12] K. Ghandi, F. E. Zahariev, and Y. A. Wang. Theoretical studies of alkyl radicals in the NaY and HY zeolites. *J. Phys. Chem. A*, 109:7242–7250, 2005.
- [13] D. G. Fleming, M. Y. Shelley, D. J. Arseneau, M. Senba, and J. J. Pan. Hyperfine and host-guest interactions of the Mu-cyclohexadienyl radical in NaY zeolite. *J. Phys. Chem. B*, 106:6395–6407, 2002.
- [14] M. D. Bridges, D. J. Arseneau, D. G. Fleming, and K. Ghandi. Hyperfine interaction and molecular motion of the Mu-ethyl radical in faujasites: NaY, HY, and USY. *J. Phys. Chem. C*, 111:9779–9793, 2007.
- [15] D. G. Fleming, M. D. Bridges, D. J. Arseneau, Y. K. Chen, and Y. A. Wang. Isotope effects and hyperfine coupling constants of muoniated butenes in condensed phases. To be submitted.
- [16] W. Meyer. Calculation of Fermi contact hyperfine splitting for small atoms and molecules. *J. Chem. Phys.*, 51:5149–5162, 1969.
- [17] I. Carmichael. Ab initio quadratic configuration interaction calculation of the isotopic hyperfine coupling constants in the ethyl radical. *J. Phys. Chem.*, 95:6198–6201, 1991.
- [18] B. Fernandez, P. Jørgensen, J. Byberg, J. Olsen, T. Helgaker, and H. J. Aa. Jensen. Spin polarization in restricted electronic structure theory: Multiconfiguration self-consistent-field calculations of hyperfine coupling constants. *J. Chem. Phys.*, 97:3412–3419, 1992.
- [19] S. A. Perera, L. M. Salemi, and R. J. Bartlett. Hyperfine coupling constants of organic radicals. *J. Chem. Phys.*, 106(10):4061–4066, 1997.
- [20] N. D. K. Petraco, S. S. Wesolowski, M. L. Leininger, and H. F. Schaefer III. Coupled-cluster studies of the hyperfine splitting constants of the thioformyl radical. *J. Chem. Phys.*, 112:6245–6254, 2000.
- [21] H. Y. Xiao, Y. J. Liu, W. H. Fang, R. Z. Liu, and M. Shiotani. Hyperfine coupling constants of fluorinated benzene radical cations: A DFT B3LYP and MP2 study. *J. Theo. Comput. Chem.*, 7:879–887, 2008.
- [22] Y. J. Liu and M. B. Huang. Hyperfine structure of some hydrocarbon radical cations: a B3LYP and MP2 study. *J. Mol. Struct. (Theochem)*, 536:133–142, 2001.
- [23] L. Hermosilla, P. Calle, J. M. Garcia de la Vega, and C. Sieiro. Density functional theory predictions of isotopic hyperfine coupling constants. *J. Phys. Chem. A*, 109:1114–1124, 2005.

- [24] M. Kaupp, M. Bühl, and V. G. Malkin. *Calculation of NMR and EPR Parameters*. Wiley-VCH Verlag GmbH & Co. KGaA, 2004.
- [25] M. Munzarová and M. Kaupp. A critical validation of density functional and coupled-cluster approaches for the calculation of EPR hyperfine coupling constants in transition metal complexes. *J. Phys. Chem. A*, 103:9966–9983, 1999.
- [26] J. W. Gault, L. A. Eriksson, and L. Radom. Assessment of procedures for calculating radical hyperfine structures. *J. Phys. Chem. A*, 101:1352–1359, 1997.
- [27] R. Improta and V. Barone. Interplay of electronic, environmental, and vibrational effects in determining the hyperfine coupling constants of organic free radicals. *Chem. Rev.*, 104:1231–1253, 2004.
- [28] V. Barone. Structure, magnetic properties and reactivities of open-shell species from density functional and self-consistent hybrid methods. In D. P. Chong, editor, *Recent Advances in density functional methods*, chapter 8, pages 287–334. World scientific publ. Co., Singapore, 1996.
- [29] J. Hrušák and S. Iwata. The vibrational spectrum of  $\text{H}_2\text{O}_2^+$  radical cation: an illustration of symmetry breaking. *J. Chem. Phys.*, 106:4877–4888, 1997.
- [30] C. J. Parkinson, P. M. Mayer, and L. Radom. Cyanovinyl radical an illustration of the poor performance of unrestricted perturbation theory and density functional theory procedures in calculating radical stabilization energies. *Theor. Chem. Acc.*, 102:92–96, 1996.
- [31] M. W. Wong and L. Radom. Radical addition to alkenes: an assessment of theoretical procedures. *J. Phys. Chem.*, 99:8582–8588, 1995.
- [32] E. F. C. Byrd, C. D. Sherrill, and M. Head-Gordon. The theoretical prediction of molecular radical species: a systematic study of equilibrium geometries and harmonic vibrational frequencies. *J. Phys. Chem. A*, 105:9736, 2001.
- [33] R. A. King, T. D. Crawford, J. F. Stanton, and III H. F. Schaefer. Conformations of [10]annulene: more bad news for density functional theory and second-order perturbation theory. *J. Am. Chem. Soc.*, 121:10788–10793, 1999.
- [34] A. Karpfen, C. H. Choi, and M. Kertesz. Single-bond torsional potentials in conjugated systems: a comparison of ab initio and density functional results. *J. Phys. Chem. A*, 101:7426–7433, 1997.
- [35] P. M. Viruela, R. Viruela, E. Ortí, and J. L. Brédas. Geometric structure and torsional potential of biisothianaphthene. a comparative DFT and ab initio study. *J. Am. Chem. Soc.*, 119:1360–1369, 1997.

- [36] J. C. Sancho-García and A. Karpfen. Conformational analysis of 2,2'-bifuran: correlated high-level ab initio and DFT results. *Theor. Chem. Acc.*, 115:427–433, 2006.
- [37] Y. Zhao and D. G. Truhlar. Density functionals for noncovalent interaction energies of biological importance. *J. Chem. Theory Comput.*, 3:289–300, 2007.
- [38] H. U. Suter and T.-K. Ha. A theoretical study on the internal rotation and hyperfine structures of the ethyl radical ( $\text{CH}_3\text{-CH}_2$ ). *Chem. Phys.*, 154:227–236, 1991.
- [39] P. M. Johnson and T. J. Sears. Vibrational effects on the torsional motion of ethyl radical. *J. Chem. Phys.*, 111:9222–9226, 1999.
- [40] T. A. Claxton and A. M. Graham. A chemical interpretation of vibrationally induced barriers to hindered internal rotation. *J. Chem. Soc., Faraday Trans. 2*, 83:2307–2317, 1987.
- [41] T. A. Claxton and Alison M. Graham. Ab initio study of propyl radicals. *J. Chem. Soc., Faraday Trans. 2*, 84:121–134, 1988.
- [42] E. Langella, R. Improta, and V. Barone. Conformational and spectroscopic analysis of the tyrosyl radical dipeptide analogue in the gas phase and in aqueous solution by a density functional/continuum solvent model. *J. Am. Chem. Soc.*, 124:11531–11540, 2002.
- [43] D. Vujošević, H. Dilger, I. McKenzie, A. Martyniak, R. Scheuermann, and E. Roduner. Local ordering in liquids: solvent effects on the hyperfine couplings of the cyclohexadienyl radical. *J. Phys. Chem. B*, 111:199–208, 2007.
- [44] P. W. Percival, J. C. Brodovitch, S. K. Leung, D. Yu, and S. F. J. Cox. Intramolecular motion in the tert-butyl radical as studied by muon spin rotation and level-crossing spectroscopy. *Chem. Phys.*, 127:137–147, 1988.
- [45] C. Heller and H. M. McConnell. radiation damage in organic crystals. ii electron spin resonance of  $(\text{CO}_2\text{H})\text{CH}_2\text{CH}(\text{CO}_2\text{H})$  in  $\beta$ -succinic acid. *J. Chem. Phys.*, 32:1535, 1960.
- [46] S. L. Mielke, D. W. Schwenke, and K. A. Peterson. Benchmark calculations of the complete configuration-interaction limit of Born-Oppenheimer diagonal corrections to the saddle points of isotopomers of the  $\text{H}+\text{H}_2$  reaction. *J. Chem. Phys.*, 122:224313, 2005.
- [47] C. Lee, W. Yang, and R. G. Parr. Development of the Colle-Salvetti correlation-energy formula into a functional of the electron density. *Phys. Rev. B*, 37:785–789, 1988.
- [48] A. D. Becke. Density functional thermochemistry. III. The role of exact exchange. *J. Chem. Phys.*, 98:5648–5672, 1993.

- [49] M. J. Frisch, G. W. Trucks, H. B. Schlegel, G. E. Scuseria, M. A. Robb, J. R. Cheeseman, Montgomery, Jr., J. A., T. Vreven, K. N. Kudin, J. C. Burant, J. M. Millam, S. S. Iyengar, J. Tomasi, V. Barone, B. Mennucci, M. Cossi, G. Scalmani, N. Rega, G. A. Petersson, H. Nakatsuji, M. Hada, M. Ehara, K. Toyota, R. Fukuda, J. Hasegawa, M. Ishida, T. Nakajima, Y. Honda, O. Kitao, H. Nakai, M. Klene, X. Li, J. E. Knox, H. P. Hratchian, J. B. Cross, V. Bakken, C. Adamo, J. Jaramillo, R. Gomperts, R. E. Stratmann, O. Yazyev, A. J. Austin, R. Cammi, C. Pomelli, J. W. Ochterski, P. Y. Ayala, K. Morokuma, G. A. Voth, P. Salvador, J. J. Dannenberg, V. G. Zakrzewski, S. Dapprich, A. D. Daniels, M. C. Strain, O. Farkas, D. K. Malick, A. D. Rabuck, K. Raghavachari, J. B. Foresman, J. V. Ortiz, Q. Cui, A. G. Baboul, S. Clifford, J. Cioslowski, B. B. Stefanov, G. Liu, A. Liashenko, P. Piskorz, I. Komaromi, R. L. Martin, D. J. Fox, T. Keith, M. A. Al-Laham, C. Y. Peng, A. Nanayakkara, M. Challacombe, P. M. W. Gill, B. Johnson, W. Chen, M. W. Wong, C. Gonzalez, and J. A. Pople. *Gaussian 03*. Gaussian, Inc., Wallingford, CT, 2004.
- [50] S. L. Thomas and I. Carmichael. Hyperfine interactions in muonium-containing radicals. *Physica B*, 374-375:290–294, 2006.
- [51] B. Webster and D. Buttar. Vibrational behaviour of the carbonmuonium bond in the muonated ethyl radical. *J. Chem. Soc. Faraday Trans.*, 92:2331–2334, 1996.
- [52] T. A. Claxton, A. M. Graham, S. F. J. Cox, D. M. Maric, P. F. Meier, and S. Vogel. Vibrationally averaged spin densities on muons and protons in the hydroxyl and ethyl radicals. *Hyperfine Interactions*, 65:913–926, 1991.
- [53] V. Barone. Anharmonic vibrational properties by a fully automated second-order perturbative approach. *J. Chem. Phys.*, 122:014108–014116, 2005.
- [54] S. Bell, B. R. Drew, G. A. Guirgis, and J. R. Durig. The far infrared spectrum, ab initio calculations and conformational energy differences of 1-butene. *J. Mol. Struct.*, 553:199–219, 2000.
- [55] S. Kondo, E. Hirota, and Y. Morino. Microwave spectrum and rotational isomerism in 1-butene. *J. Mol. Spectrosc.*, 28:471–489, 1968.
- [56] J. R. Durig and D. A. C. Compton. Spectroscopic and thermodynamic study of the conformational properties and torsional potential functions of 1-butene. *J. Phys. Chem.*, 84:773–781, 1980.
- [57] F. Wu, X. Chen, X. Shan, S. X. Tian, Z. Li, and K. Xu. Conformational stability of 1-butene: An electron momentum spectroscopy investigation. *J. Phys. Chem. A*, 112:4360–4366, 2008.



- [58] V. Barone, C. Adamo, A. Grand, Y. Brunel, M. Fontecave, and R. Subra. Conformational behavior and magnetic properties of organic radicals derived from amino acid residues. The dipeptide analog of glycine radical. *J. Am. Chem. Soc.*, 117:1083, 1995.
- [59] K. N. Houk, D. C. Spellmeyer M. N. Paddon-Row, N. G. Rondan, and S. Nagase. Theoretical transition structure for radical additions to alkenes. *J. Org. Chem.*, 51:2874–2879, 1986.
- [60] M. C. Böhm, R. Ramirez, and J. Schulte. Finite-temperature properties of the muonium substituted ethyl radical  $\text{CH}_2\text{MuCH}_2$ : nuclear degrees of freedom and hyperfine splitting constants. *Mol. Phys.*, 103:2407–2436, 2005.
- [61] J. Lounila, R. Wasser, and P. Diehl. Effects of anharmonic vibrations on molecular properties. *Mol. Phys.*, 62:19–31, 1987.
- [62] Y. Morino, K. Kuchitsu, and T. Oka. Internuclear distance parameters. *J. Chem. Phys.*, 36:1108–1109, 1962.
- [63] D. Yu. *Muonium Kinetics and Intramolecular Motion of Muonium-substituted Free Radicals*. PhD thesis, Department of Chemistry, Simon Fraser University, Canada, 1990.
- [64] D. M. Chipman. Theoretical study of hyperfine coupling constants in ethyl radical. *J. Chem. Phys.*, 94(10):6632–6637, 1991.
- [65] E. Roduner, W. Strub, P. Burkhard, J. Hochmann, P. W. Percival, H. Fischer, M. Ramos, and B. C. Webster. Muonium substituted organic free-radicals in liquids—muon electron hyperfine coupling-constants of alkyl and allyl radicals. *Chem. Phys.*, 67:275–285, 1982.
- [66] J. Pacansky and M. Yoshimine. Theoretical studies on the barriers for internal rotation of the methyl groups in the tert-butyl radical. *J. Phys. Chem.*, 90:1980–1983, 1986.
- [67] M. Yoshimine and J. Pacansky. Theoretical studies on the structure of isobutane and the tertiary-butyl radical. *J. Chem. Phys.*, 74:5168–5173, 1981.

## Chapter 6

# First-principles Studies of the Torsional Potential Energy Surface of the Sec-Butyl Radical<sup>5</sup>

### 6.1 Introduction

Numerous torsional potential energy surfaces (PES) of many chemical species have been investigated to gain key information for molecular thermodynamic state functions. It is also of theoretical interest to compare the computed PES with available experimental data to develop and improve computational methods. Even molecules as simple as ethane have attracted the attention of many theoretical researchers to investigate the physical nature of their torsional barriers. The rotational barriers of ethane and its congeners were mainly attributed to hyperconjugation interactions, challenging the conventional wisdom in many textbooks on the importance of steric repulsive interactions.<sup>1</sup> However, based on generalized valence bond theory, a recent theoretical study decomposed the torsional barrier of ethane adiabatically into steric repulsion, hyperconjugation, and several other insignificant contributions and identified the steric repulsion to be the dominant factor in the stabilization of staggered conformation.<sup>2</sup>

Without any ambiguity as to the physical origin of the torsional barriers, the conjugation effect has been widely accepted to be the leading cause of the torsional barrier in conjugated systems. However, this orthodox point of view does not promise good agreement between experiment and theory in many conformational studies. The torsional energy profile of 2,2'-bifuran was calculated using various Hamiltonians, and density functional theory (DFT) methods were found inappropriate to study the conformation of this system.<sup>3</sup>

In addition, the basis set also plays a significant role. When the PES of biphenyl was studied using several wave function theory (WFT) methods, the quality of the basis sets was found to be more important than the Hamiltonians employed.<sup>4,5</sup> Besides the separate effects of the individual Hamiltonian and the basis set, a delicate balance between the selection of the Hamiltonian and the basis set can be critical to achieve high accuracy in the calculations of these (semi)rigid molecules.

---

<sup>5</sup>A version of this chapter will be submitted for publication. Chen, Y. K.; Fleming, D. G. and Wang, Y. A. First-principles Studies of Torsional Potential Energy Surface of the sec-Butyl Radical.

Past theoretical study of the torsion barriers of biisothianaphthene showed that accurate, balanced description of both conjugation and steric repulsion between non-vicinal hydrogens can only be achieved after adopting high-level Hamiltonians and large basis sets.<sup>6</sup> Being aware of the limitations of popular theoretical tools, we must perform extensive studies to avoid false prediction even for small molecules based on calculations using a single Hamiltonian with a single basis set.

Other than those well-defined molecules mentioned above, it becomes much more challenging to investigate the conformation of some transient species, such as radicals, whose PES are usually too flat for many popular computational methods to attain a faithful description. For example, DFT methods with the generalized gradient approximation (GGA) outperformed local MP2 method in predicting the dissociation energies of haloethyl radicals.<sup>7</sup> On the other hand, large spin contamination was found in DFT calculations of OOB<sub>r</sub> and OOCl, contradicting the popular belief that DFT methods suffer less spin contamination than WFT methods.

Sometimes, many different methods may perform poorly in a single case. In a conformational study of annulene molecules, widely used MP2 and DFT methods were both found to fail one way or another.<sup>8</sup> All such uncertainties and controversies indicate that popular theoretical methods are still unable to work well universally for conformational studies of molecular systems. Therefore, a convincing conclusion of conformation analysis requires systematic studies.

In this work, the torsional PES of sec-butyl was studied theoretically to systematically assess the performance of some widely used theoretical methods. The major experimental data available are hyperfine coupling constants (HFCCs) of muoniated sec-butyl radicals formed from muonium addition to various 2-butene isomers.<sup>9</sup> Since the electronic Hamiltonian only parametrically depends on nuclear positions and has nothing to do with the nuclear mass, all sec-butyl isotopomers share the same PES within the Born-Oppenheimer (BO) approximation. Thus, a conformational study within the BO framework is equally fundamental for both regular and muoniated sec-butyl radicals. Based on the analysis of muon spin resonance spectral data, the muoniated sec-butyl radical formed from cis-2-butene had a large HFCC value on the muon at 0 K and this value was different from the muon HFCC from muonium addition to trans-2-butene.<sup>9</sup> Further temperature-dependent HFCC study also supported the existence of two distinct muoniated sec-butyl radicals, both with high HFCCs on the muon.<sup>9</sup> However, calculations using the popular hybrid-DFT B3LYP Hamiltonian, which had been believed to accurately predict HFCCs of small organic molecules,<sup>10</sup> only located two equilibrium structures on the ground-state torsional PES (Fig. 6.1). One of the two corresponded to the radical formed from muonium addition to trans-2-butene (Fig. 6.1a), and the other was a gauche conformation (Fig. 6.1b) whose HFCC on the muon was only about one third of the experimental value. The absence of experimentally observed muoniated sec-butyl formed from cis-2-butene (Fig. 6.1c) from B3LYP calculations motivated us to apply extensive theoretical calculations to study the torsional PES of the sec-butyl radical. Besides providing static conformations, the PES information can give access to dynamic (vibrational) and thermodynamic corrections, which are valuable in predicting the temperature dependence of the HFCCs.

Some other experimental results from homolysis of butyl radicals are also available. Thermodynamic and kinetic studies were carried out to decompose the sec-butyl radical into propene and methyl radical,<sup>11</sup> but detailed conformational information of the parent sec-butyl radical could not be derived because the high temperature of the homolysis experiment averaged out all conformational fingerprints. Consequently, theoretical calculations have to be performed to appreciate possible conformations of the sec-butyl radical. To the best of our knowledge, the first *ab-initio* study on the conformations of the sec-butyl radical can be traced back to the pioneer Hartree Fock (HF) calculations in the 1980's,<sup>12</sup> but without taking into account correlation. Therefore, a systematic study of the sec-butyl radical with different correlated Hamiltonians and basis sets is carried out in this work.

## 6.2 Computational details

All calculations in this study were performed using the GAUSSIAN 03 package within the BO approximation.<sup>13</sup> Different first-principles electronic Hamiltonians, including spin-unrestricted HF, MP2, CCSD, CISD, QCISD, CCSD(T) and a variety of Kohn-Sham DFT methods, were utilized. Wave functions were expanded in terms of atomic-centered one-electron basis functions, including the Pople-type basis sets: 6-31g(d), 6-311++g(d, p), and 6-311++g(3df, 2pd)<sup>14,15</sup> and Dunning's correlation consistent basis sets: cc-pVDZ, cc-pVTZ, and augmented cc-pVDZ (aug-cc-pVDZ), and aug-cc-pVTZ.<sup>16</sup> In DFT calculations, numerical integration for two-electron integrals was used with the grid quality of 75 radial shells and 302 angular points per shell unless specified otherwise.

Geometric optimization was carried out using the Z-matrix coordinate system. Completely relaxed torsional PES's of the sec-butyl radical as a function of the dihedral angle ( $\theta$ ) of the four backbone carbon atoms were plotted for selected combinations of electronic Hamiltonians and basis sets (Fig. 6.2). The dihedral angle was scanned from 0° to 180° with a step size of 5°, while all other degrees of freedom were allowed to fully relax. The PES profile for  $\theta$  from 180° to 360° is essentially the mirror image of that from 0° to 180°, if certain symmetry constraints are applied at proper points. However, for computational simplicity and uniformity, the symmetry of the molecule was not constrained unless noted otherwise.

Besides the torsional PES, optimized conformations (Fig. 6.1) were calculated at both MP2 and B3LYP levels. The diagonalized Hessian matrices were also computed to identify the nature of the stationary structures and to include the zero-point vibrational corrections.

## 6.3 Results and discussions

Because simple alkyl radicals have a localized unpaired electron at the radical center, single-reference spin-unrestricted methods should be adequate to calculate their properties and were used in this study. Spin contamination, which was believed to be responsible for the failure of UMP2 in

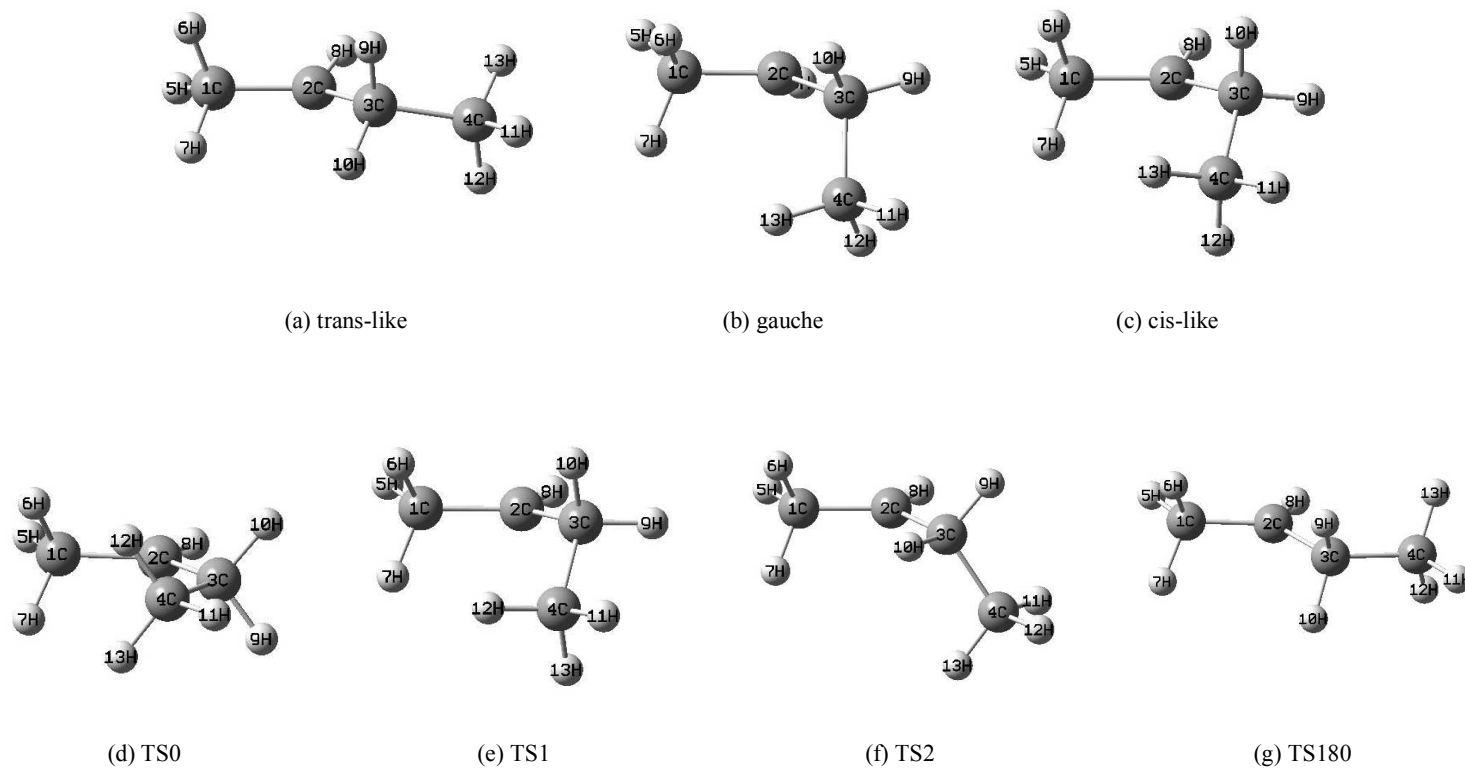


Figure 6.1: Optimized structures of the stationary points on the torsional potential energy surface of the sec-butyl radical.

determining the reaction barrier of radical formation reactions,<sup>17,18</sup> was found to be very small in all the spin-unrestricted calculations performed here.

The torsional PES profiles predicted by different Hamiltonians are shown in Figure 6.2a, where their lowest points are taken to be the common reference (zero) point to simplify comparisons. The cc-pVDZ basis set was employed for geometry optimizations because of its reliability for this purpose.<sup>3</sup> The torsional energy curve obtained from the HF calculation flies above all other PES profiles, whereas the PES profiles from CCSD, B3LYP<sup>19,20</sup> and MP2 calculations are interwoven near the bottom. Lying in the middle is the potential energy curve obtained from the CISD calculation. Compared with all other WFT methods, the PES calculated at the B3LYP level drops at a slower rate with respect to the dihedral angle increment. The B3LYP calculation predicts only two stable conformations for  $\theta < 180^\circ$ , whereas all other WFT methods show three stable conformations (Fig. 6.2a). All methods uniformly found the most stable conformation to be a trans-like structure at  $\theta \approx 170^\circ$  (Fig. 6.1a). A stable gauche conformation (Fig. 6.1b) is also universally visible at  $\theta \approx 80^\circ$ , lying about 0.3~0.6 kcal/mol above the trans-like ground state.

The existence of the stable cis-like conformation (Fig. 6.1c) is worth elaboration. All the WFT methods predict the existence of a stable structure on a relatively flat segment of the PES around  $\theta = 50^\circ$ , whereas the B3LYP method predicts an accelerated energy drop along with an increased dihedral angle in the same range. This cis-like conformation was recognized as one of three stable conformations in an early HF calculation, the very first theoretical conformational study of the sec-butyl radical.<sup>12</sup> Because the correlation effect, important for describing dispersion interaction for a correct prediction of stable conformations, is omitted in HF calculation, methods taking account of the correlation effect must be employed to reassess the conformations. Both DFT and WFT methods can incorporate the correlation, but they predict different torsional PES profiles for the sec-butyl radical (Fig. 6.2a). As verified by an electron paramagnetic resonance (EPR) experiment, the cis-like conformation does exist, so that the HFCC on the  $\beta$ -muon could be measured without ambiguity.<sup>9</sup> In this regard, WFT methods outperform B3LYP.

When  $\theta = 0^\circ$ , the HF calculation predicts that the global maximum TS0 (Fig. 6.1d), the transition state connecting the cis-like conformation with its mirror image, is 2.3 kcal/mol higher (less stable) than the trans-like global minimum. This further indicates that the HF method predicts stronger bulky/steric repulsion (by about 0.4 kcal/mol) between the two terminal methyl groups of the sec-butyl radical than any other correlated calculations because of the neglect of the correlation effect. The transition state (TS1) between the cis-like and gauche conformations (Fig. 6.1e) is located near  $\theta = 55^\circ - 60^\circ$  with a very small barrier (much less than 0.1 kcal/mol) from the cis-like structure. The transition state TS2 is well separated from the trans-like and gauche conformations (Fig. 6.1f), lying as high as 0.5 kcal/mol (from WFT calculations) to as low as 0.1 kcal/mol (from the B3LYP calculation) from the gauche conformation. At  $\theta = 180^\circ$ , since the symmetry was not constrained during the relaxed PES scan, the actual torsional barrier between the trans-like conformation and its mirror image could not be obtained directly from the profile. Instead,  $C_s$  symmetry

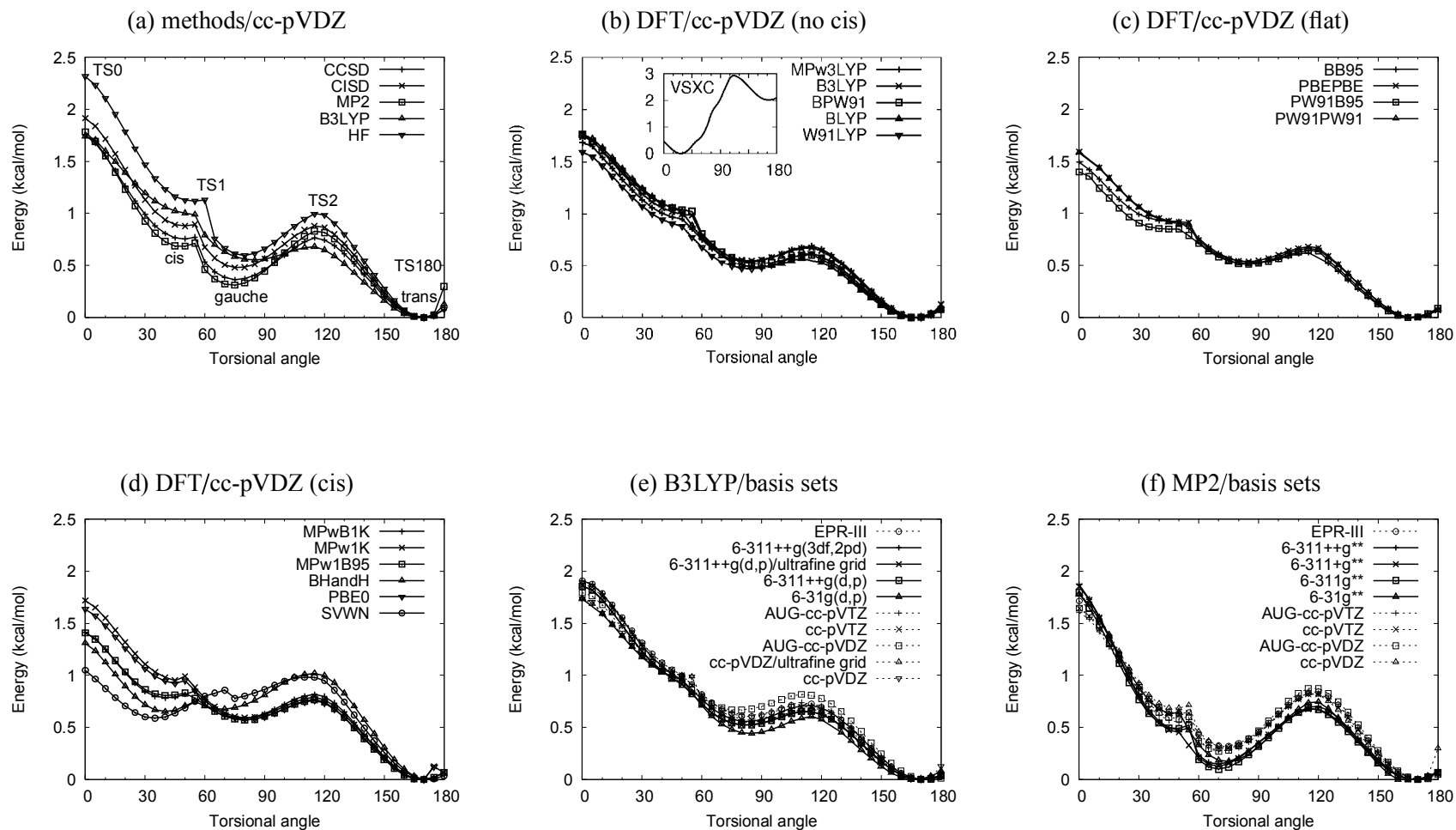


Figure 6.2: Torsional energy profiles of the sec-butyl radical predicted: (a) from different theoretical methods with the cc-pVDZ basis set; (b) from DFT methods with the cc-pVDZ basis set, showing no cis-like conformation; (c) from DFT methods with the cc-pVDZ basis set, showing relative flat curves around  $\theta = 55^\circ$ ; (d) from DFT methods with the cc-pVDZ basis set, showing the cis-like conformation; (e) from B3LYP methods with different basis sets; (f) from MP2 methods with different basis sets.

was used to help us estimate the torsional barrier at  $\theta = 180^\circ$ : 0.13 and 0.29 kcal/mol at B3LYP/cc-pVDZ and MP2/cc-pVDZ, respectively. For the sake of simplicity, no further effort was invested to calculate this barrier height.

Besides the comparison between representative WFT and B3LYP methods, DFT methods employing different density functionals of various forms were also examined with the cc-pVDZ basis set. Based on the overall shapes of the calculated PES profiles between  $\theta = 40^\circ - 60^\circ$ , where the presence of the cis-like conformation is of interest, DFT methods are classified into three categories (Fig. 6.2b-d).

Figure 6.2b shows some popular hybrid and GGA functionals which predict no cis-like minimum within the range of interest. The inset reveals the erratically different PES profile obtained from the VSXC calculation. The VSXC functional fails to describe the potential energy maximum at  $\theta = 0^\circ$  where the overall steric repulsion between the two terminal methyl groups becomes the greatest. The other functionals in this group yield very similar potential energy profiles with only two stable (gauche and trans-like) conformations.

Figure 6.2c shows the second group of functionals that predict relatively flat curves around  $\theta = 55^\circ$  before the accelerated energy drop to the gauche conformation. Some of these functionals contain components like PW91 exchange or B95 correlation functionals that were designed to characterize weak interactions.<sup>21-23</sup> These may partly compensate the weakness of those functionals in Figure 6.2b for the flat segment around  $\theta = 55^\circ$ .

Figure 6.2d shows the last group of functionals that produce a shallow potential well around  $\theta = 40^\circ$ , similar to those obtained from MP2 and other WFT calculations (Fig. 6.2a). However, it is well known that the SVWN functional, as any other functionals of local density approximation (LDA), should not be fully trusted unless the electron density only undergoes small variation in space. Isolated molecular systems, however, usually exhibit large density gradients especially around the nuclei and their electronic structure cannot be well predicted by the LDA. Just like this case, the SVWN calculation predicts a distinct PES curve, very different from the other more reasonable ones. This indicates that SVWN fails to capture non-local exchange and correlation effects. Different from what it is usually referred to, BHandH, as implemented in Gaussian 03<sup>13,24</sup> (with 50% exact exchange, 50% LDA-level exchange, and LYP correlation functionals), is also inappropriate for the conformational study of the sec-butyl radical. It yields a much deeper potential well about the cis-like conformation. The calculation using the PBE0 (*a.k.a* PBE1PBE) hybrid exchange-correlation functional (with about 25% exact exchange) predicts a potential energy curve with a shallow potential well around  $45^\circ$ , in contrast to the flat surface predicted by the pure PBE/PBE calculation. The other three functionals combine the MPw (modified PW91) exchange functional, the exact exchange functional, and PW91 or meta B95 correlation functionals that were designed to better describe long-range behavior. PBE0 and MPw1K calculations produce similar potential energy curves to those from correlated WFT calculations. MPwB1K and MPw1B95, on the other hand, predict lower-lying curves in the range of  $\theta = 0^\circ - 60^\circ$ , indicating underestimated



repulsion between the two terminal methyl groups.

Based on the PES curves of these various combinations of exchange and correlation functionals, it is evident that incorporating exact exchange is crucial for locating the cis-like conformation. This implies that the non-local exchange-correlation effect must play an important role in this conformational study. At the same time, correlation functionals should also be carefully chosen, since MPw3LYP (Fig. 6.2b), using a similar exchange-correlation functional as MPw1B95 (Fig. 6.2d), predicts a PES profile without any sign of the cis-like conformation.

Some early studies also suggested that the quality of basis functions can be more important than the form of the Hamiltonian used in conformational analysis. The cc-pVDZ and 6-31g(d) basis sets are normally regarded as being too small to correctly capture the dispersion interaction and thus overstabilize the coplanar conformer of biphenyl.<sup>4,5</sup> In a study of thermodynamic properties of radicals, calculations employing the Pople-type basis sets with various methods only achieved converged results after the size of the basis set went beyond 6-311g(d).<sup>25</sup> To visualize the basis-set effect in our current study, the torsional PES profiles of the sec-butyl radical were examined using both B3LYP and MP2 methods with different basis sets.

Because of its single-determinant nature, Kohn-Sham DFT method is often less sensitive to the variation of the basis sets than multi-determinant post-HF methods. In Figure 6.2e, the PES profiles show such insensitivity once the basis sets are beyond cc-pVDZ or 6-31g(d,p), both of which lead to a small cusp at  $\theta \approx 55^\circ$ . The calculations with larger basis sets predict smooth, closely packed, higher-lying PES curves compared with those of the cc-pVDZ or 6-31g(d,p) basis sets. Theoretical results converge very quickly once the basis set goes beyond 6-311++g(d,p). Along with the increased size of the Pople-type basis sets, the PES curve moves upwards without exception. However, the situation within the Dunning basis-set family is complicated. Adding diffuse-functions to the cc-pVDZ or cc-pVTZ basis sets increases the relative energies of the gauche conformation and TS2. On the other hand, the addition of split-valence functions or polarization functions to the basis set results in a moderately less stable gauche conformation and TS2 but a dramatic energy increase for TS0. This implies that, when  $\theta$  is between  $70^\circ$  and  $130^\circ$ , the system may be dominated by long-range interactions in which diffuse basis functions play an important role. Meanwhile, extra split-valence and polarization functions influence the PES curves at small torsion angles.

Other than basis set effects, the quality of integration also affects the accuracy of a DFT calculation. A recent DFT study showed that the quality of numerical integration based on grid summation became critical to accurately predict the equilibrium structure of the sec-butyl cation.<sup>26</sup> Thus, an ultra-fine integration grid consisting of 99 radial shells and 590 angular points per shell was tested against the default grid. No significant difference can be found in Figure 6.2e.

Unlike the Kohn-Sham DFT or HF method, MP2 as well as many other correlated WFT methods are usually sensitive to the size of the basis set because virtual orbitals used to represent excited configurations are not fully optimized during the self-consistent field procedure. MP2 calculations

often require a large basis set to attain convergence to a certain level of accuracy. Past studies of the biphenyl torsional PES indicated that the unbalanced treatment of repulsive and attractive dispersion interactions was caused by the small Dunning's correlation-consistent basis sets used.<sup>4,5</sup> In this study, calculations with the two small basis sets, cc-pVDZ and 6-31g(d,p), overestimate the repulsion between the two terminal methyl groups, whereas the PES profiles obtained from other Pople basis sets lie below those from Dunning's correlation-consistent basis sets. The congregations of the PES profiles within each basis set family suggest a fast convergence for each basis set family. On the other hand, some noticeable difference persists between the two sets of PES curves from the two basis-set families, indicating that either or both of these families are still away from the numerical Hartree Fock limit.

To draw a convincing conclusion, calculations based on more advanced Hamiltonians with larger basis sets are always desirable. Limited by our computer resources and the complexity of these open-shell systems, the most accurate calculations we could afford were single-point CCSD(T)/6-311++g(d,p) calculations at MP2/cc-pVTZ optimized geometries. A similar PES profile with three energy minima was obtained as a result. This resemblance implies that the nearly exact torsional PES profile from CCSD(T) is quite similar to the MP2 one, which thus provides a very informative, accurate description of the torsional PES.

Some key geometric parameters of the stable structures of the sec-butyl radical optimized at both B3LYP and MP2 levels with the cc-pVDZ basis set are listed in Table 6.1. Both of these methods employed predict very similar bond lengths and bond angles for the same stationary structure except that the dihedral angle of the gauche conformation calculated at the B3LYP level differs from that obtained from the MP2 calculation by about 8°. The C2–C3 bond length decreases almost monotonically as the torsional angle increases from 0° to 180°. This indicates that the C2–C3 bond grows stronger from the cis-like conformation to the trans-like conformation because of the weakened repulsion between the two terminal methyl groups. The hydrogen-hydrogen repulsion and hyperconjugation involving C2 and C3 only provide minor corrections to the overall PES, because the energy barrier between the cis-like and trans-like conformations is very small. Among all optimized structures, the C1–C2 bond stretches most in TS1, implying that the internal rotation about the C1–C2 bond plays an important role in forming the rotational barrier between the cis-like and trans-like conformations.

In an early theoretical study by Chen *et al.*, the shallow potential well embracing the cis-like conformation was regarded merely as a shoulder extending from the more stable gauche conformation.<sup>12</sup> If only the static electronic potential energy is considered, the muoniated sec-butyl formed from muonium addition to cis-2-butene will not exist or can be easily converted to the gauche conformation by an extremely small push (*e.g.*, through vibrations) to overcome the tiny barrier. This consideration seems to contradict the experimental observation in which the muon HFCC of this cis-like structure remained strong over a wide range of temperatures. Other effects that may change the stabilities of the molecules must be taken into account. In addition to the electronic

Structure	C1–C2	C2–C3	C3–C4	C2–H4	$\angle$ C1–C2–C3	$\theta$	$E_{ele}$	$E_{ZPC}$	$E_{ZPC,\mu}$
TS0	1.499/1.493	1.505/1.500	1.532/1.532	1.094/1.094	123.7/124.4	0.0/0.0	1.788/1.740	1.547/1.694	1.719/1.891
cis-like	1.500/	1.503/	1.535/	1.095/	120.9/	47.8/	0.683/	0.814/	0.819/
TS1	1.499/	1.501/	1.539/	1.093/	120.6/	55.2/	0.779/	0.476/	0.572/
gauche	1.499/1.492	1.501/1.497	1.543/1.546	1.097/1.096	120.4/122.0	74.1/84.6	0.312/0.553	0.512/0.788	0.904/1.308
TS2	1.497/1.492	1.500/1.497	1.539/1.542	1.095/1.096	121.6/122.6	116.7/114.0	0.841/0.682	0.509/0.632	0.719/0.897
trans-like	1.498/1.492	1.500/1.495	1.532/1.532	1.097/1.096	120.4/121.5	169.0/167.9	0.000/0.000	0.000/0.000	0.000/0.000
TS180	1.497/1.491	1.498/1.494	1.531/1.531	1.094/1.094	120.4/121.1	180.0/180.0	0.299/0.126	–0.293/–0.283	–0.157/–0.121

Table 6.1: Relative energies and geometric parameters of the stationary structures of the sec-butyl radical. The numbers in each column are calculated at MP2/cc-pVDZ (before the slash) and B3LYP/cc-pVDZ (after the slash) levels, respectively. Bond lengths are in Å. Bond angles and dihedral angles ( $\theta$ ) are in degrees. Energies are in kcal/mol. Relative energies ( $E_{ele}$ ) are measured from the global minimal trans-like confirmation. The vibrationally corrected energies are shown in the last two columns for regular (hydrogen) and muoniated isotopomers, respectively.

energy, the zero-point vibrational correction will certainly affect the relative energy difference between two structures in a real sense. More complex thermodynamic corrections must be included for experiments conducted at higher temperatures. In order to make a reasonable comparison with the experimental data at low temperatures, zero-point vibrational and thermal corrections were calculated (Table 6.1). It turns out that the zero-point corrected energy of the muoniated isotopomer in the cis-like form is below that of the muoniated gauche conformation, opposite to their relative stability on the BO surface. Thus, the strong signal of muon HFCC of the muoniated radical (formed from cis-2-butene) can be well understood after the inclusion of the zero-point correction. Another relative stability flip after the vibrational thermal correction occurred for the transition state TS180 connecting the trans-conformation and its mirror image: the transition-state structure becomes the lowest point. This kind of inversion of the BO energy caused by the zero-point correction has been seen in other studies, but without detailed discussion.<sup>7</sup>

## Conclusion

First-principles calculations using spin-unrestricted HF, MP2, CCSD, and a variety of DFT methods with different basis sets were employed to investigate the stable conformations of the sec-butyl radical. Several DFT methods only produced two equilibrium structures whose backbone dihedral angles are about 85° and 170°. All WFT and some DFT methods predicted an extra cis-like stable conformation with a dihedral angle of about 55°, which is separated by a low torsional barrier from the gauche conformation (at  $\theta \approx 85^\circ$ ). Inclusion of the exact exchange and correlation functionals to take care of the long-range behavior correctly is crucial to locate this additional cis-like conformation by DFT methods. The selection of basis sets in B3LYP or MP2 calculations does not alter the number of identified stable conformations, but modifies the overall shape of the PES profiles. To assess the real existence of the stable conformations beyond the electronic-only potential BO surface, vibrational thermal effects, were included. The thermally corrected energies show that the cis-like muoniated conformer could be more stable than the gauche one after the zero-point correction, which agrees with available experiment data.

# Bibliography

- [1] Schleyer, P.; Kaupp, M.; Hampel, F.; Bremer, M.; Mislw, K. *J Am Chem Soc* 1992, 114, 6791.
- [2] Mo, Y.; Gao, J. *Acc Chem Res* 2007, 40, 113.
- [3] Sancho-García, J. C.; Karpfen, A. *Theor Chem Acc* 2006, 115, 427.
- [4] Sancho-García, J. C.; Cornil, J. *J Chem Theory Comput* 2005, 1, 581.
- [5] Tsuzuki, S.; Uchimaru, T.; Matsumura, K.; Mikami, M.; Tanabe, K. *J Chem Phys* 1999, 110, 2858.
- [6] Viruela, P. M.; Viruela, R.; Ortí, E.; Brédas, J. L. *J Am Chem Soc* 1997, 119, 1360.
- [7] Ihee, H.; Zewail, A. H.; Goddard III, W. A. *J Phys Chem A* 1999, 103, 6638.
- [8] King, R. A.; Crawford, T. D.; Stanton, J. F.; Schaefer III, H. F. *J Am Chem Soc* 1999, 121, 10788.
- [9] Chen, Y. K.; Fleming, D. G.; Wang, Y. A. First principles study of hyperfine coupling constants for muoniated butyl radical isomers. To be submitted.
- [10] Hermosilla, L.; Calle, P.; Garcia de la Vega, J. M.; Sieiro, C. *J Phys Chem A* 2005, 109, 1114.
- [11] Knyazev, V. D.; Dubinsky, I. A.; Slagle, I. R.; Gutman, D. *J Phys Chem* 1994, 98, 11099.
- [12] Chen, Y.; Rauk, A.; Tschuikow-Roux, E. *J Phys Chem* 1990, 94, 6250.
- [13] Frisch, M. J.; Trucks, G. W.; Schlegel, H. B.; Scuseria, G. E.; Robb, M. A.; Cheeseman, J. R.; Montgomery, Jr., A. J.; Vreven, T.; Kudin, K. N.; Burant, J. C.; Millam, J. M.; Iyengar, S. S.; Tomasi, J.; Barone, V.; Mennucci, B.; Cossi, M.; Scalmani, G.; Rega, N.; Petersson, G. A.; Nakatsuji, H.; Hada, M.; Ehara, M.; Toyota, K.; Fukuda, R.; Hasegawa, J.; Ishida, M.; Nakajima, T.; Honda, Y.; Kitao, O.; Nakai, H.; Klene, M.; Li, X.; Knox, J. E.; Hratchian, H. P.; Cross, J. B.; Bakken, V.; Adamo, C.; Jaramillo, J.; Gomperts, R.; Stratmann, R. E.; Yazyev, O.; Austin, A. J.; Cammi, R.; Pomelli, C.; Ochterski, J. W.; Ayala, P. Y.; Morokuma, K.; Voth, G. A.; Salvador, P.; Dannenberg, J. J.; Zakrzewski, V. G.; Dapprich, S.; Daniels, A. D.; Strain, M. C.; Farkas, O.; Malick, D. K.; Rabuck, A. D.; Raghavachari, K.; Foresman,

J. B.; Ortiz, J. V.; Cui, Q.; Baboul, A. G.; Clifford, S.; Cioslowski, J.; Stefanov, B. B.; Liu, G.; Liashenko, A.; Piskorz, P.; Komaromi, I.; Martin, R. L.; Fox, D. J.; Keith, T.; Al-Laham, M. A.; Peng, C. Y.; Nanayakkara, A.; Challacombe, M.; Gill, P. M. W.; Johnson, B.; Chen, W.; Wong, M. W.; Gonzalez, C.; Pople, J. A. Gaussian 03 Gaussian, Inc. Wallingford, CT 2004.

- [14] Frisch, M. J.; Pople, J. A.; Binkley, J. S. *J Chem Phys* 1984, 80, 3265.
- [15] Clark, T.; Chandrasekhar, J.; Spitznagel, G. W.; Schleyer, P. *J Comput Chem* 1983, 4, 294.
- [16] Kendall, R. A.; Jr., T. H. D.; Harrison, R. J. *J Chem Phys* 1992, 96, 6796.
- [17] Wong, M. W.; Radom, L. *J Phys Chem* 1995, 99, 8582.
- [18] Wong, M. W.; Radom, L. *J Phys Chem A* 1998, 102, 2237.
- [19] Becke, A. D. *J Chem Phys* 1993, 98, 5648.
- [20] Lee, C.; Yang, W.; Parr, R. G. *Phys Rev B* 1988, 37, 785.
- [21] Perdew, J. P. *Electronic Structure of Solids*; Ziesche, P.; Eschrig, H., Eds.; Akademie Verlag, Berlin, 1991; p. 11.
- [22] Burke, K.; Perdew, J. P.; Wang, Y. *Electronic Density Functional Theory: Recent Progress and new Directions*; Dobson, J. F.; Vignale, G.; Das, M. P., Eds.; Plenum, 1997; p. 81.
- [23] Becke, A. D. *J Chem Phys* 1995, 104, 1040.
- [24] Becke, A. D. *J Chem Phys* 1993, 98, 1372.
- [25] Mayer, P. M.; Parkinson, C. J.; Smith, D. M.; Radom, L. *J Chem Phys* 1998, 108, 604.
- [26] Vrček, V.; Kronja, O.; Saunders, M. *J Chem Theory Comput* 2007, 3, 1223.

## Chapter 7

# Conclusions and Future Directions

We have studied the effect of introducing single transition metal (TM) atoms into different systems, including small Au clusters, pristine, Stone-Wales defected and single-vacancy defected boron nitride nanotubes (BNNTs), and single-vacancy defected carbon nanotubes (CNTs).

In Chapter 2, small homonuclear  $\text{Au}_m$  ( $m \leq 5$ ) and bimetallic  $\text{PtAu}_n$  ( $n \leq 4$ ) clusters were studied using DFT. Both homonuclear and bimetallic clusters tend to form compact 2-dimensional structures. In  $\text{PtAu}_n$  ( $n > 2$ ) clusters, the Pt atom tends to situate at the location that maximizes its coordination number. All the low-lying  $\text{Au}_m$  clusters have delocalized highest occupied molecular orbitals (HOMOs), whereas all the  $\text{PtAu}_n$  clusters have more localized HOMOs on the Pt atom. The localized HOMO makes the  $\text{PtAu}_n$  clusters more regioselective towards electrophilic reactions than the  $\text{Au}_m$  clusters. In open-shell bimetallic clusters, the spin density is localized on the Pt atom, which behaves as the active center in further reactions with radicals.

Adsorptions of  $\text{N}_2$  and  $\text{O}_2$  onto these metal clusters were also studied. In  $\text{N}_2$  adsorption, the metal clusters donate their electrons primarily to the  $\sigma^*$  orbitals of  $\text{N}_2$  to form end-on complexes preferably. In  $\text{O}_2$  adsorption, complicated  $\pi$  orbital interactions between the cluster and  $\text{O}_2$  dominate to form side-on complexes with relatively larger binding energies. The HOMOs of the  $\text{N}_2$ -bimetallic cluster adsorption complexes remain localized on the Pt site, but with varied directionality, while the adsorption of  $\text{O}_2$  onto the Pt site delocalizes the HOMO onto the O atoms.

We have exhibited the dependence of electronic structure of  $\text{PtAu}_m$  clusters on their compositions. These results are helpful for further studies that seek to optimize the reactivity of Pt based catalysts. The result of the  $\text{O}_2$ -cluster adsorption study is also a good starting point for further investigation of the cathode reaction of fuel cells: a reaction bottlenecks fuel cell efficiency and performance.

In Chapter 3, we examined the possibility of doping first-row TM atoms in the single-vacancy defect in (5,5) CNTs to the exterior and interior in order to find the stable TM-doped SWCNTs, and to investigate their properties.

Before this study, we had studied the relative stabilities of endo- and exo- halogen atom (Se, Te) doped SWCNTs.<sup>1</sup> The endo configuration were revealed to be unfavorable compared with the exo one. The dopant chalcogen atom forms only two bonds with two of the vacancy site carbon atoms, leaving the third vacancy site carbon atom with dangling bonds. Therefore, TM atoms, with their versatile bonding capabilities and large radii, were expected to be more favorably doped on the interior into the single vacancy defected SWCNTs.

We have studied single-walled carbon nanotubes (SWCNTs) doped with transition metal (TM) atoms with both exo and endo doping configurations. The electronic and geometric properties of these TM-doped SWCNTs were calculated within density functional theory. It was found that the endo-doped SWCNTs are less stable than the associated exo-doped systems due to the large geometric strain of the deformation in the endo-doped nanotubes. Based on Mulliken charge analysis, the TM-doped SWCNTs have localized net charge distributions, whereas the spin densities in Sc-, Co-, and Cu-doped SWCNTs are delocalized over the entire nanotubes. The TM-doped SWCNTs are mostly metallic or narrow-gap semiconductive. With highly localized frontier molecular orbitals, the exo-doped SWCNTs are better electron donors than the corresponding endo-doped ones. As the dopant TM changes from Sc to Zn in the same row of the periodic table or from the top to the bottom in the same Pt group, the energy of the highest occupied crystal orbital of the TM-doped SWCNTs decreases, indicating a reduced electron donating ability. The TM-doped SWCNTs were also found to exhibit similar properties for dopant atoms within the same Pt group.

Though not all the TMs were examined, one can conjecture that the endo second and third row TM doped SWCNTs should be even much less stable than their exo-doped counterparts, as demonstrated by the study of Ni, Pd, and Pt doped CNTs. This conjecture roots in the fact that the energy and radius differences between  $4s$  and  $3d$  orbitals for the first TM row are generally larger than that between  $5s$  and  $4d$  or  $6s$  and  $5d$  orbitals for the second and third TM rows, respectively. To understand the energy difference between the endo- and exo-doped CNTs extensively at a quantitative level, theoretical calculations involving more transition metals and carbon nanotubes of other sizes will be carried out by other members in our group.

In this study, endo-TM doped CNTs proved to be always less stable than their exo doped counterparts, but the door to functionalizing the SWCNTs interiorly is not shut completely because other than doping single TM atoms interiorly, the interior adsorption of Co in the (8,8) SWCNTs<sup>2</sup> proved to be more stable than the exterior adsorption. In addition to this, functionalizing SWCNTs interiorly can also be achieved by attaching bulky groups to the dopant or adsorbate inside nanotubes so as to prevent their outward configurational inversion. There can be more mean to functionalize nanotubes on the interior.

In Chapter 4, interactions between atomic Pt and pristine or Stone-Wales-defected (5,5) single-walled boron nitride nanotubes (BNNTs) were studied using density functional theory (DFT) with truncated nanotube models. The atomic Pt adsorption on the pristine BNNTs results in a relatively constant adsorption energy of about 20 kcal/mol regardless of adsorption site, which implies the possible mobility on the outside surface of pristine BNNTs. On the other hand, the Pt is preferably absorbed around the defect site of a SW defected BNNT. By alleviation of the geometric strain and the frustrated direct B–B bond, the Pt can be favorably inserted between the frustrated B–B bond, with an adsorption energy of about 60 kcal/mol. But this adsorption energy decreases drastically to about 20 kcal/mol even if the adsorbate Pt atom moves only several bonds away from the B–B bond. This indicates the Pt will be eventually trapped in the defect site if a SW defect site exists in



a BNNT. Electronic structures were studied by analyzing the density of states (DOS) and frontier orbitals of these systems. The Pt atom can modify the electronic structures of pristine and SW-defective BNNTs by introducing Pt states into the nanotube band gaps and can thus make these nanotubes mildly more reactive. In comparison, the Pt atom filling into a B or N single vacancy on a BNNT changes the electronic structure of the vacancy-defected BNNT so dramatically that the Pt-doped BNNT becomes semiconducting with much improved reactivity.

Based on this study, the finetuning of the reactivity of the absorbed Pt atom can be achieved through introducing various defect sites, such as Stone-Wales defect, single-vacancy defect, into a pristine BNNT.

From the above three studies, the Pt atom introduced to the small gold clusters and nanotubes usually use its outmost 6s orbital to form chemical bonds with the hosting systems. Therefore, the HOMOs of the adsorption or doping products are mainly composed of 5d orbitals of the Pt atom. Similarly, the HOMOs of the TM doped CNTs are mainly constituted by the valence *d* orbitals of the transition metals. Introducing TM atoms in these hosting systems typically results in localized HOMOs and enhanced regioselective electron donating abilities.

Moreover, some Pt-modified systems exhibit tunable electron donating abilities. This is very important for some reactions catalyzed by TM atoms and TM compounds, especially for some multi-step reactions that involve binding and unbinding between the intermediates and TM catalysts. Based on several studies here, the finetuning of the reactivity of the absorbed Pt atom is accessible by loading Pt to different sites of some hosting systems.

Besides several potential applications of the Pt modified systems revealed here, there is also a trend observed that can be predicted by a principle in conceptual DFT—the maximized hardness principle (MHP), which states that the hardness (approximately proportional to the HOMO-LUMO gap) tends to increase as analogous molecules become more stable. In Chapter 2, the largest hardness values is often accompanied with the most stable N<sub>2</sub>/O<sub>2</sub>-cluster complexes, and the hardness value is lowered gradually along with the decrease of the stability for the same isomer. The same trend is also found in the case of Pt atom absorption onto pristine and SW-defected BNNTs: as the Pt is trapped between the two boron atoms, which is the most stable adsorption complex, the HOMO-LUMO gap of the absorption adduct reaches its maximum and the hardness becomes smaller when Pt moves to other less favorable sites.

In Chapter 5, in collaboration with Prof. Donald G. Fleming, a theoretical study of muon (Mu) hyperfine coupling constants (HFCCs) was carried out to assign structures and to reveal the physics relevant to temperature-dependent HFCCs.

We have studied HFCCs of the radicals produced by muonium (Mu) addition to butene isomers (1-, 2-, and iso-butene) by first-principles calculations. The equilibrium geometries and HFCCs for muons and protons of these muoniated butyl radicals and their proton isotopomers were obtained at the spin-unrestricted MP2/EPR-III and B3LYP/EPR-III levels of theory. Based on comparisons with experiment, the muon adducts are believed to be eclipsed radicals. A C–Mu bond elonga-

tion scheme that stretches the equilibrium C–H bond length by a factor of 1.076 was exploited to estimate the vibrationally corrected muon HFCCs. Calculated HFCCs were used to assign experimental HFCCs of the muoniated radicals discussed in the companion experimental paper. In comparison with the B3LYP method, the MP2 method is more reliable in predicting the equilibrium conformations according to the experimental results. In many cases, B3LYP calculations yielded much higher muon HFCCs at 0 K that agree better with the experimental HFCCs extrapolated to 0 K than MP2 calculations. This better agreement is likely due to error cancellations, which makes up for the vibrational and environmental effects not included in both calculations. The electronic contributions to torsional barriers were also calculated in comparison with the barriers determined phenomenologically in the companion experimental paper. The temperature dependences of the muon and proton HFCCs were also discussed at a qualitative level. The reason for the discontinuities appeared in the temperature-dependent HFCC plot were also rationalized qualitatively.

Though first order and partial second order vibrational corrections can be obtained by using the average geometry scheme, the rest of second order and higher order corrections are still at large and usually cause up to 10% difference between theoretical predictions and low-temperature experimental observations. Perturbation theory has shown some power for calculating up to second order corrections and in principle can be used for higher order corrections. Nevertheless, to obtain the first and second order corrections requires many extra single point calculations that are only realistic for small molecules. Further thermal corrections can also be calculated using perturbation theory together with the Maxwell-Boltzmann formula to account for thermally excited populations. Further work is still desired to reveal how the vibrational and thermal corrections affect (temperature-dependent) HFCCs.

Another mystery that remains is the role of the environmental, which was believed to be responsible for the discontinuities of the temperature dependent HFCCs for some muoniated butyl isomers. Because of the lack of solid state parameters of the precursor alkenes and the large demands in the calculation of liquid phase using explicit solvation models, it is very hard for us to explain which effect is mainly responsible for these discontinuities by using contemporary theoretical methods, not to mention that we are short of tools for calculating vibrational and environment corrections simultaneously at an acceptable cost.

Overall, even a qualitative explanation of the temperature-dependent HFCCs still needs large amounts of computation that can treat the electronic, vibrational, thermal, and environmental effects at the same time. Moreover, non-Born-Oppenheimer behaviors can also complicate the situation. Therefore, there is still much work to do to achieve a quantitative understanding of temperature-dependent HFCCs of muoniated radicals.

As a secondary study to the HFCC calculations, the sec-butyl torsional PES was studied in Chapter 6. First-principles calculations were carried out to investigate the torsional potential energy surface (PES) of the sec-butyl radical. All methods based on wave function theory predict a cis-like stable conformation with the C–C–C–C dihedral angle of about  $47^\circ$ , in addition to two more

energy minima: the global minimum trans-like conformation and a gauche conformation. Most popular density functional theory (DFT) approaches miss the experimentally observed cis-like conformation. However, some DFT methods that incorporate the exact exchange and asymptotically corrected correlation functionals can locate the cis-like conformation successfully. The basis-set effect was also analyzed with popular B3LYP and MP2 Hamiltonians. Upon changing the basis sets, we only observed some moderate variations in the shapes of the PES profiles. The stationary structures and their Hessians were calculated at both MP2 and B3LYP levels of theory, with or without incorporating the zero-point vibrational energies. Consistent with the experiment observations, the cis-like conformation is more stable than the gauche one upon the zero-point correction.

The electronic internal rotation about the C–C bond in an ethyl radical was calculated to be 0.17 kcal/mol, one order of magnitude smaller than the ethane internal rotation barrier, which is already small and whose physical nature is still under debate. High-level correlated calculations, such as at CI and CC levels, should be used to verify the real torsional PES. However, for practical calculations with limited computational resources, in addition to the MP2 method that was found to be adequate for the PES study of sec-butyl radical, DFT with exact-exchange incorporated exchange functionals and have asymptotic behavior corrected correlation functionals can be another choice.

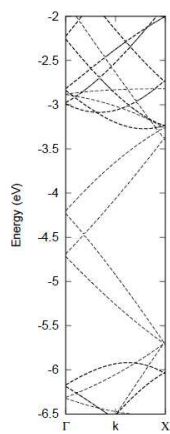
From the above two chapters, it can be seen that theoretical tools are quite useful and sometimes crucial in explaining experimental results. The sole knowledge of experimental muon or proton HFCCs can only provide local spin charge distribution information. To get a complete view of the system, the experimental HFCC information must be used together with other techniques, in this case, theoretical calculations to assign the structures and reveal the physics behind the experimental results.

# Bibliography

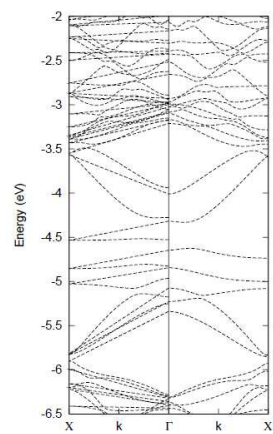
- [1] W. Q. Tian, L. V. Liu, Y. K. Chen, and Y. A. Wang. *Electronic Structure and Reactivities of Perfect, Defected, and Doped Single-Walled Carbon Nanotubes*. Springer, Heidelberg, 2009.
- [2] Y. Yagi, T. M. Briere, M. H. F. Sluiter, V. Kumar, A. A. Farajian, and Y. Kawazoe. Stable geometries and magnetic properties of single-walled carbon nanotubes doped with 3d transition metals: a first-principles study. *Phys. Rev. B*, 69:075414, 2004.

## **Appendix A**

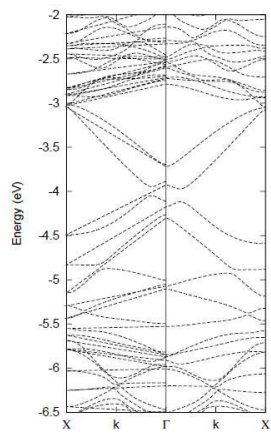
### **Supporting Information for Chapter 3**



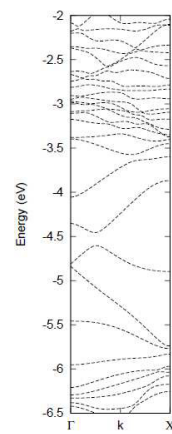
pristine



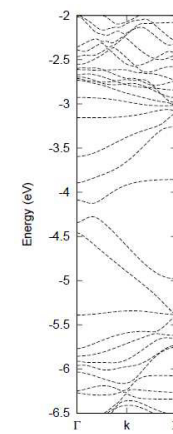
endo-Sc-doped



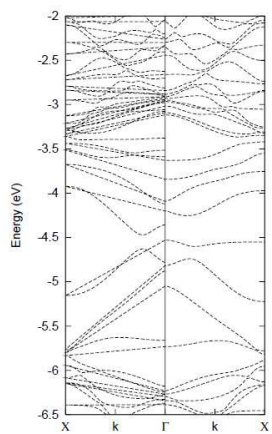
exo-Sc-doped



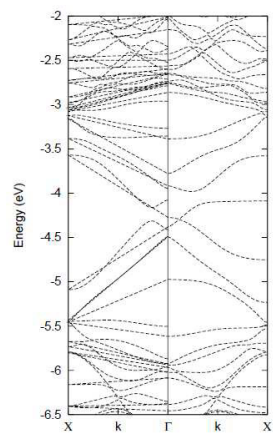
endo-Ti-doped



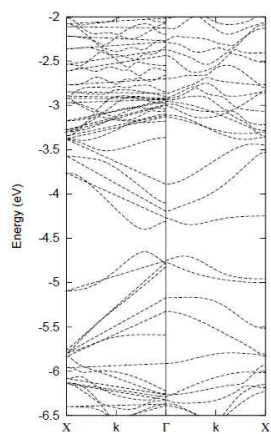
Ti exo-Ti-doped



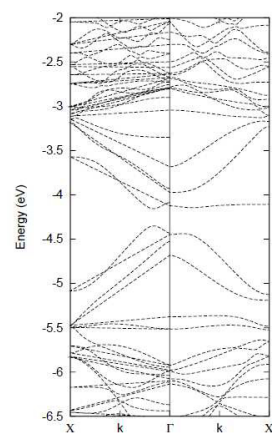
endo-V-doped



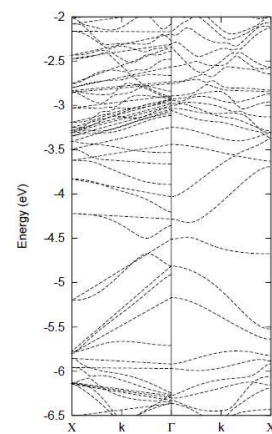
exo-V-doped



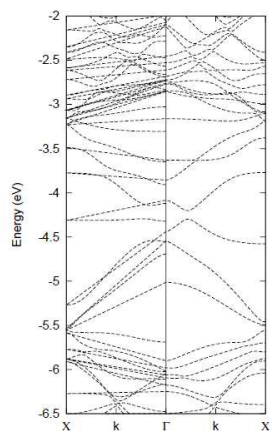
endo-Cr-doped



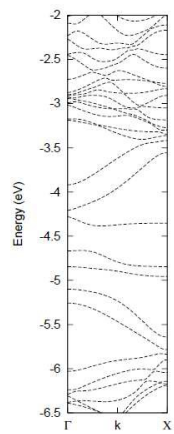
exo-Cr-doped



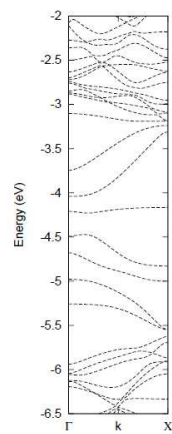
endo-Mn-doped



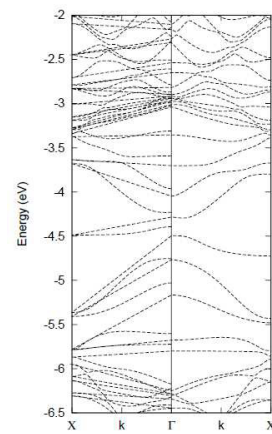
exo-Mn-doped



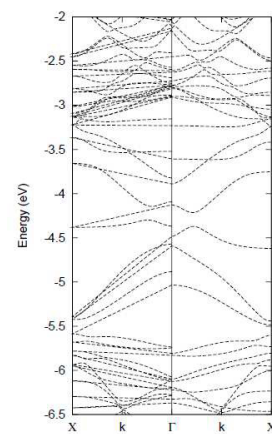
endo-Fe-doped



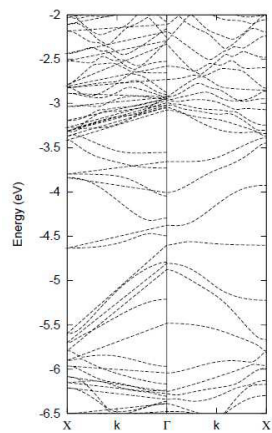
exo-Fe-doped



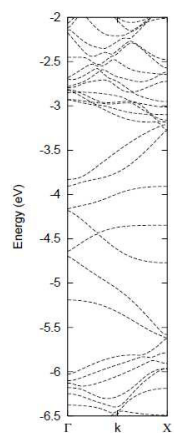
endo-Co-doped



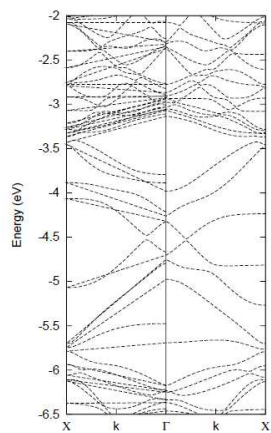
exo-Co-doped



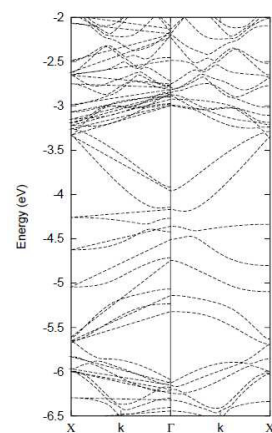
endo-Ni-doped



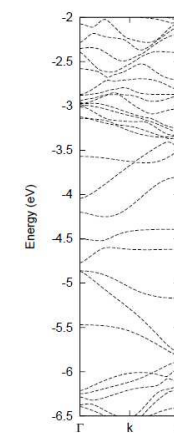
exo-Ni-doped



endo-Cu-doped



exo-Cu-doped



endo-Zn-doped

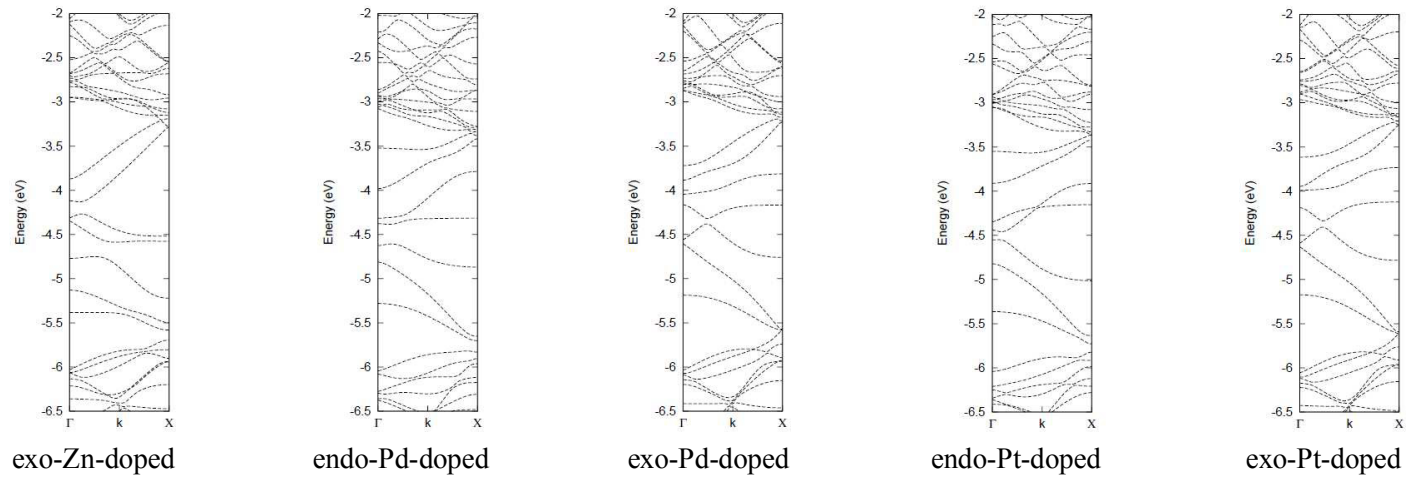


Figure A.1: Band structures for pristine and doped (5,5) SWCNTs. For spin-unsaturated systems, the left panel is for  $\beta$  spin and the right panel,  $\alpha$  spin.